UNIVERSITY OF LIVERPOOL

# Using nanotopography and macromolecular crowding to influence *in vitro* collagen deposition in a corneal stroma model

Thesis submitted in accordance with the requirements of the University of Liverpool for the degree of Doctor in Philosophy

By

Danielle April O'Loughlin

August 2021

## Abstract

The corneal stroma is a transparent and avascular tissue constituting 90% of the cornea. The stroma comprises collagenous lamellae, oriented roughly orthogonally, and is populated by quiescent keratocytes. *In vitro* models of the stroma can be used for a variety of applications from drug toxicity to investigating the mechanisms of collagen fibril alignment. There are several drawbacks of current models: the orientation of collagen is not always considered; cell sheets are often manually stacked, a technically challenging and unreliable method; and cells typically require an extended culture period (several months) to create a construct that resembles the stroma. This project aimed to overcome these problems by providing cells with topographical cues to induce the deposition of an aligned matrix, with stratification and rotation of the deposited collagens. Macromolecular crowding (MMC) was incorporated into the model to accelerate collagen deposition.

The aim of this study was to develop an *in vitro* model that faithfully resembled the corneal stroma. Corneal stromal stem cells (hCSSCs), human corneal fibroblasts (hCFs) and human bone marrow mesenchymal stromal cells (hMSCs) were isolated, characterised and assessed for their ability to resemble keratocytes using immunocytochemistry. hCFs were readily expanded whilst hMSCs showed differentiation potential towards keratocyte lineage. hCSSCs could not be isolated and cultured in sufficient quantities, therefore, this cell type was not taken forward for subsequent use.

Two substrates, polytetrafluoroethylene nanofibres on glass and polycarbonate Transwell membranes, were investigated. hMSCs were cultured in control and differentiating media for 21 days. Differentiated hMSCs often formed cell pellets, regardless of the substrate or presence of topographical cues and lacked the expression of keratocyte markers. hCFs, cultured for up to 30 days, positioned themselves to align along the nanofibres and the orientation of deposited collagen was found to follow the direction of the cells. There was a shift in orientation as the cells stratified, resembling the lamellae of the stroma. hCFs cultured on the Transwell membranes stratified and appeared to deposit more collagen, although alignment was reduced.

MMC accelerates the deposition of extracellular matrix proteins such as collagen. To increase matrix deposition within the tissue engineered construct MMC was used. The use of carrageenan as a crowder accelerated the deposition of collagen, determined by ICC and the use of a collagen probe. However, the deposition of collagen was disrupted forming aggregates that showed little alignment. Crowding with a Ficoll cocktail appeared to increase the deposition of collagen without disrupting alignment but ultrastructural analysis suggested there was cellular uptake of Ficoll.

Collectively, these results suggest that culturing hCFs on aligned PTFE nanofibres is the most efficient method to mimic a lamella of the corneal stroma. Crowding with a Ficoll cocktail can enhance collagen deposition but the effects of the cellular uptake of Ficoll molecules may require further investigation.

## Acknowledgments

Firstly, I would like to say a huge thank you to my supervisory team – Elizabeth Laird, Hannah Levis, Victoria Kearns and Carl Sheridan. I could not have completed this project without their endless support, patience and guidance, particularly when things did not go to plan.

Thank you to Adam Janvier and Daniel Green for both the supply of MSCs and their contribution to the flow cytometry data. I would also like to thank Alison Beckett, within the University of Liverpool's Biomedical EM unit, for her help with processing samples for TEM and guidance with imaging. Thank you to Stephanie Edwards for her help with the DLS. A special thanks to both James Funderburgh and Martha Funderburgh for the invitation to their lab in Pittsburgh to learn first-hand how to isolate CSSCs. You made my first trip to America so enjoyable and it is a memory I will always cherish.

I would like to thank everyone in both EVS and CMS who has supported me throughout this project and offered their guidance and support. I'd particularly like to thank Jess, Alys, Georgia, Katie and Megan not only for their help in the lab but for also making the difficult times a lot easier.

Finally, I would like to thank my family and friends outside of the lab. To my mum and dad, thank you for always believing in me. Saghi and Haleh, thank you for your support, particularly whilst I was writing my thesis. Arsham, from the bottom of my heart, thank you for everything. Your support has meant so much to me and it would have been very difficult to complete this project without your love and encouragement.

Funding acknowledgements: This project was funded by Samuel Crossley Barnes Bequest studentship. I would also like to acknowledge the University of Liverpool's Technology Directorate for co-funding the live cell imaging work.

# Table of Contents

## Index of figures

## Index of tables

## List of abbreviations

| | |
|---|---|
| 18S RNA | 18S ribosomal RNA |
| A2P | L-ascorbic acid 2-phosphate sesquimagnesium salt hydrate |
| A2PM | Media supplemented with A2P |
| AB | Alcian blue |
| ABCG | Adenosine triphosphate (ATP)-binding cassette super-family G |
| ACTB | Actin beta |
| ADAMTs | A disintegrin and metalloproteinase with thrombospondin motifs |
| AF | Annulus fibrosus |
| AGE | Advanced glycation end-products |
| ALDH | Aldehyde dehydrogenase |
| ANOVA | Analysis of variance |
| AQP | Aquaporin |
| AR | Alizarin red |
| B2M | Beta-2 microglobulin |
| BCA | Bicinchoninic acid |
| Bp | Base pairs |
| BSA | Bovine serum albumin |
| CAR | Media supplemented with carrageenan |
| CD34 | Haematopoietic progenitor cell antigen CD34 |
| CD73 | 5'-nucleotidase |
| CD90 | Thy-1 |
| cDNA | Complementary deoxyribonucleic acid |
| CHST | Carbohydrate sulfotransferase |
| Col/COL | Collagen |
| CTR | Cell tracker red |
| Da | Dalton |
| DAPI | 4', 6-Diamidino-2-Phenylindole |
| DLS | Dynamic light scattering |
| DMEM | Dulbecco's modified Eagle's medium |
| DMMB | Dimethyl-methylene blue |
| DMSO | Dimethyl sulfoxide |
| DNA | Deoxyribonucleic acid |
| ECM | Extracellular matrix |
| EGF | Epidermal growth factor |
| ER | Endoplasmic reticulum |
| FACS | Fluorescently activated cell sorting |
| F-actin | Filamentous actin |
| FBS | Foetal bovine serum |
| FC | Media supplemented with Ficoll cocktail |
| FGF | Fibroblast growth factor |
| FLS | Fibrous long-spacing |
| FSC | Forward scatter |
| FVO | Fractional volume occupancy |
| GAG | Glycosaminoglycan |
| GAPDH | Glyceraldehyde 3-phosphate dehydrogenase |
| hCF | Human corneal fibroblast |

| | |
|---|---|
| hCK | Human corneal keratocytes |
| hCSSC | Human corneal stromal stem cells |
| hMNC | Human mononuclear cells |
| hMSC | Human mesenchymal stromal cell |
| IBMX | 3-isobutyl-1-methylxanthine |
| ICC | Immunocytochemistry |
| IGF | Insulin-like growth factor |
| IgG | Immunoglobulin G |
| IL | Interleukin |
| IPTG | Isopropyl β-d-1-thiogalactopyranoside |
| ISCT | International Society for Cellular Therapies |
| ITS | Insulin, transferrin, selenium |
| KDM | Keratocyte differentiating media (KDM) |
| KERA | Keratocan |
| KSPGs | Keratan sulphate proteoglycans |
| LB | Luria broth |
| LESCs | Limbal epithelial stem cells |
| LSM | Laser scanning microscope |
| LUM | Lumican |
| MEM | Minimum essential medium |
| MMC | Macrmolecular crowding |
| M-MLV RT | Moloney Murine Leukemia Virus Reverse Transcriptase |
| MMP | Matrix metalloproteinase |
| MPC | 2-methylacryloyloxyethyl phosphorylcholine |
| Ms. | Mouse |
| MW | Molecular weight |
| NBF | Neutral buffered formalin |
| NC | Non-collagenous |
| NEAA | Non-essential amino acids |
| NES | Nestin |
| NHS | *N*-hydroxysuccinimide |
| OCT | Octamer-binding transcription factor |
| ORO | Oil red O |
| PAX | Paired box protein |
| PBS | Phosphate buffer solution |
| PBST | 0.1% Tween-20 in PBS |
| PCPE | Procollagen proteinase enhancer |
| PCR | Polymerase chain reaction |
| PDGF | Platelet-derived growth factor |
| PEG | Polyethylene glycol |
| PGs | Proteoglycans |
| Pn | Passage n (e.g. passage 3 (P3)) |
| PSS | Polysodium-4-styrene sulfonate |
| PTFE-nf | Polytetrafluoroethylene nanofibres |
| PTGDS | Prostaglandin D2 synthase |
| PVP | Polyvinylpyrrolidone |
| Rb. | Rabbit |
| RFU | Relative fluorescent units |

| | |
|---|---|
| RHC | Recombinant human collagen |
| RNA | Ribonucleic acid |
| ROCK | Rho-associated protein kinase |
| ROI | Region of interest |
| RT-qPCR | Reverse transcription quantitative real-time polymerase chain reaction |
| SCM | Stromal cell media (hMSCs) |
| SLRPs | Small leucine-rich proteoglycans |
| SMA | Smooth muscle actin |
| SOX | Sex determining region Y box |
| SSEA | Stage-specific embryonic antigen |
| T25/T75/T175 | Culture flasks with surface area of 25/75/175cm$^2$ |
| TE | Tris-ethylenediaminetetraacetic acid |
| TEM | Transmission electron microscopy |
| TGF | Transforming growth factor |
| TIMP | Tissue inhibitor of metalloproteinase |
| TNF | Tumour necrosis factor |
| UV | Ultraviolet |
| VIM | Vimentin |
| VSI | Vertical scanning interferometry |
| α-SMA | α-smooth muscle actin |

# Chapter 1. Introduction

## 1.1 Overview

The corneal stroma, a transparent tissue, makes up approximately 90% of the total cornea. It is composed primarily of heterotypic type I/V collagen fibrils that are restricted in diameter to maintain transparency of the tissue. Keratocytes are the quiescent cells that are responsible for maintaining the collagens and proteoglycans within the tissue. Keratocytes express corneal crystallins to reduce light scattering, allowing for light transmission onto the retina.

In accordance with the National Centre for the Replacement, Refinement & Reduction of Animals in Research, there is a need to reduce the use of animal models. One such alternative is the use of *in vitro* models and there is, therefore, a need for models of the corneal stroma. These models would enable the investigation of wound healing, collagen fibrillogenesis and pharmacological testing, all whilst reducing the number of animals used in research. Given the complex microarchitecture of the stroma, several challenges arise when trying to tissue engineer an *in vitro* model, such as selecting an appropriate cell type (as described in Chapter 2) and substrate (described in Chapter 3) that leads to the deposition of a uniform extracellular matrix (ECM), resembling that found *in vivo*.

Drawbacks of current *in vitro* models include the use of cell sheets cultured on tissue culture plastic which do not share the unique, organised collagen layers. Furthermore, the current models can take up to 9 weeks to create, risking the cells undergoing phenotypic drift and increasing the risk of contamination. Culturing cells on a substrate that provides topographical cues to induce the deposition of aligned collagen fibrils combined with a method of increasing ECM deposition, such as macromolecular crowding (Chapter 4), holds the potential to overcome these shortcomings.

### 1.1.1 The basic structure and function of the human cornea

The cornea is a transparent, avascular tissue which forms the outermost layer of the eye. Its key functions are to protect the eye, by acting as physical barrier; to transmit light by maintaining transparency; and to provide the majority of the refractive power necessary to focus light on to the retina (Meek and Knupp, 2015). Each of the cellular layers plays a unique role to maintain homeostasis within the tissue (Figure 1.1).

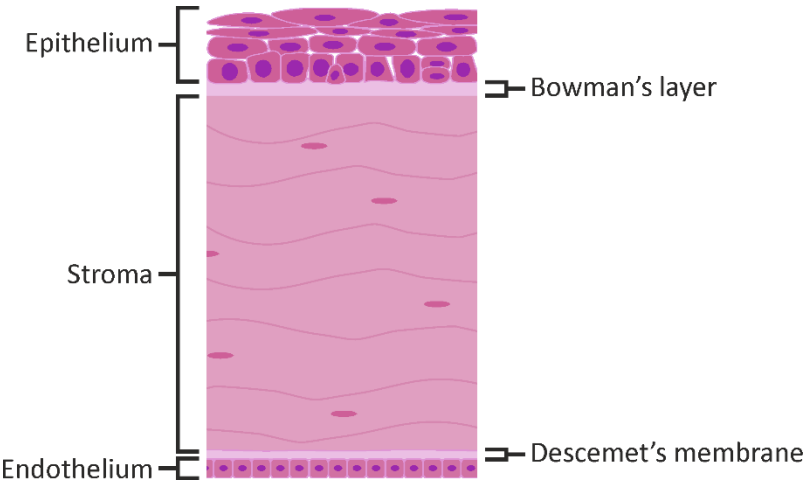


**Figure 1.1 Diagrammatic representation of the distinct layers within the cornea.**

The tear film is the outermost layer of the ocular surface, providing a boundary between the epithelium and the environment. The tear film lubricates the surface of the eye whilst also protecting the eye from microbes via the secretion of defensins (Zhou *et al.*, 2004; Pflugfelder and Stern, 2020). The epithelium is at the surface of the cornea and provides the majority of the refractive power at the air/tear interface whilst also providing a surface barrier that prevents the encroachment of pathogens (Eghrari *et al.*, 2015). It is composed of 5-6 layers of stratified epithelial cells that turnover approximately every 7 days (Hanna *et al.*, 1961). Tight junctions provide a continuous seal around the superficial cells that prevents the passage of molecules and pathogens between adjacent epithelial cells and into the stroma (Sugrue and Zieske, 1997; DelMonte and Kim, 2011). The cells in the basal layer of the epithelium are columnar in shape and are connected to the basement membrane, comprised of type VI collagen and laminin, via hemidesmosomes (Wijnholds, 2019). Beneath the basement membrane lies the Bowman's layer, an acellular layer comprised of collagen types I, III, V and VII fibrils which are randomly arranged and have an average diameter of 20-25 nm (Komai and Ushiki, 1991). The function of the Bowman's layer is not completely understood but it has been hypothesised that it plays a role in facilitating stromal wound repair (Lagali *et al.*, 2009).

Beneath the Bowman's layer is the corneal stroma, the primary component of the cornea making up around 90% of the cornea with an average thickness of 461.8 – 465.4 µm (Reinstein *et al.*, 2009). The stroma is composed of layers of aligned collagen fibrils (lamellae) which are oriented roughly orthogonally throughout (Radner *et al.*, 1998; Chen *et al.*, 2015). Interspersed between these lamellae are quiescent keratocytes, neural crest-derived mesenchymal cells with an almost dendritic morphology with lamellipodia that connect the

cells together (Fini, 1999; West-Mays and Dwivedi, 2006). The Descemet's membrane resides below the stroma and is both collagenous and acellular (Eghrari *et al.*, 2015). This membrane is the basement membrane of the corneal endothelium and contains both collagen types IV and VIII. There have also been reports of an acellular pre-Descemet's layer termed Dua's layer (Dua *et al.*, 2013, 2014; Zaki *et al.*, 2015; Dua and Said, 2016) however there is some controversy around this and the tissue identified may be a section of the stroma where the keratocytes are more widely spaced (Jester *et al.*, 2013; McKee *et al.*, 2014; Schlötzer-Schrehardt *et al.*, 2015).

The innermost layer of the cornea is the corneal endothelium, a monolayer of non-replicative cells. Most of the nutrients required by the cornea are transported from the aqueous humour in the anterior chamber through the endothelium. The endothelium is also responsible for maintaining transparency by regulating the hydration of the cornea through a 'leaky' barrier and active sodium-potassium adenosine triphosphase pumps (Bonanno, 2012). The endothelium pumps fluid out of the stroma, preventing swelling and haze whilst also 'leaking' to allow water and nutrients into the stroma (Hertsenberg and Funderburgh, 2015). The loss of cells from the endothelium leads to swelling of the stroma which results in a loss of transparency (Meek *et al.*, 2003).

## 1.2 The corneal stroma

The stroma, constituting a large proportion of the cornea, must provide mechanical support to protect the eye, whilst also remaining transparent so that light can be refracted on to the retina. Keratocytes, the main cell within the stroma, are responsible for synthesising the ECM whilst also expressing cytosolic corneal crystallins to reduce light scattering. The intricate microarchitecture of the stroma, with its lamellae of collagen, is responsible for both withstanding intraocular pressure and ensuring transparency.

### 1.2.1 Collagens

Collagens are triple helical proteins that are found in the ECM. They can be classified based on their structure and supramolecular assembly such as fibril-forming (e.g., type I), fibril-associated collagens with interrupted triple helices (FACIT; e.g., type IX) and beaded-filament-forming collagens (e.g., type VI) (Kadler *et al.*, 2007). The polypeptide chains that form the triple helix are comprised of the sequence glycine-X-Y in which X and Y are often proline and hydroxyproline (Kadler *et al.*, 1996).

Fibrillar collagens are the most abundant collagens in vertebrates and their formation has been extensively studied (Birk and Trelstad, 1986; Canty *et al.*, 2004; Canty and Kadler, 2005; Kadler *et al.*, 2008). The secretory pathway is where proteins are synthesised and carried to the cell surface membrane, via the ER and Golgi apparatus, to be secreted into the extracellular space, depicted in Figure 1.2. Following translation, procollagen chains in the endoplasmic reticulum (ER) undergo hydroxylation of proline and lysine (Harwood *et al.*, 1975). Prolyl hydroxylase and lysyl hydroxylase, enzymes required to convert proline and lysine to hydroxyproline and hydroxylysine, both require ascorbic acid (vitamin C) as a cofactor to function (Gelse *et al.*, 2003). In the absence of ascorbic acid, hydroxyproline is not usually formed, which is necessary for the formation of the triple helix and thus procollagen cannot easily leave the ER (Canty and Kadler, 2005). Similarly, hydroxylysine is required for the cross-linking of collagen fibres and so in the absence of ascorbic acid, collagen fibres are unstable (Eyre and Wu, 2005). Glycosylation, an additional post-translational modification, can also occur on lysine and hydroxylysine residues (Perdivara *et al.*, 2013). Although the role of collagen glycosylation is not clearly defined, it is thought to play a role in fibrillogenesis, cross-linking and, collagen-cell interactions (Yamauchi and Sricholpech, 2012). Following post-translational modifications, triple helix nucleation occurs at the C-propeptides of procollagen chains and a procollagen triple helix is formed (Canty and Kadler, 2005). This is a precursor for collagen molecules in that it is flanked at either end by N- and C- propeptides. The procollagen is then transported to the plasma membrane, via the Golgi apparatus, in Golgi-to-plasma-membrane carriers (GPCs) and released from the cell. Here, procollagen is cleaved by C-proteinases (BMP-1/tolloid family) and N- proteinases (a disintegrin and metalloproteinase with thrombospondin motifs; ADAMTS 2, 3 and 14) to form tropocollagen, a collagen monomer (Kadler *et al.*, 2007). Procollagen cleavage can be enhanced by proteins such as procollagen C-proteinase enhancer 1 protein (PCPE-1) and this conversion of procollagen to collagen has also been shown to occur intracellularly within GPCs prior to exocytosis (Canty *et al.*, 2004; Steiglitz *et al.*, 2006). *In vivo* fibril nucleation occurs in a crowded environment as collagen spontaneously self-assembles to form cross-striated fibrils which are stabilised through cross-linking, initiated by lysyl oxidase.

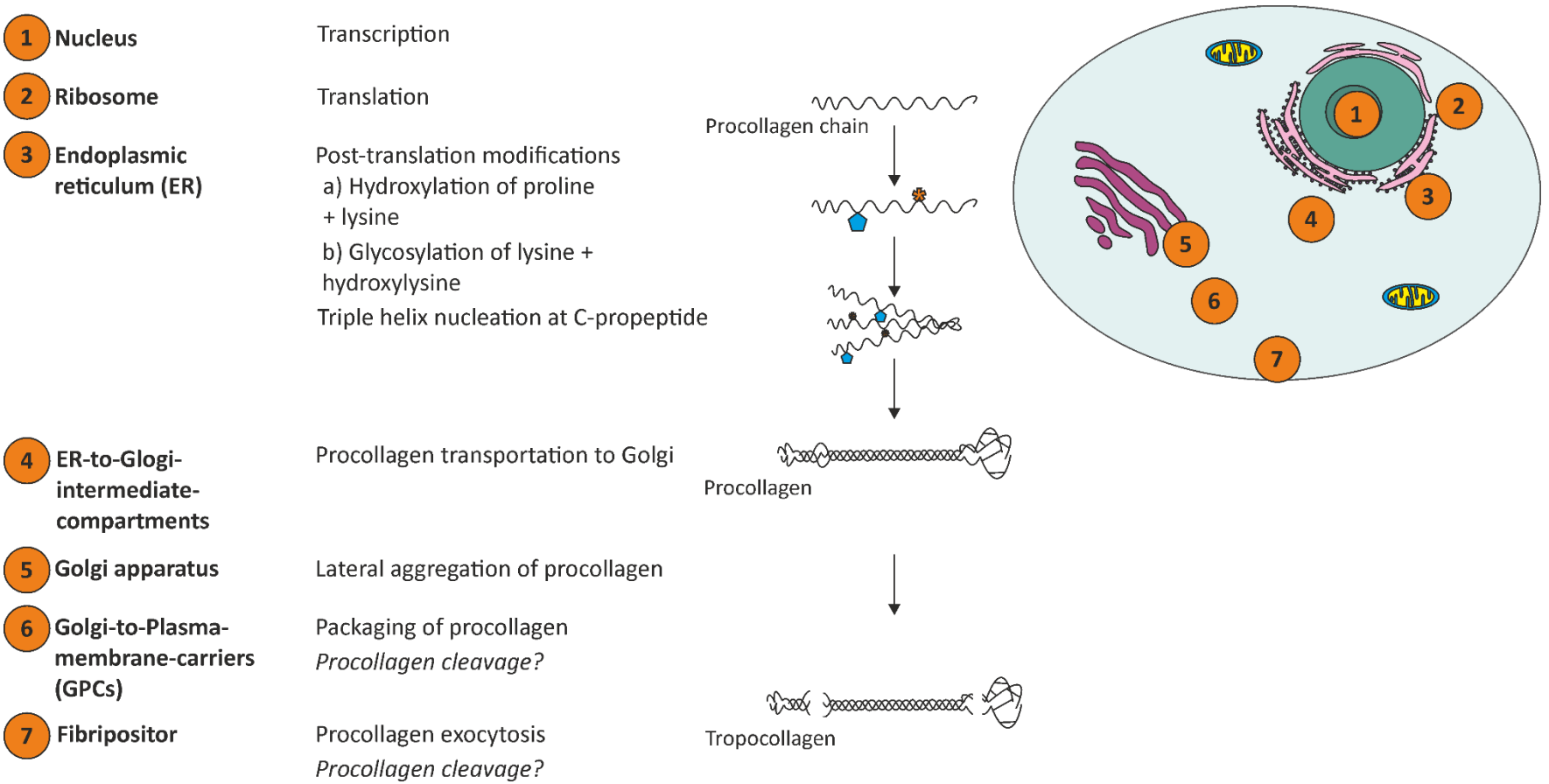


**Figure 1.2 A schematic of collagen biosynthesis.** Following transcription and translation (1), procollagen undergoes hydroxylation and glycosylation in the ER (3). Nucleation of the triple helix occurs at the C-propeptide of procollagen chains to form procollagen which is then transported to the Golgi apparatus where lateral aggregation occurs (4 – 5). From here, procollagen is transported to the plasma membrane in GPCs and procollagen is cleaved by C- and N-proteinases to form tropocollagen (6 – 7) (collagen monomer) (Canty and Kadler, 2005). Blue pentagon represents hydroxylation of amino acids and orange star represents glycosylation.

Within the stroma fibril-forming collagen types I and V form heterotypic fibrils where each fibril is 25 – 30 nm in diameter in the adult cornea (Craig and Parry, 1981; Birk *et al.*, 1988; Daxer *et al.*, 1998). These fibrils are arranged in such a way that they have consistent interfibrillar spacing and form lamellae (layers of collagen fibrils) with each lamellae oriented roughly orthogonally to adjacent layers (Chen *et al.*, 2015). The small fibril diameter, necessary for stroma transparency, is regulated by type V collagen which is also a nucleator of fibrillogenesis (Kadler *et al.*, 2008). The diameter of fibrils has been linked to the number of nucleation sites, with an increase in nucleation sites resulting in a decrease in fibril diameter (Sun *et al.*, 2011; Espana and Birk, 2020). In the stroma, collagen fibrils can form in the type V collagen knockout models but this is thought to be a result of the high concentration of type I collagen which can undergo self-assembly. These self-assembled fibrils, however, are large and irregular with decreased interfibrillar spacing, leading to corneal opacity (Sun *et al.*, 2011). The expression of fibrillar type III collagen in the normal stroma is debated, with early reports suggesting it is expressed in the adult human stroma (Newsome *et al.*, 1982), but later studies finding its expression in normal tissue is restricted to the limbus and sclera (White *et al.*, 1997). Type III collagen is, however, deposited during corneal wound repair (Priyadarsini *et al.*, 2016a; Lorenzo-Martín *et al.*, 2019).

It should be noted that X-ray diffraction studies have revealed that collagen lamellae are not consistently orthogonal to their adjacent layers throughout the stroma (Aghamohammadzadeh *et al.*, 2004; Abahussin *et al.*, 2009). The orientation of collagen varies depending on the position (nasal-temporal and superior-inferior) as well as the location within the tissue (posterior, middle or anterior) (Figure 1.3 A and B, respectively), where collagen is roughly orthogonally arranged in the central cornea but more tangential at the periphery. This change in orientation can explain the differences in strength observed across the different regions of the cornea. Strip testing of the stroma has revealed that the stroma isolated in the inferior-superior direction has a greater strength than those isolated in the nasal-temporal direction and those isolated diagonally (Elsheikh *et al.*, 2008).

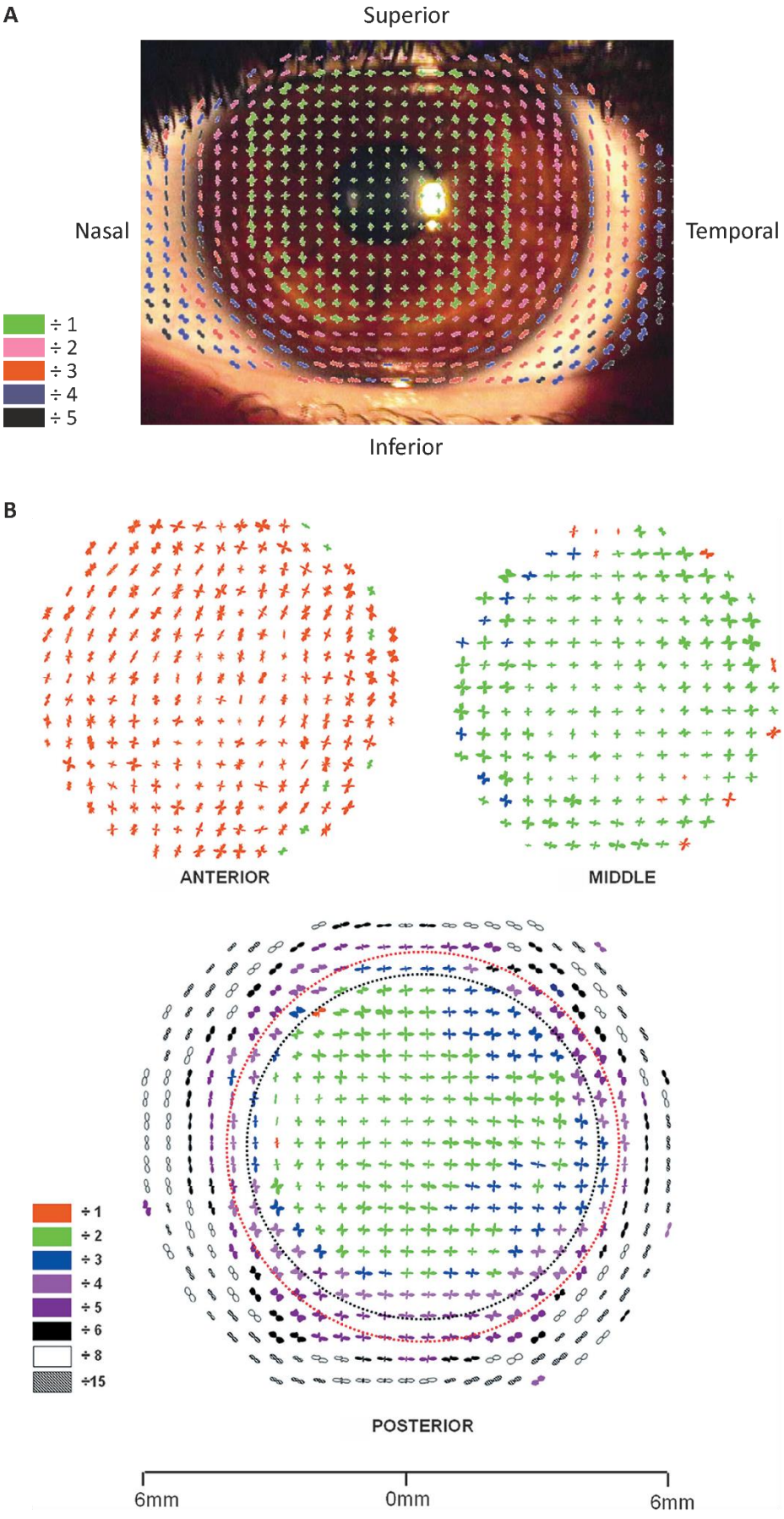
A
Superior
Nasal
Temporal
Inferior
÷ 1
÷ 2
÷ 3
÷ 4
÷ 5
B
ANTERIOR
MIDDLE
POSTERIOR
÷ 1
÷ 2
÷ 3
÷ 4
÷ 5
÷ 6
÷ 8
÷15
6mm
0mm
6mm

**Figure 1.3 Polar plot maps showing collagen fibril orientation.** A: The preferred fibril direction, as determined by X-ray diffraction studies, across the entire cornea is shown overlaid onto an image of the human eye. As scattering increases at the periphery of the cornea, the plots became too large to fit onto the image and were, therefore, scaled down. The key represents the factor by which the polar plots were scaled down in order to fit them all on one figure. Figure in A is adapted from (Aghamohammadzadeh *et al.*, 2004)**.** B: Polar plots of the preferred fibril direction across the anterior, middle and posterior cornea are also shown. Again, the key represents the factor by which the polar plots were scaled down. Figure in B is adapted from (Abahussin *et al.*, 2009)**.**

Another ubiquitously expressed collagen in the stroma is type VI collagen, a beaded-filament-forming collagen that is thought to make up 17% of all collagens in the cornea (Table 1.1) (Zimmermann *et al.*, 1986; Michelacci, 2003). Beaded-filament collagen consists of a triple helical domain, flanked by large N- and C-terminal domains. Type VI collagen undergoes assembly intracellularly, beginning with the formation of a triple-helix monomer from three α chains, followed by dimer assembly, stabilised by disulphide bonds. These dimers then assemble to form a tetramer which is secreted extracellularly where they assemble, end-to-end, to form beaded microfilaments (Cescon *et al.*, 2015). The microfilaments can also aggregate laterally, creating large banded structures, typically associated with pathological tissues (Knupp *et al.*, 2002, 2006). Type VI collagen can bind to many other matrix proteins, such as type I collagen and proteoglycans. In fact, binding to the proteoglycan biglycan can induce a third supramolecular structure, the hexagonal lattice (Wiberg *et al.*, 2002). The beaded microfilaments of type VI collagen are distributed throughout the stroma (Zimmermann *et al.*, 1986; Cho *et al.*, 1990). Given its ability to bind to many other matrix proteins, type VI collagen is thought to influence matrix integrity by binding to different levels within the stroma (Cescon *et al.*, 2015; Chen *et al.*, 2015).

FACIT collagens comprise non-collagenous domains interspersed amongst several triple helical domains (Ricard-Blum, 2011). Collagen types IX, XII and XIV are examples of FACIT collagens which do not form fibrils themselves but, instead, interact with collagen fibrils. Type IX collagen interacts with fibrillar type II collagen (Diab *et al.*, 1996), whereas collagen types XII and XIV interact with type I collagen and can modulate tissue stiffness (M. Sun *et al.*, 2020). The role of FACIT collagen types XII and XIV in the stroma are not fully understood. In an unwounded cornea, only weak expression of type XII collagen has been observed (Massoudi *et al.*, 2012). A recent study by Sun *et al.* (2020) suggests that type XII collagen plays a role in maintaining the structure of the stroma (M. Sun *et al.*, 2020). Although collagen type XII-null mouse corneas were transparent, the collagen fibrils were smaller in diameter and more densely packed with decreased interfibrillar spacing and

disrupted lamella organisation. Interestingly, type XII collagen is upregulated in corneal wounds, particularly in areas with an increased expression of α-smooth muscle actin (α-SMA) and may play a role in ECM remodelling (Massoudi *et al.*, 2012). Type XIV collagen is present during early development but its expression is dramatically reduced in the adult avian cornea (Young *et al.*, 2002).

Collagen types VII, VIII and XIII may also play a role in the development of the stroma. Type VII collagen is an anchoring fibril that extends from the epithelium and bowman's layer into the stroma, connecting the different structures. The anchoring fibrils are predominantly located in the basal lamina with few fibrils extending deep into the stroma (Gipson *et al.*, 1987). Network forming type VIII collagen is predominantly expressed in the Descemet's membrane. A mouse knockout model of *col8a1* revealed that the stroma was significantly thinner when compared to wild types, suggesting type VIII collagen plays a role in development (Hopfer *et al.*, 2005). Although its role is unclear, transmembrane type XIII collagen has been found in the posterior of the stroma during corneal development but no corneal knockout has been studied (Sandberg-Lall *et al.*, 2000). Type XIII collagen is also expressed by myofibroblasts in corneal wounds, suggesting that it may play a role in wound healing (Määttä *et al.*, 2006).

**Table 1.1 Collagens within the corneal stroma and their relative abundance in the entire cornea.**

| Collagen type | Classification | Distribution | % of total collagens |
|---|---|---|---|
| **I** | Fibrillar | Ubiquitous | 75 |
| **III** | Fibrillar | Wound healing | |
| **V** | Fibrillar | Ubiquitous | 2 |
| **VI** | Beaded-filament | Ubiquitous | 17 |
| **XII** | FACIT | Weak expression in adults, upregulated in wounds | |
| **XIV** | FACIT | Expressed during development, reduced in adults | |

Table adapted from (Michelacci, 2003).

The rate of collagen turnover in the corneal stroma is unclear. It has previously been reported to be in the range of 2 – 7 years but there is little evidence to support this estimation (Paik *et al.*, 2018). Pulse-chase experiments, using radiolabelled proline, performed on a calf corneal stroma indicated that the turnover time for type I collagen was 36 hours (10 and 6 hours for type V and VI collagens respectively) (Kern *et al.*, 1991). A radiolabelled rabbit cornea (using radiolabelled glycine) implanted into an unlabelled host cornea persisted up

to 17 months, the length of the study (Smelser *et al.*, 1965). However, it should be noted that a corneal graft may not behave the same way as an intact cornea. Collagens can be degraded by matrix metalloproteinases (MMPs) and cathepsins and both have been observed in pathological corneas (Brookes *et al.*, 2003). Cathepsins are lysosomal enzymes that can cleave collagen molecules (Turk *et al.*, 2012). MMPs are a group of proteinases responsible for degrading the ECM and its subsequent remodelling (Löffek *et al.*, 2011). Tissue inhibitors of matrix metalloproteinases (TIMPs) and other non-specific inhibitors, such as the fragment from the proteolytic conversion of PCPE-1, can inhibit MMPs (Mott *et al.*, 2000). Fibrillar collagens, such as those found in the corneal stroma, are mostly cleaved by a group of MMPS called collagenases (MMP-1, -8 and -13) and the gelatinase MMP-2 (Löffek *et al.*, 2011). The expression of MMP-2, -3, -9 and proMMP-13 have all been shown to be upregulated in diseased and injured corneas (Mulholland *et al.*, 2005; Predović *et al.*, 2008).

### 1.2.2 Corneal transparency

The organisation of collagen plays a key role in maintaining corneal transparency. Initial models suggested that the stroma is transparent as a result of its constituents all having the same refractive index, however this was disproved and replaced with a model by Maurice, called Lattice Theory (Maurice, 1957). This theory proposes that the small, uniform diameter of collagen fibrils, with consistent interfibrillar spacing results in the lateral scattering of light. Secondary radiation of light travelling in the non-forward direction destructively interferes with other back-scattered light, maintaining transparency whilst the light travelling forward propagates through the cornea. Later theories, based on observations from transmission electron micrographs, suggested the lattice structure is not necessary throughout the entire stroma, but that short-range order is sufficient (Hart and Farrell, 1969). This was further supported by Benedek who proposed that the cornea will be transparent so long as the spacing between the collagen fibrils is smaller than half the wavelength of light (Benedek, 1971). More recently, Doutch *et al.* outlined the crucial parameters thought to affect corneal transparency and these are: the number of collagen fibrils; collagen fibril diameter; the order in interfibrillar spacing; differences in refractive index between fibrils and interfibrillar substances; and the thickness of the stroma (Doutch *et al.*, 2008). Models of collagen organisation have revealed that increasing collagen fibril diameter can result in the back-scattering of light (Meek and Knupp, 2015). Furthermore, increasing interfibrillar spacing, such as that observed in corneal swelling, can also result in the backwards scattering of light. The corneal endothelium regulates the hydration of the cornea through a leaky barrier. If the

endothelium becomes damaged, such as in Fuchs' endothelial dystrophy, the stroma can swell and increase interfibrillar spacing. The backward scattering of light reduces the intensity of light travelling in the forward direction thus impairing corneal transparency.

### 1.2.3 Proteoglycans within the stroma

Proteoglycans (PGs) consist of glycosaminoglycan (GAG) side chains attached to a core protein. There are four main proteoglycans found within the corneal stroma and these are members of the small leucine-rich proteoglycans (SLRPs). These can be further classified based on the sulphate chains they contain with decorin containing chondroitin/dermatan sulphate side chains whereas lumican, keratocan and mimecan all comprise keratan sulphate side chains and are referred to as keratan sulphate proteoglycans (KSPGs) (Funderburgh *et al.*, 1998; Iozzo, 1999; Dunlevy *et al.*, 2000; Michelacci, 2003). Biglycan, a proteoglycan with a dermatan sulphate side chain, has been detected at low levels in the human corneal stroma and is observed at increased levels in pathologic corneas (Funderburgh *et al.*, 1998).

#### 1.2.3.1 Decorin

Decorin is expressed across the stroma, typically decorating collagen fibrils and its crystal structure can be seen in Figure 1.4 (Kimura *et al.*, 1995). Decorin-null mice present with lateral fusion of collagen fibrils in both the skin and tail tendon but not in the corneal stroma (Danielson *et al.*, 1997; Zhang *et al.*, 2009). In the stroma there are not many distinguishable features when comparing the ultrastructure of corneal collagen fibrils of decorin-null mice to wild-types, with only the occasional fibril found to have a larger diameter (Zhang *et al.*, 2009). However, the expression of biglycan has been shown to be upregulated when decorin is knocked out. In a decorin-/biglycan-null mouse severe disruptions to the ultrastructure are observed in the posterior stroma, with lateral fusion of fibrils that also have a large diameter (Zhang *et al.*, 2009). Interestingly, this phenotype is not observed in early stages of mouse corneal development suggesting that both decorin and biglycan play roles in regulating mature fibril formation at later stages of development.

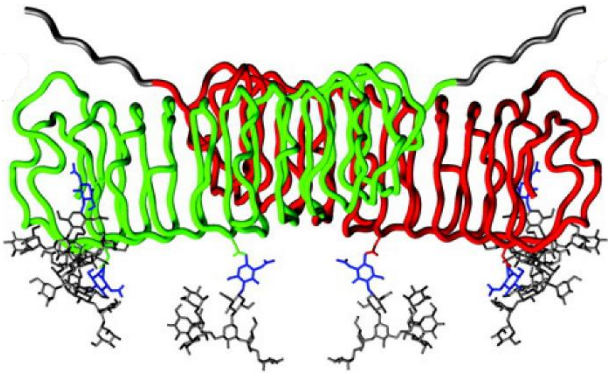

**Figure 1.4 Rope diagram of a glycosylated model of decorin.** Decorin is composed of two horseshoe-shaped monomers depicted here in green and red. The N-termini have been extended by a few residues to show directionality (grey; top of image). Glycosylation occurs in the C-terminal half of the protein; oligosaccharide chains are modelled (grey; bottom of image). Other SLRPs have a similar structure. Figure adapted from (Scott *et al.*, 2004)**.**

#### 1.2.3.2 Lumican

Lumican plays a role in regulating collagen fibrillogenesis and its presence is necessary for the formation of thin collagen fibrils found within the stroma. Lumican is homogenously expressed in the developing murine cornea but in adult mice greater expression is observed in the posterior stroma (Chakravarti *et al.*, 2006; Chen *et al.*, 2014). *In vitro* assays have shown that the addition of lumican to acetic acid-extracted collagen significantly decreases the diameter of collagen fibrils formed when compared to fibrils formed in the absence of PGs (Rada *et al.*, 1993). The regulatory role of lumican has been further investigated *in vivo* in mice. Lumican knockout mice displayed collagen fibrils with a larger diameter than those observed in wild type mice and lateral fibril fusion was also observed (Chakravarti *et al.*, 1998, 2000). These effects are more pronounced in the posterior stroma and it has been suggested that lumican is necessary for maintaining hydration (Chakravarti *et al.*, 2000). Phenotypic manifestations of lumican-null mice include corneal hazing and a thin stroma. Interestingly, the overexpression of lumican has no observable effect on collagen arrangement or corneal transparency (Carlson *et al.*, 2005). However, it has been shown that lumican regulates keratocan expression with an increase in lumican resulting in an increase in keratocan (Carlson *et al.*, 2005). Although not considered a major PG in the stroma, the expression of fibromodulin, a KSPG expressed during development and wound healing, has been shown to increase in lumican knockout models (Chen *et al.*, 2010).

#### 1.2.3.3 Keratocan

Keratocan is a KSPG found throughout the corneal stroma (Liu *et al.*, 2003). It has been reported that knocking out the gene encoding keratocan in mice does not affect corneal

transparency but results in abnormal interfibrillar spacing of collagen fibrils within the stroma (Kao and Liu, 2003). Similarly, keratocan-null mice exhibited larger collagen fibril diameters but a thinner stroma suggesting that keratocan plays a role in maintaining corneal shape (Liu *et al.*, 2003). This is further supported by pathologies observed in human corneas. Cornea plana, a condition where the cornea is flattened, can be caused by mutations in the gene encoding keratocan (KERA), which are likely to cause a loss of function of keratocan (Pellegata *et al.*, 2000). Interestingly, an increase in keratocan expression has been observed in patients with keratoconus, a condition in which the stroma thins and the cornea protrudes (Wentz-Hunter *et al.*, 2001). Corneal thinning is a phenotype in both conditions, suggesting that an optimal level of keratocan expression is required for normal corneal thickness. Histopathology of keratoconic corneas shows a decrease in the number of collagen lamellae and irregular arrangements of collagen fibrils (Rabinowitz, 1998). Keratocan is, therefore, likely to play an important role in regulating matrix assembly.

#### 1.2.3.4 Mimecan

Mimecan, also referred to as osteoglycin, is another KSPG detected in the cornea although its exact function in the stroma is unknown. Mouse knockout models have revealed that mimecan may play a role in regulating fibril diameter although these corneas remained transparent (Tasheva *et al.*, 2002). Together, these SLRPs are essential for regulating collagen fibril assembly, restricting lateral fibril growth and maintaining corneal shape.

### 1.2.4 Cells within the corneal stroma

#### 1.2.4.1 Keratocytes

The predominant cell type in the stroma is the keratocyte. These quiescent cells have a dendritic-like morphology with interconnecting lamellipodia and are fundamental to the maintenance of the ECM, synthesising collagens and proteoglycans. Furthermore, these cells express corneal crystallins which reduce light scattering and corneal opacities.

Keratocytes have a small cell body with numerous process and cortical filamentous-actin (F-actin) bordering the cells, revealed by phalloidin staining (Jester *et al.*, 1994; Funderburgh *et al.*, 2003). This morphology limits the surface area exposed to light and may contribute to their reduced light scattering. *In vivo* confocal microscopy of the stroma has revealed that the main source of light scattering is from keratocyte nuclei, and not the cell body itself (Møller-Pedersen, 2004). The refractive index of the large number of organelles and macromolecules within a cell is unknown but, it is thought that these would scatter light

(Jester, 2008). As the cell body is not the predominant source of light scattering in keratocytes, Jester *et al.* hypothesised that fluctuations in the refractive index of the cytoplasm are reduced by corneal crystallins (Jester *et al.*, 1999).

The cell body of keratocytes can vary in size from 200 – 600 nm which, according to the aforementioned models of corneal transparency, should result in light backscattering (Jester, 2008). It has been proposed that corneal crystallins, such as aldehyde dehydrogenase (ALDH) and transketolase (TKT), create short range order within keratocytes thus minimising fluctuations of the refractive index both within the cell and also between the cell and the collagenous matrix (Jester *et al.*, 1999). ALDH3A1 is the most common corneal crystallin in mammals and a knockout mouse model revealed that keratocytes scattered more light than wild type controls (Jester, 2008; Chen *et al.*, 2017). Both ALDH1A1 and ALDH3A1 indirectly protect against ultraviolet (UV) light via the generation of nicotinamide adenine dinucleotide phosphate. ALDH3A1 has also been shown to protect against UV-induced apoptosis and has an antioxidant function in stromal cells *in vitro* (Lassen *et al.*, 2006; Estey *et al.*, 2007).

To characterise keratocytes, particularly *in vitro*, phenotypic markers have been identified, the most common of which are: keratocan (KERA), lumican (LUM), aldehyde dehydrogenase 1A1 and aldehyde dehydrogenase 3A1 (ALDH1A1 and ALDH3A1), where the associated gene is written in parentheses (Carlson *et al.*, 2005; Pei *et al.*, 2006; Yam *et al.*, 2020). Other proteins used to identify keratocytes are prostaglandin D2 synthase (PTGDS), an enzyme thought to behave as a proteoglycan in the stroma (Berryhill *et al.*, 2001; Du *et al.*, 2007), and carbohydrate sulfotransferase 6 (CHST6), an enzyme that transfers sulphate residues to keratan sulphate proteoglycans (Wu *et al.*, 2013). CD34, a cell surface sialomucin, is thought to play a role in anchoring keratocytes between collagen lamellae and has also been considered a phenotypic marker for keratocytes (Joseph *et al.*, 2003; Perrella *et al.*, 2007; Sidney *et al.*, 2014). Aquaporin 1 (AQP1), a protein that transports water across the cell, is also highly expressed by keratocytes although its exact role in the stroma remains unclear (Ruiz-Ederra and Verkman, 2009). Finally, keratocytes do not express Thy-1/CD90 (THY-1) nor α-smooth muscle actin (α-SMA) (ACTA2), which are associated with corneal fibroblasts and myofibroblasts (Pei *et al.*, 2004).

#### 1.2.4.2 Activated keratocytes, fibroblasts and myofibroblasts

Many studies have investigated the change in keratocyte phenotype observed when the cornea is wounded (Jester *et al.*, 1995; Fini, 1999; Mohan *et al.*, 2003; Torricelli *et al.*, 2013). Here, the focus is on cells that are likely to have originated from the keratocyte, however

other cells, such as those derived from bone marrow, are also involved in the response to injury. Within minutes of wounding, keratocytes adjacent to the site of injury undergo apoptosis (Wilson *et al.*, 1996). Keratocytes from elsewhere in the stroma transition into an activated phenotype, where their morphology changes from the typical dendritic shape to a larger, more fusiform shape, resembling fibroblasts (Fini and Stramer, 2005; Hassell and Birk, 2010). These fibroblasts proliferate and migrate to the edge of the wound where they then begin to synthesise and deposit new matrix (Figure 1.5) (Mohan *et al.*, 2003). The haze associated with early wound repair is likely due to the presence of these fibroblasts, which have a decreased expression of corneal crystallins (Pei *et al.*, 2006). A proportion of these cells then differentiate into myofibroblasts. Several different phenotypes have been observed at different timepoints during corneal wound healing, from those that express just vimentin to those that express vimentin, α-SMA, and desmin, suggesting ordered differentiation in response to wounding (Powell *et al.*, 1999; Chaurasia *et al.*, 2009; Torricelli *et al.*, 2016). During normal wound healing, myofibroblasts secrete collagen, hyaluronic acid and proteoglycans. These proteoglycans, however, tend to be those with chondroitin/dermatan sulphate side chains and there is a reduction in KSPGs compared to those secreted by keratocytes (Funderburgh *et al.*, 2003). There is also an increase in the expression of type III collagen in both fibroblasts and myofibroblasts (Funderburgh *et al.*, 2003; Galiacy *et al.*, 2011). Consequently, the matrix deposited is often disorganised, with large collagen fibrils, and is not transparent. Myofibroblasts then either transition into wound fibroblasts or undergo apoptosis. Wound fibroblasts secrete collagenases, MMPs and TIMPs which remodel the matrix and the cells start to re-stratify (Lim *et al.*, 2003). Normal wound healing requires re-epithelialisation and the secretion of the epithelial basement membrane. If this does not occur, epithelial cells continue to release growth factors (e.g. platelet-derived growth factor, PDGF and transforming growth factor, TGFβ) and cytokines (e.g. interleukin-1 and tumour necrosis factor alpha) which subsequently enter the stroma (Wilson *et al.*, 2001, 2003). These chemicals continue to signal the recruitment of myofibroblasts to the wound site and either prevent the apoptosis or the transition of cells to wound fibroblasts which results in the continuous formation of disorganised ECM (Wilson, 2020). It is worth mentioning that upon wounding, cells derived from the bone marrow migrate into the stroma. The labelling of bone marrow cells with green fluorescent protein revealed that once in the cornea, these cells can also differentiate into myofibroblasts (Barbosa *et al.*, 2010). More research is required to explore the complex interactions between each of the cells involved (epithelial cells, keratocytes, fibroblasts, myofibroblasts,

bone marrow-derived cells), growth factors, cytokines and exactly how the matrix is remodelled to avoid corneal haze.

Keratocytes extracted from the cornea and subsequently cultured in serum-containing media also exhibit a morphology change to a fusiform conformation (Funderburgh *et al.*, 2003). Treatment with serum results in a phenotypic switch from keratocytes to corneal fibroblasts, characterised by a change in F-actin distribution, a decrease in the expression of KSPGs and an increase in the expression of Thy-1 (Beales *et al.*, 1999; Pei *et al.*, 2004).

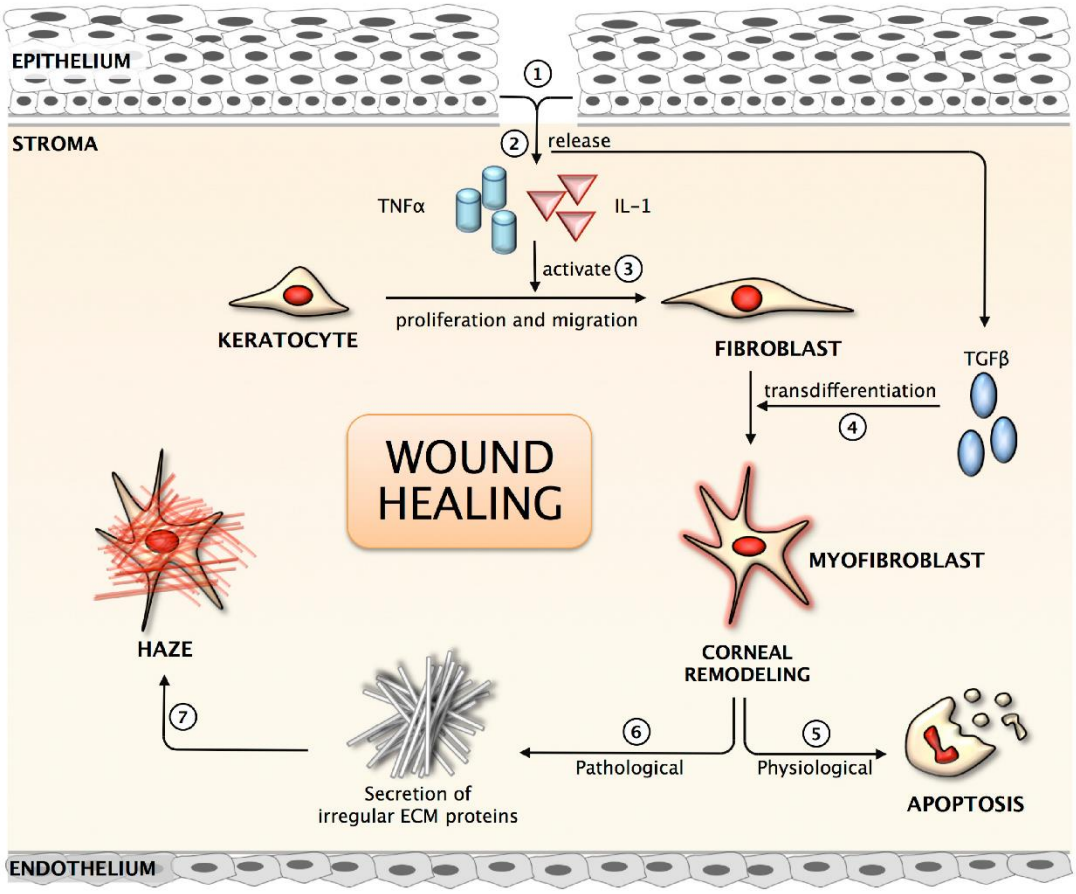


**Figure 1.5 Diagrammatic representation of corneal wound healing.** 1) Corneal wound occurs, resulting in the loss of the epithelial basement membrane; 2) cytokines and growth factors are secreted by epithelial cells and keratocytes and can also enter the cornea from tears; 3) following keratocyte apoptosis at the site of injury, peripheral/distal keratocytes become activated and transition to fibroblasts; 4) Growth factors, including TGFβ, result in the transition of fibroblast to myofibroblast; 5) under physiological conditions, following the deposition and remodelling of the ECM, myofibroblasts undergo apoptosis; 6) in pathological conditions, myofibroblasts continue to be exposed to growth factors and cytokines resulting in the continued deposition of an irregular matrix; 7) the irregular matrix ultimately results in corneal haze and opacity. Image from (Chaurasia *et al.*, 2015).

#### 1.2.4.3 Corneal stromal stem cells

Residing within the anterior stroma, at the periphery of the cornea and in close proximity to the limbal epithelial stem cell niche, are multipotent cells that are categorised as stem cells (Figure 1.6). These multipotent cells were coined corneal stromal stem cells (CSSCs) by Funderburgh's group but have also been referred to as limbal mesenchymal stromal cells (Bray *et al.*, 2014; Shaharuddin *et al.*, 2016). Funderburgh's group were amongst the first to identify this population of cells that exhibited characteristics of mesenchymal stromal cells (MSCs) as characterised by the International Society for Cellular Therapies (ISCT) (Du *et al.*, 2005; Funderburgh *et al.*, 2005; Dominici *et al.*, 2006). Unlike keratocytes, CSSCs express PAX6, a protein that's ocular expression is limited to progenitor cells, the retina and the corneal epithelium (Funderburgh *et al.*, 2005; Polisetty *et al.*, 2008). CSSCs possess the potential to differentiate down neurogenic, osteogenic, chondrogenic and adipogenic lineages, alongside their ability to differentiate into keratocytes (Dravida *et al.*, 2005; Du *et al.*, 2005). The potential use of CSSCs clinically has also been investigated. The application of CSSCs to a mouse wound model has been shown to prevent corneal scarring by significantly reducing the expression of type III collagen and reducing neovascularisation (Basu *et al.*, 2014). These results are likely amplified as a result of the immunosuppressive nature of CSSCs, which not only suppress T-cell proliferation but also stimulate the growth of epithelial cells, which in turn would result in the apoptosis of corneal myofibroblasts (Bray *et al.*, 2014). These cells typically express markers of pluripotent cells, such as stage-specific embryonic antigen 4 (SSEA4) and octamer-binding transcription factor 4 (OCT4); markers associated with mesenchymal stromal cells, for example adenosine triphosphate (ATP)-binding cassette super-family G member 2 (ABCG2); markers of neural progenitor cells, such as nestin (NES); and markers for ocular precursors such as paired box protein Pax-6 (PAX6) (Dravida *et al.*, 2005; Du *et al.*, 2005; Funderburgh *et al.*, 2016).

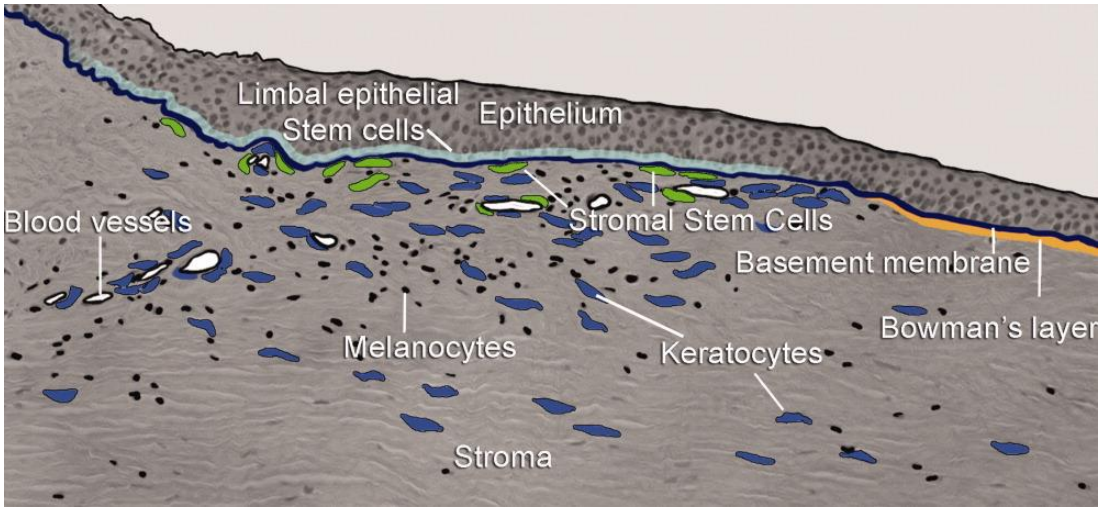


**Figure 1.6 Location of CSSCs in the limbus.** The section shows the corneal limbus where limbal epithelial stem cells (light blue) are localised. Unlike the central cornea, the limbal stroma is vascularised and contains melanocytes (black) and keratocytes (blue). CSSCs (green) are located subjacent to the basement membrane near limbal epithelial stem cells. Image from (Pinnamaneni and Funderburgh, 2012).

Interestingly, keratocytes isolated from corneoscleral rims have shown the ability to transition to a MSC phenotype (Branch *et al.*, 2012). As cells were expanded, the expression of CD34 decreased with passaging, until it was negligible at passage 3 (P3). The authors then showed that at P3 these cells met the minimal criteria set by the ISCT to define multipotent MSCs, including trilineage differentiation (Dominici *et al.*, 2006). Moreover, these cells could then be differentiated back into keratocytes, however they still expressed surface markers associated with MSCs (Sidney and Hopkinson, 2018). These data are further supported by an earlier study which found that cells isolated from limbal biopsies expressed the same surface markers as bone marrow-derived MSCs at P2 (Polisetty *et al.*, 2008). Whilst these cells did not express PAX6, they showed osteogenic and adipogenic differentiation potential and did not express markers associated with limbal epithelial cells.

### 1.2.5 Corneal stroma assembly during development

Whilst the adult cornea contains resident stem cells and a continuous renewal of the corneal epithelium, most of the stroma formation occurs during development. Much of the research on embryonic stroma development has been carried out on chick corneas. Although this is similar to the events that occur in humans, it differs in that a distinct primary stroma is first formed, an event not present in human stroma development (Espana and Birk, 2020). During development keratoblasts, cells derived from the neural crest and the precursor to keratocytes, begin to synthesise a hyaluronic acid-rich ECM with few collagen fibrils (Hassell

and Birk, 2010). These cells then differentiate to form keratocytes, which replace the hyaluronic acid-rich ECM with collagen fibrils (Chen *et al.*, 2015). Keratocytes extend several processes that have two major axes which are almost perpendicular to one another. Collagen is secreted between these processes from fibripositors and fibrillogenesis occurs before the keratocyte processes then retract and bundles of fibrils are formed (Birk and Trelstad, 1984; Feneck *et al.*, 2019; Young *et al.*, 2019). This process continues allowing bundles of fibrils to continue to form, resulting in lamellae. Simultaneously, the formation of fibril bundles also occurs at the keratocyte processes oriented at approximately 90°, creating orthogonally arranged fibrils (Birk and Trelstad, 1984). *En face* serial bock face scanning electron micrographs have revealed that from as early as day 12 in the embryonic chick, an orthogonal template is formed by keratocyte processes (Young *et al.*, 2014). A recent study of mouse corneal development did not show any evidence of fibripositors (Feneck *et al.*, 2019). This suggests that collagen alignment in mouse (and perhaps mammal) cornea differs to that described in avian models where, as opposed to fibripositors, keratocyte projections align the collagen fibrils. Proteoglycans and FACITs are thought to interact with collagen fibrils to regulate fibril diameter, interfibrillar spacing and lamellae formation (Chen *et al.*, 2015).

## 1.3 Tissue engineering of the corneal stroma

The act of replacing damaged tissue has been around for centuries, from wooden toes to clay ocular prostheses (Thurston, 2007; Sajjad, 2012). As technology has advanced there has been a shift in the major role of these replacements where value is now placed on maintaining the tissues' function.

There are several design requirements that must be met when creating a tissue replacement, and whilst these often vary depending on the tissue, one key requirement must be met – tissue replacements must be biocompatible. Cytotoxicity must be avoided and unwanted immune responses circumvented. The design requirements of the tissue replacement must be identified and every effort should be made to ensure that each of these is met whilst maintaining biocompatibility. The key design requirements for a replacement of the corneal stroma are that it: maintains structural integrity (is mechanically strong); is transparent; does not unintentionally degrade; provides the appropriate shape for light refraction; and has good handleability (Brunette *et al.*, 2017). When creating an *in vitro* model of the stroma, the design requirements shift and focus less on the handleability and the mechanical properties of the construct. The primary focus of an *in vitro* model is to recapitulate the native tissues composition and structure. In the case of the corneal stroma

this refers to the organisation of collagen fibrils and keratocytes throughout. A model of the stroma can reduce the use of animals models whilst still allowing for investigative studies, such as the study of MMP expression during wound healing (Couture *et al.*, 2016).

### 1.3.1 Design criteria and applications of a corneal model

*In vitro* models of the cornea can be used for a multitude of applications, some of which may result in a reduction of the number of animal models used. The success of a stroma model is dependent on the intended use and the associated design criteria. With the minimum design criteria changing with application (as highlighted in Table 1.2), there may not be a "one size fits all" model and, in fact, several versions may be required. Certain applications, for example drug testing, may only require the corneal epithelium whilst others, such as investigating collagen fibrillogenesis, requires corneal keratoblasts and/or fibroblasts.

MatTek is a biotechnology company that produces *in vitro* models of a variety of different tissues. Aware of the fact that different applications require different attributes, MatTek has developed two models of the cornea, EpiCorneal™ and EpiOcular™ which are commercially available. EpiOcular™ is a standard Organisation for Economic Co-operation and Development model for eye irritation tests. However, the EpiOcular™ model is composed of normal human epidermal keratinocytes that have been derived from neonatal-foreskin and stratified to mimic the corneal epithelium. Not only are these cells not derived from ocular tissue, and may therefore react differently to the corneal epithelium but the stroma, the major component of the cornea, is ignored. The EpiCorneal™ model is composed of normal corneal epithelial cells with applications including corneal drug delivery, corneal wound healing and dry eye disease (Kaluzhny *et al.*, 2016, 2018). However, as with EpiOcular™, this model lacks the stroma – a key component in corneal wound healing, as aforementioned (1.2.4.2). To improve on commercial products, such as those supplied by MatTek, the corneal stroma should be incorporated into the model. This would allow for further research into corneal wound healing as well as the communication between keratocytes/fibroblasts and epithelial cells under a variety of conditions (i.e. possible cytotoxic conditions of novel drugs).

**Table 1.2 Minimal design criteria for the different applications of a corneal model.**

| Application | Design criteria | Comparison to OECD model (EpiOcular™) |
|---|---|---|
| Drug testing* | 5-6 layers of epithelial cells plus target layer<br><br>Thickness: variable (50 – 200 µm) | Consists only of 5-8 layers of epithelial cell<br><br>Used to differentiate irritant and non-irritant materials |
| Corneal wound healing* | 5 – 6 layers of epithelial cells plus keratocytes and/or fibroblasts<br><br>Organised collagenous layer composed of heterotypic type I/V collagen fibrils<br><br>Thickness: variable (50 – 200 µm) | Consists of 5-8 layers of epithelial cells cultured in media supplemented with growth factors |
| Collagen fibrillogenesis* | Collagen-producing cells (e.g. keratoblasts or fibroblasts)<br><br>Extracellular matrix consisting of at least collagen types I, V and VI<br><br>Thickness: variable (10 – 200 µm) | Unsuitable for this purpose |
| Clinical replacement | Mechanically strong<br><br>Transparent<br><br>Good handleability<br><br>Provides necessary refractive power | Unsuitable for this purpose |

*These models may also replace animal models.

### 1.3.2 Acellular biomaterials

There is currently a global shortage in donor corneal tissue, with just one cornea available for every 70 patients that require a transplant (Gain *et al.*, 2016). The use of acellular biomaterials has been explored as an alternative to an allogenic stroma graft. Given that collagen is the primary component of the corneal stroma, most research has focused on using this protein to create a biocompatible structure. Recombinant human collagen (RHC)

types I and III, produced in yeast, have been cast into curved moulds to form hydrogels via cross-linking with 1-ethyl-3-(3-dimethyl aminopropyl) carbodiimide and *N*-hydroxysuccinimide (NHS) (Liu *et al.*, 2008). Hydrogels made from RHC type III (RHCIII) were more transparent, likely as a result of the collagen fibrils having a smaller diameter than RHC type I. RHCIII also had better mechanical properties and was able to absorb more UV light, essential properties of the stroma that protect the posterior parts of the eye. More recently, RHCIII has been combined with a polymer, 2-methacryloyloxyethyl phosphorylcholine, to reduce neovascularisation post-implant (Buznyk *et al.*, 2015). Whilst these implants have been trialled clinically, with some promising results, they are not yet available for commercial use (Islam *et al.*, 2018). Furthermore, their composition and disorganised structure does not recapitulate the corneal stroma (Hayes *et al.*, 2015).

### 1.3.3 Top-down approaches to engineering the stroma

A top-down approach to engineering the corneal stroma involves culturing stromal cells on a three-dimensional scaffold, which is often primed with either chemical or mechanical cues to encourage cells to deposit their own ECM. As the scaffold often forms part of this structure, their applications tend to be limited to graft-alternatives and for this reason, they will only be briefly introduced.

#### 1.3.3.1 Collagen scaffolds

Collagen has been used in other constructs as a scaffold for corneal cells. Type I collagen gels have been created with orthogonal layers of fibrils, achieved by placing a collagen solution onto a magnetic bore, increasing the temperature to induce fibrillogenesis and then rotating the gel by 90° before adding more collagen solution (Torbet *et al.*, 2007). These collagen gels supported corneal fibroblast growth but lacked transparency, which was subsequently improved by the addition of proteoglycans to the gels, reducing the diameter of the collagen fibrils (Torbet *et al.*, 2007). The corneal fibroblasts in this model successfully synthesised and deposited their own collagen fibrils, with smaller diameters than the surrounding collagen gel (Builles *et al.*, 2010). Acellular collagen gels have been implanted in to rabbit models, however, of the five grafts implanted, only one was retained with the failed grafts exhibiting signs of poor wound healing and neo-vascularisation (Builles *et al.*, 2010).

Plastic compressed collagens, via the Real Architecture for 3D Tissues process, have been used as an alternative to typical collagen gels, given their improved mechanical properties (Jones *et al.*, 2011). Whilst the primary aim of these constructs is to support limbal

epithelial cells and act as a cell carrier, with data showing they supporting epithelial cell growth (Levis *et al.*, 2010), the technique has recently been modified for a stromal application (Mukhey *et al.*, 2017). Here, collagen gels were cast into a mould prior to plastic compression which resulted in the parallel alignment of collagen fibrils and the cells cultured within. This tissue equivalent may be a feasible alternative to partial thickness stromal grafts although further work is required to investigate the transparency of the constructs.

#### 1.3.3.2 Silk scaffolds

Silk fibroin is a naturally occurring polymer with excellent mechanical properties and can be reconstituted to create a number of different scaffolds, from fibres and films to sponges and gels (Altman *et al.*, 2003). Of particular interest within the field of corneal tissue engineering is the processing of silk to create films, which are transparent and thus incredibly useful. Silk has been cast onto patterned surfaces to create films with grooves that provide topographical cues. Stromal cells have been shown to align along the grooves and deposit an aligned matrix (Zhang *et al.*, 2016). Zhang *et al.* also cast a collagen hydrogel on top of corneal cells, cultured in 2% serum, to create a 3D environment which models the stroma (Zhang *et al.*, 2016). Equibiaxial strain was incorporated into the system to create a biomimetic model. The 3D environment and the incorporation of mechanical strain significantly upregulated the expression of lumican and keratocan. A similar 3D model, with silk films surrounded by a collagen hydrogel, has also been peripherally capped with silk sponges (Wang *et al.*, 2017). The sponges were used to support the growth of dorsal root ganglion cells to model corneal innervation in a construct that comprised both hCSSCs and epithelial cells.

#### 1.3.3.3 3D bioprinting

An emerging area within tissue engineering is the use of bioinks and 3D printing. Extrusion-based (Isaacson *et al.*, 2018; Kim *et al.*, 2019; Kilic Bektas and Hasirci, 2020), laser-assisted (Sorkio *et al.*, 2018), and drop-on-demand (Duarte Campos *et al.*, 2019) bioprinting have all been used to print hydrogels for corneal stroma tissue engineering.

In extrusion-based bioprinting, loaded biomaterials are forced out of a nozzle in a continuous stream (Zhang *et al.*, 2019). A proof-of-concept study used extrusion-based bioprinting to successfully print a collagen-alginate bioink containing stromal cells (Isaacson *et al.*, 2018). Despite the printed structures unravelling during culturing, keratocytes were shown to still be viable at day 7, however their phenotype was not analysed. Extrusion-based printing of methacrylated gelatin had a more stable structure and hCFs were shown to be

viable up to day 21 but were rounded in shape (Kilic Bektas and Hasirci, 2020). Decellularised bovine cornea has also been used as a bioink with extrusion-based bioprinting to print a hydrogel encapsulating human turbinate-derived MSCs which were then differentiated into keratocytes (Kim *et al.*, 2019). By day 28, cells showed positive expression for KERA, ALDH with little ACTA2 expression and collagen was deposited, detected by a hydroxyproline assay. Implantation into rabbit models revealed that the printed hydrogels were more transparent than the pipetted (non-printed) control after 28 days with no evidence of degradation.

In laser-assisted bioprinting, the bioink sits atop a donor slide, onto which a laser is fired. This results in the evaporation of the donor slide, releasing a droplet of the bioink which falls onto the receiving substrate (Li *et al.*, 2016). Laser-assisted bioprinting of adipose-derived MSCs encapsulated in human type I collagen has been used to successfully print viable human cells (Sorkio *et al.*, 2018). Despite being printed in the same orientation, the cells were seen to rotate across the printed layers, creating a structure that somewhat resembles the corneal stroma. The printed structure was incorporated in to a porcine cornea organ culture model and cultured for 7 days. Immunohistochemical staining revealed that the cells migrated and infiltrated into the porcine model.

Inkjet bioprinting is a technique where droplets of a bioink are dispensed in a predetermined pattern (Rider *et al.*, 2018). Drop-on-demand bioprinting is a type of inkjet printing that has been used by Duarte Campos *et al.* to create a dome-shaped stroma substitute, encapsulating keratocytes in bovine type I collagen blended with agarose (Duarte Campos *et al.*, 2019). Although the mechanical properties were considerably poorer than the native tissue, the keratocytes were cultured in 0.5% FBS and appeared to maintain their phenotype.

At present, bioprinted structures are focusing on an alternative to allogeneic corneal grafts with the primary focus being on transparency, tissue integration and mechanical properties. Although these stroma equivalents may be used in the future to alleviate the demand for corneal grafts, the use of a matrix-derived protein as a bioink restricts their use to just that and not as a model which can be used to investigate corneal wound healing, collagen fibrillogenesis and cell stratification.

### 1.3.4 A bottom-up approach using corneal keratocytes and fibroblasts

A bottom-up approach to engineering the corneal stroma has involved culturing corneal keratocytes/fibroblasts to produce a tissue construct that recapitulates the nano-structure of the stroma. Early attempts at creating an *in vitro* model focused on culturing sheets of

dermal and corneal fibroblasts in culture flasks (Carrier *et al.*, 2008). One dermal and one corneal fibroblast sheet, plus their associated ECM, could then be stacked on top of one another to create a thick, fibrous construct. Dermal fibroblasts were incorporated into the model as they reportedly supported the stratification of corneal epithelial cells more than the use of corneal fibroblasts alone. Corneal epithelial cells were cultured on the surface at the air-liquid interface and the construct could also support the adherence of corneal endothelial cells, which appeared to reduce swelling of the stroma-equivalent (Proulx *et al.*, 2010). The model has since been improved, by replacing the dermal fibroblasts with a second sheet of corneal fibroblasts, and it has been used to study MMP expression during wound healing, however, the orientation of collagen has not been investigated (Couture *et al.*, 2016). As the fibroblasts used in this model are cultured in flasks, without the provision of topographical cues, it is likely that they will be oriented randomly across the cell sheet with little organisation. The formation of roughly orthogonal lamellae within the stroma relates to its function and is key to ensuring the tissue can withstand intraocular pressure, therefore the orientation of collagen is an important requirement of recapitulating the stroma.

#### 1.3.4.1 Transwell membrane as a substrate for hCF cornea model

Human corneal fibroblasts (hCFs) supplemented with ascorbic acid and foetal bovine serum (FBS) have been shown to deposit orthogonal layers of collagen when cultured on a polycarbonate Transwell membrane (Guo *et al.*, 2007) (Figure 1.7). Transmission electron microscopy (TEM) revealed that the collagen fibrils within the lamellae-like matrix had an average fibril diameter of 38.1 nm, larger than that found in the stroma (25 – 30 nm). Different iterations of this model have been investigated, from changing the initial seeding density to supplementing culture media with growth factors. It has also been used to model pathologic conditions such as fibrosis and keratoconus (Karamichos *et al.*, 2010, 2012). In these models, hCFs consistently deposited collagen types I, V and VI. However, the expression of type III collagen and α-SMA has varied (Guo *et al.*, 2007; Karamichos *et al.*, 2010, 2012; Lee *et al.*, 2018). The cell sheets varied in thickness, between 20 and 40 µm and are commonly referred to as 2.5D cultures. In an effort to create a more 3D model, these cell sheets have been stacked to create a construct greater than 300 µm (D. Karamichos *et al.*, 2014; Priyadarsini *et al.*, 2017a). Furthermore, the Transwell model has recently been modified to incorporate additional cell types such as a neuroblastoma cell lines to investigate the interaction between the corneal stroma and nerve cells in the diabetic cornea

(Priyadarsini *et al.*, 2017b). The Transwell membrane shows great promise as a substrate for an *in vitro* model, supporting the deposition of an ECM that resembles the native stroma.

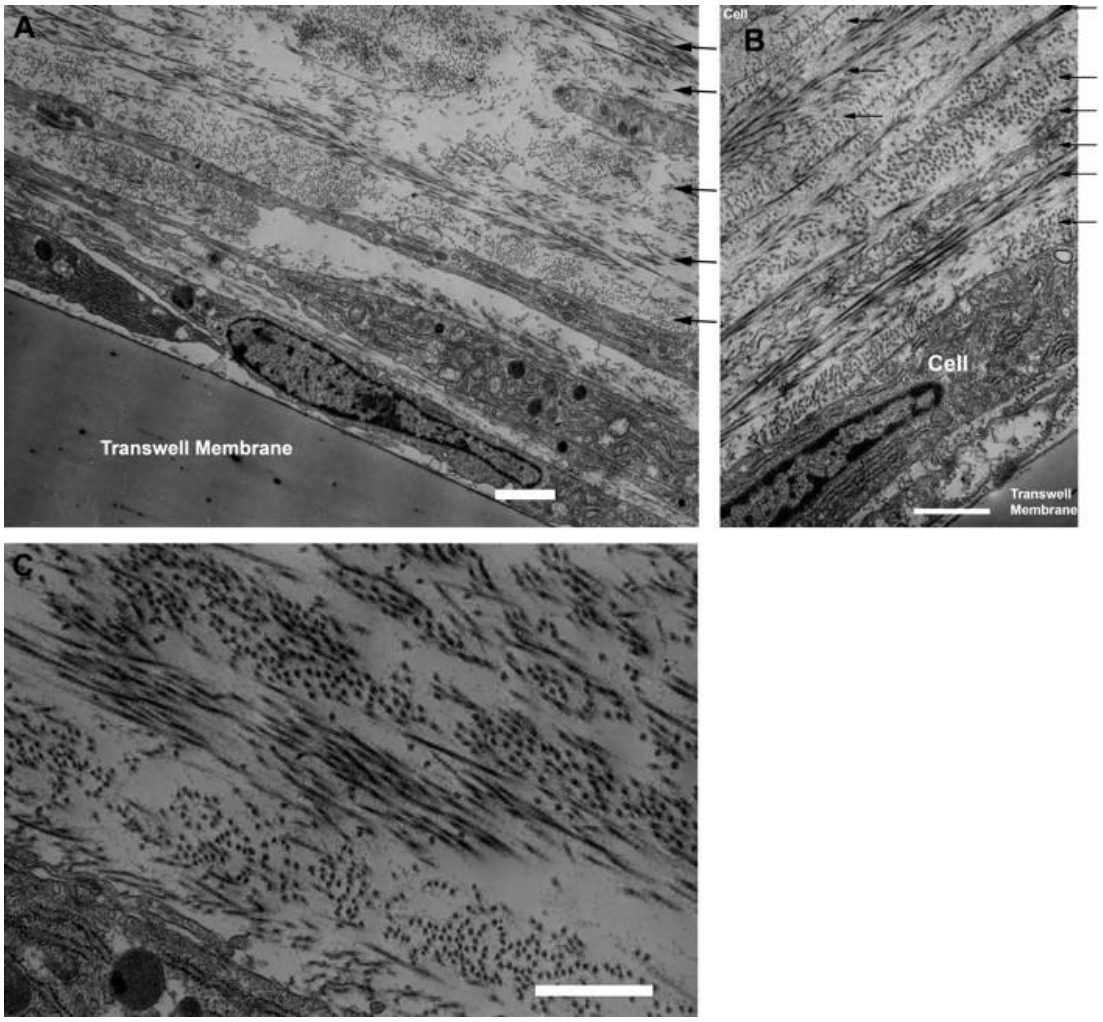


**Figure 1.7 TEM of hCFs cultured on Transwell membrane for 4 weeks.** A: Low magnification image of the hCFs that had been cultured on the Transwell membrane which is also in view. A change in the collagen fibril orientation is observed (black arrows). B: As the magnification is increased the change in organisation of the collagen fibrils becomes more apparent (black arrows). C: A high magnification image shows the orthogonally arranged collagen fibrils. Scale bars are A and B: 2 µm and C: 1 µm. Figure from (Guo *et al.*, 2007).

### 1.3.4.2 The influence of contact guidance and topographical cues on corneal stromal cells

Cells are known to react and respond to the underlying topography of the substrate on which they are cultured via contact guidance (Tamiello *et al.*, 2016). Contact guidance has been shown to affect cell morphology, orientation and migration in a number of different cell types from fibroblasts (Vrana *et al.*, 2008) and endothelial cells (Dreier *et al.*, 2013a) to neuronal cells (Lizarraga-Valderrama *et al.*, 2019) and osteoblasts (Refaaq *et al.*, 2020). The process of cell alignment, depicted in Figure 1.8 A, begins shortly after cells adhere to the

substrate, where the cell undergoes spreading before responding to the cues and orienting itself along the direction of the grooves. There are several theories that suggest how contact guidance occurs, and these have been thoroughly reviewed (Tamiello *et al.*, 2016). The first is the mechanical restriction theory whereby the distance between the anisotropic features, such as nanofibres, is the primary factor for cell alignment (Figure 1.8 B) (Dunn and Heath, 1976). If the groove width is so great that cellular processes and filopodia cannot bridge across, the cells become polarised and align parallel to the grooves. Actin filaments and focal adhesions (multi-protein complexes, directly connected to actin filaments and components of the ECM) also align in a parallel direction. The second theory suggests that focal adhesion formation and maturation, and subsequently cell alignment, only occurs if the width of the feature is greater than 2 µm – the size of a focal adhesion (Figure 1.8 C) (Ohara and Buck, 1979). By aligning in the direction of the anisotropic features, there is a greater length of substrate available for the formation of focal adhesions. An alternative theory is that cells react to substrate discontinuities, such as an edge, by forming focal adhesions (Figure 1.8 D) (Curtis and Clark, 1990). Increasing the height of the anisotropic features results in the cells being more exposed to discontinuities and they consequently align in the direction of the features (Tamiello *et al.*, 2016). No consensus has yet been reached on precisely how contact guidance occurs, and any of these hypotheses may explain the alignment of corneal stromal cells when cultured on anisotropic substrates.

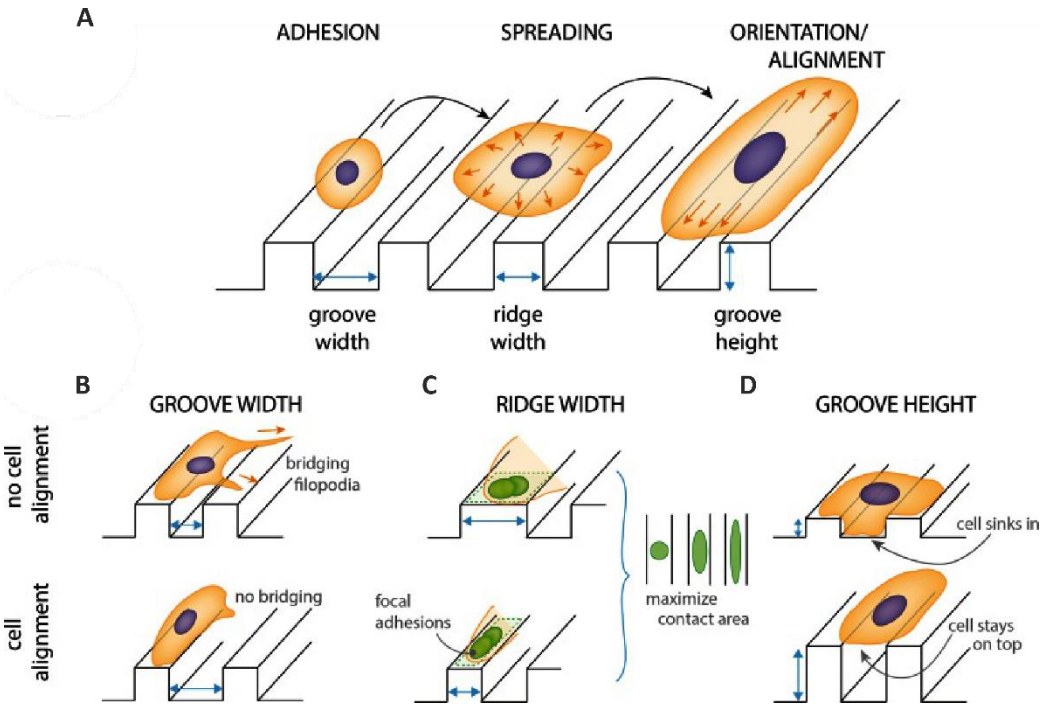


**Figure 1.8 A schematic representation of cellular orientation in response to aligned, linear topographical features.** A: Cell orientation response, from adhesion to alignment on a substrate with aligned topographical cues. The parameters characterising microgrooved substrates are indicated (groove width, ridge width and groove height). B-D: Conditions in which cell alignment are thought to occur are indicated. B: If the groove width is so great that cell processes cannot bridge across it, the cells become polarised and align parallel to the grooves. C: The width of the ridge can influence focal adhesion and, consequently, cell orientation. D: Sufficiently high grooves are thought to result in the formation of focal adhesions along the groove edge, as the cells respond to substrate inconsistency. Image from (Tamiello *et al.*, 2016).

The orientation of corneal stromal cells has been shown to improve the transparency of tissue engineered stroma constructs and can prevent the transdifferentiation of hCFs to myofibroblasts (Vrana *et al.*, 2008; Myrna *et al.*, 2012). Furthermore, the use of topographical cues to align cells can induce the secretion of a more organised matrix. Micro-structured substrates, such as those with grooves, have been shown to support hCF proliferation and alignment (Guillemette *et al.*, 2009). In fact, hCFs stratified and formed a second layer which rotated by approximately 50°, whilst still remaining aligned (Figure 1.9). TEM showed organised matrix deposited by hCFs when cultured on the substrates with topographical cues, particularly when compared to the flat controls. Furthermore, when these sheets of cells were stacked on top of one another, the constructs cultured on micro-structured substrates macroscopically appeared to be more transparent than the controls.

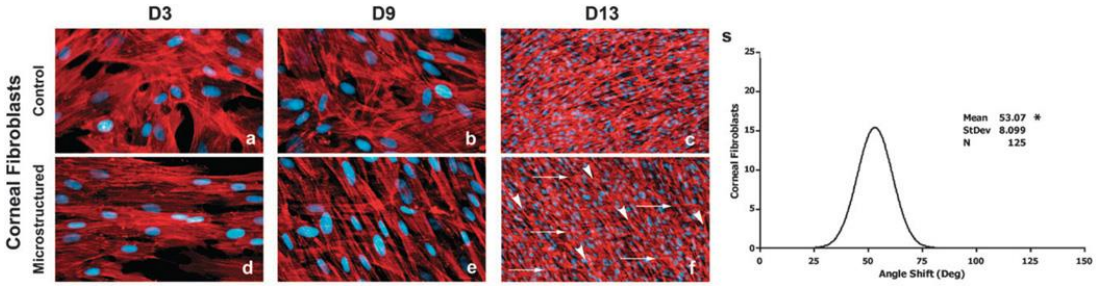


**Figure 1.9 Immunofluorescence staining of actin filaments of hCFs cultured on a substrate with topographical cues.** A-C: hCFs cultured on the control substrate are randomly oriented at time points day 3, 9 and 13. D-F: When cultured on a substrate with topographical cues, hCFs align in the direction of cues, evident by day 3. As time progresses the hCFs continue to follow the topographical cues (long white arrows) but are also observed stratifying and rotating (white arrow heads). S: As the hCFs stratify and form a second layer they rotate by 53.07°. Figure adapted from (Guillemette *et al.*, 2009).

Electrospinning is a method of extruding fibres, with diameters in the nano- to micro-range, from a polymer solution. This method, which can produce both aligned and randomly oriented fibres, has been used to create substrates for corneal stromal cells. A variety of polymers have been trialled, from poly lactic acid to collagens, which have all supported corneal cell growth (Wray and Orwin, 2009; Wilson *et al.*, 2012; Yan *et al.*, 2012; Fernández-Pérez *et al.*, 2020a). The alignment of these electrospun fibres not only resulted in the alignment of stromal cells but also influenced cell phenotype. Corneal fibroblasts isolated from rabbits and cultured on aligned electrospun type I collagen fibres had a reduced expressed of α-SMA compared to those cultured on randomly oriented fibres (Wray and Orwin, 2009). Moreover, aligned rabbit corneal fibroblasts scattered less light than those cultured on randomly oriented fibres and those cultured in a collagen gel (Phu *et al.*, 2011). Surprisingly, cells cultured on orthogonally aligned electrospun scaffolds had a significant reduction in ALDH3A1 expression compared to those cultured on randomly oriented fibres (Fernández-Pérez *et al.*, 2020a). A reduction in ALDH3A1, a corneal crystallin, could result in an increase in light scattering and reduction in transparency, although this was not measured. To create a construct resembling the corneal stroma, Wilson *et al.* incorporated layers of electrospun poly (L, D lactic acid) fibres and a type I collagen hydrogel (Wilson *et al.*, 2012). Human corneal stromal cells were seeded onto the orthogonally arranged electrospun fibres prior to the addition of a collagen solution, which was added to provide support to the fibre layers. The incorporation of fibres within the hydrogel significantly reduced the gene expression of THY-1 and ACTA2, markers typically used to characterise fibroblasts and myofibroblasts (Pei *et al.*, 2004). Whilst this substrate can support the growth of stromal cells; the ultrastructure of the collagenous matrix is unlikely to resemble the

native stroma. Poly lactic acid is a biodegradable polymer and this construct may be better suited as a graft-alternative.

An alternative method of producing substrates with topographical cues is the use of friction transfer. Friction transfer of polymers has been shown to produce nanofibres when the polymer is rubbed against a smooth, flat surface (Myshkin *et al.*, 2005; Kearns *et al.*, 2010). Polytetrafluoroethylene (PTFE) is the polymer most commonly associated with friction transfer where either a thin film or a series of nanofibres is created (Beamson *et al.*, 1996). Several different parameters can influence how PTFE is transferred, including: the temperature of both the substrate (where the fibres are deposited) and the PTFE blade; the speed at which the polymer slides across the substrate; and the pressure exerted on the substrate (Beamson *et al.*, 1996; Kearns *et al.*, 2010). Kearns *et al.* identified that increasing the substrate temperature to 250°C caused the PTFE fibres produced to have minimal spacing between them and covered more of the substrate when compared to lower temperatures (200 – 225°C), which tended to produce surfaces with large uncoated areas (Kearns *et al.*, 2010). The research to date has allowed for the creation of nanofibres of a non-uniform diameter and spacing. In general, the fibres have a nanoscale diameter with fibres ranging from 100 – 800 nm and spacing between the fibres ranging from 0.5 – 10 μm (Kearns *et al.*, 2010, 2013). The culturing of human gingival fibroblasts on PTFE nanofibres (PTFE-nf) resulted in the alignment of cells (Kearns *et al.*, 2010). Similarly, murine fibroblasts cultured on PTFE-nf deposited aligned collagen (Schofield *et al.*, 2011).

PTFE-nf have also been used in corneal stroma tissue engineering. Gouveia *et al.* cultured corneal fibroblasts on PTFE-nf alone and PTFE-nf coated with a peptide amphiphile in serum-free media (to reverse the phenotype back to a keratocyte-like cell) for 21 days (Gouveia *et al.*, 2013; Foster *et al.*, 2015). Although the addition of a peptide amphiphile coating (which can be enzymatically degraded to release a cell sheet) created irregular topography, hCFs still successfully aligned on both substrates. The provision of topographical cues provided by the PTFE-nf was found to be important not only for reversing the phenotype of hCFs to keratocyte-like cells, but also for the deposition of aligned collagen which increased the stiffness of the tissue construct (Gouveia *et al.*, 2017a). PTFE-nf support the alignment of cells and the deposited matrix, showing potential as a substrate for creating an equivalent of a stroma lamella.

#### 1.3.4.3 The influence of substrate stiffness on corneal stromal cells

Substrate stiffness can also influence cell behaviour and phenotype (Wells, 2008). The reported stiffness of the stroma is 33 kPa (Last *et al.*, 2012). A recent study compared the cellular response of corneal stromal cells cultured on tissue culture plastic ($10^6$ kPa) to those cultured on Softwell plates which are coated with a polyacrylamide hydrogel to give substrates with a stiffness of 1 kPa and 25 kPa (Chen *et al.*, 2020). Culturing stromal cells (in 2% FBS) on the substrate with a stiffness that more closely resembles the cornea resulted in an increase in the gene expression of ALDH1A1, ALDH3A1, CD34 and LUM (the gene coding for lumican) when compared to tissue culture plastic ($10^6$ kPa). An increase in these genes suggests that stromal cells cultured on more compliant substrates can revert back to a more keratocyte-like phenotype. The expression of corneal crystallins could reduce light scattering if employed in a tissue engineered stroma equivalent. This is further supported by Dreier *et al.* who reported that hCFs cultured on tissue culture plastic also exhibited increased expression of α-SMA when induced with TGF-β1, compared to more compliant substrates (Dreier *et al.*, 2013b). Stiffness, along with topographical cues, can modulate cell phenotype and may be an important factor to consider when creating a tissue engineered equivalent of the stroma.

In summary, culturing corneal stromal cells on substrates with topographical cues shows a lot of potential for the creation of a construct that resembles one or two lamellae within the stroma. One drawback of the above-mentioned studies is their use of corneal fibroblasts as opposed to keratocytes. Whilst some research suggests that this phenotype can be reversed, and fibroblasts can de-differentiate, an alternative strategy is to use multipotent cells that can be differentiated into keratocytes.

### 1.3.5 A bottom-up approach using stem and mesenchymal stromal cells

Fibroblasts can secrete a matrix that is typically associated with a wound environment, such as type III collagen (Funderburgh *et al.*, 2003). Stem cells, which can be differentiated into keratocytes, have been incorporated into *in vitro* models because the ECM they secrete is more likely to accurately resemble that found within the stroma. Multipotent cells can be isolated from a variety of tissues and many have been used in an effort to obtain keratocytes, including cells derived from adipose tissue (Du *et al.*, 2010), bone marrow (Dos Santos *et al.*, 2019), umbilical cord (Dos Santos *et al.*, 2019), dental pulp (Syed-Picard *et al.*, 2015), periodontal ligament (Yam *et al.*, 2018) and the cornea itself (Du *et al.*, 2005; Wu *et al.*, 2013). A table summarising the most commonly used cell sources can be found in Table 1.3.

#### 1.3.5.1 The influence of topographical cues on stem/progenitor cells

As with hCFs, electrospun substrates have also been used to culture CSSCs. Aligned poly(ester urethane) urea fibres resulted in the deposition of an aligned matrix composed of collagen types I, V and VI (Wu *et al.*, 2012). They also supported the differentiation of CSSCs into keratocytes to a greater extent than those that were randomly oriented, characterised by the increased gene expression of KERA, CHST6 and ALDH (Wu *et al.*, 2012). The addition of fibroblast growth factor-2 (FGF-2) and TGF-β3 to keratocyte differentiating medium (KDM) further improved matrix deposition and resulted in the formation of a thick, multi-layered construct with orthogonal collagen fibrils (Wu *et al.*, 2013). When directly compared to hCFs in the same medium, CSSCs deposited more collagen whilst expressing significantly less α-SMA (Wu *et al.*, 2014a). Furthermore, the constructs created by CSSCs were not only thicker than the hCF constructs but the cells also deposited orthogonal layers of collagen (Figure 1.10). Similar results have also been shown when hCFs and CSSCs were cultured for up to 9 weeks on films of silk that had previously been cast on a patterned surface to form grooves (Wu *et al.*, 2014b). CSSCs cultured on the silk films produced a construct much thicker than hCFs, with orthogonal layers of collagen (Wu *et al.*, 2014b). As with electrospun fibres, these films have also been stacked to create constructs that somewhat mimic the stroma with an increased expression of keratocyte markers such as keratocan, lumican and ALDH3A1 (Ghezzi *et al.*, 2017). Polydimethylsiloxane cast onto a patterned surface has also supported the formation of a CSSCs cell sheet, after culture in KDM, composed of aligned collagen that could be peeled off the substrate (Syed-Picard *et al.*, 2016). 5 weeks post-implant into a mouse model, light scattering from the cell sheets was similar to control corneas suggesting that the sheets had become transparent. Dental pulp stem cells cultured in KDM exhibited upregulation of keratocyte markers such as KERA, ALDH3A1 and CHST6 (Syed-Picard *et al.*, 2015). When cultured on aligned electrospun nanofibres for 4 weeks, the dental pulp cells aligned with the orientation of collagen shifting by approximately 80° throughout the 30 µm thick construct, although the authors do not measure the angle.

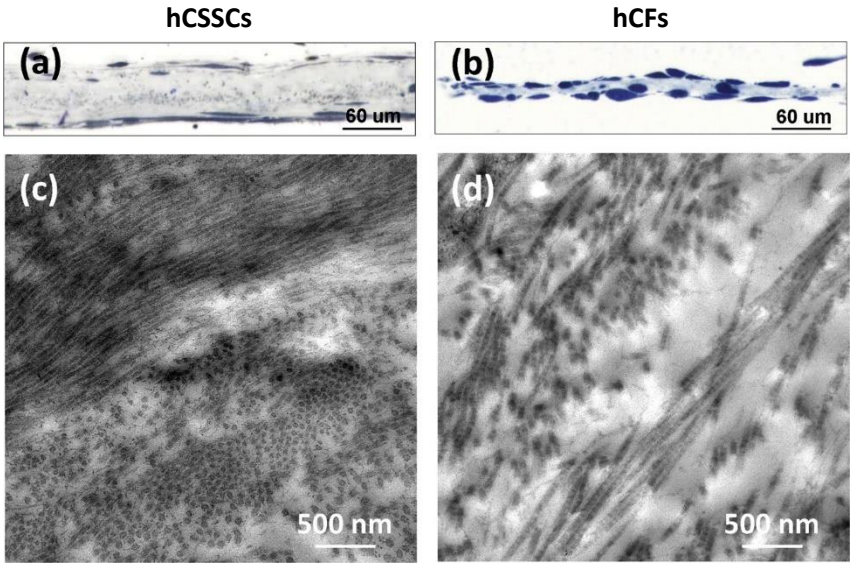


**Figure 1.10 A comparison between constructs generated by hCSSCs and hCFs cultured on electrospun poly(ester urethane) urea for up to 9 weeks.** A-B: The ECM secreted by hCSSCs is demonstrably thicker than that secreted by hCFs. C-D: The ultrastructure of the matrix, evaluated by TEM, shows that hCSSCs secreted collagen in tightly packed, orthogonal layers.

#### 1.3.5.2 Transwell membrane as a substrate for stem cell-based cornea model

Stem cells isolated from the cornea have also been cultured on polycarbonate Transwell membranes, similar to the model described by Guo *et al.* (Guo *et al.*, 2007; Dimitrios Karamichos *et al.*, 2014). Interestingly, in this model the hCF-generated construct was greater in thickness than that generated by CSSCs. The cells aligned and, upon the supplementation with TGF-β3, formed orthogonal layers of collagen, whereas the collagen secreted by CSSCs was more randomly oriented. The polycarbonate Transwell membranes were found to have parallel features along the surface of the membrane (Figure 1.11) (Dimitrios Karamichos *et al.*, 2014). These features had an average spacing of 218 nm and likely acted as topographical cues for the cells, resulting in cell alignment. They may also explain the orthogonal lamellae formed in the hCF Transwell models described by Guo *et al.* (Guo *et al.*, 2007). In the Transwell model, the gene expression of KERA and CHST6, genes associated with a keratocyte phenotype, increased after hCFs were cultured in the Transwell model for 4 weeks (Dimitrios Karamichos *et al.*, 2014). Mesenchymal stromal cells isolated from umbilical cords have also been incorporated into the Transwell model (Karamichos *et al.*, 2011). The addition of TGF-β1 to culture media increased the diameter of deposited collagen fibrils, from 28 nm to 32 nm, whilst also disrupting the orthogonal arrangement of the matrix. Furthermore, the supplementation of TGF-β1 resulted in a decrease in the expression of keratocan, but type V collagen expression was upregulated. A reduction of

keratocan could be indicative of cells transitioning to a more fibroblast-like phenotype and may explain the increased collagen fibril diameter. An increase in type V collagen suggests that the umbilical cord cells can synthesise a matrix that somewhat resembles the stroma. Whilst these results show potential, the expression of fibroblast and myofibroblast markers was not investigated and it is, therefore, unclear just how well MSCs derived from umbilical cords can differentiate into keratocytes. A more recent study directly compared the differentiation capacity toward keratocyte lineage of multipotent cells from adipose tissue, bone marrow, umbilical cord, and CSSCs (Dos Santos *et al.*, 2019). Here, umbilical cord cells did not show an increase in the expression of genes KERA nor CHST6 and the authors concluded that CSSCs showed the greatest potential to be differentiated toward keratocyte lineage.

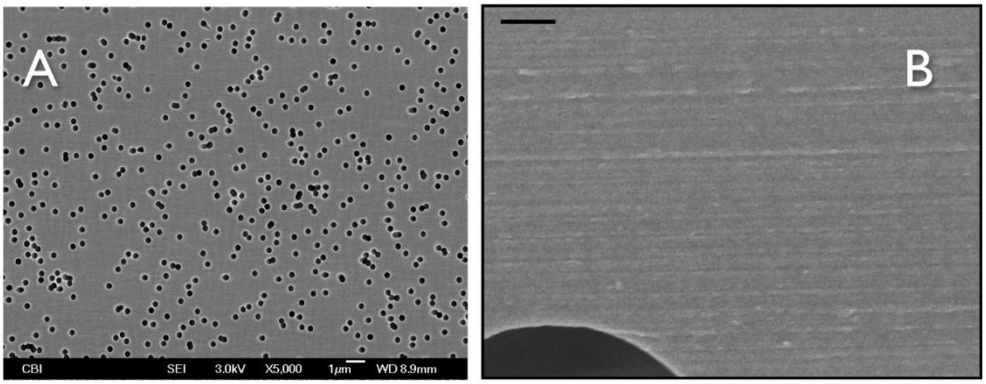


**Figure 1.11 Topographical cues present on the surface of polycarbonate Transwell membranes.** A: Scanning electron micrograph (SEM) at 5000X shows the 0.45 µm pores. B: At 20,000X faint lines can be seen across the surface of the membrane. Reported scale bars are A: 10 µm and B: 1 µm. Figure adapted from (Dimitrios Karamichos *et al.*, 2014).

#### 1.3.5.3 Induced pluripotent stem cells

Although not directly used to create a construct that mimics the corneal stroma, another source of cells used to differentiate down a keratocyte lineage is induced pluripotent stem cells (iPSCs). In one study, iPSCs were first differentiated into neural crest cells before pelleting and culturing in KDM for 21 days (Naylor *et al.*, 2016). The pelleted cells expressed keratocan, however, when directly compared to isolated keratocytes, the gene expression of markers such as ALDH3A1 and CHST6 was significantly lower. Corneal organoids, produced from iPSCs after neural crest induction, also expressed keratocan alongside lumican and collagen types I and V (Foster *et al.*, 2017). TEM analysis revealed collagen accumulation similar to that seen in the developing cornea, suggesting that perhaps iPSC-derive cornea organoids could be used to model corneal stroma development.

**Table 1.3 Potential cell sources for corneal stroma tissue engineering.**

| Cell type | Advantages | Limitations |
|---|---|---|
| Keratocytes | Native cell type<br>Tissue readily available<br>Deposits collagen similar to that *in vivo* | Difficult to expand in culture<br>Cells readily transition into fibroblasts and/or myofibroblasts, although can reportedly be dedifferentiated (Foster *et al.*, 2015; Sidney and Hopkinson, 2018) |
| Corneal fibroblasts | Tissue readily available<br>Cells easily isolated and expanded<br>Commonly used to model the stroma | Deposits collagen similar to that found during wound healing |
| Corneal stromal stem cells | Tissue readily available<br>Can be differentiated into keratocytes (Du *et al.*, 2007; Wu *et al.*, 2012) | |
| MSCs | Available from multiple source tissues<br>Can be differentiated into keratocytes (Du *et al.*, 2010; Dos Santos *et al.*, 2019) | Differentiation potential towards keratocyte lineage not as great as CSSCs (Dos Santos *et al.*, 2019)<br>Cost |
| iPSCs | Available from multiple source tissue<br>Can be differentiated into keratocytes | Requires two differentiation steps (Naylor *et al.*, 2016)<br>Cost |

Whilst there has been great progress in creating constructs and scaffolds as an alternative to allogeneic grafts, there are still several challenges that must be overcome to create an *in vitro* model that recapitulates the corneal stroma. To date, one of the biggest drawbacks is the time it takes for cells to deposit an organised matrix. Cells have been cultured for up to 3 months in an effort to create a structure resembling just several lamellae of the stroma; reducing this time could allow for high-throughput models to be created.

## 1.4 Macromolecular crowding

Typical two-dimensional (2D) cell culture removes cells far from their typical microenvironment, where they are usually surrounded by ECM, other cell types, and chemical cues such as cytokines, hormones and growth factors (Barthes *et al.*, 2014). Most cells within the body are not surrounded by large volumes of aqueous media, with the approximated concentration of macromolecules in tissues ranging from 50 – 400 mg/ml (Minton, 2001). In contrast, typical cell culture media has macromolecule concentrations of as little as 1 mg/ml (Ellis, 2001). This can be slightly increased with the addition of serum which contains 80 mg/ml of protein however, as serum is commonly used at 10% (v/v), this only equates to 8 mg/ml (Lareu *et al.*, 2007a). In an effort to place cells in an environment that somewhat resembles the *in vivo* microenvironment, macromolecular crowding (MMC) has been employed. The addition of inert macromolecules to aqueous cell culture media can effectively crowd the media and this has been shown to have a number of advantages from upregulating the expression of certain genes, such as COL1A1, to increasing the processing of procollagen to collagen (Bateman *et al.*, 1986; Kumar *et al.*, 2015b).

The addition of macromolecules to media results in the exclusion of volume, restricting the area that other macromolecules, such as proteins, can occupy. The fraction of volume occupied (fractional volume occupancy; FVO) can be approximated by assuming the macromolecule is a hard sphere; with a well-defined molecular weight; is neutrally charged; and that there is only a single macromolecule present (Hall and Minton, 2003; Chen *et al.*, 2011). The calculations used to estimate the FVO are found in Table 1.4 (Chen *et al.*, 2011). The total excluded volume that a molecule of interest will experience is greater than just the FVO, as depicted in Figure 1.12, as a result of the unavailable space between macromolecules (Chen *et al.*, 2011). This effect can be enhanced further by the use of charged macromolecules, which will repel from one another creating an even larger excluded volume. Given that most proteins at physiological pH are negatively charged, the excluded volume effect will be greater when a negatively charged crowder is used, with macromolecules and proteins repelling one another (Harve *et al.*, 2006).

Upon the addition of macromolecules to an aqueous media, cells are immersed in an environment that more accurately captures their surroundings *in situ.* Crowding increases the apparent concentration of molecules of interest by reducing the available space (Figure 1.13). This ultimately increases thermodynamic activity (effective concentration of a species in a mixture) and is, therefore, different to simply reducing the volume of media added to cultured cells, which does not increase collagen deposition (Peng and Raghunath, 2010).

MMC is thought to increase the deposition of ECM via the following mechanisms: 1) increasing the relative density of both procollagen and proteinases (Satyam *et al.*, 2014) 2) increasing the proteolytic conversion of PCPE-1 to its active form, enhancing procollagen C-proteinase (Kessler and Adar, 1989; Takahara *et al.*, 1994; Lareu *et al.*, 2007b); 3) proteolytic conversion of PCPE-1 also produces a small fragment that can inhibit MMP-2, reducing collagen degradation and remodelling (Mott *et al.*, 2000); 4) increasing lysyl oxidase activity, which increases collagen crosslinking (C. Chen *et al.*, 2009; Peng and Raghunath, 2010).

The ideal crowder is one that does not self-aggregate and is biologically inert, only exerting steric repulsion on the molecules of interest within the culture media. At 80 mg/ml albumin, the main protein in serum, has been estimated to wield an FVO of 18% *in vivo* (Chen *et al.*, 2011). Albumin itself has been used as a crowder in cell-free *in vitro* collagen fibrillogenesis but aggregates of type I collagen were formed (Zeiger *et al.*, 2012). It would, therefore, be logical to identify and use a crowder that exerted a similar FVO in culture media to mimic the crowded conditions found *in vivo*. A recent study by Gaspar *et al.* suggests that, along with negative charge, the polydispersity (distribution of particle sizes) of a crowder can enhance matrix deposition (Gaspar *et al.*, 2019a). Polydispersity can be achieved either by using a single inherently polydisperse molecule, such as carrageenan, in a mono-crowded system or by combining two crowders of different molecular weights, otherwise known as mixed-MMC.

**Table 1.4 Calculations to approximate FVO.**

$$Volume\ of\ crowder\ molecule = \frac{4}{3}\pi r^3 \quad \text{(Eq. 1.4.1)}$$

$$Number\ of molecules\ in\ X\ mg = \frac{(X \times 10^{-3}) \times (6.022 \times 10^{23})}{MW} \quad \text{(Eq. 1.4.2)}$$

$$FVO\ (\%) = \frac{Volume\ of\ crowder\ molecule}{Number\ of\ molecules\ in\ X\ mg} \times 100 \quad \text{(Eq. 1.4.3)}$$

Where r, hydrodynamic radius; X, mass of crowder added per ml; 6.022 x $10^{23}$ Avogadro number; MW, molecular weight of crowder used; FVO, fractional volume occupancy. Equations described by (Chen *et al.*, 2011).

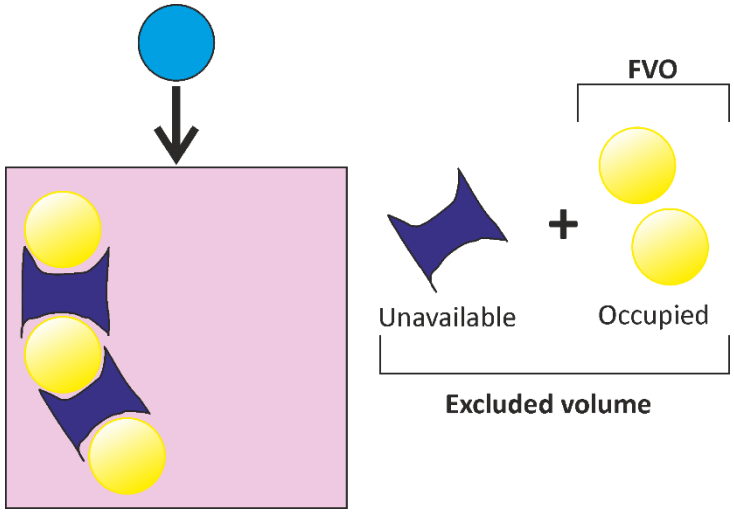


**Figure 1.12 A simplified model of MMC and the excluded volume effect.** In this model, the molecule of interest (blue) encounters a volume (pink box). The macromolecular crowders (yellow) occupy a given volume, termed the fractional volume occupancy (FVO). This, combined with the additional unavailable space, between the macromolecules, is the excluded volume. The unavailable volume is challenging to calculate due to the number of factors in play, such as electrostatic repulsion. Image adapted from (Chen *et al.*, 2011).

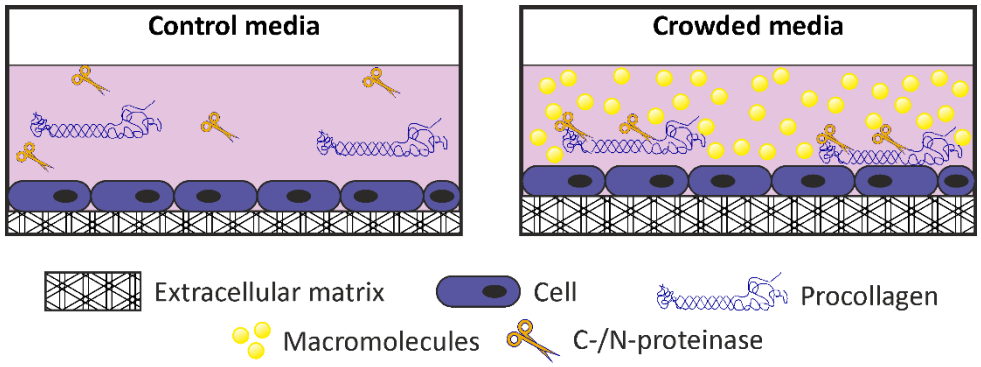


**Figure 1.13 A schematic representation of the effects of MMC in cell culture media.** In normal culture media collagen deposition is slow and procollagen often dissolves before it can be processed into collagen (left). In crowded media (right), volume is occupied by macromolecules which has been suggested to increase the relative density of both procollagen and proteinases, thus accelerating collagen deposition. Image adapted from (Satyam *et al.*, 2014).

### 1.4.1 Mono-Macromolecular Crowding

Crowding with a single macromolecule has been referred to as mono-MMC, and this can be with either a neutrally charged or a negatively charged crowder. Relatively neutral crowders, such as polyethylene glycol (PEG) (Bateman *et al.*, 1986; Gonzalez-Molina *et al.*, 2019), polyvinylpyrrolidone (PVP) (Bateman *et al.*, 1986; Rashid *et al.*, 2014), Ficoll (Lareu *et al.*, 2007b) and dextran (Bateman *et al.*, 1986; Lareu *et al.*, 2007a) have previously been added to cell cultures in an attempt to increase the deposition of the ECM, with varying success.

Negatively charged crowders such as dextran sulphate (Bateman and Golub, 1990; Lareu *et al.*, 2007a; Kumar *et al.*, 2015b), polysodium-4-styrene sulfonate (PSS) (Lareu *et al.*, 2007b), hyaluronic acid (Shendi *et al.*, 2019) and carrageenan (Satyam *et al.*, 2014; Kumar *et al.*, 2015b; Gaspar *et al.*, 2019b) have all been used to enhance matrix deposition *in vitro*.

#### 1.4.1.1 Neutral crowders

PEG was one of the first crowders to be added to cell culture media and it has been shown that crowding with PEG results in the complete processing of collagen, secreted by dermal fibroblasts, into cell layers by 24 hours (Bateman *et al.*, 1986). This is in contrast to control samples where procollagen and partially processed procollagen were secreted in culture media. Similar results have also been observed with the addition of PVP as a crowder (Bateman *et al.*, 1986). This was supported by Rashid *et al.* who found that MMC with PVP increased the deposition of type I collagen in cell layers in both dermal fibroblasts and in mesenchymal stromal cells (Rashid *et al.*, 2014). More recently, PEG has been added to the culture medium of a cancer cell line to mimic the tumour microenvironment (Gonzalez-Molina *et al.*, 2019). MMC with PEG increased the deposition of collagens and caused cell elongation, resulting in some cell alignment.

Ficoll is a neutral polysaccharide that has been used in Ficoll-Paque for the isolation of mononuclear cells from blood samples via a density gradient. The 70 kDa version of Ficoll was unable to accelerate the rate of type I collagen deposition in lung fibroblasts (Lareu *et al.*, 2007b). Similar results have been shown with dermal fibroblasts where type I collagen deposition was not increased but, interestingly, type III collagen was (Gaspar *et al.*, 2019a). Increasing the molecular weight of Ficoll does not appear to improve the crowding effect and the use of Ficoll 400 kDa also failed to enhance type I collagen deposition after 48 hours (Lareu *et al.*, 2007b). Similar to the low molecular weight version of the polymer, type III collagen deposition increased after 14 days in dermal fibroblast cultures crowded with Ficoll 400 kDa, but this appeared to be less than that observed when crowded with Ficoll 70 kDa (Gaspar *et al.*, 2019a).

Another neutrally charged polymer that has been used as a macromolecular crowder is dextran. Dermal fibroblasts crowded with dextran (40 kDa) induced the processing of procollagens secreted by dermal fibroblasts and the incorporation of processed collagen in the cell layer (Bateman *et al.*, 1986). Interestingly, Lareu *et al.* found that crowding with dextran (670 kDa) did not increase the incorporation of processed collagen into the cell layer but, the negatively charged dextran sulphate (500 kDa) did (Lareu *et al.*, 2007a).

#### 1.4.1.2 Negatively charged crowders

Negatively charged crowders have been shown to further increase the crowding effect, and thus increase the deposition of ECM, compared to neutral molecules of a similar size (Lareu *et al.*, 2007a; Gaspar *et al.*, 2019a). Crowding with dextran sulphate (500 kDa) can increase the proportion of secreted collagen incorporated into the cell layer compared to the media (Bateman and Golub, 1990; Lareu *et al.*, 2007a; Gaspar *et al.*, 2019a). Lareu *et al.* have also shown that whilst crowding with dextran sulphate did not increase the amount of procollagen C-proteinase present, it did increase the presence of the active form of PCPE-1, which is known to enhance procollagen cleavage (Steiglitz *et al.*, 2006; Lareu *et al.*, 2007b). Additionally, the authors note that the PCPE-1 C-terminus can inhibit MMP2 activity, further contributing to the increased amount of collagen in the cell layer by limiting degradation (Mott *et al.*, 2000). The addition of dextran sulphate has also been shown to upregulate the expression of COL1A1 and COL5A1 in corneal fibroblasts, with a corresponding increase of collagen deposition in the cell layer observed (Kumar *et al.*, 2015b). However, the expression of ACTA2, the gene coding for α-SMA and a marker for myofibroblasts, was also increased. This suggested that the addition of dextran sulphate may result in myofibroblast transdifferentiation although this was not seen at the protein level with immunocytochemistry. Negative effects, such as cell death, have been reported when dextran sulphate was added to bone marrow-derived MSC cultures (Prewitz *et al.*, 2015). Similarly, PSS (200 kDa) was incompatible with MSCs despite enhancing collagen deposition into the cell layer of lung fibroblasts (Lareu *et al.*, 2007b; Prewitz *et al.*, 2015).

Carrageenans are a natural mucopolysaccharide derived from red seaweed and are commonly used as a gelling agent in the food industry. They can be distinguished by the number of sulphate groups (one, two or three) per disaccharide unit and are denoted by the prefixes κ-, ι-, and λ- respectively (Carneiro-Da-Cunha *et al.*, 2011). Given its inherent polydispersity, carrageenan has been regularly used to increase collagen deposition in cultures of bone marrow-derived MSCs (Cigognini *et al.*, 2016), corneal fibroblasts (Kumar *et al.*, 2015b), dermal fibroblasts (Satyam *et al.*, 2016) and tenocytes (Tsiapalis *et al.*, 2020). In contrast to dextran sulphate, crowding corneal fibroblasts with carrageenan did not cause a change in gene expression in either COL1A1, COL5A1 or ACTA2 (Kumar *et al.*, 2015b). This suggests that carrageenan could be used to accelerate the formation of a corneal stroma model.

### 1.4.2 Mixed-MMC

The combination of a larger and a smaller macromolecule within medium can increase polydispersity, a factor shown to improve the effects of crowding (Gaspar *et al.*, 2019a). This further increases the excluded volume effect, with the smaller crowder occupying additional space including in between the larger molecules. An example of such a combination is a Ficoll cocktail, often containing 37.5 mg/ml Ficoll 70 kDa and 25 mg/ml Ficoll 400 kDa. The Ficoll cocktail has successfully increased the deposition of type I collagen by fibroblasts, unlike each of the Ficoll solutions alone (Satyam *et al.*, 2020). Similarly, the Ficoll cocktail increased collagen deposition in bone marrow-derived MSCs (Zeiger *et al.*, 2012), dermal fibroblasts (Graham *et al.*, 2019) and corneal fibroblasts (Kumar *et al.*, 2015a). Similar to carrageenan, crowding with a Ficoll cocktail did not upregulate the hCF gene expression of COL1A1, COL5A1 or ACTA2. Dextran sulphate cocktails have also been used, either combining different dextran sulphates of various molecular weights (Gaspar *et al.*, 2019a), or by adding dextran sulphate to a Ficoll cocktail (Prewitz *et al.*, 2015). Dextran sulphate cocktails (10, 100 and 500 kDa) increased the deposition of type I collagen by dermal fibroblasts (Gaspar *et al.*, 2019a). Crowding bone marrow-derived MSCs with a dextran sulphate (10 kDa) and Ficoll cocktail (70 and 400 kDa) increased type IV collagen deposition in the absence of ascorbic acid (Prewitz *et al.*, 2015). Interestingly, when the culture media were supplemented with ascorbic acid collagen deposition was not increased but thicker fibrils were formed.

### 1.4.3 MMC and tissue engineering of the corneal stroma

A bottom-up approach to the engineering of the corneal stroma aims to create a microarchitecture that resembles the native stroma. This usually involves starting with relevant cells, such as keratocytes or stem cells, and culturing them in media supplemented with ascorbic acid to stimulate collagen deposition. Work by Proulx *et al.* (2010) has shown that after approximately 30 days in culture, supplemented with ascorbic acid, fibroblasts can produce sheets that can be peeled off and superimposed to create an engineered stroma construct (Proulx *et al.*, 2010). Similarly, work by Wu *et al.* (2014) has shown that the culture of corneal fibroblasts on patterned silk for 9 weeks can create a construct that is approximately 30 µm thick (Wu *et al.*, 2014b). Extensive culture periods can cause problems such as phenotypic drift whilst also increasing the risk of contamination. One of the main drawbacks of the self-assembly method, therefore, is the long culture period required to create a tissue construct.

Macromolecular crowding can accelerate the rate of collagen deposition and thus reduce the necessary culture period to create a tissue engineered stroma equivalent. Research by Kumar *et al.* has shown that mixed-MMC with a neutrally charged Ficoll cocktail can increase the deposition of type I collagen from as early as 2 days (Kumar *et al.*, 2015a). Immunocytochemistry (ICC) revealed an increase in the deposition of collagen types I, III, IV, V and VI and fibronectin but no change in gene expression was observed. The use of a thermal-responsive polymer allowed the detachment of cell sheets after 6 days and no differences were observed in the transparency of the cell sheets produced under crowded conditions when compared to a PBS buffer. The sheets transmitted > 90% of light across a range of wavelengths (380 – 780 nm). This is greater than the native cornea which typically allows < 60% transmittance at wavelengths shorter than 400 nm, increasing to around 90% transmittance at 700 nm (Fernández-Pérez *et al.*, 2020b). Kumar *et al.* also trialled the use of negatively charged crowders, carrageenan and dextran sulphate, to enhance collagen deposition (Kumar *et al.*, 2015b). Whilst both crowders were shown to increase the same ECM proteins via ICC, only dextran sulphate appeared to increase the gene expression of COL1A1, COL5A1, CD34 and ACTA2. CD34 is considered a phenotypic marker for keratocytes and its positive expression is indicative of corneal stromal cells maintaining a keratocyte-like phenotype (Sidney *et al.*, 2014). Conversely, ACTA2, the gene encoding for α-SMA, is a phenotypic marker for myofibroblasts typically observed in corneal wounds. However, immunocytochemistry did not reveal an increase in the expression of the protein α-SMA (Kumar *et al.*, 2015b). As with the mixed-MMC, no differences were observed in the transparency of the cell sheets crowded with carrageenan. In a more recent study, carrageenan was used as a crowder in corneal fibroblast cultures for up to 14 days at varying oxygen and serum concentrations (Kumar *et al.*, 2018). Culturing hCFs at 2% oxygen and 0.5% serum resulted in the greatest deposition of collagen types I, V and VI and fibronectin, although transparency was not assessed. Whilst the authors do not analyse collagen alignment, construct thickness and cell orientation, there is an apparent increase in the rate that the ECM is deposited. The crowded culture periods are much shorter than those typically used with the self-assembly approach of recapitulating the stroma. It is therefore possible that, by extending the culture period, a tissue engineered equivalent of the full corneal stroma can be created. As corneal stromal cells are particularly susceptible to phenotypic drift, care should be taken to ensure the cells do not transition into myofibroblasts.

MMC has also been used with *in vitro* collagen fibrillogenesis to create aligned fibrils which can form multiple layers, resembling the structure of tissues such as the corneal stroma (Saeidi *et al.*, 2012b). Young *et al.* recently presented a model suggesting that collagen organisation can occur in a cell-free system and may be influenced by proteoglycans (Young *et al.*, 2019). Manipulating crowding conditions can tune collagen matrices, produced by *in vitro* fibrillogenesis, to create a 3D matrix with narrow collagen fibrils that are more resistant to degradation which, in turn, can affect cell morphology (Ranamukhaarachchi *et al.*, 2019). To further optimise this system, exogenous proteoglycans could be added to the collagen solution which may improve fibril diameter and organisation.

## 1.5 Summary

The corneal stroma is a complex structure, with collagen fibrils arranged in such a way that they do not scatter light. Keratocytes, the main cell within the stroma, express corneal crystallins, allowing their cytoplasm to match the refractive index of the surrounding matrix, further reducing light scatter. For these reasons, tissue engineering of the cornea poses several challenges including: identifying an appropriate cell type; selecting an appropriate substrate which will result in the alignment of cells and thus the deposited matrix; and accelerating the rate of collagen deposition for the creation of a high throughput model.

There are several cell types that can be implemented into a corneal stroma model, such as cells isolated from the cornea, MSCs and iPSCs. A high throughput model requires cells that are easy to obtain. The Department of Eye and Vision Science regularly receives donated corneoscleral rims after the central tissue has been removed for transplantation and MSCs are frequently purchased for use in the adjacent Department of Musculoskeletal and Ageing Science. A search of relevant literature yielded only a handful of articles where iPSCs have been differentiated into keratocytes (Joseph *et al.*, 2016; Naylor *et al.*, 2016; Foster *et al.*, 2017). In contrast, CSSCs are cornea-derived cells that have been reported by several different groups and are frequently used in stroma tissue engineering (Wu *et al.*, 2014b; Syed-Picard *et al.*, 2016; Ghezzi *et al.*, 2017). In Chapter 2 hCFS, hCSSCs and bone marrow-derived MSCs were chosen based on the ease of obtaining tissue and their reported abilities to deposit a matrix resembling the stroma. hCFs are easy to obtain from corneoscleral rims, easy to expand and are frequently used in corneal tissue engineering. CSSCs can also be obtained from corneoscleral rings, excess tissue after a corneal graft, and can be differentiated into keratocytes. MSCs, such as those derived from adipose tissue have

also been shown to have the potential to differentiate into keratocytes and deposit an aligned matrix.

To support the deposition of an organised matrix, substrates for a stromal model should provide cues to ensure that cells can secrete collagen fibrils in such a way that it resembles the microarchitecture of the stroma. Both PTFE-nf and Transwell membranes show potential as substrates, with hCFs reportedly depositing organised collagen on both. Furthermore, the Transwell membrane is a commonly used substrate in corneal tissue engineering showing the deposition of lamellar-like collagen and will act as a comparator in Chapter 3 (Guo *et al.*, 2007; Priyadarsini *et al.*, 2017a; Brown *et al.*, 2021).

Carrageenan is a negatively charged macromolecule that can exert a large excluded volume effect and has been shown to increase collagen deposition without inducing the expression of ACTA2, suggesting it could play a useful role in accelerating the formation of a corneal stroma tissue construct. The deposition of collagen by corneal fibroblasts has also been increased when crowding with a Ficoll cocktail, composed of relatively neutral macromolecules. Hence, carrageenan and a Ficoll cocktail are good candidates to take forward and their impact on collagen deposition will be assessed in Chapter 4.

## 1.6 Hypothesis

This study will address the hypothesis that progenitor cells and/or cells residing in the limbal stroma can be influenced by nanotopography to deposit an organised matrix resembling the microarchitecture of the corneal stroma. It is further hypothesised that macromolecular crowding will increase matrix deposition without disrupting the organisation of the matrix.

## 1.7 Aims

1. To isolate and characterise hCFs and hCSSCs from corneoscleral rings, and MSCs from bone marrow; including analysis of stem and MSC marker expression. Further, to identify at least one cell type to carry forward for the creation of an *in vitro* stroma model.
2. To compare two substrates, one with nanofibres and a polycarbonate Transwell model; including analysis of cell alignment, collagen deposition and, where applicable, successful differentiation into keratocytes. Further, to identify the optimal method to create a stroma model.
3. To compare two macromolecular crowders, carrageenan and a Ficoll cocktail; including the analysis of collagen deposition via immunocytochemistry. Further, to

compare the ultrastructure of deposited collagens via transmission electron microscopy.

# Chapter 2. Cell isolation and characterisation

## 2.1 Overview

To establish an *in vitro* model of the corneal stroma, suitable cell types must first be selected. Current cell culture models typically use corneal fibroblasts (hCFs) isolated from a corneo-scleral rim. This chapter focuses on isolating and characterising cells that have the potential to create a stromal equivalent. hCFs, corneal stromal stem cells (hCSSCs) and bone marrow-derived mesenchymal stromal cells (hMSCs) were expanded and the cell phenotype, stability and protein expression were analysed.

## 2.2 Aims and Objectives

**The aim of this chapter was to isolate and characterise suitable cell sources for the development of an *in vitro* corneal stroma model.**

The objectives of this chapter were:

1. To isolate and expand hCFs and hCSSCs
2. To characterise hCFs, hCSSCs and hMSCs
3. To determine which of these cell types can be used to represent keratocytes

## 2.3 Materials

**Sigma/Merck (Germany):** Amphotericin B solution (A2942); β-glycerophosphate (G9422); Bovine serum albumin (BSA; A2153); Collagenase type-L (C8176); Dexamethasone (D4902); Fibronectin (F4759); Goat serum (G9023); Greiner culture flasks 75 $cm^2$ (T75; C7231) and 175 $cm^2$ (T175; C7356); Greiner CELLSTAR 96 well plates (M9936); 3-Isobutyl-1-methylxanthine (IBMX; I5879); Indomethacin (I7378); Insulin (I9278); L-Ascorbic acid 2-phosphate sesquimagnesium salt (A2P; A8960); Millicell EZ SLIDE 8-well glass, sterile (PEZGS0816); 10% neutral buffered formalin solution (NBF; HT501128); Papain from papaya latex (P3125); Penicillin-Streptomycin (P4333); Triton-X (23,472-9); Trypsin-EDTA (T4174); MCDB-201 (M6770); Tween-20 (P1379)

**Thermo Fisher (USA): Advanced** Dulbecco's Modified Eagle Medium (DMEM) (12491); AlbuMAX I (11020-021); DMEM GlutaMAX (61965); DMEM/F-12 (31331); DMEM low glucose, no phenol (118800-28); DMEM low glucose (21885); 4',6-Diamidino-2-Phenylindole, dilactate (DAPI; D3571); Epidermal Growth Factor (EGF; PHG0311); Gentamicin (15750-060); Insulin, Transferrin, Selenium (ITS; A8960); Minimum essential medium (MEM) Non-Essential Amino Acids Solution (11140035); Mr Frosty™ Freezing Container (5100-0001); Nunc™ Cell Culture Treated Flasks 25 $cm^2$ (T25; 136196); Oxoid™ Phosphate Buffered Saline Tablets (PBS; BR0014G); Quant-iT™ PicoGreen™ dsDNA Assay Kit (P7589); TRI Reagent solution (AM9738); TrypLE express (12604-013)

**Corning (USA):** Costar® 6-well/24-well/48-well TC-treated Well Plates (3516/3524/3548)

**Promega (USA):** M-MLV Reverse Transcriptase (M1701); Nuclease free water (P1195); Polymerase chain reaction (PCR) nucleotide mix (C1145); Random primers (C1181); RNasin Ribonuclease Inhibitors (N2615)

**LabTech (England):** Heat Inactivated Foetal Bovine Serum (batches 013BS145 and 70428)

**Eurogentec (Belgium):** Takyon Rox SYBR MastrMix dTTP Blue (UF-RSMT-B0710)

**R&D Systems (USA):** Human Mesenchymal Stem Cell Verification Kit (FMC020); Platelet-Derived Growth Factor (PDGF; 520-BB-050)

**Enzo Life Sciences (USA):** FNC coat (AES-0407-L050)

**BD Biosciences (USA):** BD CompBeads Anti-Mouse Ig, κ/Negative Control Compensation Particles Set (552843)

**Smith Scientific (England):** Academy 22 x 50 mm coverslip (NPS16/2250)

**Lonza (Switzerland):** Human bone marrow aspirate (1M-105); Human bone marrow mononuclear cells (19TL071807)

**Agilent (USA):** Dako fluorescent mounting medium (S3023)

## 2.4 Methods

### 2.4.1 Isolation of human corneal fibroblasts

Human corneoscleral rims (Figure 2.1) were obtained either from the Royal Liverpool University Hospital, after a corneal button had been removed for transplantation, or from the Venice eye bank (Fondazione Banca Degli Occhi Del Veneto Onlus). The use of human tissue was approved by a Research Ethics Committee (16/EM/0090). The rims were washed thrice in DMEM GlutaMAX with high glucose, the epithelium gently scraped off and excess sclera was trimmed. The remaining cornea was dissected into small chunks and digested overnight at 37°C in 1 mg/ml collagenase type L. The resulting cell suspension was centrifuged at 160 x g for 5 minutes and the supernatant discarded. The hCFs were resuspended in hCF growth medium (Table 2.1) and plated in T75 culture flasks. These freshly isolated cells were at passage 0 (P0) and were cultured at 37°C, 5% $CO_2$ and 20% $O_2$ for 21 days or until confluent. If large epithelial colonies were observed, cells were treated with 1X trypsin-EDTA for 4 to 5 min, leaving behind the epithelial cells, and re-plated in a new T75 culture flask (P1). If no epithelial colonies were present, hCFs were passaged directly into a T175 flask (P1). From P2 all hCFs were passaged in T175 culture flasks. For freezing, 1 x $10^6$ cells were resuspended in hCF freezing medium (Table 2.1) in a cryovial that was transferred to -80°C in a 'Mr Frosty'. The Mr Frosty contained isopropanol for a freezing rate of -1°C/min. Cells were transferred to vapour phase nitrogen for long term storage.

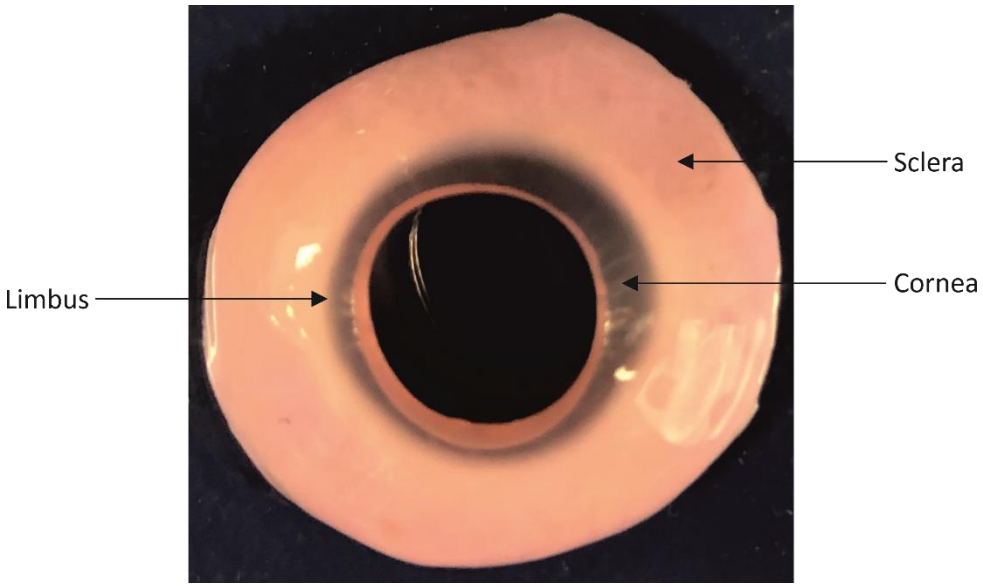


**Figure 2.1 Human corneoscleral rim indicating the main regions: sclera, limbus and cornea.**

### 2.4.2 Isolation of human corneal stromal stem cells

#### 2.4.2.1 Method 1

Human corneal rims were washed thrice in hCSSC wash medium (Table 2.1), the epithelium and endothelium scraped off and the superficial limbus was dissected out. The limbal stroma was dissected further and digested in 0.5 mg/ml collagenase-L overnight at 37°C. The resulting cell suspension of hCSSCs was centrifuged at 360 x g for 5 min. Cells were resuspended in CSSC growth medium (Table 2.1), plated into a T25 culture flask coated with FNC and cultured until small polygonal cell colonies were visible. Cells were then passaged using TrypLE Express and again when at 70-80% confluent.

#### 2.4.2.2 Method 2

Cells were isolated as described above however, after a visit to The University of Pittsburgh to learn the technique first-hand, a few alterations to the protocol were made. A narrower section of the limbus was taken to reduce corneal/scleral fibroblast contamination (Figure 2.2). After overnight digestion, the cell suspension was pipetted up and down to break up any larger pieces of tissue and, if required, incubated again for an additional 1 hour at 37°C. The suspension was then passed through a 70 µm cell strainer, centrifuged, and plated into an FNC coated T25 flask. Cells were cultured until colonies were visible and then passaged using TrypLE Express at room temperature. After the first passage, cells were seeded at 300-500 cells/cm$^2$ to prevent differentiation. When cells reached approximately $10^3$ cells/cm$^2$ they were passaged again.

**Table 2.1 Media and supplements used for each of the different cell types.**

| Cell type | Application | Basal media | Supplements |
|---|---|---|---|
| hCFs | Wash | DMEM high glucose GlutaMAX | None. |
| | Growth | DMEM high glucose GlutaMAX | 10% foetal bovine serum (FBS), 100 U/ml penicillin, 100 µg/ml streptomycin and 2.5 µg/ml amphotericin B. |
| | Freezing | DMEM high glucose GlutaMAX | 20% FBS and 10% dimethyl sulfoxide (DMSO). |
| hCSSCs | Wash | Equal volumes of DMEM GlutaMAX and DMEM/F-12 | 100 U/ml penicillin, 100 µg/ml streptomycin and 50 µg/ml gentamicin. |
| | Growth | 300 ml DMEM low glucose GlutaMAX and 200 ml MCDB-201 | 2% FBS, 1 mg/ml AlbuMaxI, 0.12 mM L-ascorbic acid 2-phosphate sesquimagnesium salt hydrate (A2P), 1 µg/ml insulin, 0.55 µg/ml transferrin, 670 ng/ml (ITS), 10 ng/ml platelet-derived growth factor (PDGF), 10 ng/ml epidermal growth factor (EGF), 10 nM dexamethasone, 100 U/ml penicillin, 100 µg/ml streptomycin and 50 µg/ml gentamicin |
| | Freezing | DMEM/F-12 | 20% FBS and 10% DMSO. |
| Mononuclear cells (hMNCs) | Growth | DMEM low glucose, no phenol | **Up to passage 3:** 10% FBS, 1% L-glutamine, 1 mM A2P, 100 U/ml penicillin, 100 µg/ml streptomycin and 2.5 µg/ml amphotericin B. |
| hMSCs | Growth | DMEM low glucose, no phenol | **0-14 days:** DMEM low glucose, 5% FBS, 1% GlutaMAX, 1% MEM non-essential amino acids (NEAA), 100 U/ml penicillin, 100 µg/ml streptomycin and 2.5 µg/ml amphotericin B.<br>**Day 15 onwards:** As above but increased FBS to 20%. |
| | Freezing | DMEM low glucose, no phenol | 20% FBS and 10% DMSO. |

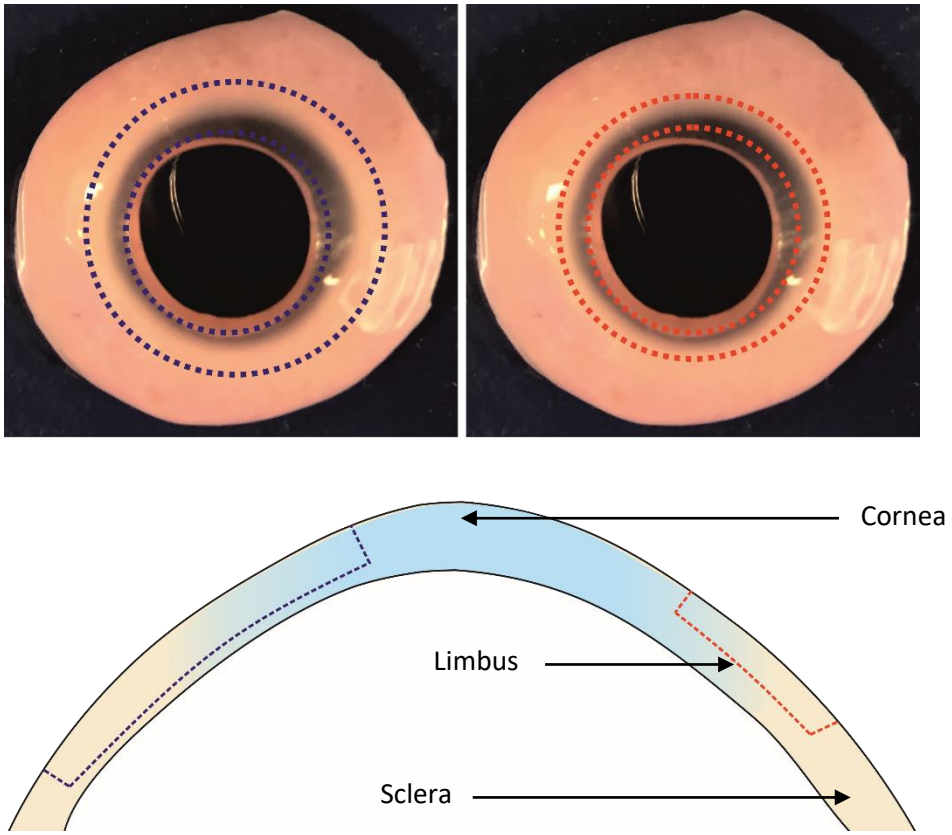


**Figure 2.2 A diagram to highlight the differences between the methods used to isolate hCSSCs.** The sections outlined in blue (left) show where the tissue was taken from in method 1. A smaller section was isolated in method 2, as outlined in red.

### 2.4.3 Expanding human bone marrow derived mesenchymal stromal cells

Adherent human mesenchymal stromal cells (hMSCs) were recovered from human bone marrow aspirate from 2 different donors (donors 1 and 2) following an established protocol (Rotherham *et al.*, 2018). Briefly, T175 flasks were coated with 10 ng/ml fibronectin solution in PBS for 1 h at room temperature. hMSC growth medium was added to each flask before aspirating 1 x $10^5$ cells/$cm^2$ (Table 2.1). After a 7-day incubation period (37°C, 5% $CO_2$ and 20% $O_2$) a 50% media change was performed. After a further 7 days a complete media change was executed and MSC colonies were visible. Cells were passaged when they reached 70-80% confluency and switched to complete media with 10% FBS. Human mononuclear cells (hMNCs) were purchased from Lonza and seeded at 12.5 x $10^6$ cells per T75 flask (donor 3) in hMNC growth medium (Table 2.1). Cells were allowed to attach for 5 days (37°C, 5% $CO_2$ and 5% $O_2$) before a complete media change was performed. After P3, cells were transferred to 37°C, 5% $CO_2$ and 20% $O_2$ and cultured in hMSC growth medium as above. These cells are referred to as hMSCs from this point onwards.

### 2.4.4 Immunocytochemistry

#### 2.4.4.1 Validating primary antibodies

A human cornea, purchased from the Liverpool Research Eye Bank, was washed thrice in DMEM high glucose and the epithelium and endothelium were scraped off. The stroma was then minced and digested in 1 mg/ml collagenase-L overnight at 37°C. The resulting cell suspension was strained through a 70 µm cell strainer and centrifuged at 360 x g for 5 min. Cells were resuspended in phosphate buffer solution (PBS) at a concentration of 1.5 x $10^5$ cells/ml. 200 µl of the cell suspension was added to a cytospin funnel chamber and centrifuged in a Shandon Cytospin 3 at 800 rpm for 5 min onto Shandon cytoslides. The cells were allowed to air dry at room temperature before fixing in 10% neutral buffered formalin (NBF) for 10 min. Rapid Romanovsky staining was used to confirm the presence of cells, which consists of 30 s in methanol, 20 s in eosin red and 20 s in methylene blue (Figure 2.3).

Freshly isolated corneal stromal cells (keratocytes) on cytoslides were permeabilised with 0.5% Triton-X in PBS prior to blocking with 10% goat serum in 1% bovine serum albumin (BSA). Primary antibodies (Table 2.2) were diluted in BSA and added to cells overnight at 4°C. Unbound primary antibody was removed with two washes in 0.1% Tween-20 in PBS (PBST) at room temperature. Secondary antibodies (Table 2.3) were diluted to 5 µg/ml and added to cells for 1 hour at 37°C in the dark. Where possible, conjugated phalloidin (Table 2.3) was added in conjunction with the secondary antibodies to label F-actin. Two PBST washes removed unbound secondary antibody prior to the addition of 364 nM 4',6-Diamidino-2-Phenylindole (DAPI) to label the nucleus which was incubated at room temperature for 15 min in the dark. A final wash with PBS followed by distilled water was performed and the slides were mounted using Dako, a hardset fluorescent mounting medium, and a 22 x 22 mm coverslip. The mounting medium was left to set for 40 min and the slides stored in 4°C until imaged on the Zeiss confocal laser scanning microscope 800 (LSM). Images were analysed using Zen Lite (v 3.1 blue edition; Zeiss) and Fiji (ImageJ v 1.52p) (Schindelin *et al.*, 2012). Results shown in Appendix A.

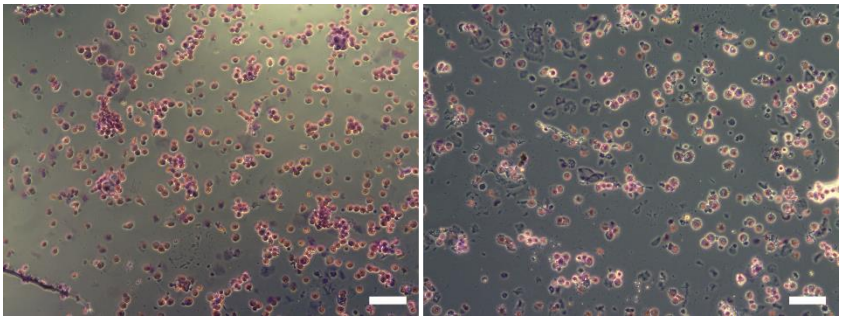

**Figure 2.3 Rapid Romanovsky staining shows the presence of corneal stromal cells (keratocytes) after cytospinning.** Eosin red stains the cytoplasm and methylene blue stains the nucleus. Scale bar represents 100 µm.

#### 2.4.4.2 Characterisation of cells

For the characterisation of all cell types, 700 cells/cm$^2$ were seeded into an EZ 8-well glass slide and cultured for up to 1 week. The cells were then stained for phenotype-specific proteins (Table 2.2) as described above.

**Table 2.2 Primary antibodies used for ICC characterisation of hCFs, hMSCs and CSSCs.**

| Clone | Primary antibody | Species | Supplier/Catalogue number | Concentration (μg/ml) |
|---|---|---|---|---|
| | | **Keratocyte/Fibroblast/Myofibroblast** | | |
| Poly | Keratocan (**KERA**) | Rabbit | Sigma HPA039321 | 1.50 |
| Mono | Lumican (**LUM**) | Rabbit | Abcam ab168348 | 3.23 |
| Mono | Aldehyde dehydrogenase 3A1 (**ALDH3A1**) | Mouse | ThermoFisher; MA5-25098 | 9.60 |
| Mono | Hematopoietic progenitor cell antigen CD34 (**CD34**) | Rabbit | Abcam ab81289 | 5.14 |
| Mono | Alpha-smooth muscle actin (**α-SMA**) | Mouse | Abcam ab7817 | 2.00 |
| Mono | Vimentin (**VIM**) | Rabbit | Abcam Ab92547 | 0.53 |
| | | **Collagens** | | |
| Poly | Collagen I (**Col I**) | Rabbit | Abcam ab34710 | 2.00 |
| Mono | Collagen III (**Col III**) | Mouse | ThermoFisher MA1-22147 | 4.00 |
| Poly | Collagen V (**Col V**) | Rabbit | Abcam ab7046 | 4.20 |
| Poly | Collagen VI alpha 1 (**Col VI**) | Rabbit | ThermoFisher PA5-13534 | 40.0 |
| | | **Stem cell** | | |
| Poly | Paired box protein Pax-6 (**PAX6**) | Rabbit | Abcam ab5790 | 20.00 |
| Mono | Thy-1 (**CD90**) | Mouse | Abcam ab23894 | 10.00 |
| Mono | 5'-nucleotidase (**CD73**) | Rabbit | Abcam Ab133582 | 20.00 |
| Mono | ATP-binding cassette super-family G member 2 (**ABCG2**) | Mouse | Merck MAB4146 | 12.50 |
| Mono | Stage-specific embryonic antigen 4 (**SSEA4**) | Mouse | R&D Systems MAB1435 | 10.00 |
| Mono | Octamer-binding transcription factor 4A (**OCT4A**) | Mouse | R&D Systems MAB17591 | 10.00 |
| Poly | Sex determining region Y-box 2 (**SOX2**) | Rabbit | Sigma SAB3500363 | 10.00 |

**Table 2.3 Secondary antibodies and phalloidin used in ICC.**

| Secondary antibody | Conjugate | Supplier/Catalogue number | Concentration (µg/ml) |
|---|---|---|---|
| Goat anti-mouse IgG | 488 | Invitrogen A-11029 | 4 |
| Goat anti-rabbit IgG | 488 | Invitrogen A-11008 | 4 |
| Goat anti-mouse IgG | 594 | Invitrogen A-11005 | 4 |
| Goat anti-rabbit IgG | 594 | Invitrogen A-11012 | 4 |
| Goat anti-mouse IgG | 647 | Invitrogen A-21235 | 4 |
| Goat anti-rabbit IgG | 647 | Invitrogen A-21244 | 4 |
| **Conjugated Phalloidin** | **Supplier/ Catalogue number** | | **Concentration** |
| Alexa Fluor™ 488 Phalloidin | Invitrogen A22287 | | 3 U |
| Alexa Fluor™ 647 Phalloidin | Invitrogen A12379 | | 7.5 U |

### 2.4.5 Optimising RNA extraction from tissue

#### 2.4.5.1 Homogenising tissue

Corneal buttons from porcine eyes, purchased from Morphets abattoir (Widnes, UK), were minced and added to a microcentrifuge tube along with a stainless-steel bead. The microcentrifuge was then placed into a homogeniser and homogenised in bursts of 20 s. TRI reagent was added to the tube and stored at -80°C until the ribonucleic acid (RNA) was extracted. RNA was purified using Zymo's Direct-zol RNA MiniPrep Plus kit, as per the manufacturer's instructions.

#### 2.4.5.2 Dismembrating tissue

Porcine corneal buttons were minced and snap frozen in liquid nitrogen in a dismembrator chamber. The chamber was then placed into the Mikro-dismembrator U at 2000 rpm for 30 s. The tissue was scraped out and placed into a microcentrifuge tube before TRI reagent was added. Samples were stored at -80°C and RNA was purified using Zymo's Direct-zol RNA MiniPrep Plus kit.

#### 2.4.5.3 Collagenase digesting tissue

Porcine corneal buttons were minced and digested in 2 mg/ml collagenase-L overnight at 37°C. The cell suspension was strained through a 70 µm cell strainer, centrifuged at 360 x g for 5 min, washed with PBS and then stored in TRI reagent at -80°C. RNA was purified using Zymo's Direct-zol RNA MiniPrep Plus kit. The collagenase digest was deemed to be the best method (Figure 2.4) and was used to extract RNA from human corneas from this point

onwards but the concentration was decreased to 1 mg/ml for human corneas as RNA extraction was unsuccessful with 2 mg/ml.

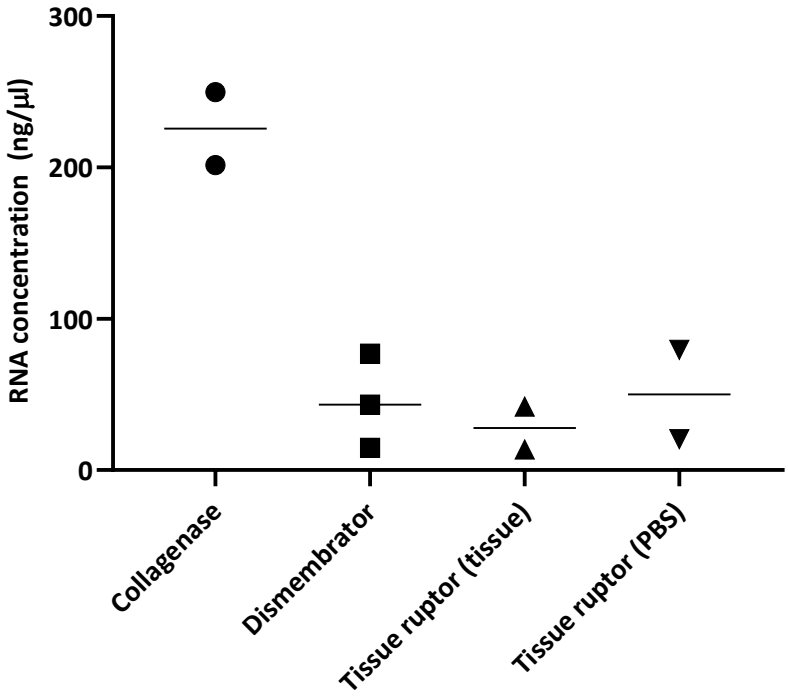


**Figure 2.4 RNA yields using different extraction methods.** RNA was purified from cell lysates using Zymo's Direct-zol kit following the above extraction methods. Collagenase digest yields the highest concentration of RNA and was selected going forward.

### 2.4.6 RNA extraction from cultured cells

Cells cultured in a 6-well plate were rinsed twice with distilled PBS before adding 500 µl TRI reagent to each well. The well was then scraped and the solution transferred to a microcentrifuge tube and stored at -80°C.

Cells cultured in a T75 flask were trypsinised using 1X trypsin for 4 min at 37°C. The cell suspension was centrifuged at 360 x g for 5 min, the pellet washed twice in distilled PBS and 350 µl TRI reagent was added to the tube. RNA was purified using Qiagen's RNeasy Plus Micro Kit. The quality and quantity of RNA was examined using the NanoDrop 2000.

### 2.4.7 Reverse Transcription and RT-qPCR

Complementary DNA (cDNA) was produced from RNA in a 25 µl reaction. 500 µg/ml random primers (1 µl) was added to RNA in a total volume of 12.4 µl and heated to 70°C for 5 min in a Bio-Rad Thermal Cycler T100. M-MLV buffer (5 µl), 8 U/µl M-MLV (1 µl) reverse transcriptase, 10 mM PCR nucleotide mix (5 µl), and 1 U/µl RNasin Ribonuclease Inhibitor

(0.6 µl) was added to each PCR tube, mixed and incubated at 37°C for 60 min. The reaction was inactivated by heating to 93°C for 5 min.

Reverse transcription quantitative real-time polymerase chain reaction (RT-qPCR) was performed using Takyon Rox SYBR MastrMix dTTP Blue and 10 ng of cDNA was amplified in a 25 µl reaction in a LightCycler 480 (Roche). Following Takyon activation at 95°C for 3 min, 40 PCR cycles were completed consisting of 10 s denaturation at 95°C followed by 45 s at 60°C. Relative gene expression was calculated according to the efficiency corrected ΔCT method (Svec *et al.*, 2015).

Primers were either designed using Primer-BLAST (NCBI), found in the literature or purchased from Qiagen (see Table 2.4). Both the designed primers and those found in literature were subjected to a BLAST search to check primer specificity. The designed primers were also quality tested using NetPrimer (Premier Biosoft). The efficiency of GAPDH, ALDH3A1, AQP1, KERA and PTGDS primers were tested on the collagenase-digested corneal stroma. Where primer efficiencies were not measured, 100% efficiency was assumed. GAPDH was selected as the best housekeeping gene following efficiency testing and GeNorm analysis (Appendix B) (Vandesompele *et al.*, 2002).

**Table 2.4 Forward and reverse primer sequences.**

| Gene | Forward | Reverse | Source |
|---|---|---|---|
| GAPDH | ATGGGGAAGGTGAAGGTCG | TAAAAGCAGCCCTGGTGACC | (McDermott *et al.*, 2016) |
| ALDH3A1 | CATTGGCACCTGGAACTACC | GGCTTGAGGACCACTGAGTT | (Du *et al.*, 2007) |
| AQP1 | CCACTGGATTTTCTGGGTG | CCAGACCCCTTCTATTTGGGC | Designed |
| KERA | CCTGGAAGGCAAGGTGCTA | AGTAGGAAAACTGGGTGGGC | Designed |
| PTGDS | CCTGCCCCAAACCGATAAT | CAGAGACATCCAGAGCGTGG | Designed |
| ABCG2 | ACGAACGGATTAACAGGGTCA | CTCCAGACACACCACGGAT | (Liang *et al.*, 2017) |
| NES | Hs_NES_2_SG QuantiTect Primer Assay | | Qiagen |
| NOTCH1 | Hs_NOTCH1_2_SG QuantiTect Primer Assay | | Qiagen |

## 2.4.8 Growth curves

### 2.4.8.1 Growth curve of hCFs

To determine the growth rate of hCFs, growth curves were set up for 21 days. hCFs were seeded in to a 48-well plate at a density of 5 x $10^3$ cells/$cm^2$. A cell standard curve was created by seeding 1 x $10^3$ – 1 x $10^5$ cells directly into tubes and centrifuging at 360 x g for 5 min to remove excess media. The cell pellets were then lysed with 200 µl of lysis buffer (1X Tris-EDTA (TE) + 1% Triton-X). At days 1, 3, 5, 7, 14 and 21 cells were rinsed with PBS and lysis

buffer (200 µl) was added to each well. The wells were scraped before transferring the cell lysate to microcentrifuge tubes and storing at -80°C.

The quantification of DNA, assessed using a PicoGreen assay, was used as an estimate of cell number. Cell lysates were thawed to room temperature and the 200X PicoGreen solution was diluted to a working solution in 1X TE buffer. Cell lysate (50 µl) and PicoGreen (50 µl) were added to a black 96-well plate and incubated at room temperature for 5 – 10 min in the dark. The plate was then read on a FLUO star OPTIMA plate reader at excitation/emission of 490/525 nm. Cell number was calculated using the cell standards (Figure 2.5).

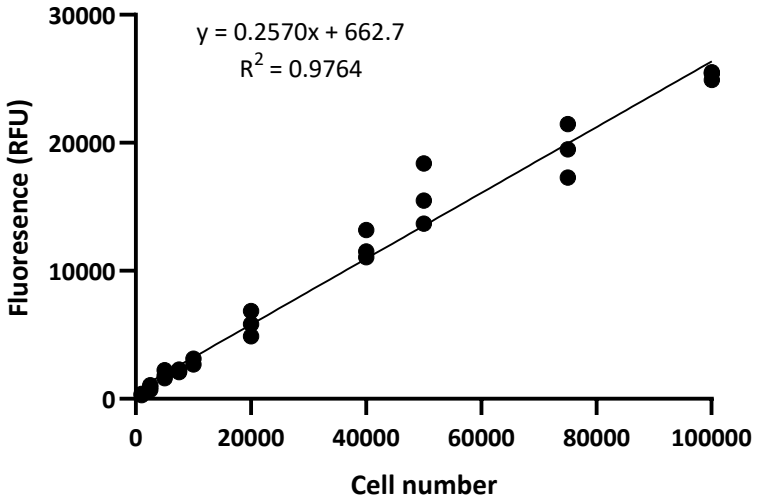


**Figure 2.5 Representative standard curve to determine hCF cell number from relative fluorescence units (RFU).** The cells were analysed in triplicate to account for any pipetting error when seeding the cells.

### 2.4.8.2 Growth curve of hMSCs

To determine the growth rate of hMSCs cells were set up as described in 2.4.8.1 however a few alterations were made. hMSCs were seeded in to a 24-well plate at a density of 5 x $10^3$ cells/$cm^2$ and lysed with 500 µl of lysis buffer at each time point.

Room temperature cell lysates (100 µl) were added to a black 96-well plate along with working PicoGreen solution (100 µl). The plates were analysed as described above with the optimal gain for each plate used. To correct for the variation in gain, a subset of samples from day 7 were read at gains from 1000-2000. A standard curve was generated and the equation of the curve was used to correct for variations in the optimal gain used and allow for comparisons between plates (Figure 2.6).

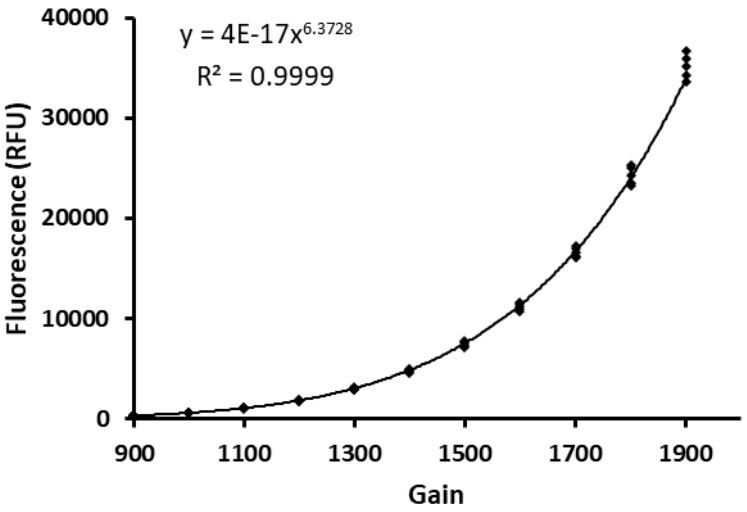


**Figure 2.6 Representative gain curve for correcting PicoGreen data.** DNA samples were read at each gain to create a standard curve. Experimental samples were then read at their optimal gain and corrected for using the above equation.

### 2.4.9 Flow Cytometry

The International Society for Cellular Therapies (ISCT) defined cell surface markers that an MSC population must express in addition to markers that they must lack (≤ 2% positive) (Dominici *et al.*, 2006). To verify that the hMSCs expressed the necessary cell surface antigens, flow cytometry using R&D Systems Human Mesenchymal Stem Cell Verification kit was performed on donor 1 at passages 1 and 4 and donor 3 at P4. Briefly, cells were trypsinised, counted and washed in staining buffer (2 ml). The cells were resuspended at 1 x $10^5$ cells/ml in staining buffer with 1% FBS. The cell suspension (100 µl) was added to a microcentrifuge tube and each positive antibody (10 µl) and the negative marker cocktail (10 µl) was added to the cell suspension, mixed, and incubated for 40 min at room temperature in the dark. Excess antibody was removed by centrifuging the cell suspension and washing the resultant pellet in staining buffer. The final cell pellet was resuspended in 500 µl PBS and the samples were analysed on the BD FACS Canto II. Cells in the absence of an antibody were used as negative controls. Data of donor 2 at passage 1 (P1) and P3 were provided by Adam Janvier and the data for donor 3 P1 were provided by Daniel Green.

Owing to the fact that multiple fluorochromes were used in a singular sample, flow cytometric compensation was performed to remove any spillover fluorescence from one channel to another. To do this, one drop of CompBeads was added to a microcentrifuge tube along with 10 µl of one antibody. The bead suspension was then treated the same as the cells and each of the samples were read separately.

Data obtained were analysed on a dotplot and histogram using FlowJo™ (v 10.6.1). Dead cells were excluded by plotting the area for side scatter against the area for forward scatter (FSC) and doublets were excluded by plotting the height against the width of the FSC. To identify the positive dataset, histograms of the stained sample and the unstained control were plotted. Gating was performed to eliminate the effects of autofluorescence of the cells and any overlap was manually deconvoluted as shown in Figure 2.7.

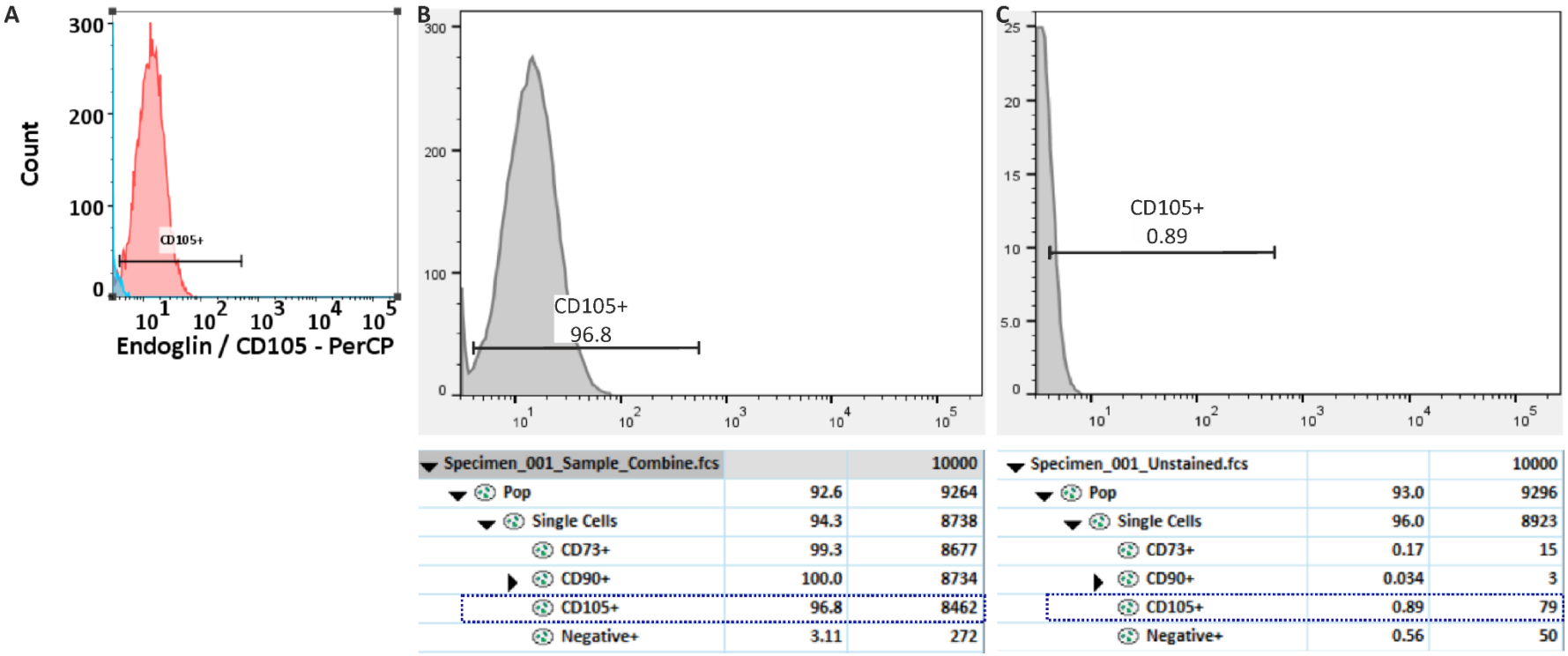


| Specimen_001_Sample_Combine.fcs | | 10000 |
|---|---|---|
| Pop | 92.6 | 9264 |
| Single Cells | 94.3 | 8738 |
| CD73+ | 99.3 | 8677 |
| CD90+ | 100.0 | 8734 |
| CD105+ | 96.8 | 8462 |
| Negative+ | 3.11 | 272 |

| Specimen_001_Unstained.fcs | | 10000 |
|---|---|---|
| Pop | 93.0 | 9296 |
| Single Cells | 96.0 | 8923 |
| CD73+ | 0.17 | 15 |
| CD90+ | 0.034 | 3 |
| CD105+ | 0.89 | 79 |
| Negative+ | 0.56 | 50 |

**Figure 2.7 An example to show the method used to analyse flow cytometry data.** A: Histograms of both the stained sample (red) and unstained control (blue) were plotted to identify where the overlap, if any, began. B: This gating was then applied to both the stained sample and C: the unstained control. Manual deconvolution was used to identify the true positive dataset: the number of unstained cells that were autofluorescent was subtracted from the number of positive cells in the stained sample to obtain the true positive dataset.

### 2.4.10 Trilineage differentiation of hMSCs

The ISCT defines MSCs as cells with the potential to differentiate to osteoblasts, adipocytes and chondroblasts (Dominici *et al.*, 2006). Studies were, therefore, conducted to verify the trilineage differentiation potential of the hMSCs.

#### 2.4.10.1 Osteogenic induction and characterisation

hMSCs at P4-5 were seeded into a 6-well plate at 3 x $10^3$ cells/$cm^2$ and cultured in growth hMSC medium overnight. After 24 hours, the medium was switched and cells were cultured for 21 days in osteogenic medium (DMEM low glucose, 10% FBS, 100 nM dexamethasone, 10 mM β-glycerophosphate and 50 µM A2P). Control cells were cultured in growth medium. After culturing, cells were washed twice with PBS prior to fixation with 10% NBF for 30 min. Cells were then washed with PBS followed by the addition of 0.5% Alizarin red for 45 min in the dark. Alizarin red stains calcified matrix and is used to confirm *in vitro* bone formation (Javidan and Schilling, 2004). To remove any unbound stain, cells were washed 4 times with distilled water prior to imaging.

#### 2.4.10.2 Adipogenic induction and characterisation

hMSCs at P4-5 were seeded into a 6-well plate at 1 x $10^4$ cells/$cm^2$ in growth medium overnight before commencing adipogenic induction with DMEM low-glucose supplemented with 10% FBS, 1 µM dexamethasone, 100 µM indomethacin, 10 µg/ml insulin and 500 µM 3-isobutyl-1-methylxanthine for 21 days. Control cells were cultured at the same seeding density in growth DMEM. To assess adipogenic differentiation, Oil Red O staining was used. Oil Red O stains neutral triglycerides and lipids (Koopman *et al.*, 2001). Cells were rinsed 3 times with PBS prior to fixation in 10% NBF for 30 min. Cells were then washed with PBS before incubation in 60% isopropanol for 5 min at room temperature. The isopropanol was then removed, cells rinsed once more, before the addition of 1% Oil Red O for 15 min at room temperature. To remove any unbound stain, cells were washed 4 times with distilled water prior to imaging.

#### 2.4.10.3 Chondrogenic induction and characterisation

Cell pellets containing either 5 x $10^5$ (high density) or 2.85 x $10^5$ (low density) were cultured in screw-cap microcentrifuge tubes for 21 days in chondrogenic medium (DMEM low glucose, 100 nM dexamethasone, 10 ng/ml TGF-β3, 1X ITS and 86.34 µM A2P). Control cells were also cultured in high- and low-density cell pellets in growth DMEM.

High density cell pellets were washed with PBS prior to fixation in 10% NBF for 1 hour. The pellets were then paraffin embedded (Appendix C) and 4 µm sections were mounted onto microscope slides. Samples were rehydrated in sequential 2 x 5 min xylene, 100% ethanol for 5 min, 90% ethanol for 5 min, 70% ethanol for 5 min followed by a wash in water. 1% Alcian blue was added to the sample for 30 min at room temperature before dehydrating the sample in increasing concentrations of ethanol for 30 s followed by xylene washes. Alcian blue stains the proteoglycans of the extracellular matrix associated with chondrocytes (Javidan and Schilling, 2004). Slides were then mounted and imaged.

Low density cell pellets were washed with PBS and transferred to clean microcentrifuge tubes. The pellets were then digested in 500 µl 10 U/ml papain solution for 4 h at 60°C and stored at 4°C overnight before analysis. Equal volumes of the digested material and dimethyl methylene blue (DMMB) were added to a 96-well plate and the absorbance read immediately at 570 nm. The glycosaminoglycan (GAG) content was calculated from a standard curve produced using chondroitin sulphate standards (Figure 2.8).

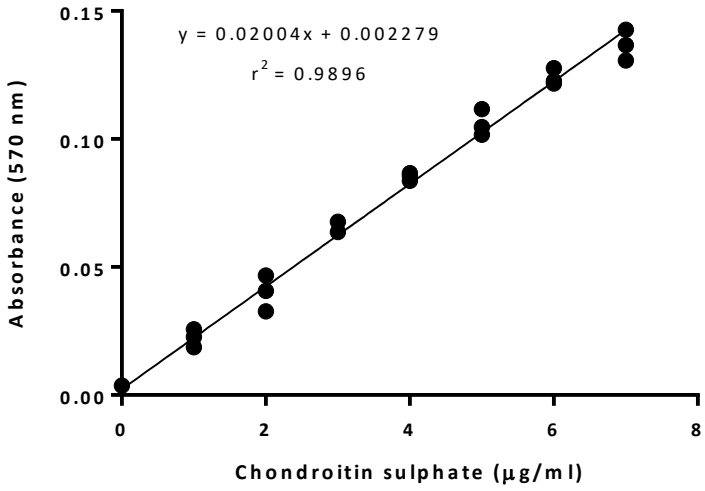


**Figure 2.8 Representative standard curve produced using chondroitin sulphate standards.** The standard curve enabled quantification of sulphated GAG in the cell pellets.

### 2.4.11 Keratocyte differentiation of hMSCs

To determine the differentiation potential of hMSCs into keratocytes 5000 cells/cm$^2$ were seeded into a Millicell EZ 8-well glass slide and cultured in growth medium overnight at 37°C, 5% $CO_2$, 20% $O_2$. The following day, the media of 4 wells was switched to keratocyte differentiating medium (KDM) for 21 days (Table 2.5). Control cells were cultured in stromal cell medium (SCM) (Table 2.5).

Cells were rinsed with PBS and fixed in 10% NBF for 15 min before being processed and stained as described in 2.4.4.1. hMSCs were stained with anti-keratocan and anti-lumican antibodies and co-stained with phalloidin and DAPI.

**Table 2.5 Media and supplements used to treat hMSCs.**

| Cell type | Treatment | Basal media | Supplements |
|---|---|---|---|
| hMSCs | Stromal cell medium (SCM) | DMEM low glucose, no phenol | 10% FBS, 1% GlutaMAX, 1% NEAA, 1 mM A2P, 100 U/ml penicillin, 100 µg/ml streptomycin and 2.5 µg/ml amphotericin B. |
| | Keratocyte differentiating medium (KDM) | Advanced DMEM GlutaMAX | 1 mM A2P, 10 ng/ml basic fibroblast growth factor (FGF-2) and 0.1 ng/ml transforming growth factor, beta 3 (TGF-β3). |

### 2.4.12 Statistical analysis

Statistical analysis was performed using GraphPad Prism software (v 9.0.0). Where $n > 2$, data were reported as mean ± 1 standard deviation (SD). A significance level of $p < 0.05$ was set for all experiments. Data were analysed for significance using paired t-tests. To ensure data were normally distributed a Shapiro-Wilk test was performed. Statistical analysis was not performed on RT-qPCR data (Figure 2.20) or flow cytometry data (Figure 2.23) due to the low number of replicates ($n = 1$).

## 2.5 Results

### 2.5.1 hCF characterisation

#### 2.5.1.1 hCFs maintain their morphology through passaging

hCFs were cultured *in vitro* up to P5 and used in experiments at this passage. Phase contrast images of isolated hCFs showed that the cells maintained their spindle-shaped morphology across passages (Figure 2.9).

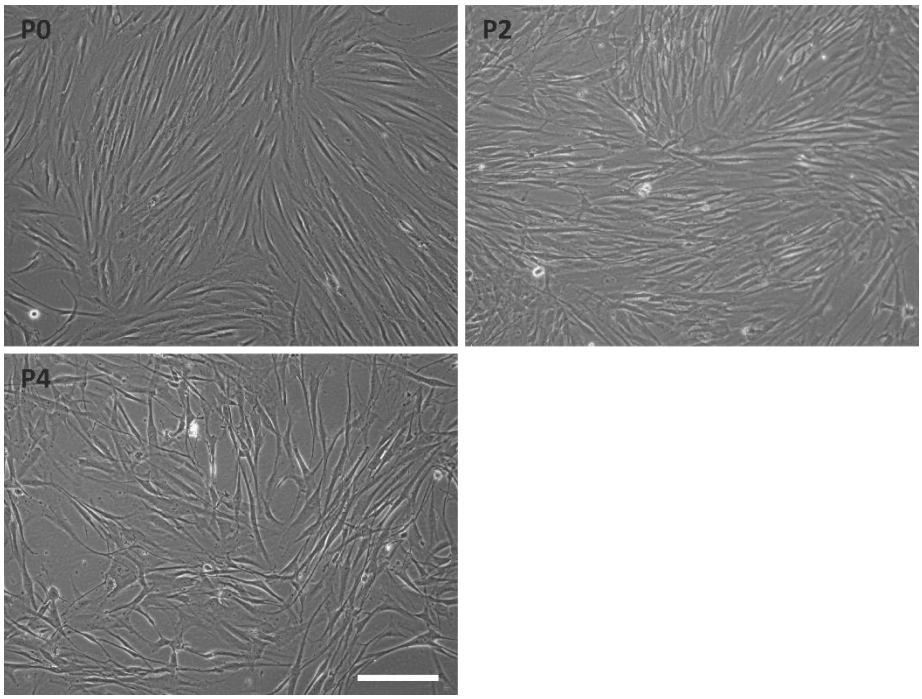


**Figure 2.9 Representative phase contrast images of hCFs at different passages.** hCFs maintain their spindle-shaped morphology with passaging as shown in the micrographs. n = 4. Scale bar represents 200 µm.

#### 2.5.1.2 hCFs expand and proliferate with minimal donor variation

hCFs at P5 proliferated and increased in cell number up to day 7 where a slight decrease was observed in two of the donors (Figure 2.10). Between days 14 and 21 cell number declined, as expected in *in vitro* culture.

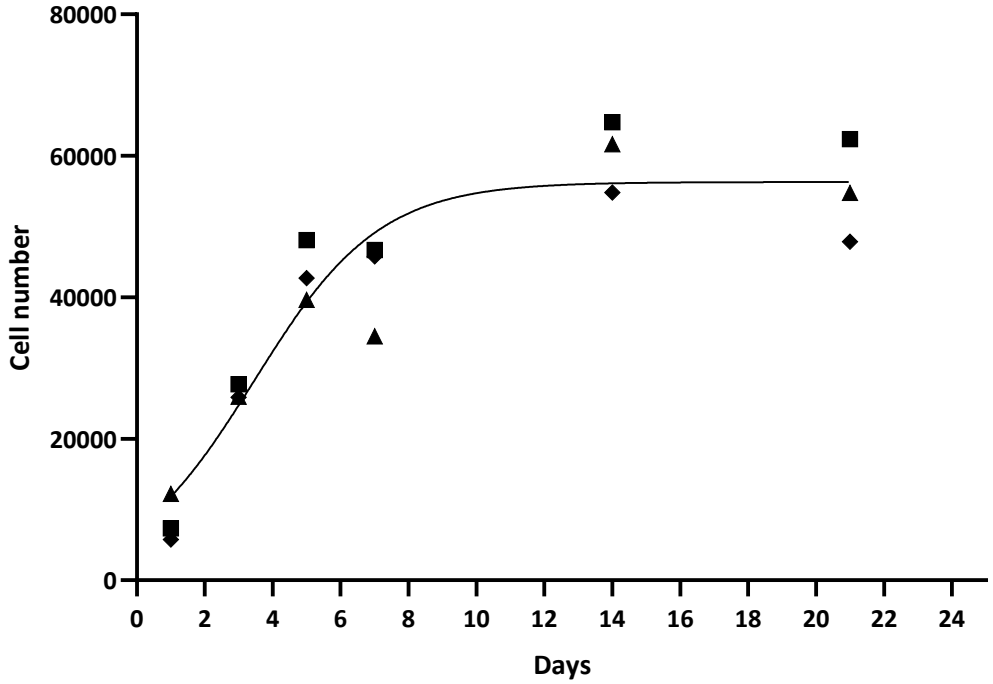


**Figure 2.10 Growth curve of hCFs at P5.** hCFs were seeded at 5 x $10^3$ cells/$cm^2$ and cultured for up to 21 days prior to PicoGreen analysis. n = 3 and a logistic growth curve was applied. $R^2$ = 0.90. All cells increased in number up to day 14 before plateauing.

### 2.5.1.3 hCFs do not appear to express all of the typical keratocyte-associated markers

Immunocytochemistry (ICC) of hCFs at P5 was used to further characterise the cells and assess if the fibroblasts retained any features typically associated with keratocytes (Figure 2.11). In this study, hCFs expressed cell surface marker CD34 and lumican (LUM) – markers commonly used to confirm keratocyte phenotype in cell culture (Dunlevy *et al.*, 2000; Wu *et al.*, 2013; Sidney *et al.*, 2014). In contrast, there was little expression of keratocan (KERA), aldehyde dehydrogenase 3A1 (ALDH3A1), and collagen types V and VI (Col V and Col VI) which are also used as markers to identify keratocytes (Carlson *et al.*, 2005; Pei *et al.*, 2006; Wu *et al.*, 2014a). In addition, CD73 was expressed but CD90 expression was not seen. There was diffuse staining of α-SMA, but no evidence of the stress fibres associated with myofibroblasts. Vimentin (VIM) and F-actin were stained to visualise the cytoskeleton and revealed stress fibres traversing the cell.

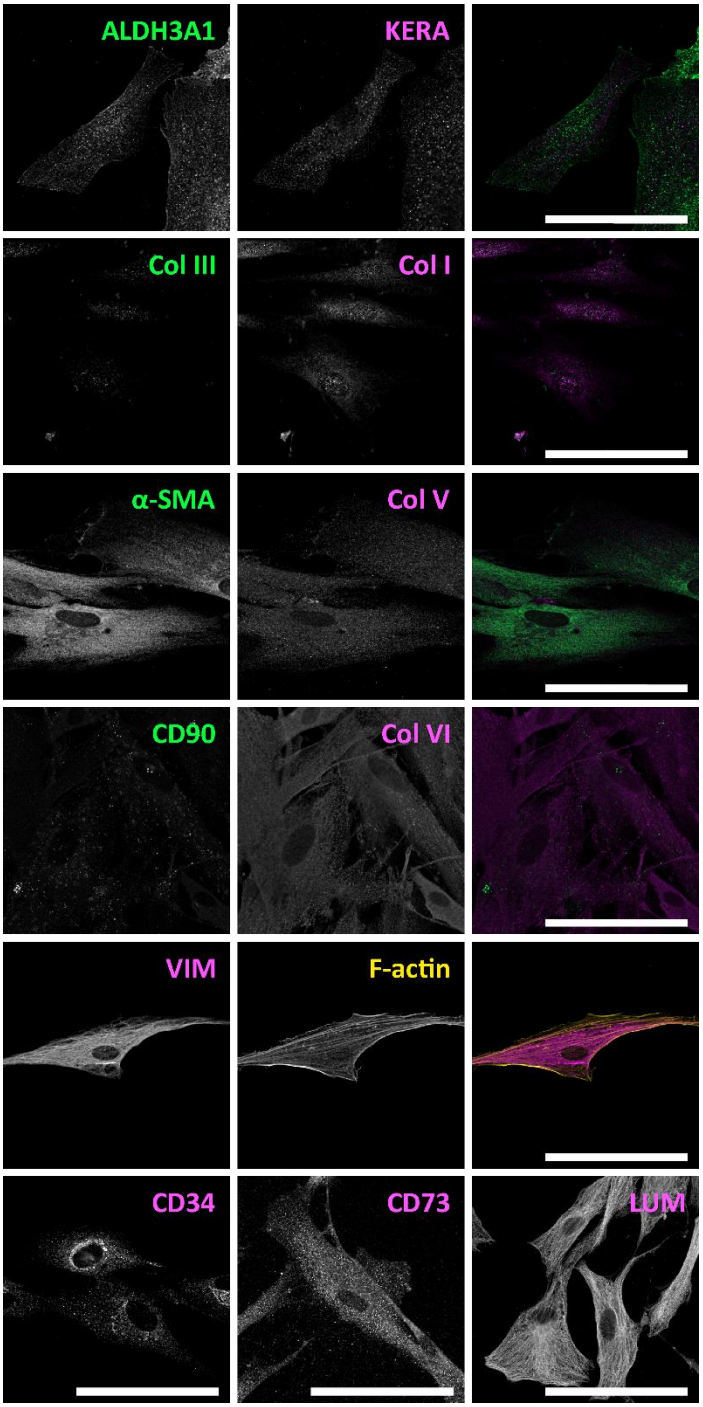


**Figure 2.11 ICC characterisation of hCFs at P3.** Representative images of single or double immunofluorescent staining used to characterise hCFs. Cellular expression of keratocyte markers: ALDH3A1 (green), keratocan (magenta), type I collagen (magenta), type V collagen (magenta) type VI collagen (magenta), CD34 (magenta) and lumican (magenta) are shown. Expression of fibroblast and myofibroblast markers: type III collagen (green), α-SMA (green), CD90 (green), CD73 (magenta) were also assessed. Vimentin (magenta) and F-actin (yellow) were stained to analyse the arrangement of the cytoskeleton. n = 1. Scale bars represent 100 µm.

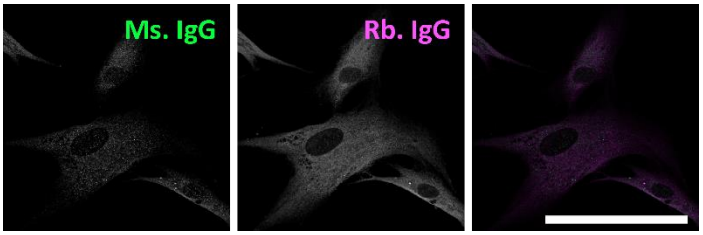


**Figure 2.12 IgG negative controls for rabbit and mouse primary antibodies.** n = 1 biological replicate. Scale bar represents 100 µm.

## 2.5.2 CSSC characterisation

### 2.5.2.1 Morphology of CSSCs varies depending on the method of isolation used

Phase contrast images of CSSCs isolated using two slightly different methods showed variation between passages**.** Small, polygonal shaped cells can be seen in cultures isolated using both method 1 (Figure 2.13 A) and 2 (Figure 2.13 B), however, this was always a heterogeneous population with several fibroblastic cells present too.

The cells expanded using the first methodology seemed to undergo phenotypic drift and transdifferentiate into fibroblast and myofibroblast-like cells after the first passage. This is indicated by the presence of cells with a large, flat cell body. Conversely, the cells that were passaged at a seeding density of 400 cells/cm$^2$, as in method 2, appeared to maintain their morphology at P1 although a heterogeneous population was still observed.

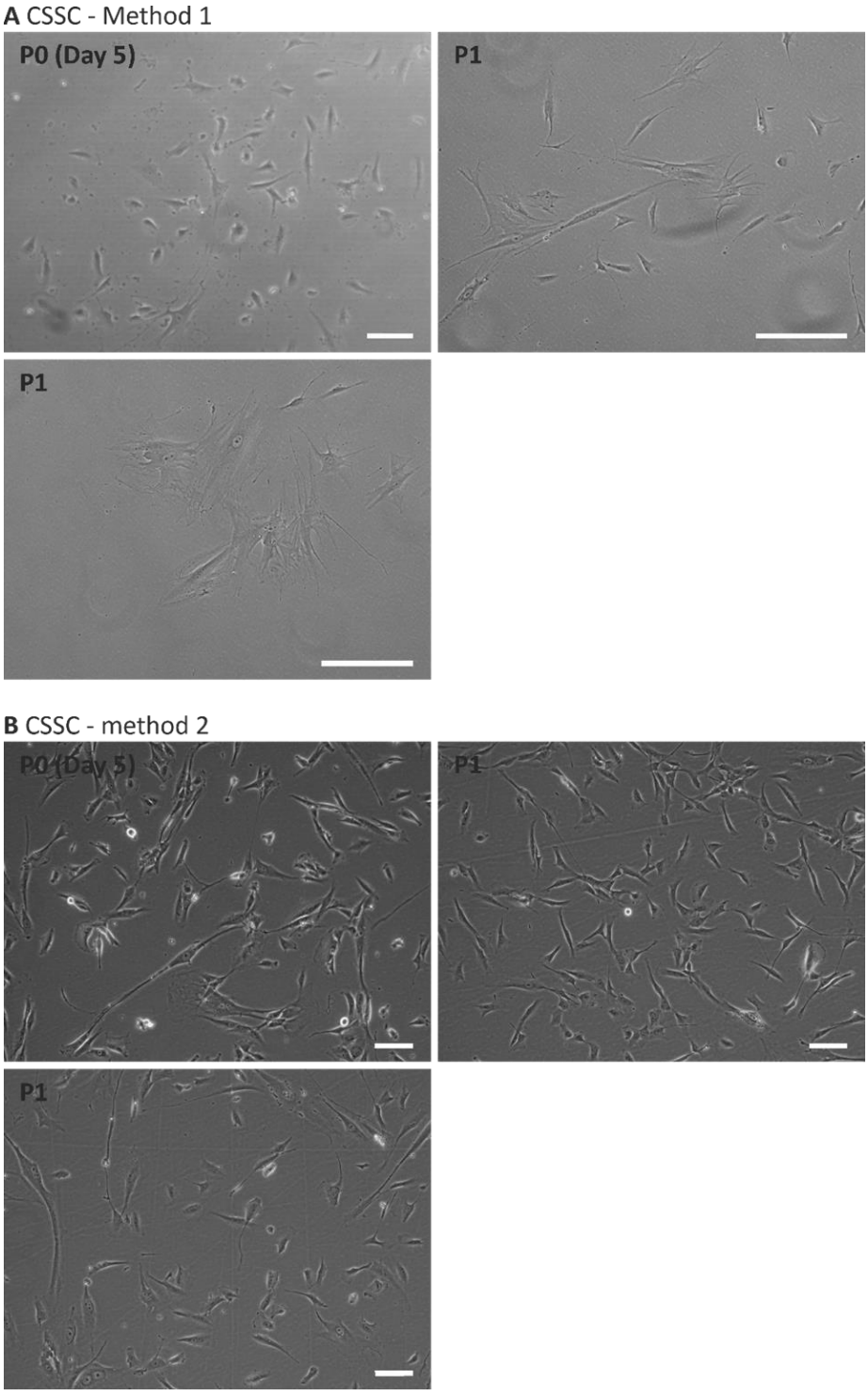


**Figure 2.13 Phase contrast images of CSSCs using two different methods.** Images show small, polygonal shaped cells that resemble the morphology of CSSCs at P0. A: Using method 1 these cells began to transdifferentiate into a more fibroblast-like cell by P1. B: In contrast, more of the cells isolated using method 2 maintain their polygonal shape. n = 7 for method 1; n = 9 for method 2. Scale bars represent 100 µm.

#### 2.5.2.2 ICC characterisation of CSSCs is inconclusive

To further characterise the cells isolated using the two different methods, immunocytochemistry was performed. Initially, only the expression of MSC markers CD90 and CD73 were assessed (Figure 2.14). The cells expressed CD73 with mixed positive and negative expression of CD90. Co-staining with DAPI allows us to see the nucleus which also suggests there was a heterogeneous population of smaller and larger cells. Interestingly, the cells isolated using the second method did not appear to express CD73 and had low expression of CD90 (Figure 2.15). A more in-depth characterisation was performed on hCSSCs isolated using method 2, based on the fact that this is the published method and the cells had the desired polygonal morphology.

OCT-4A, a transcription factor associated with stem cells, was observed in donors 1 and 5 (Figure 2.16) (Sidney *et al.*, 2015). Similarly, punctate staining of PAX6, a progenitor marker of corneal stromal cells, was observed in the nucleus of cells isolated from these same donors, however no expression was seen in donor 3 (Figure 2.17) (Funderburgh *et al.*, 2005; Sidney *et al.*, 2015). Both donors 1 and 5 also expressed ABCG2, a progenitor cell marker, across the cell membrane but it was not observed in isolates from the donor 3 (Figure 2.17) (Basu *et al.*, 2014). Phalloidin staining of F-actin showed the cytoskeletal differences amongst cells isolated from the same donor. Donor 1 consisted of cells of a similar size whereas donors 3 and 5 both contained a heterogeneous population of cells with mixed sizes.

To further characterise the cells, the expression of typical keratocyte and fibroblast/myofibroblast markers was explored (Figure 2.18). Cells from all 3 donors expressed α-SMA, although stress fibres were absent, and cells isolated from donors 1 and 5 appeared to express CD34. All donors exhibited negative expression of keratocan but donor 5 did express the corneal crystallin ALDH3A1. IgG controls showed non-specific staining (Figure 2.19).

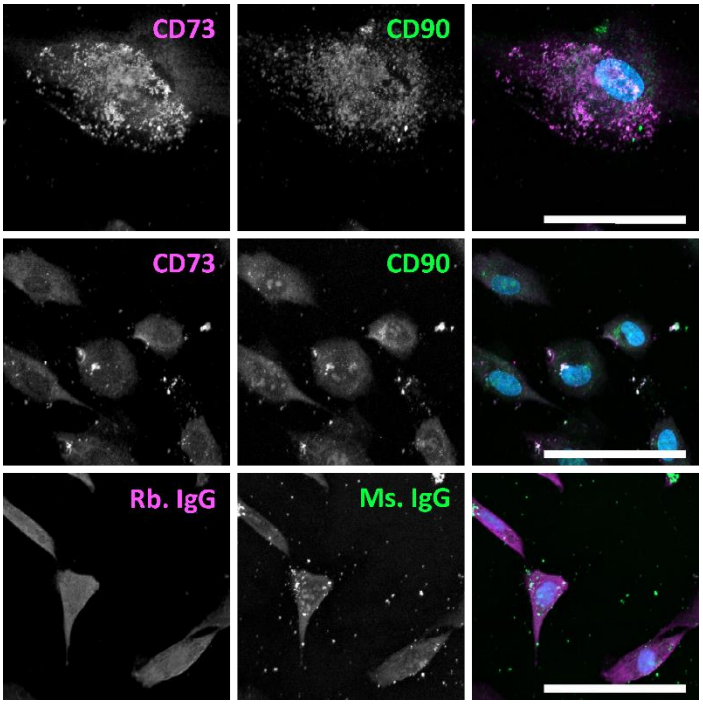


**Figure 2.14 ICC characterisation of Method 1-isolated CSSCs.** Cells were stained with antibodies for two cell surface markers commonly associated with multipotent cells, CD73 (magenta) and CD90 (green). Cells were co-stained with DAPI (blue) and merged images are also shown. n = 1 biological replicate. Scale bars represent 100 µm.

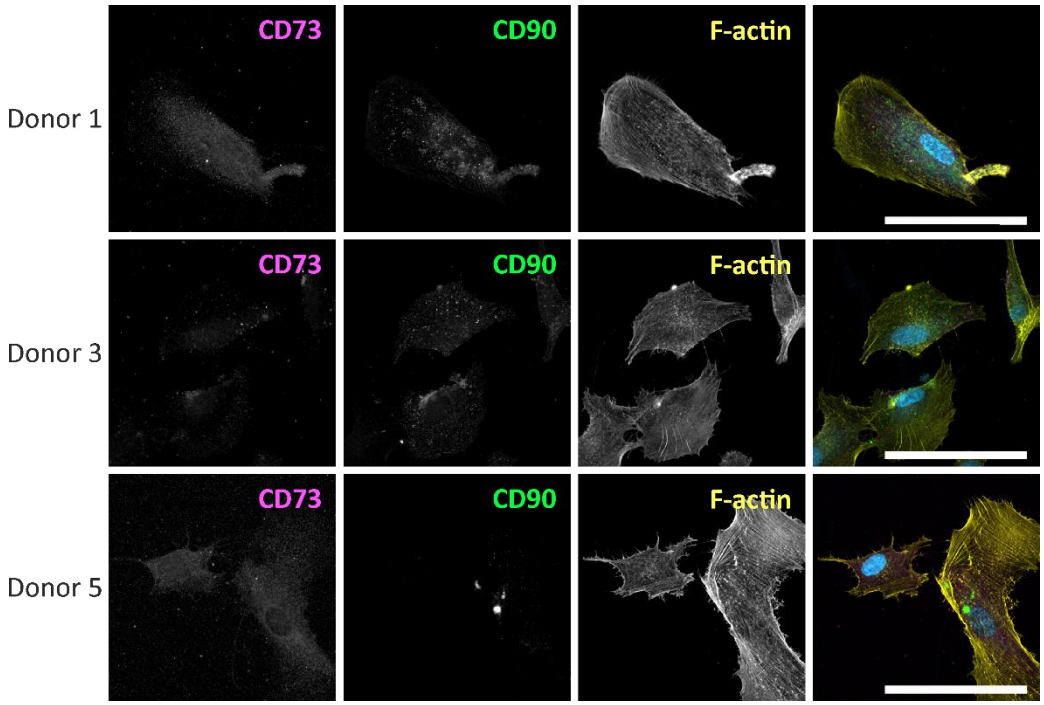


**Figure 2.15 ICC of stem cell markers on CSSCs isolated using Method 2.** Cells isolated from 3 different donors were stained with multipotent cell markers, CD73 (magenta) and CD90 (green) and representative images are shown. All cells were co-stained with phalloidin (yellow) and DAPI (blue) with the merged images also shown. Scale bars represent 100 µm.

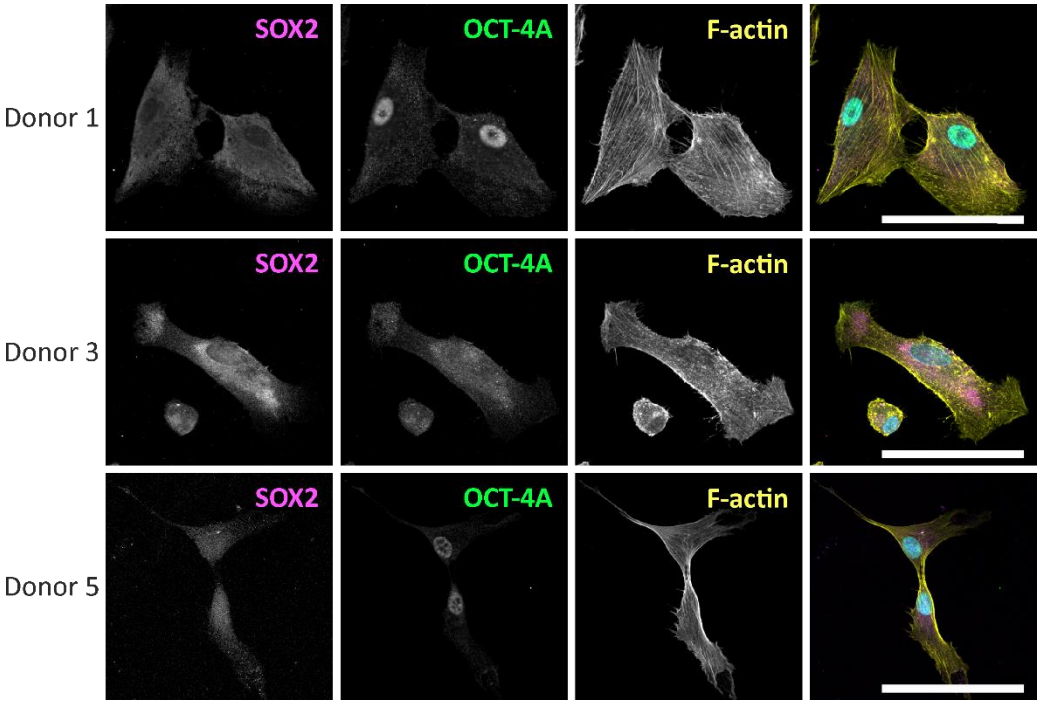


**Figure 2.16 ICC of pluripotent cell markers on CSSCs isolated using Method 2.** Cells isolated from 3 different donors were stained with SOX2 (magenta) and OCT-4A (green) and representative images are shown. All cells were co-stained with phalloidin (yellow) and DAPI (blue) with the merged images also shown. Scale bars represent 100 µm.

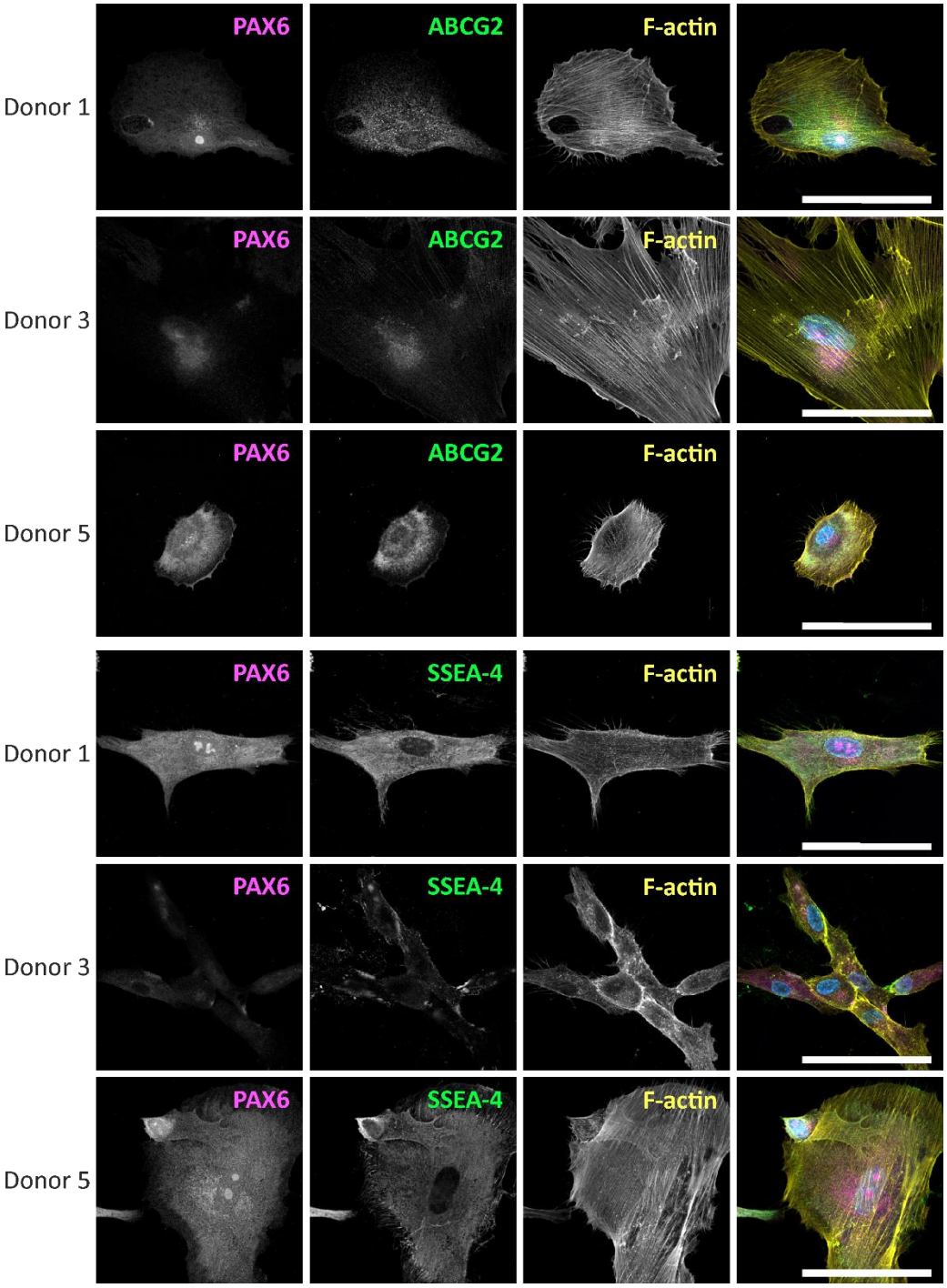


**Figure 2.17 ICC of pluripotent and progenitor cell markers on CSSCs isolated using method 2.** Cells isolated from 3 different donors were stained with PAX6 (magenta), ABCG2 (green) or SSEA-4 (green). All cells were co-stained with phalloidin (yellow) and DAPI (blue) with the merged images also shown. Scale bars represent 100 µm.

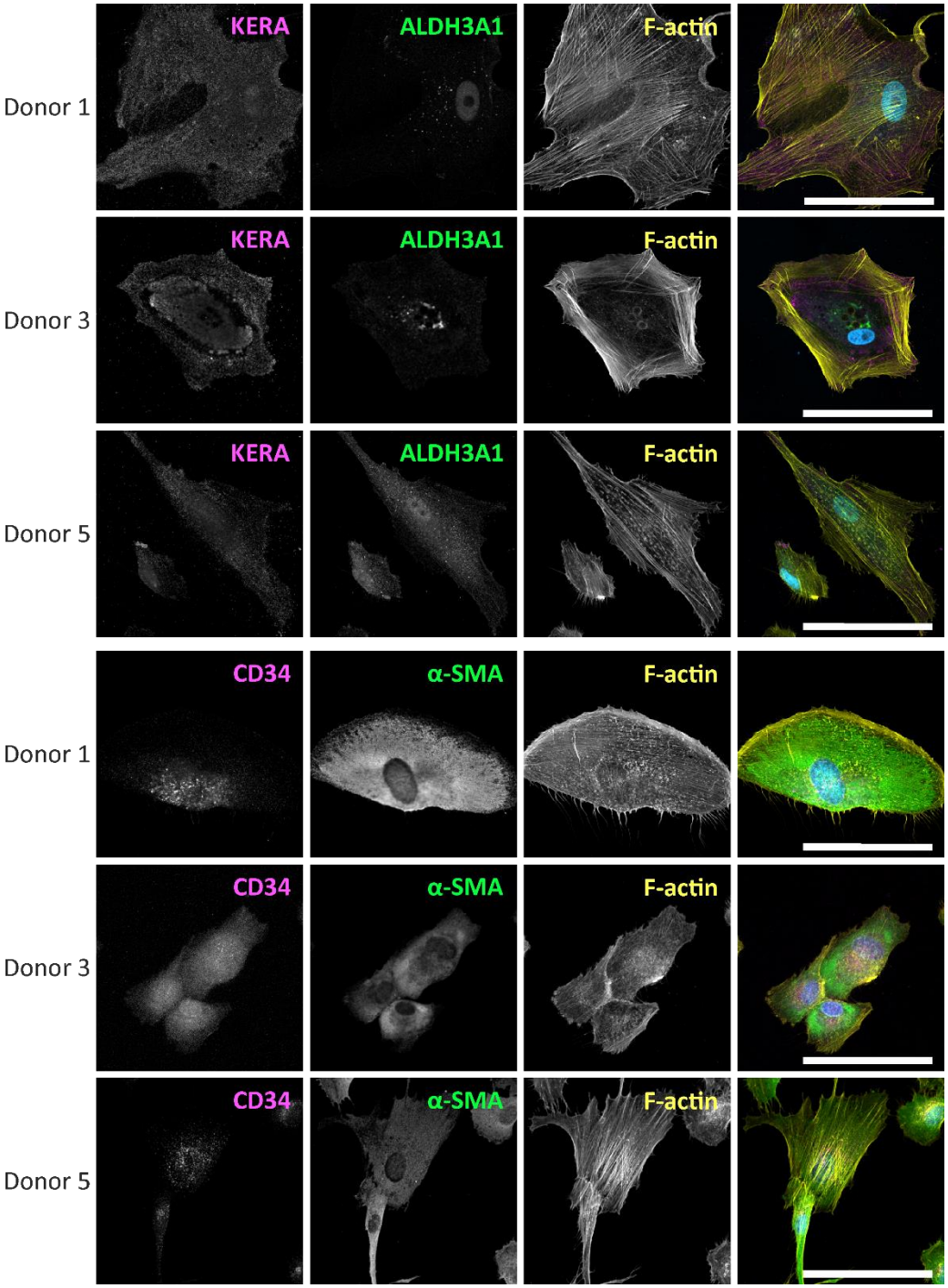


**Figure 2.18 ICC of keratocyte/fibroblast markers on CSSCs isolated using Method 2.** Cells were stained for negative markers of CSSCs and positive markers for keratocytes or fibroblasts: keratocan (magenta), ALDH3A1 (green), cD34 (magenta), α-SMA (green). All cells were co-stained with phalloidin (yellow) and DAPI (blue) with the merged images also shown. Scale bars represent 100 µm.

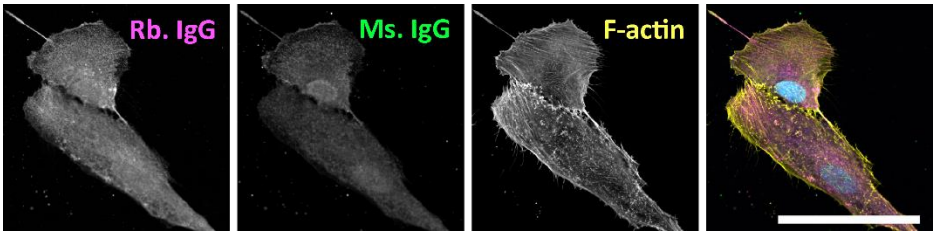


**Figure 2.19 IgG negative controls for rabbit and mouse primary antibodies.** Cells were co-stained with phalloidin (yellow) and DAPI (blue) with the merged images also shown. Scale bar represents 100 µm.

### 2.5.2.3 CSSCs isolated using method 2 vary in stem cell marker expression

The gene expression of stem cell and keratocyte markers was assessed using RT-qPCR (Figure 2.20). CSSCs are known to express progenitor markers NES, ABCG2 and NOTCH1 and have low expression of keratocyte markers KERA, ALDH3A1, PTGDS and AQP1 (Funderburgh *et al.*, 2005, 2016; Du *et al.*, 2007; Basu *et al.*, 2014; Dos Santos *et al.*, 2019). The data highlight the donor-to-donor variation found when attempting to isolate CSSCs. NES, NOTCH1, ABCG2 and AQP1 were expressed at similarly low levels by donors 1 and 5. However, stark differences were observed in the expression levels of PTGDS and ALDH3A1. Interestingly, the passaging of donor 5 seemed to alter the expression levels of each of the genes. Between P4 and P5 there was a decrease in the expression of NES, NOTCH1, ABCG2 and AQP1 which was then partially recovered by P6. Similarly, there was a decrease in PTGDS and ALDH3A1 however this was consistent with passaging and does not recover.

Donors 2, 3 and 4 exhibited similar expression of NES, NOTCH1 and ABCG2 – genes associated with stem cells. These same donors also had similar expression of keratocyte markers: KERA and AQP1. Differences were observed between the two different populations derived from donor 2 at P4. The cells isolated from the first parent flask (P4a) had greater expression of NES, NOTCH1, KERA and AQP1 when compared to its sister flask (P4b).

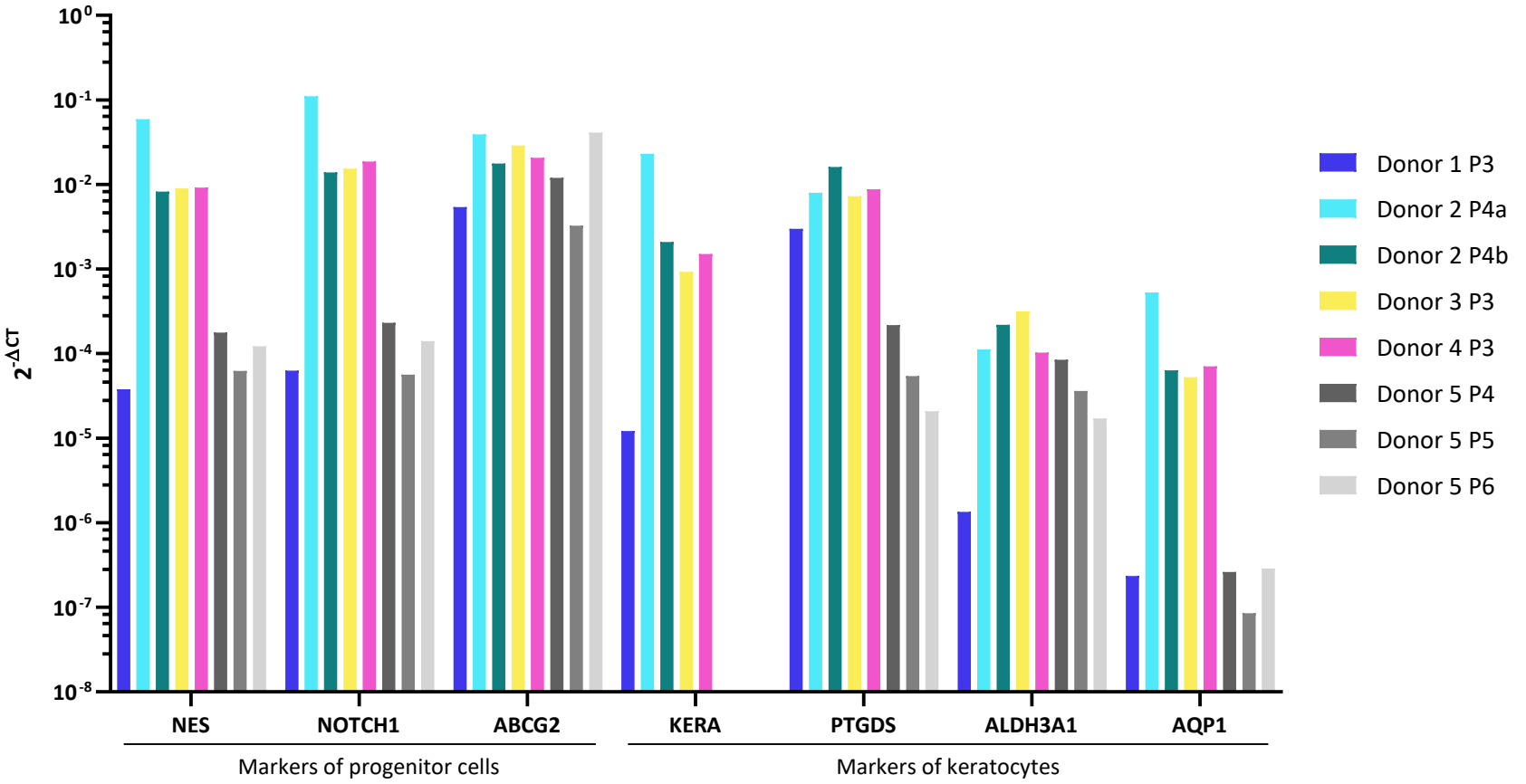


**Figure 2.20 Gene expression analysis of stem cell and keratocyte markers in isolated CSSCs.** Values are shown on a logarithmic scale and normalised to GAPDH. Passages of cell cultures isolated from the same donor but different parent flasks are distinguished by the letters 'a' and 'b' following passage number. n = 1 for all samples.

### 2.5.3 hMSC characterisation

#### 2.5.3.1 hMSCs can maintain their morphology through passaging

hMSCs were cultured *in vitro* up to passage 4 (P4). At P1, donor 1 exhibited the typical MSC morphology with a population of spindle-shaped cells (Figure 2.21 A). With passaging, these cells became a more heterogeneous population with fewer spindle-shaped cells and a greater number of cells with a flattened, irregular geometry which were also larger in size. Donors 2 and 3 retained a spindle-shaped morphology throughout passaging (Figure 2.21 B and C).

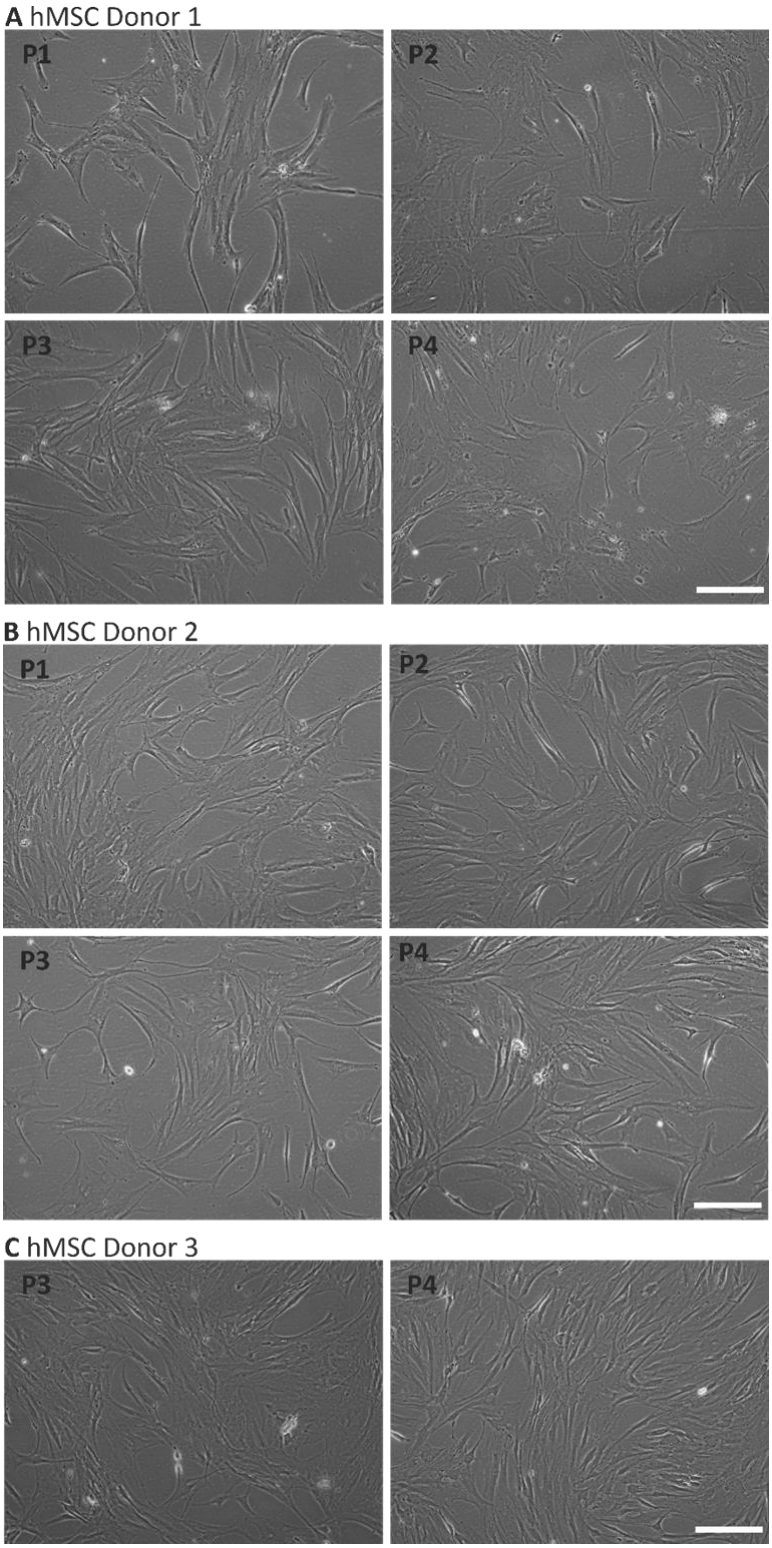


**Figure 2.21 Phase contrast images of hMSCs through passages.** A: Morphological changes of donor 1 through passaging. B: Morphology of cells isolated from donor 2. C: Spindle-shaped morphology of cells isolated from donor 3. Scale bar represents 200 µm.

### 2.5.3.2 Growth rate of hMSCs is consistent between donors

hMSCs at P5 showed an increase in cell number up to day 21 (Figure 2.22). All 3 donors followed the initial trend of the typical sigmoid growth curve for cultured cells and proliferated as expected.

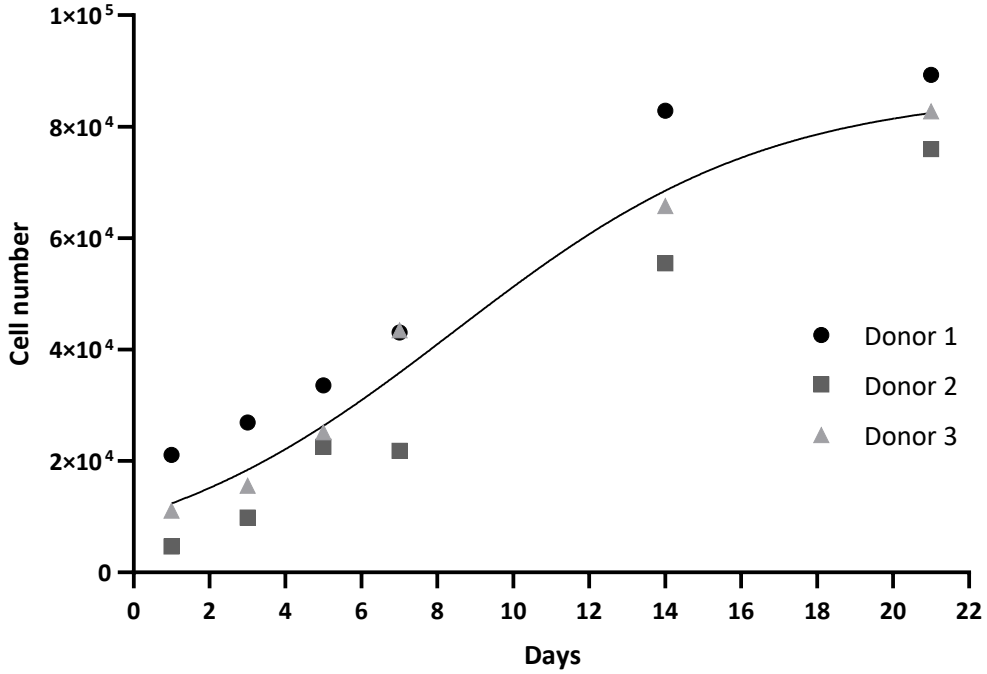


**Figure 2.22 Growth curve of hMSCs at P5.** hMSCs were seeded at 5 x $10^3$ cells/$cm^2$ and cultured for up to 21 days prior to PicoGreen analysis. n = 3 and a logistic growth curve was applied. $R^2$ = 0.91. All cells continued to increase in cell number up to day 21.

### 2.5.3.3 A change in phenotype occurs after *in vitro* culture

Flow cytometry was used to assess the expression of typical MSC markers, with the data from donor 2 at both P1 and P3 and the data from donor 3 at P1 being provided by colleagues. The expression of CD73 decreased in all donors after passaging (Figure 2.23). Conversely, CD90 expression increased in donor 1 following passaging but was consistent between passages in donors 2 and 3. CD105 expression decreased after passaging in donors 1 and 3 (43.7% to 26.8% and 95.9% to 86.9% respectively) but increased in donor 2 from 61.2% to 85.2%.

The percentage of cells that express all 3 positive MSC markers decreased with passaging in both donors 1 and 3 (Table 2.6). Donor 2, however, showed an increase in the number of cells that expressed the positive markers after *in vitro* culture (66.2% at P1 to 88.7% at P3). In contrast, after passaging donors 1 and 2 showed a decrease in the expression

of the negative markers whereas the expression of these markers increased in donor 3 from 2.3% to 99.4%.

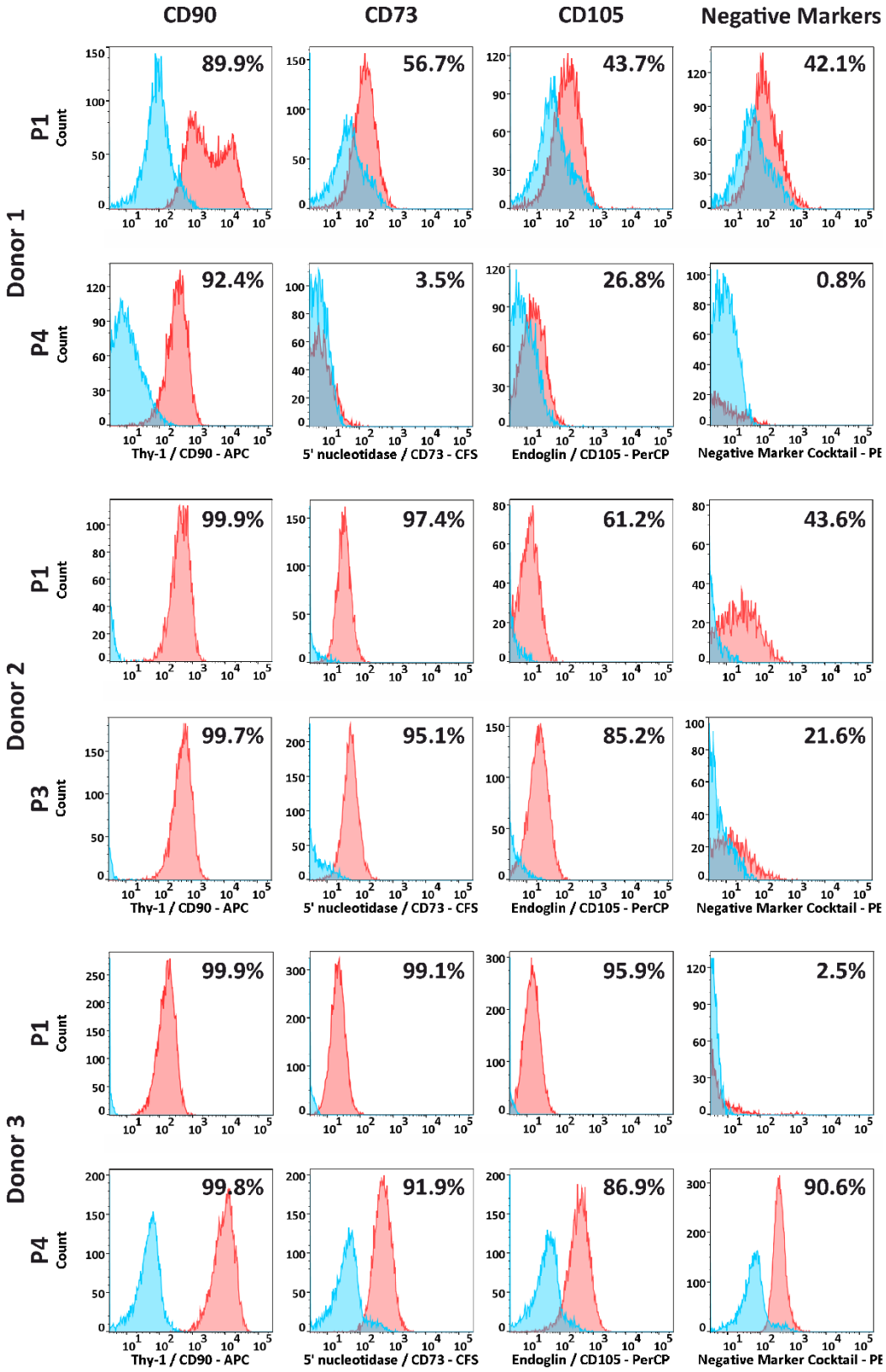


**Figure 2.23 Flow cytometric analysis of MSC markers expressed by hMSCs at early and late passages.** The blue peaks represent the control unstained samples and the red peaks represent samples in the presence of each antibody. Results are shown as percentage of positive cells after the subtraction of control fluorescence.

**Table 2.6 Summary of flow cytometric analysis of hMSCs.**

| | Passage | % of cells expressing all positive markers* | % of positive cells that express negative markers† |
|---|---|---|---|
| **Donor 1** | Early | 64.0 | 82.9 |
| | Later | 4.4 | 0.9 |
| **Donor 2** | Early | 66.2 | 33.8 |
| | Later | 88.7 | 13.5 |
| **Donor 3** | Early | 96.4 | 2.3 |
| | Later | 94.8 | 99.9 |

* Percentage of cells that express CD90, CD73 and CD105. † Percentage of those cells that also express the markers in the negative marker cocktail (CD45, CD34, CD11b, CD79A, HLA-DR).

#### 2.5.3.4 hMSCs are capable of trilineage differentiation

The ability to differentiate hMSCs into different cell lineages was assessed using histology and a glycosaminoglycans (GAGs) assay. Oil Red O stains neutral triglycerides and lipids red which can be seen in all 3 donors, suggesting successful adipogenic differentiation (Figure 2.24). Alizarin Red stains calcium deposits red which can be seen in donors 2 and 3 after osteogenic induction. Donors 2 and 3 also successfully differentiated into chondrocytes and GAGs have been stained blue in the chondrogenic pellets. A low cell number from donor 1 prevented osteo- and chondrogenic inductions for histological analysis. GAG content was also analysed using the DMMB assay. Donor 1 showed a high GAG content prior to chondrogenic induction which did not increase with chondrogenic differentiation (Figure 2.25). Conversely, both donors 2 and 3 showed an increase in the mean total GAG content after chondrogenic induction (from 2.20 µg to 6.55 µg and 2.59 µg to 4.10 µg respectively) as anticipated.

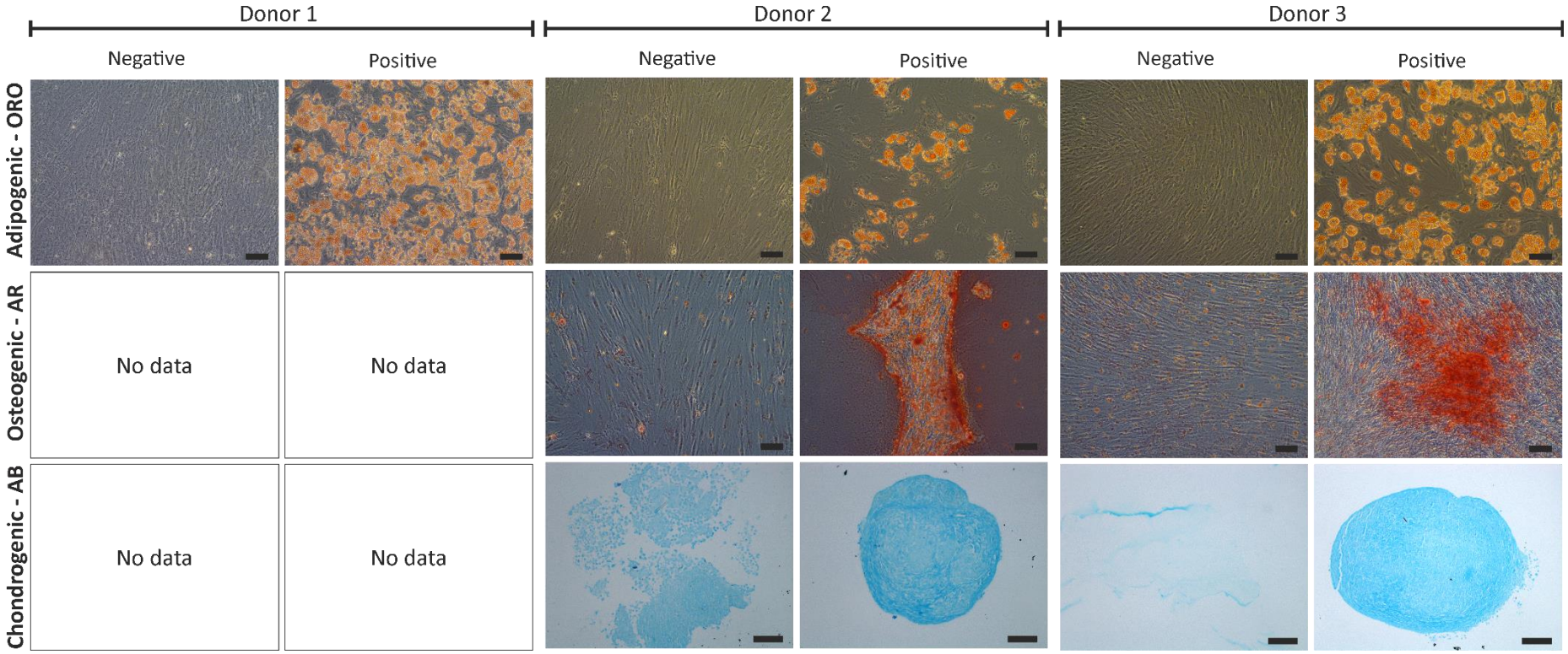


**Figure 2.24 Histological analysis of trilineage differentiation potential of hMSCs.** Representative images are shown for each donor before (negative) and after (positive) adipogenic, osteogenic and chondrogenic differentiation. hMSCs subjected to adipogenic induction stained positively with Oil Red O to show lipid formation. A low cell number from donor 1 prevented osteo- and chondrogenic inductions for histological analysis. Cells subjected to osteogenic induction stained positively with Alizarin red to highlight calcium deposits. Cell pellets subjected to chondrogenic differentiation were stained with Alcian blue which labelled GAGs. Scale bars represent 100 µm.

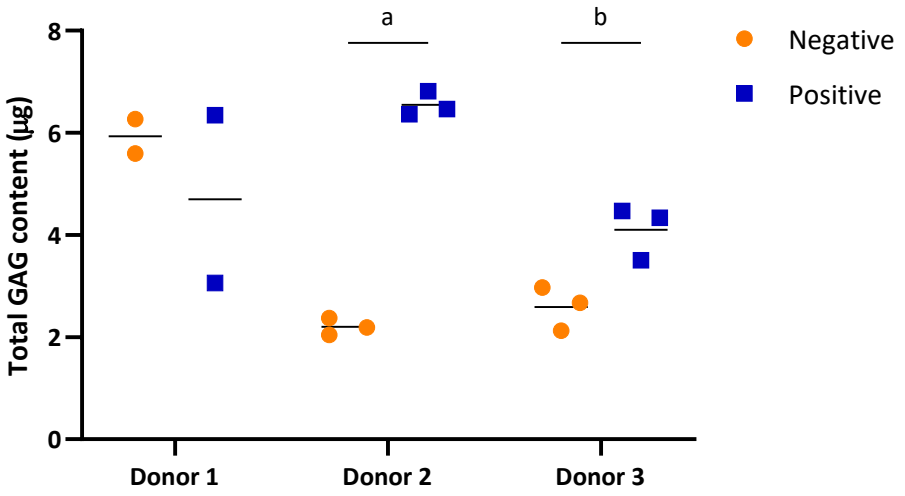


**Figure 2.25 Total glycosaminoglycan (GAG) content without (negative) and with (positive) chondrogenic induction.** n = 2 technical repeats for donor 1 and n = 3 technical repeats for donors 2 and 3; bar represents the mean. Multiple paired t-tests were performed. p values reported are: a = 0.00125 and b = 0.00862.

#### 2.5.3.5 hMSCs have the potential to differentiate into keratocyte-like cells

ICC was used to assess the ability of hMSCs to differentiate into keratocyte-like cells. Qualitatively, the cells cultured in keratocyte differentiating medium (KDM) appeared to have an increased expression of keratocan, a proteoglycan found in the corneal stroma, when compared to cells cultured in standard medium (SCM) (Figure 2.26). Interestingly, cells cultured in both KDM and SCM expressed lumican.

The phalloidin staining of F-actin revealed that the differentiated hMSCs had a different morphology to the control hMSCs with a smaller, more spindle-shaped cell body. A cell sphere was also present in one of the wells cultured in KDM.

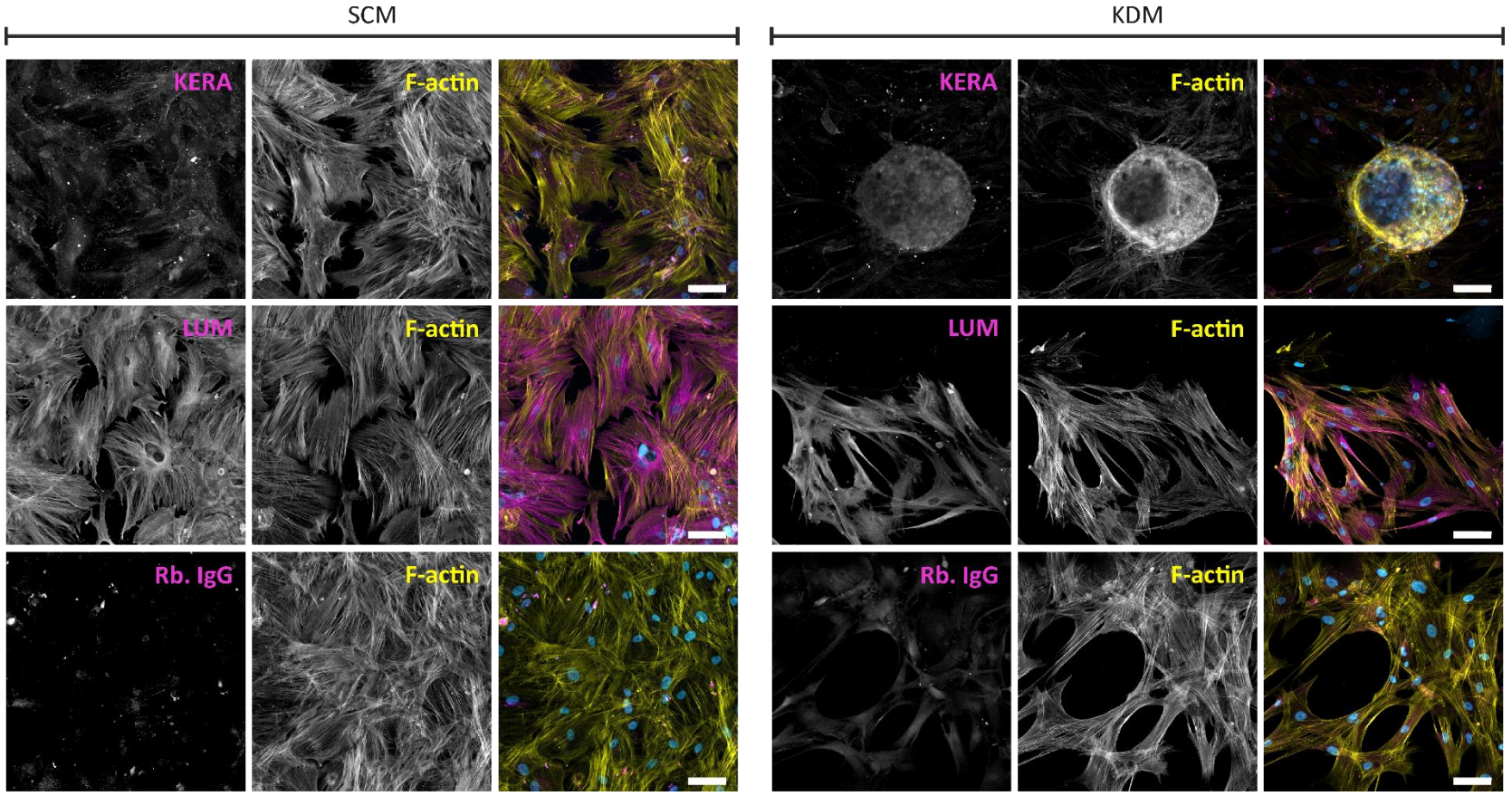


**Figure 2.26 Representative images show ICC of differentiated hMSCs.** hMSCs were seeded into 8-well chamber slides and cultured in either stromal cell medium (SCM) or keratocyte differentiating medium (KDM) for 21 days. Cells were stained for keratocyte markers keratocan (magenta) and lumican (magenta) with the IgG negative controls also shown. Nuclei are co-stained with DAPI (blue) and F-actin stained with phalloidin (yellow) with the merged image also shown. n = 1 biological replicate. Scale bars represent 100 µm.

## 2.6 Discussion

The aim of this chapter was to characterise different cell types in order to identify a suitable cell source to use in an *in vitro* corneal stroma model. hCFs were easily isolated and expanded, unlike hCSSCs. A heterogeneous population of cells were obtained when trying to isolate hCSSCs, which readily transitioned into cells resembling fibroblasts, suggesting phenotypic drift had occurred. hMSCs did not meet all of the criteria set out by the ISCT but two donors exhibited trilineage differentiation potential. Expression of keratocan and lumican, after keratocyte lineage induction, suggests that hMSCs can be differentiated into keratocytes.

### 2.6.1 Characterisation of hCFs

The nomenclature for cells isolated from the corneal stroma varies in the literature and is often dependent on the conditions used to culture these cells (Beales *et al.*, 1999; Funderburgh *et al.*, 2003; Pei *et al.*, 2004; Musselmann *et al.*, 2005). It is widely accepted that corneal stromal cells cultured in ≥ 10% FBS transdifferentiate from a keratocyte phenotype to a fibroblast- or myofibroblast-like cell (Fini, 1999; Funderburgh *et al.*, 2001; Berryhill *et al.*, 2002; Pei *et al.*, 2006; Foster *et al.*, 2015). However, culturing stromal cells in the absence of FBS results in slower cell growth (Beales *et al.*, 1999; Lynch *et al.*, 2016). In this study, human corneal stromal cells that had been cultured in 10% FBS were characterised and so these are referred to as human corneal fibroblasts (hCFs).

The phase contrast images revealed that culturing stromal cells in growth medium resulted in the cells exhibiting a spindle shaped morphology from as early as P0. This morphology is associated with the transdifferentiation from a keratocyte – which is typically dendritic with multiple processes – to a fibroblast phenotype (Jester *et al.*, 1999; Funderburgh *et al.*, 2003; Jester, 2008). To further evaluate this change in phenotype, ICC was used to assess the expression and distribution of proteins. F-actin in keratocytes is restricted to the cortical region of the cell, whereas the F-actin staining in this study revealed stress fibres traversing the cell (Jester *et al.*, 1994; Funderburgh *et al.*, 2003; Ruberti and Zieske, 2008). This phenomenon has previously been reported and the change in phenotype, from keratocyte to fibroblast, has been associated with the development of actin stress fibres (Foster *et al.*, 2015; Yam *et al.*, 2015).

The induction of CD90 and decreased expression of both ALDH3A1 and keratocan has also been reported when keratocytes activate and transition into fibroblasts (Pei *et al.*, 2004, 2006; Ren *et al.*, 2008; Hassell and Birk, 2010). The lack of keratocan and ALDH3A1

expression supports the evidence that the cells had become activated and transitioned into fibroblasts during culturing however, this is contradicted by the low expression of CD90 seen with ICC. The present study also found positive expression of lumican which is associated with keratocytes and typically downregulated, but still expressed, in hCFs (Funderburgh *et al.*, 2001; Yam *et al.*, 2015). Similarly, the hCFs exhibited weak punctate expression of CD34, a phenotype that is reportedly lost during keratocyte activation (Espana *et al.*, 2004; Sidney *et al.*, 2014). The expression of CD34 has been reported to decrease with the passaging of hCFs, but low levels of expression have been observed beyond P3 (Branch *et al.*, 2012). This can be recovered by culturing keratocytes in either low-glucose, serum-free media (Foster *et al.*, 2015) or in 10% FBS on amniotic membrane (Espana *et al.*, 2004). Corneal cells cultured in ≥ 10% FBS have also been found to express CD73 and this study supports these findings (Choong *et al.*, 2007; Sidney and Hopkinson, 2018). Diffuse α-SMA expression was observed however the staining does not show strong microfilament bundles as would be expected in myofibroblasts (West-Mays and Dwivedi, 2006; Myrna *et al.*, 2009; Torricelli and Wilson, 2014). Ainscough *et al.* have previously shown via western blotting that there is a gradient of α-SMA expression, with expression lowest in corneal cells followed by limbal cultures and finally scleral cultures (Ainscough *et al.*, 2011). Given that the cells used in this study were isolated from a corneoscleral ring, it is very likely that some of these cells will express α-SMA, supporting the staining observed in the present study.

The corneal stroma is composed primarily of collagen; the most common types being I and V. In this study we found that the hCFs weakly expressed type I collagen but not collagen types V and VI. Interestingly, no expression of type III collagen was observed, which has previously been shown to be elevated in fibroblasts and myofibroblasts (Funderburgh *et al.*, 2003). The hCFs in this chapter were not treated with ascorbic acid, a co-factor thought to be essential for the synthesis of collagen (Murad *et al.*, 1981, 1983; Hata and Senoo, 1989). It is therefore likely that treating the hCFs with ascorbic acid would stimulate the synthesis and deposition of collagen as shown in previous studies (Guo *et al.*, 2007; Saeidi *et al.*, 2012a; Wu *et al.*, 2014a).

hCFs have been used routinely when attempting to replicate the corneal stroma (Guo *et al.*, 2007; Karamichos *et al.*, 2010; Couture *et al.*, 2016). Here they displayed weak expression of markers usually associated with keratocytes, such as lumican and CD34, which may be a result of the cells used being at a low passage number (Branch *et al.*, 2012). The use of hCFs warrants further investigation into their ability to replicate the corneal stroma as it has previously been shown that supplementation with ascorbic acid can lead to the

production of stroma-like constructs (Guo *et al.*, 2007). Furthermore, a more metabolically active cell type may be of benefit when pursuing a bottom-up to engineering of the corneal stroma. Fibroblasts are known to actively synthesise and deposit ECM, unlike quiescent keratocytes, and may in fact be a more suitable cell type.

### 2.6.2 Characterisation of hCSSCs

A population of cells in the corneal stroma have been identified with characteristics consistent with those laid out in the ISCT for defining MSCs (Dravida *et al.*, 2005; Du *et al.*, 2005; Funderburgh *et al.*, 2005; Dominici *et al.*, 2006; Choong *et al.*, 2007; Polisetty *et al.*, 2008; Branch *et al.*, 2012). Funderburgh and colleagues found that, along with the typical MSC markers, these cells also express ABCG2 and PAX6 (Du *et al.*, 2005; Funderburgh *et al.*, 2005). These CSSCs possess the ability to be differentiated into keratocytes where an increase in the expression of keratocan and ALDH3A1 was observed in addition to the deposition of a collagenous ECM (Du *et al.*, 2007; Wu *et al.*, 2012, 2013, 2014a). Therefore, CSSCs could be a suitable cell source to use to accurately recapitulate the native stroma.

CSSCs have been described as being small, polygonal cells that form colonies when cultured *in vitro* (Kureshi *et al.*, 2014). A heterogeneous population of cells were isolated in this study using different methods of isolation and culture conditions. Whilst populations of small polygonal cells were observed, larger spindle-shaped cells were also detected and these were more prevalent in passaged populations which were isolated using Method 1. CSSCs with this morphology have been seen in populations from passage 4 and are associated with a transition to a fibroblast phenotype (Y. Sun *et al.*, 2020).

Cells within the corneal limbus, with a similar phenotype to MSCs, have been found to express CD90 and CD73 but had low CD105 expression (21.4%) (Polisetty *et al.*, 2008). Method 1-isolated cells expressed CD73 with variable expression of CD90, likely due to the heterogeneous population of cells that are obtained. As the expression of CD90 is consistent across all MSC-like cells commonly isolated from the corneal/limbal-stroma, it is unlikely that the cells isolated here shared the phenotype of those previously reported, or they were a mixed population (Polisetty *et al.*, 2008; Branch *et al.*, 2012; Li *et al.*, 2012; Kureshi *et al.*, 2014; Sidney *et al.*, 2015). ICC analysis revealed that some of the cells isolated using method 2 expressed ABCG2, OCT-4A and PAX6, markers associated with precursor cells (Riekstina *et al.*, n.d.; Zhou *et al.*, 2001; Funderburgh *et al.*, 2005; Adewumi *et al.*, 2007; Ding *et al.*, 2010; Wee *et al.*, 2016). The gene expression of SOX2 is associated with pluripotent cells and has been found in both CSSCs (Funderburgh *et al.*, 2016) and in multipotent fibroblast-like cells

isolated from the corneo-limbal region (Dravida *et al.*, 2005), but protein expression was not observed in this study.

The gene expression profile of stem cells isolated from the corneal/limbal-stroma show greater expression of NOTCH1, ABCG2 and NES when compared to keratocytes (Du *et al.*, 2007; Basu *et al.*, 2014). Similarly, the stem cells have little expression of genes associated with keratocytes such as KERA, ALDH3A1, AQP1 and PTGDS (Du *et al.*, 2007; Basu *et al.*, 2014). Unfortunately, due to the difficulty of obtaining freshly excised human corneas with a high cell number and minimal RNA degradation, the gene expression of hCSSCs could not be directly compared to that of keratocytes. Donor variation was evident in this study, with some donors showing greater expression of NES, NOTCH1 and ABCG2 – genes associated with stem cells. However, these same cells also expressed KERA, PTGDS, ALDH3A1 and AQP1 at similar levels and so are unlikely to be stem cells. One possible method for identifying and isolating cells that meet the necessary criteria is that of magnetic-activated cell sorting (MACs). MACs works by using primary antibodies specific for cell surface antigens combined with a magnetically labelled secondary antibody. The cells that express the specific surface antigens can then be isolated and a more homogenous population of cells can then be sub-cultured. In the case of hCSSCs, the possible markers include: CD90, CD73, CD105, ABCG2 and SSEA-4. The use of such a method may improve the yield of hCSSCs and the sub-culturing of a pure population, with minimal contamination from other cell types, may improve the propagation of the stem cells, improving the yield. Alternatively, after applying MACs to isolate cells, single-cell cloning could be used to expand the cells. Although MACs provides a method of isolating cells that positively express a specific surface antigen, it can be damaging to the target cell membrane and can make it difficult to isolate a high percentage of cells (Faraghat *et al.*, 2017). For this reason, MACs typically requires a large number of cells and so would need to be applied with caution if used to isolate hCSSCs.

In the present study, difficulties arose when trying to expand CSSCs to a high cell number, necessary for tissue engineering. A heterogeneous population of cells was isolated which varied both in size and in the expression of CSSC markers. Furthermore, the cells readily increased in size, losing their characteristic polygonal shape which suggests they had transitioned into a more fibroblast-like cell. There are many possible explanations for the problems encountered in obtaining CSSCs. Given that most of the tissue used in this study was clinical waste from corneal surgeries, one such explanation could be the size and position of the corneal graft used for transplants prior to cell isolation. Occasionally, the tissue supplied from the RLUH had a corneal button removed that was not central and

encompassed part of the limbus, and which had been performed to increase the number of peripheral endothelial cells present in the graft (Romano *et al.*, 2015). As the CSSCs have been shown to reside below the limbal niche it could be possible that these cells were included in the corneal button used for surgery (Branch *et al.*, 2012; Pinnamaneni and Funderburgh, 2012; Hertsenberg and Funderburgh, 2015; Funderburgh *et al.*, 2016). If this is the case, there would be fewer CSSCs present in the remaining corneoscleral rim received post-transplant reducing the chance of successful isolation. Furthermore, with the corneal button traversing the limbus the resident stem cells may become activated and transition into a keratocyte/fibroblast phenotype. Acquired limbal stem cell deficiency (LSCD), such as from surgeries involving the limbus or from chemical injuries, can result in either a loss of or the dysfunction of limbal epithelial stem cells (LESCs) (Ahmad, 2012; Sejpal *et al.*, 2013). Given that wounds to the limbal niche can have a detrimental effect on the LESCs, it is plausible that a similar effect will be observed on the CSSCs.

The length of time between donor death and cell isolation may have had a deleterious effect on the stem cells within the corneal stroma. The first identified CSSCs were isolated from corneoscleral rims which had been stored in Optisol medium which are typically stored at 4°C for up to 2 weeks (Kaufman *et al.*, 1991; Lindstrom *et al.*, 1992; Du *et al.*, 2005). It has been reported that CSSCs can still be isolated from corneoscleral rims that have been stored in organ culture medium at 31 – 37°C for up to 4 weeks (Pels, 1997; Kureshi *et al.*, 2014). In this study the average length of time between donor death and cell isolation was 41.6 ± 16.3 days (see Appendix D). However, for donors isolated using Method 1, this assumes that the tissue was stored in organ culture medium for no more than 3 weeks prior to supplementing the medium with dextran, but this could be as great as 5 weeks (Pels, 1997). Limited information regarding the time between enucleation and corneal stroma stem cell isolation has been published and so the true effects of this are currently unknown. It has been shown that an increase in storage time can have deleterious effects on cell numbers, notably on those isolated using digestion methods (Iftimia-Mander *et al.*, 2013). It is possible that the extended period of time between enucleation and cell isolation reduced the number of stem cells present within the limbal region and so only a heterogeneous population could be isolated with a greater ratio of fibroblast-like cells.

An additional explanation for the difficulties encountered in this study could be related to the culture conditions of the CSSCs. It has been well reported that stem cells are sensitive to their cultured environment, including the substrate on which they are seeded (Eroshenko *et al.*, 2013; Gerardo *et al.*, 2019). It can therefore be hypothesised that the cell

culture flask used can impact cell propagation; as this information is rarely reported it is impossible to keep this variable consistent across research groups. Furthermore, FBS batch-to- batch variation can also affect stem cell attachment and proliferation (Honn *et al.*, 1975; Menendez *et al.*, 2013). The batches of FBS used could be another problematic factor of isolating CSSCs in this study, although this has not been found by others working with CSSCs (Alvena Kureshi, personal communication, 2017).

There are many variables that can influence the successful isolation and expansion of CSSCs. Two methods of propagating stem cells were trialled using a total of 65 donor tissues but, unfortunately, neither produced cells which were positively classified as stem cells. This is despite a visit to two labs (University College London and The University of Pittsburgh) to learn the technique first-hand. It is because of these reasons, and the trouble with accurately identifying the cells isolated, the use of hCSSCs as a cell source for an *in vitro* model of the stroma was not taken forward.

### 2.6.3 Characterisation of hMSCs

The corneal stroma is formed by neural crest cells, derived from the surface ectoderm, that migrate into the developing cornea (Feneck *et al.*, 2019). It would, therefore, be logical to use neural crest stem cells which can differentiate into keratoblasts and/or keratocytes. Whilst human neural crest cells have been isolated from adult tissue, they are rare with restricted self-renewal capacity (Achilleos and Trainor, 2012). Although adipose-derived MSCs are believed to originate from the mesoderm, they have been used in corneal tissue engineering and differentiate into keratocytes *in vitro* (Du *et al.*, 2010; Zhang *et al.*, 2013; Ahearne *et al.*, 2014; Lynch and Ahearne, 2017; Miwa and Era, 2018). Given the success found with adipose-derived MSCs, the feasibility of expanding bone marrow-derived MSCs for this purpose was investigated and hMSCs from three donors were characterised.

The expression of MSC markers varied greatly between donors, with the percentage of cells that expressed CD90, CD73 and CD105 ranging from 4 to 95% at passages 3-4. Despite this, all 3 donors displayed differentiation potential towards adipocyte lineage. The analysis of GAG content, after chondrogenic induction, suggests that donor 1 may be susceptible to phenotypic drift towards the chondrocyte lineage. Unfortunately, donor information from both donors 1 and 2 was unavailable; we can, therefore, only hypothesise the reason behind the variation observed between donors. MSC preparations from female donors have been found to contain cells that are slightly, but significantly, smaller in diameter and they tend to have more colony forming cells than male donors (Siegel *et al.*, 2013). However, trilineage

differentiation potential does not seem to be affected by donor gender (Siegel *et al.*, 2013) or age (Wagner *et al.*, 2009; Siegel *et al.*, 2013). Similarly, the expression of typical MSC markers, as defined by the ISCT, does not vary between genders (Siegel *et al.*, 2013). Donor age has been linked to a proportional increase in the number of senescence-associated, β-galactosidase-positive MSCs, a phenotype associated with decreased adipogenic differentiation potential and increased osteogenic potential (Wagner *et al.*, 2008; Zhou *et al.*, 2008). Conversely, a recent study by Andrzejewska and others (2019) concluded that donor age had little impact on the MSC phenotype (Andrzejewska *et al.*, 2019). It is possible that hMSCs isolated from donors 1 and 2 were from donors older than donor 3 (23 yrs) which may give rise to an explanation behind the differences observed.

A third hypothesis for the variance between donors is the method of isolation of MSCs. Donors 1 and 2 were isolated from unprocessed bone marrow aspirates, whereas donor 3 was purchased as a cryovial of mononuclear cells which were isolated using density gradient separation. Moreover, due to reasons beyond our control (customs clearance), there was a delay in the time between bone marrow aspirate extraction from donor 1 and the cells then being subjected to plastic adherence. Differences in the growth rate of MSCs isolated from the same donor but at different time points have been observed, leading the authors to conclude that heterogeneity can be produced by the method of harvest (Phinney *et al.*, 1999). It may, therefore, be possible that the donor variation observed is as a result of both the harvest and the method of isolating/expanding MSCs.

The reported number of adipose-derived MSCs required to induce keratocyte differentiation varies from $1 \times 10^4$ cells/cm$^2$ in monolayer to $1.2 \times 10^7$ cells in fibrin gel (Du *et al.*, 2010; Zhang *et al.*, 2013; Ahearne *et al.*, 2014; Lynch and Ahearne, 2017). For this reason, the hMSCs required expansion up to P5 to achieve the desired cell number. The phenotype of primary cells in culture is known to change with passaging and this is seen in MSCs too. Morphological changes such as an increase in cell diameter and cell volume between P3 and P6 have been observed in MSCs isolated from elderly patients (72.2 ± 7.5 yrs.) (Andrzejewska *et al.*, 2019). The same study also found that the expression of CD105 decreases after passaging which supports the flow cytometry data of donors 1 and 3 in this study. In contrast, the expression of CD105 increased in donor 2 whilst the typical negative markers (CD45, CD34, CD11b, CD79A, HLA-DR) decreased with passaging. Interestingly, at the late passage donor 1 also experienced a decrease in the expression of negative markers whereas donor 3 increased expression of these markers. The increased expression of these markers could suggest that the cells had either begun to differentiate or a sub-population of MSCs, that

were positive for these markers, out-competed other sub-populations. Alternatively, as there is only one technical replicate for each donor, these results may not be representative and result from technical variation alone. The flow cytometry data for donor 2 at both passages and donor 3 at P1 were provided by colleagues so it is possible that the culture methods and protocol for flow cytometry differed slightly thus causing a discrepancy with the published literature.

Despite the hMSCs not expressing the cell surface markers defined by the ISCT, they were assessed for their trilineage capability. It has been found that human MSCs at passage 8 (P8) had reduced osteo- and adipo-genic differentiation capacity when compared to cells at P4 (Yang *et al.*, 2018). In the present study, hMSCs at the later passages were at P3 and P4 and still successfully exhibited adipogenic differentiation. Whilst this study did not investigate the effects of cell culture expansion on trilineage differentiation capabilities, both donors 2 and 3 were successfully differentiated down all three lineages. Due to a lack of cell number, donor 1 could only be subjected to adipogenic differentiation for histological analysis. A study by Muraglia *et al.* across 185 human bone marrow-derived MSC clones observed that MSC clones that displayed the potential to differentiate towards the adipogenic lineage could also be differentiated towards the osteo- and chondro-genic lineages. No unipotent or bipotent adipogenic clones were observed (Muraglia *et al.*, 2000). These findings have been contradicted by other studies which have shown that unipotent adipogenic differentiation is possible, as is bipotent differentiation down adipo-/osteo-genic and adipo-/chondro-genic lineages (Okamoto *et al.*, 2002; Bajpai *et al.*, 2012). The discrepancies in the literature could be attributable to the source of MSCs which differ from immortalised MSCs (Okamoto *et al.*, 2002) to those derived from human hair follicles (Bajpai *et al.*, 2012). The observation of the lack of unipotent and bipotent adipogenic clones may indicate that the cells from donor 1 could have successfully differentiated down by osteogenic and chondrogenic lineages.

The GAG analysis in this study supports the histological staining with Alcian blue which shows chondrogenic differentiation in 2 out of 3 of the donors. Donor 1 did not show any differences in the total GAG content however, the hMSCs in growth medium alone (no chondrogenic induction) showed a much higher GAG content than donors 2 and 3. This data could suggest that perhaps the cell pellets from donor 1 had already started differentiating into chondrocytes, hence the high GAG content. The expression of CD73 has been found to remain consistently high in chondrocytes across passaging whereas the flow cytometry data

in this study found a sharp decrease in the number of cells expressing this particular antigen (Cournil-Henrionnet *et al.*, 2008).

Given that the hMSCs still maintained their trilineage differentiation potential at later passages, their ability to differentiate into keratocytes was investigated. The vast majority of MSCs that have been successfully differentiated into keratocytes are those that are derived from adipose tissue (Du *et al.*, 2010; Zhang *et al.*, 2013; Ahearne *et al.*, 2014; Harkin *et al.*, 2015; Lynch and Ahearne, 2017). A study by Park *et al.* (2012) found that bone marrow-derived MSCs cultured in α-MEM expressed keratocan (Park *et al.*, 2012). When these MSCs were subjected to conditioned medium, termed keratocyte conditioned medium, there was an increase in lumican expression. Interestingly, the keratocyte conditioned medium contained 10% FBS which has previously been associated with keratocytes differentiating into fibroblasts, the repair phenotype of keratocytes (Beales *et al.*, 1999; Long *et al.*, 2000; Pei *et al.*, 2004). Liu *et al.* reported that murine bone marrow-derived MSCs did not express keratocan when cultured on tissue culture plastic (Liu *et al.*, 2012). When transplanted into the stroma of keratocan knockout mice these MSCs expressed keratocan, suggesting the potential for bone-marrow MSCs to differentiate into keratocytes *in vivo* (Liu *et al.*, 2012). Due to the limited number of papers differentiating bone marrow-derived MSCs into keratocytes, a preliminary experiment was conducted. The expression of two proteoglycans, keratocan and lumican, were investigated as these are markers that are typically associated with keratocytes (Corpuz *et al.*, 1996, 2000; Liu *et al.*, 1998; Carlson *et al.*, 2005; Park *et al.*, 2012). Similar to the findings of Liu *et al.,* the present study did not observe any keratocan expression in undifferentiated hMSCs (Liu *et al.*, 2012). After keratocyte induction for 21 days, the hMSCs revealed expression of keratocan and lumican. Interestingly, hMSCs in both media conditions (KDM and SCM) expressed lumican. One possible explanation for the unexpected lumican expression of hMSCs in SCM is the length of time cells were in culture for. The immunofluorescent images suggest that the cells in SCM proliferated more and became confluent which may have caused the hMSCs in SCM to experience phenotypic drift and become fibroblastic. However, this has been contradicted by a group that did not observe any phenotypic drift with increased cell density (Haack-Sørensen *et al.*, 2013).

The F-actin staining in this study showed that the hMSCs in KDM exhibited a different morphology to those in the control SCM. The differentiated cells had a smaller cell body with a more spindle-like shape when compared to the cells in the control medium which had a large, flattened cell shape. The F-actin of keratocytes is typically in the cortical region of the

cell and the stress pattern, fibres running transversely across the cell, is associated with fibroblasts and myofibroblasts (Jester *et al.*, 1994; Funderburgh *et al.*, 2003; Yam *et al.*, 2015). The hMSCs in KDM still exhibited transverse F-actin fibres indicative of a more fibroblast phenotype.

It has been reported that bovine keratocytes spontaneously formed spheres in adherent monolayer culture (Scott *et al.*, 2011). This study found evidence of sphere formation of hMSCs treated with KDM which could provide further evidence of successful differentiation into keratocytes. Human keratocytes have not previously shown the ability to spontaneously form keratocytes from adherent cultures (Scott *et al.*, 2011). However, they can successfully form spheres when cultured on low-adhesive surfaces and these spheres had an increased expression of keratocyte markers compared to their adherent counterparts (Uchida *et al.*, 2005; Funderburgh *et al.*, 2008; Scott *et al.*, 2011; Lai and Tu, 2012). CSSCs differentiated on unmodified, micropatterned silk substrates have been shown to aggregate and form spheres (Wu *et al.*, 2014b). These spheres also exhibited increased expression of typical keratocyte markers such as keratocan and carbohydrate sulfotransferase 6 (CHST6) compared to fibroblasts. Interestingly, when the micropatterned substrates were modified with arginine-glycine-aspartic acid (RGD) peptide, the expression of keratocan and CHST6 increased further still. Whilst these results suggest that an RGD peptide is necessary for CSSC attachment to silk, it could also suggest that the micropatterned topography is necessary to enhance the differentiation of stem cells into keratocytes (Wu *et al.*, 2012). Together, these results suggest that the hMSCs may be a suitable cell source for a corneal stroma model. Although the cells in KDM showed transverse F-actin fibres, properties associated with fibroblasts, they expressed both keratocan and lumican. It is possible culturing cells on a substrate that encourages alignment may enhance the keratocyte phenotype to allow the production of a stroma-like matrix.

## 2.7 Conclusions

In this study three potential cell sources were characterised and assessed for their potential use in creating a stroma equivalent. hCFs were readily expanded and maintained their spindle-shaped morphology throughout passaging. They are a frequently used cell type when studying the corneal stroma and whilst they do not maintain all characteristics of keratocytes, at low passage numbers they exhibit CD34 – a characteristic of the quiescent keratocyte. Conversely, hCSSCs could not be isolated in sufficient quantity and quality for subsequent use. They transitioned into a more fibroblast-morphology after passaging and a

heterogeneous population was obtained. There was inter- and intra-donor variability in the expression of stem cell markers which was likely a result of the heterogeneous populations obtained. Similarly, inter-donor variability was observed in the hMSCs, particularly in the expression of cell surface markers CD90, CD73 and CD105. Despite this variability, two donors were successfully differentiated down osteogenic, adipogenic and chondrogenic lineages. hMSCs also showed potential to be differentiated into keratocytes with expression of keratocan and lumican.

## 2.8 Limitations and future work

The limitations of this study include, but are not limited to, a low number of biological replicates and high donor variation. An increase in the number of biological and technical replicates of hMSCs analysed via flow cytometry would have greatly improved these data and allowed more concrete conclusions to be drawn. Unfortunately, cell number was a limiting factor here and so this could not be easily remedied. Despite the hMSCs not expressing all of the cell surface markers defined by the ISCT to be positively identified as mesenchymal stromal cells, they were capable of trilineage differentiation. Preliminary studies suggest that the hMSCs also display the potential to differentiate into keratocytes, and although further experiments are required, a spheroid was identified, a phenotype that has been displayed by keratocytes *in vitro.*

To accurately model the stroma *in vitro*, keratocytes that synthesise an organised ECM are preferable. As keratocytes are neural crest-derived, differentiating neural crest stem cells, as opposed to mesenchymal stromal cells, may offer an alternative cell source. Of note are induced pluripotent stem cells which can be reprogrammed into neural crest cells before differentiation into keratocytes (Foster *et al.*, 2017). Whilst these cells still express genes associated with keratocytes at a much lower level than those *in vivo* it could have been interesting to compare these with hMSCs and hCFs (Naylor *et al.*, 2016).

The data presented in this chapter suggest that hCFs and hMSCs are a suitable cell source for development of a corneal stroma model; the cells are readily available and can be easily expanded *in vitro*. Furthermore, the differentiation potential of hMSCs offers promise of a cell type that closely resembles keratocytes and can, with substrate influence, begin to mimic the stroma. For these reasons, hCFs and hMSCs were taken forward and used to optimise an *in vitro* stroma model.

# Chapter 3. An *in vitro* model of the corneal stroma

## 3.1 Overview

Both hCFs and MSCs have previously been used in the tissue engineering of the corneal stroma (Guo *et al.*, 2007; Karamichos *et al.*, 2011). To ensure that an organised matrix is deposited, cells are seeded onto substrates with topographical cues that result in cell alignment. Polytetrafluoroethylene nanofibres (PTFE-nf) have been shown to align fibroblasts and result in the deposition of aligned type I collagen (Kearns *et al.*, 2010; Schofield *et al.*, 2011). PTFE-nf can also support corneal stromal cell growth and alignment and were therefore selected as an appropriate substrate (Gouveia *et al.*, 2013). Another substrate used to develop stroma models is a polycarbonate Transwell membrane (Guo *et al.*, 2007; D. Karamichos *et al.*, 2014). This substrate has been shown to feature nanoscale grooves which is believed to support the deposition of orthogonally arranged collagen fibrils (Dimitrios Karamichos *et al.*, 2014). This chapter focuses on the development of an *in vitro* model of the corneal stroma. hCFs and hMSCs were cultured on both PTFE-nf and Transwell membranes and the cell phenotype, alignment and collagen deposition were analysed.

## 3.2 Aims and Objectives

**The aim of this chapter was to identify a suitable cell type and substrate for the development of an *in vitro* corneal stroma model.**

The objectives of this chapter were:

1. To culture cells (hCFs and hMSCs) on substrates that provide topographical cues
2. To measure the alignment of hCFs on glass, PTFE-nf and Transwell membranes
3. To differentiate hMSCs into keratocytes, assessed via ICC and RT-qPCR, with a view to determining how keratocytes behave on each substrate

## 3.3 Materials

**Sigma/Merck (Germany):** Agarose (A9539)**;** Amicon Ultra-15 Centrifugal Filter Unit (UFC901008); Ampicillin sodium salt (A0166); BL21(DE3) Singles Competent Cells (70235-3); BugBuster Ni-NTA His-Bind Purification Kit (70751-3); Isopropyl β- d-1-thiogalactopyranoside (IPTG; 420322); Luria broth (LB broth; Miller) (L3522); LB Broth with agar (Lennox) (L2897); Resazurin sodium salt (R7017); 4X SDS Sample Buffer (70607-3)

**Thermo Fisher (USA):** Pierce bicinchoninic acid (BCA) Protein Assay Kit (23227); CellTracker™ Red CMTPX Dye (C34552); Pierce Dimethylformamide (DMF; 20673); DyLight 488 NHS Ester (46402); GelCode Blue Stain Reagent (24590); Novex™ Sharp Pre-stained Protein Standard (LC5800); NuPAGE™ 4-12% Bis-Tris Protein Gels (NP0335BOX); TrackIt 1 Kb Plus DNA ladder (10488085)

**Fisher Scientific (USA):** 22 x 22 mm glass coverslips, no. 1.5 (12363138); Corning™ Transwell™ Multiple Well Plate with Permeable Polycarbonate Membrane Inserts (10301031)

**Qiagen (Germany):** QIAshredder (79654); qPCR primers

**Promega (USA):** PureYield™ Plasmid Miniprep System (A1223)

**Roche (Switzerland):** cOmplete™ ULTRA Tablets, Mini, EDTA-free EASYpack Protease Inhibitor Cocktail (REF05892791001)

**Goodfellow (England):** 1 mM PTFE sheet (FP303050)

**New England Biolabs (USA):** BamHI-HF (R3136S); PstI-HF (R3140S)

**VWR (USA):** PeqGREEN (732-3196)

**Live Cell Instrument (Republic of Korea):** 1 well Chamlide CMS for 22x22mm coverslip (CM-S22-1)

## 3.4 Methods

### 3.4.1 Preparation and analysis of substrates

#### 3.4.1.1 Semi-automated friction transfer

To create aligned nanofibers of polytetrafluoroethylene (PTFE) a specifically designed apparatus was used, termed the friction transfer machine (Beamson *et al.*, 1996; Kearns *et al.*, 2010). The machine is composed of three main parts: the heater block, the motor, and a clamp to hold the PTFE blade (Figure 3.1 A). The blade was cut from a sheet of 1 mm thick PTFE in to a 20 x 10 mm rectangle and one of the longer edges was bevelled where it contacted the substrate. A glass coverslip was placed on the heating block set to 250°C, giving a surface temperature of approximately 235°C, and allowed to reach thermal equilibrium for approximately 5 min. The PTFE blade was lowered onto the surface of a glass coverslip and drawn across at a constant speed of 0.6 mm/s whilst under a 1 kg load, as depicted in Figure 3.1 B.

To ensure the fibres were present, the glass substrate was sprayed with 70% ethanol and held vertically. When nanofibers had successfully been transferred onto the glass the solvent ran off the glass along the fibres in straight lines. The coverslips were then rinsed with distilled water and sterilised on both sides using a CL-1000 Ultraviolet crosslinker (UVP; Cambridge) at 1500 μJ/cm$^2$ for 5 min. This substrate is referred to as PTFE nanofibres (PTFE-nf) throughout.

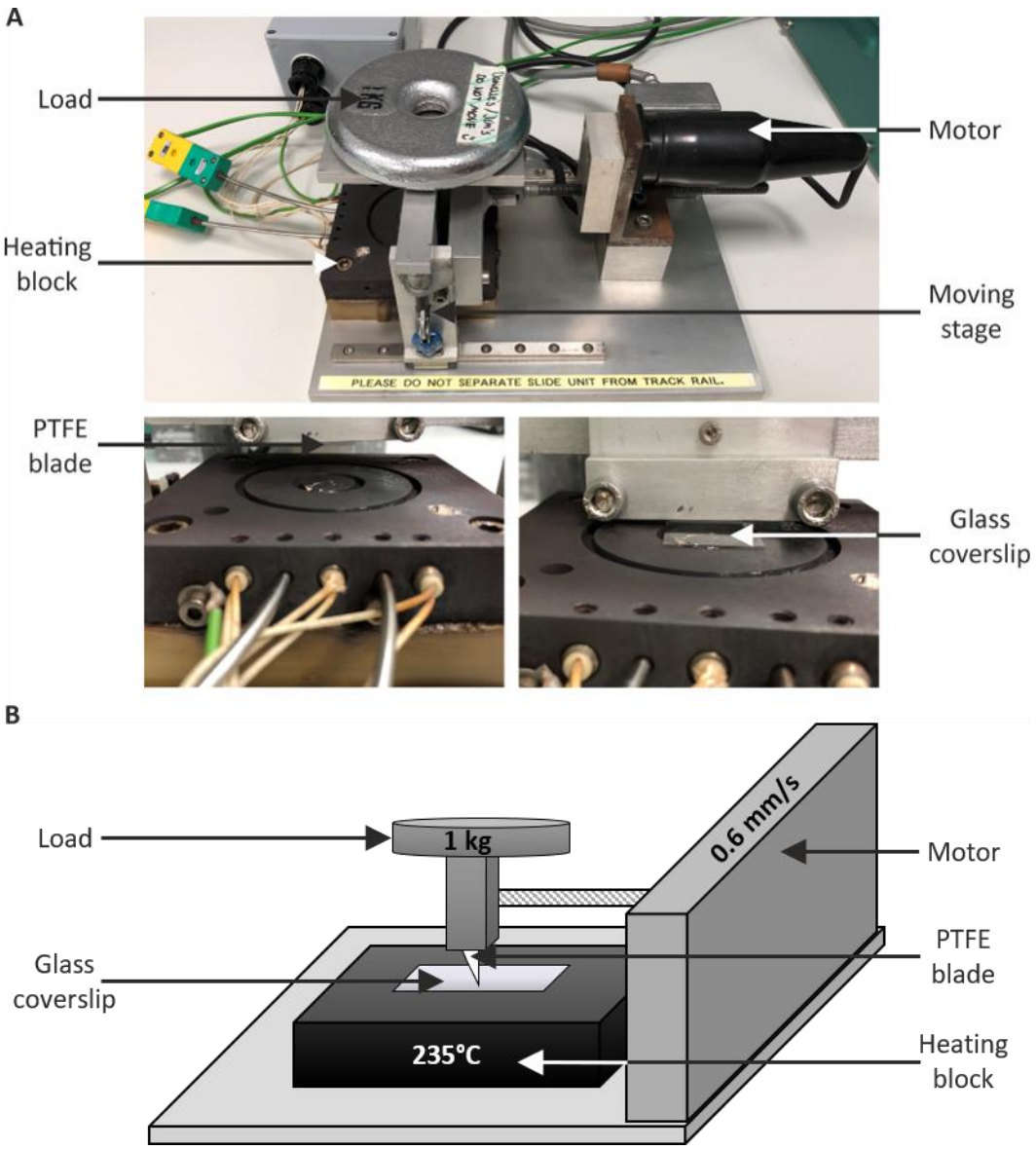


**Figure 3.1 The semi-automated apparatus used for performing friction transfer.** A: Images of the friction transfer machine show the main components required to create PTFE nanofibres. B: Diagram depicts the basic components of the machine in one image. The PTFE blade traverses the coverslip at 0.6 mm/s.

#### 3.4.1.2 White light interferometry

To enable the visualisation of the PTFE nanofibres the glass coverslips had to be made partially reflective. A Q150T-ES Turbo-Pumped sputter coater with a chromium target (Quorum) was used to coat the coverslips with approximately 40 nm of chromium (120 mA for 120 s).

A white light interferometer was used to analyse the surface topography of the PTFE-coated coverslips. The light intensity was adjusted to just below saturation and the substrate was brought into focus. The objectives were tilted to null the fringe which minimises the scan length needed to measure the surface. Vertical scanning interferometry (VSI) was used and two to three fringes were in the field of view. Data were captured using a backscan of 10 µm and a length of 12 µm and presented in the form of contour topographical representations.

#### 3.4.1.3 Scanning electron microscopy

Samples were kindly prepared and imaged by Dr. Lucy Bosworth. The 0.4 µm pore, polycarbonate Transwell membranes were cut out of the plastic holder prior to being sputter coated with 10 nm of gold and palladium (AuPd). Areas of the polycarbonate Transwell membrane were imaged at random using a FEI Quanta 250 FEG SEM operating at high vacuum with 5 keV electron beam.

Image analysis was then performed on 4 fields of view using FIJI and pore size, number and porosity were calculated using the *Analyse Particles* plugin (Schindelin *et al.*, 2012).

### 3.4.2 Expression of CNA35

A collagen probe, CNA35, enables the fluorescent labelling of collagens (Krahn *et al.*, 2006). pQE30CNA35 plasmid DNA, containing the collagen binding part of the A domain of *Staphylococcus aureus* collagen adhesion, fused to an N-terminal His tag, was kindly provided to Dr Elizabeth Laird (supervisor) by Prof. Magnus Höök at Texas A & M University, USA (Xu *et al.*, 2004).

#### 3.4.2.1 Preparation of Luria Broth (LB) and LB agar plates

LB broth (12.5 g) (Miller) was dissolved in $dH_2O$ (500 ml) and autoclaved. Once cool, ampicillin was added to a final concentration of 100 µg/ml.

LB broth with Agar (11.65 g) (Lennox) was dissolved in $dH_2O$ (333 ml), autoclaved and allowed to cool. Prior to pouring, ampicillin was added to a final concentration of 100 µg/ml and mixed thoroughly. Plates were poured in a Class II Microbiological Safety Cabinet.

#### 3.4.2.2 pQE30CNA35 plasmid transformation

The pQE30CNA35 plasmid (Appendix C) was transformed into BL21 (DE3) competent cells. A single vial was slowly thawed on ice then the pQE30CNA35 plasmid (1 µl) was added directly to the cells and gently mixed. The suspension was incubated on ice for 5 min, heat-shocked at 42°C for 30 s and again placed on ice for a further 2 min. Room temperature SOC medium (250 µl) was then added to the vial and incubated at 37°C for 1 h, shaking at 250 rpm. The cell suspension was then spread across the LB ampicillin plate using an L-shaped spreader and incubated inverted at 37°C overnight.

#### 3.4.2.3 Bacterial amplification and protein expression

A single colony was selected and transferred to LB broth with ampicillin (25 ml) in a 50 ml Falcon tube using aseptic technique and incubated overnight, shaking at 250 rpm. Following overnight incubation, LB broth (500 ml) with ampicillin was inoculated with the bacterial culture (25 ml) in a 1 L conical flask. The culture was incubated at 37°C, 250 rpm and monitored until OD600 reached 0.1, approximately 1 hour later. Isopropyl β-D-1-thiogalactopyranoside (IPTG) was added to the culture to a final concentration of 1 mM and incubated for a further 6 h. An aliquot (500 µl) used to inoculate LB broth with ampicillin (5 ml) and cultured overnight for use with PureYield™ Plasmid Miniprep System to isolate the plasmid DNA. The remainder of the culture was transferred into 50 ml Falcon tubes and centrifuged at $10^4$ x g for 10 min to pellet cells. The wet weight of the pellet was determined and then stored at -20°C until required.

#### 3.4.2.4 Isolation of plasmid DNA

Following overnight incubation, to eliminate the effect of the IPTG induction, 3 ml of the culture was transferred into a microcentrifuge tube and centrifuged at 13000 x g for 30 s to pellet cells. Plasmid DNA was extracted using PureYield™ Plasmid Miniprep System following the manufacturer's protocol: 'Alternative Protocol for Larger Culture Volumes'. Eluted DNA was quantified using a NanoDrop™ 2000 Spectrophotometer and stored at -20°C until required.

### 3.4.2.5 Restriction enzyme digest

To determine whether or not the selected *E. coli* colonies had incorporated the plasmid with the inserted CNA35 gene, a restriction enzyme digestion was performed. The enzymes (BamHI and PstI) were predicted to excise the insert from the multiple cloning site of the vector (Appendix C).

Agarose (1 g) was dissolved in 1X Tris-acetate-EDTA (100 ml) buffer by heating in a microwave with intermittent stirring. Agarose was poured into a gel tank and peqGREEN (5 µl) was added and stirred into the gel before placing the comb and allowing to set.

Plasmid DNA (1 µg), CutSmart buffer (5 µl), BamHI-HF (1 µl), PstI-HF (1 µl) were added to a microcentrifuge tube and the total volume made up to 50 µl with nuclease free $H_2O$. The solution was incubated at 37°C for 15 min and the 6X gel loading dye (10 µl) was added to the tube. The DNA ladder and sample were loaded into the agarose gel and run at 90 V for 1 h. The gel was imaged using a ChemiDoc XRS+ (Biorad).

The digest revealed two bands consistent with both the pQE30 vector size, 3461 bp, and the size of CNA35 gene, 948 bp suggesting the pQE30CNA35 plasmid was correctly inserted (Figure 3.2).

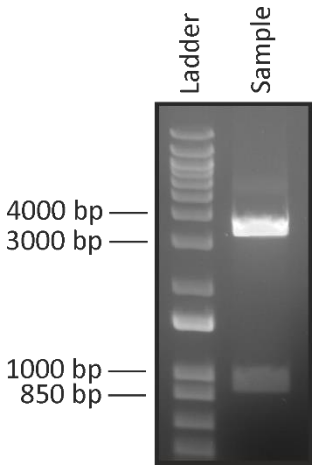


**Figure 3.2 Agarose gel electrophoresis of restriction-enzyme-digested plasmid for confirmation of CNA35 gene insertion.** The gel shows two products: one at approximately 3500 bp and the other ar approximately 900 bp. These values are consistent with the pQE30 vector (3461 bp) and CNA35 (948 bp) expected to be excised by the restriction enzymes used.

### 3.4.2.6 Protein extraction

The cell pellet (from 3.4.2.3) was resuspended in BugBuster Protein Extraction Reagent and the soluble fraction was prepared as per the manufacturer's protocol: 'BugBuster Protein Extraction Reagent User Protocol TB245 Rev. F 1108'. A 50 µl aliquot of the bacterial lysate was taken for SDS-PAGE analysis.

#### 3.4.2.7 Protein purification

A 1X Ni-NTA Bind Buffer, 1X Ni-NTA Wash Buffer and 1X Ni-NTA Elute Buffer were prepared as described in the manufacturer's protocol: 'Ni-NTA His•Bind Resins User Protocol TB273 Rev. D 0412JN'. A chromatography column from the BugBuster Ni-NTA His-Bind Purification Kit was prepared by pipetting Ni-NITA His•Bind Resin (2 ml) into the column and allowing to settle before Bind Buffer (5 ml) was added to equilibrate the column. Imidazole was added to the bacterial lysate to a final concentration of 10 mM before applying to the column. The flow-through was collected. The column was washed twice with 8 ml of the Wash Buffer and the flow-through collected. The protein was then eluted with 6 runs of 1 ml Elute Buffer and each run was collected in a separate microcentrifuge tube. A 50 µl aliquot from each flow-through was taken for SDS-PAGE analysis.

#### 3.4.2.8 SDS-PAGE analysis

Equal volumes of sample and 4X SDS Sample Buffer were mixed together and heated to 85°C for 3 min. Samples and the Protein Standard were loaded on to a 4-12% precast Bis-Tris gel and run with MES buffer for 30 min at 200 V. After running, the gels were fixed in 50% methanol, 7% acetic acid for 15 min and stained with GelCode Blue as per the manufacturer's instructions. The gel was imaged using a ChemiDoc XRS+.

Samples from each step in the protein purification process, along with the 6 eluates, were run on an SDS-PAGE gel (Figure 3.3). Eluates 1 to 3 had the highest amount of protein with a prominent band at 35 kDa, the size of CNA35. To ensure there was enough CNA35 protein, eluates 1 and 2 were pooled together, as were eluates 3 and 4. Eluates 3 and 4 gave consistent BCA assay readings and were therefore taken forward for further use.

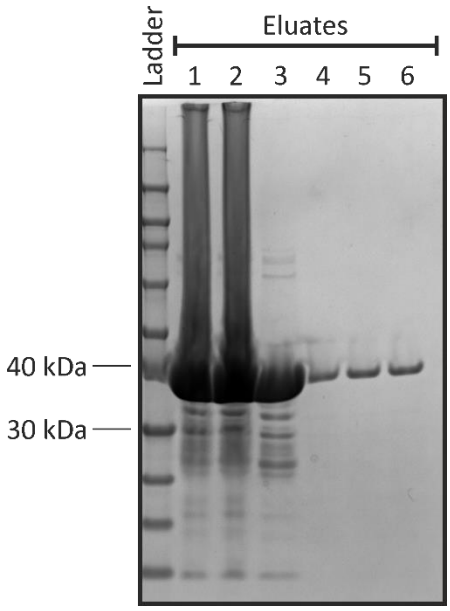


**Figure 3.3 SDS-PAGE gel of samples eluted from column after protein extraction using the BugBuster Ni-NTA His-Bind Protein Purification kit.** The gel shows large amounts of protein at 35 kDa, the size of CNA35. Eluates 3 and 4 were pooled together and were subsequently used.

#### 3.4.2.9 Buffer exchange

1X Protease Inhibitor Cocktail was added to all 6 eluates. Based on the SDS-PAGE gel eluates 3 + 4 were pooled together. The eluates were added to Amicon Ultra-15 Centrifugal Filter Devices and centrifuged at 4000 x g for 20 min at 4°C. The flow-through was discarded and 10 ml 0.1 M sodium bicarbonate buffer was added and centrifuged at 4000 x g for 20 min at 4°C, this was repeated twice. 1X Protease Inhibitor Cocktail was added to the eluates in the sodium bicarbonate buffer.

#### 3.4.2.10 Bicinchoninic acid (BCA) assay

The protein concentration was calculated using a BCA Protein Assay using a 1 in 10 dilution of the samples as per the manufacturer's instructions (Smith *et al.*, 1985). A protein standard curve was created using 0.1 M sodium bicarbonate as the diluent (Figure 3.4). Briefly, 50-parts of BCA Reagent A and 1-part BCA Reagent B were mixed together to create the working reagent. Each standard and unknown sample (10 µl) were added to a 96-well plate. The working reagent (200 µl) was added to each well, mixed and incubated at 37°C for 30 min. The absorbance was measured at 562 nm using a BMG SPECTROstar Nano microplate reader. The protein concentration was determined using the equation derived from the standard curve.

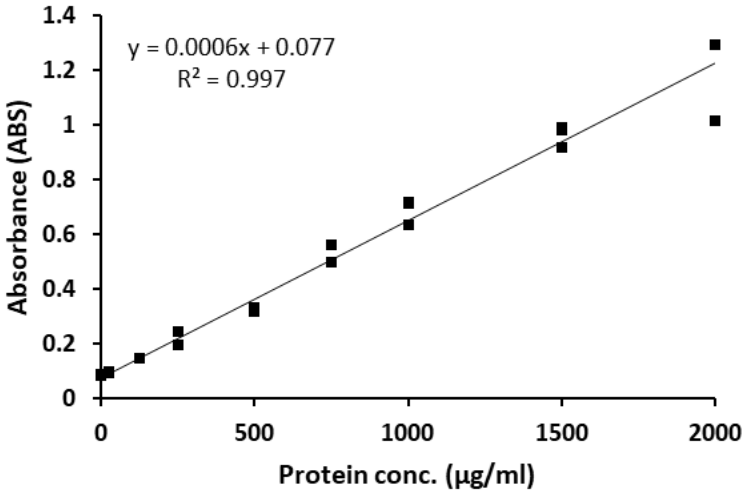


**Figure 3.4 Standard curve to determine protein concentration via a BCA assay.** Samples were analysed in triplicate to account for pipetting errors.

### 3.4.2.11 Fluorescent labelling

The BCA assay showed that the pooled eluates (3 & 4) had a protein concentration of 4.2 mg/ml. 2.1 mg of protein was used and DyLight 488 NHS Ester was prepared as described in the manufacturer's instructions. The amount of dye to be added to the labelling reaction was calculated using (Eq. 3.4.2.1):

$$\frac{amount\ of\ protein\ (mg)}{MW\ of\ protein} \times 15 \times MW\ of\ fluor \qquad \text{(Eq. 3.4.2.1)}$$

An Amicon Ultra-15 Centrifugal Filter Device was used to remove the unbound dye and replace the buffer with PBS by centrifuging at 4000 x g for 20 min three times. 1X Protease Inhibitor Cocktail was added to the protein in PBS. The absorbance of the labelled protein was measured at 280 nm and 495 nm. The protein concentration and degree of labelling were calculated as described in the manufacturer's instructions using (Eq. 3.4.2.2) to (Eq. 3.4.2.5):

$$Protein\ conc.\ (M) = \frac{[A_{280} - (A_{495} \times CF)]}{\varepsilon_{protein}} \times dilution\ factor \qquad \text{(Eq. 3.4.2.2)}$$

Where CF = correction factor and is 0.147

$$\frac{[1.72 - (5.412\ \times 0.147)]}{33176} = 27.86 \times 10^{-6}\ M \qquad \text{(Eq. 3.4.2.3)}$$

$$Moles\ dye\ per\ mole\ protein = \frac{A_{495} \times dilution\ factor}{\varepsilon_{fluor} \times protein\ conc.} \quad \text{(Eq. 3.4.2.4)}$$

$$Moles\ dye\ per\ mole\ protein = \frac{5.412}{70000 \times 0.00002786} = 2.775 \quad \text{(Eq. 3.4.2.5)}$$

Hence, each CNA35 protein was predicted to contain almost 3 fluorescent labels, consistent with previous reports (Krahn *et al.*, 2006).

## 3.4.3 hCF seeding and culture on substrates

### 3.4.3.1 Culturing hCFs

hCFs at P4 – 6 were seeded onto PTFE-nf and glass coverslips at a seeding density of 5 x $10^3$ cells/$cm^2$ or onto a 6-well polycarbonate Transwell membrane at a density of 1.06 x $10^5$ cells/$cm^2$ and allowed to attach for 2.5 h before being topped up with hCF growth medium (Table 2.1) and incubated overnight. The following day, the medium was switched to medium supplemented with 1 mM L-ascorbic acid 2-phosphate sesquimagnesium salt (A2P) (Gouveia *et al.*, 2013, 2015; Wu *et al.*, 2014a) and cells were cultured for up to 30 days. Information pertaining to the use of different biological donors in each experiment can be found in Table 3.2.

### 3.4.3.2 PicoGreen analysis of cell attachment to substrates

hCFs were seeded onto PTFE-nf, glass coverslips and Transwell membranes as described above. After an incubation period of 2.5 h, the wells were rinsed with growth medium which was collected and any unattached cells were pelleted by centrifugation at 360 x g for 5 min. The cell pellets were then washed in PBS, pelleted again and lysed with lysis buffer (500 µl). The remaining cells attached to each substrate were rinsed with PBS buffer and lysis buffer (500 µl) was added to each well. The wells were scraped prior to the transfer of cell lysate to a microcentrifuge tube. Samples were stored at -80°C until analysed.

Lysates were thawed to room temperature and a PicoGreen assay was carried out as described in 2.4.8.1, with exception that the volume of cell lysate and working PicoGreen solution were both increased to 100 µl. The proportion of cells attached to the substrate was calculated as described in (Eq. 3.4.3.1).

$$Proportion\ attached = \frac{No.\ attached}{No.\ attached + No.\ in\ media} \quad \text{(Eq. 3.4.3.1)}$$

### 3.4.3.3 Cell growth and metabolic activity

To determine the metabolic activity of hCFs cultured in growth medium and in medium supplemented with 1 mM L-ascorbic acid 2-phosphate sesquimagnesium salt hydrate, a resazurin assay was used. Resazurin sodium salt was dissolved in PBS to create a stock solution at a concentration of 0.1 mg/ml which was stored at 4°C in the dark prior to use. Cells were seeded in to a 48-well plate at a density of 5 x $10^3$ cells/$cm^2$ and at days 1, 3, 5, 7, 14 and 21 the culture media were aspirated from the cells and the wells were rinsed with PBS to remove any serum. The resazurin stock solution was further diluted to a concentration of 0.01 mg/ml in serum-free medium and 500 µl was added to each well along with a cell-free resazurin blank. The hCFs were placed back into the incubator, in the dark, for 2.5 h. 100 µl aliquots of the resazurin medium were transferred to a black 96-well plate in duplicate. The plates were analysed immediately using FLUO star OPTIMA plate reader at excitation/emission of 560/590 nm, using the optimal gain for each plate. The average of the cell-free resazurin blanks were deducted from their respective readings to correct for the autofluorescence of resazurin. To correct for variations in gain, samples were read at gains from 1000 – 2000. A standard curve was generated (Figure 3.5) and the equation of the curve was used to correct the data.

Following the resazurin assay, the cell number was also determined. The quantification of DNA per well using a PicoGreen assay was used to calculate the cell number as described in 2.4.8.1. This experiment was performed on one occasion comparing growth, medium supplemented with A2P (A2PM), and FC with the same data being reported in both Chapter 2 (2.5.1.2) and Chapter 4 (4.5.4).

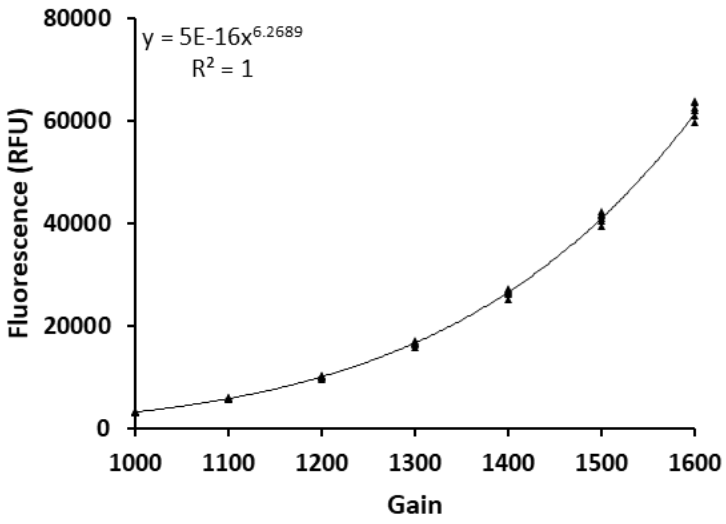


**Figure 3.5 Gain curves for correcting hCF Resazurin data.** Experimental samples were then read at their optimal gain and corrected for using the above equation.

#### 3.4.3.4 ICC of deposited collagens

To analyse the deposition of collagen types I, III, V and VI, hCFs were fixed in 10% NBF for 10 – 15 min at room temp. Samples were subjected to an immunocytochemistry staining procedure as described in Chapter 2 (2.4.4), however cells were not permeabilised. Primary antibodies used were: anti-collagen I, anti-collagen III, anti-collagen V, and anti-α-SMA (Table 2.2). Anti-collagen VI was also used; however, this was from a different supplier (Table 3.1). Where co-staining with CNA35 and anti-collagen I was performed, 0.5 µM CNA35 was added in conjunction with the primary antibody. Conjugated phalloidin was added in conjunction with secondary antibodies to label F-actin (Table 2.3). Images were acquired using a Zeiss LSM 800 microscope.

CNA35 was also used to stain collagen prior to cell fixation and cells were co-labelled with CellTracker Red (CTR). CTR was diluted in DMSO (7.2 µl) to form a stock at 10 mM. The stock solution was further diluted to 10 µM in serum-free medium before adding to the attached hCFs for 45 min. CTR was then aspirated out of the well and rinsed with medium supplemented with A2P (A2PM). 0.5 µM of the CNA35 488-labelled probe was added to A2PM for 90 min. Cells were then rinsed with PBS prior to fixation in 10% NBF.

**Table 3.1 Primary antibody used for ICC of hCF-deposited type VI collagen.**

| Clone | Primary antibody | Species | Supplier/Catalogue number | Concentration (µg/ml) |
|---|---|---|---|---|
| Poly | Collagen VI (Col VI) | Rabbit | Abcam Ab6588 | 2 |

#### 3.4.3.5 Imaging processing

Samples were imaged using a Zeiss LSM 800 and Zen Blue software (v 2.3). For cultures where cells had stratified into at least two layers, a z-stack image was acquired by finding the first and last view of the sample and using the 'optimal' function to image optical sections, where each section has a 50% overlap with the previous section. Following z-stack acquisition, images were analysed using FIJI (v 1.52p) (Schindelin *et al.*, 2012). Maximum (max.) z-projections were then created to visualise each slice in a single image and these are presented throughout this chapter. For tiled images, a 3 x 3 grid was imaged with a 10% overlap between each tile to allow for automated stitching performed by the Zen blue software.

#### 3.4.3.5.1 Cell alignment analysis

For each sample, 5 regions of interest (ROI) were selected, as depicted in Figure 3.6 A and a z-stack image was acquired at each region (Figure 3.6 B). The orientation of phalloidin-stained F-actin was analysed using the OrientationJ plugin from FIJI, as previously described (Rezakhaniha *et al.*, 2012; Franco-Barraza *et al.*, 2016). OrientationJ characterises the orientation of a region of interest based on the evaluation of structure tensors of each pixel, where the pixels represent F-actin filaments. The distribution was determined by running OrientationJ Distribution with a Gaussian Gradient and the local window, σ, set to 3 pixels. OrientationJ Analysis was used to achieve a colour survey, an image where hue represents the angle of orientation; saturation represents coherency; and brightness is the same as the input image. To ensure that the plugin was working as expected, images from one sample were rotated 20° in ImageJ prior to running the OrientationJ Distribution plugin (Appendix E).

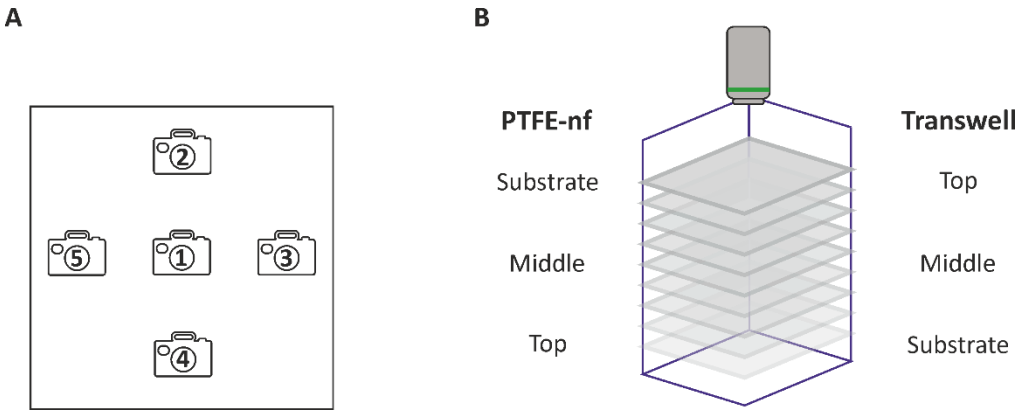


**Figure 3.6 Image acquisition for OrientationJ analysis.** A: 5 ROIs were selected and images were acquired from these regions. B: At each region of interest, a z-stack was acquired. For PTFE-nf and glass coverslips, the substrate was positioned closest to the objective; for those on Transwell membranes, the top of the cell layer was closest to the objective. For OrientationJ analysis, slices from the top, middle and bottom (substrate) were selected for analysis.

The OrientationJ plugin was used on slices that corresponded to the substrate and the distribution at each of the 5 ROI were summed for each sample. The distribution for each sample was then normalised to the cumulative dominant direction by identifying the modal angle of distribution. This angle was subtracted from the rest of the angles which corrected the mode value to 0°. Where angles were then greater than 90°, 180° was subtracted from the angle; and where the angles were then smaller than -90°, 180° was added to the angle, maintaining the angle distribution between -90° and 90°. The normalised distributions were

used to compare the three substrates, PTFE-nf, glass and Transwell membranes. To analyse the percentage of pixels that were aligned within a certain degree of the dominant direction, the absolute (non-negative) value of angles were taken and the distribution collated into 20° bins (e.g. ±10°), as depicted in Figure 3.7. To observe the possible change in orientation as cells stratify, 3 slices of the z-stack (top, middle and substrate) were selected and the distributions across the 5 ROI were again summed. The data from each donor were presented separately.

OrientationJ was also performed on 1 representative ROI to quantify the alignment of collagens and CNA35 on slices corresponding to the substrate, with the exception of images where individual z-slices are shown. The percent of collagen alignment within ± 10° is reported in the text.

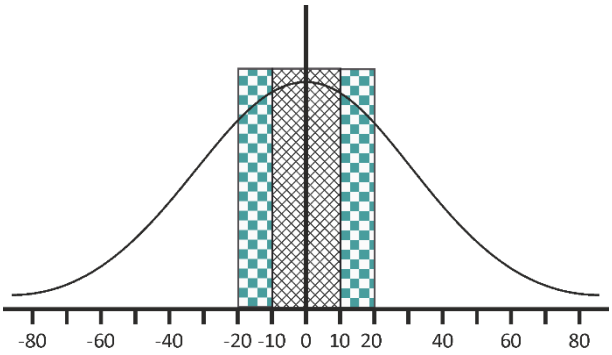


**Figure 3.7 Normalised OrientationJ distribution analysis.** To analyse the percentage of alignment with respect to the dominant direction, the distribution was grouped in to 10° bins representing ± 10° of the dominant direction (shaded with grey crosshatch) followed by 10° increments (10° to 20°+ -10 to -20°; teal squares) up to 90° and -90°.

### 3.4.4 Live cell imaging of hCFs

A 22 x 22 mm glass coverslip with PTFE nanofibres drawn across it was inserted into a 1 well Chamlide CMS chamber (Figure 3.8) to create a glass bottomed dish with PTFE-nf. 3 x $10^3$ hCFs at P4 were seeded onto PTFE-nf in the Chamlide CMS. Cells were incubated in hCF growth medium (100 µl) for 3 h to allow the cells to attach before topping up with 1 ml medium and incubating overnight. The following day, CTR was diluted in serum-free medium and added to hCFs, as previously described (3.4.3.4). CTR was then aspirated out of the Chamlide CMS and rinsed with growth medium. 0.5 µM of the CNA35 488-labelled probe was added to 1 ml of A2PM. Cells were imaged every 60 min using a Zeiss laser scanning microscope (LSM) 710 with a stage-top incubator (to ensure the same field of view was imaged). For each of the lasers (488 and 561 nm) a laser power of 1% was used to avoid cell damage. A z-stack of 3 slices was imaged to account for evaporation of culture medium

affecting the working distance. Images were analysed using ImageJ and max. z-projections are shown.

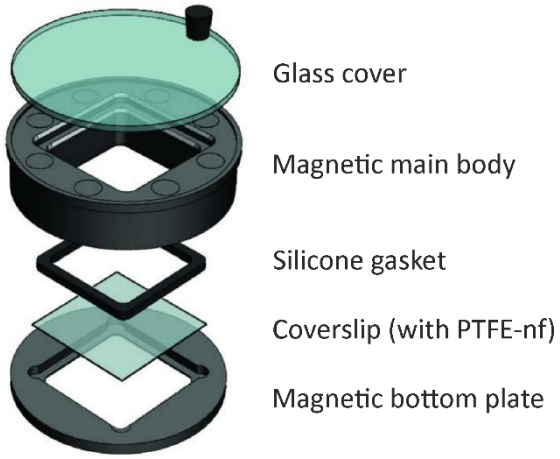


**Figure 3.8 The Chamlide CMS chamber (Live Cell Instrument) used for live cell imaging.** The Chamlide chamber allowed the incorporation of the coverslip coated with PTFE-nf.

Cell alignment analysis was performed using the OrientationJ plugin for ImageJ as previously described (3.4.3.5.1) however, only one field of view was assessed over time. The distribution was normalised to the direction of the nanofibres. The percentage of fibrils that were aligned within ±10° of the PTFE-nf was also calculated. To quantify the amount of collagen deposited the integrated density (fluorescence intensity) was measured via ImageJ. Three regions with no fluorescence were also measured and were averaged to give background readings. The corrected fluorescence was calculated using (Eq. 3.4.3.1):

$$CF = integrated\ density\ -\ (area\ \times BG\ fluorescence) \quad \text{(Eq. 3.4.4.1)}$$

Where CF = corrected fluorescence; area = area of ROI; BG = mean background fluorescence.

**Table 3.2 Details of hCF donors used in each experiment.**

| Donor number | Age (sex)* | Days between date of death and cell isolation | Experiments performed |
|---|---|---|---|
| Donor 6 | 57 (M) | 37 | **A2PM**: ICC analysis on glass, PTFE-nf and Transwell membranes; OrientationJ analysis; attachment to substrate; growth curves and metabolic activity. |
| Donor 7 | Unknown | 40 | **A2PM**: ICC analysis on glass, PTFE-nf and Transwell membranes; OrientationJ analysis; growth curves and metabolic activity. |
| Donor 8 | Unknown | 66 | **A2PM**: ICC analysis on glass, PTFE-nf and Transwell membranes; phase contrast images; OrientationJ analysis; growth curves and metabolic activity. |
| Donor 9 | Unknown | 41 | **A2PM**: Attachment to substrate. |
| Donor 10 | Unknown | 47 | **A2PM**: Attachment to substrate. |
| Donor 11† | 35 (M) | 8 | **A2PM**: ICC of intracellular collagen at 24 days; visualisation of cell stratification after 28 days utilising CNA35/CTR |
| Donor 12† | 35 (M) | 8 | **A2PM**: ICC of intracellular collagen at 24 days; live cell imaging of collagen deposition. |

†tissue donated by the same biological donor but treated separately.

### 3.4.5 hMSC differentiation in keratocyte differentiating medium

#### 3.4.5.1 Metabolic activity of hMSCs

Cell metabolic activity of hMSCs in SCM and KDM was measured using resazurin sodium salt, as described in 3.4.3.3. hMSCs were seeded at 5 x $10^3$ cells/$cm^2$, as previously described (Chapter 2, 2.4.8.2). At days 1, 3, 5, 7, 14 and 21 the culture media were aspirated from the cells and the assay was performed. The average of the cell-free resazurin blanks were deducted from their respective readings to enable the comparison between phenol-containing and phenol-free media. To correct for variations in gain, a subset of samples were read at gains from 1000 – 2000. A standard curve was generated (Figure 3.9) and the equation of the curve was used to correct the data and allow for comparisons between plates.

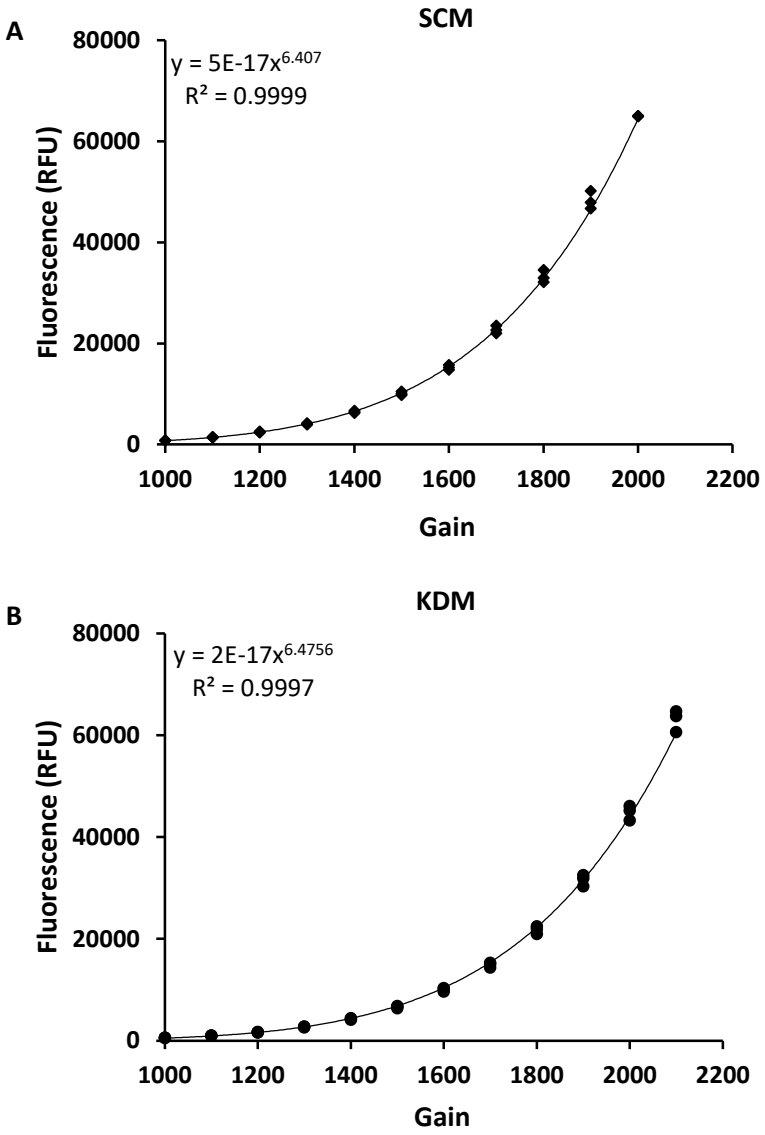


**Figure 3.9 Gain curves for correcting hMSC Resazurin data.** A: Samples in SCM were read at each gain to create a standard curve. B: A standard curve was also created for samples in KDM. Experimental samples were then read at their optimal gain and corrected for using the above equations.

### 3.4.5.2 Growth curve of hMSCs

Following the resazurin assay, the cell number in each well was also determined. The quantification of DNA per well using a PicoGreen assay was used as an estimate of cell number as described in Chapter 2 (2.4.8.2). To correct for the variation in gain used, a subset of samples from day 7 in KDM were read at gains from 1000-2000 and a standard curve was generated which was used to correct the data. These data were then compared to growth curves of hMSCs in SCM obtained in Chapter 2 (2.5.3.2).

#### 3.4.5.3 Differentiation of hMSCs on substrates

hMSCs were seeded onto glass coverslips at a density of 5 x $10^3$ cells/$cm^2$ or onto a 6-well polycarbonate Transwell membrane at a density of 1.06 x $10^5$ cells/$cm^2$ and allowed to attach for 2.5 h before additional hMSC growth medium was added. The following day, the medium was switched to KDM, as described in Chapter 2 (2.4.11), and cells were cultured for 21 days. Control hMSCs were cultured in stromal cell medium (SCM) (Table 2.5).

#### 3.4.5.4 ICC of differentiated cells

To characterise the differentiated hMSCs, cells were fixed, permeabilised and stained for keratocan, lumican, aldehyde dehydrogenase 3A1, CD34, α-SMA and collagen types I, III, V and VI as described in Chapter 2 (2.4.4). Where co-staining with CNA35 and anti-lumican was performed, 0.5 µM CNA35 was added in conjunction with the primary antibody.

OrientationJ analysis was also performed on 1 representative ROI to quantify the alignment of F-actin on slices corresponding to the substrate. The percent of cell alignment at ± 10° is reported in the text.

#### 3.4.5.5 RNA extraction, reverse transcription and RT-qPCR

RNA was extracted from cells cultured on coverslips as described in Chapter 2 (2.4.6) using Qiagen's RNeasy Plus Micro Kit. hMSCs cultured on Transwell membranes were subjected to treatment with Qiagen's RLT buffer followed by passing through a QiaShredder to homogenise the sample. RNA was then extracted as described previously.

RNA was converted to cDNA as described in Chapter 2 (2.4.7). The relative gene expression of keratocyte markers and collagens were analysed using primers designed using Primer-BLAST, found in the literature or purchased from Qiagen (see Table 3.3) (described in Chapter 2, section 2.4.7). Following GeNorm analysis (Appendix B), GAPDH was selected as the housekeeping gene and expression was normalised to GAPDH. Relative gene expression was calculated according to the comparative Ct method and primer efficiency was corrected for as described in Chapter 2.

**Table 3.3 Forward and reverse primer sequences.**

| Gene | Forward | Reverse | Source |
|---|---|---|---|
| GAPDH | ATGGGGAAGGTGAAGGTCG | TAAAAGCAGCCCTGGTGACC | (McDermott *et al.*, 2016) |
| ALDH1A1 | CTGGTTATGGGCCTACAGCA | ATTGTCCAAGTCGGCATCAG | (Park *et al.*, 2012; Yam *et al.*, 2015) |
| ALDH3A1 | CATTGGCACCTGGAACTACC | GGCTTGAGGACCACTGAGTT | (Du *et al.*, 2007) |
| AQP1 | CCACTGGATTTTCTGGGTG | CCAGACCCCTTCTATTTGGGC | Designed |
| CHST6 | CTCACCGGGTGTCGCTTAAT | GGTTCCTCAGCACCCCAAAG | Designed |
| KERA | CCTGGAAGGCAAGGTGCTA | AGTAGGAAAACTGGGTGGGC | Designed |
| LUM | GCAGTGTCAAGACAGTAAGGATT | TTGGGTAGCTTTCAGGGCAG | Designed |
| PTGDS | CCTGCCCCAAACCGATAAT | CAGAGACATCCAGAGCGTGG | Designed |
| COL1A1 | GTTCAGCTTTGTGGACCTCCG | GATTGGTGGGATGTCTTCGTCT | (Williamson *et al.*, 2020) |
| COL3A1 | Hs_COL3A1_1_SG QuantiTect Primer Assay | | Qiagen |
| COL5A1 | Hs_COL5A1_1_SG QuantiTect Primer Assay | | Qiagen |
| COL6A1 | Hs_COL6A1_1_SG QuantiTect Primer Assay | | Qiagen |

### 3.4.6 Statistical analysis

Statistical analyses were performed using MiniTab (v 19.2020.1), SPSS (IBM; v 26), SigmaPlot (v 14.0) and/or GraphPad Prism 9 (v 9.0.0) software. A significance level of $p < 0.05$ was set for all experiments. Data were reported as mean ± 1 standard deviation (SD). To ensure all data were normally distributed, a Shapiro-Wilk test was performed. Where data were not normally distributed, Box-Cox transformations were applied to determine a suitable transformation. Datasets were re-tested for normality and equal variances before parametric tests were used. One-way ANOVA with Tukey's *post hoc* test for multiple comparisons was performed to report both cell attachment and alignment data and a Brown-Forsythe test was used to ensure equal variances. For comparing three or more groups with two factors, a two-way ANOVA was performed and a Spearman's test for heteroscedasticity was used to ensure equal variances. With RT-qPCR data, where no expression was detected, this value was eliminated from the analysis. If the residuals after fitting the model were not normally distributed and data could not be suitably transformed, either a one-way ANOVA (where data were normally distributed) or a Kruskal-Wallis one-way ANOVA was performed. Multiplicity adjusted p values are reported.

## 3.5 Results

### 3.5.1 Characterisation of substrates

#### 3.5.1.1 PTFE nanofibres

The deposition of PTFE nanofibres on to glass coverslips was explored using white light interferometry. The VSI scan showed aligned, parallel features traversing the glass coverslip (Figure 3.10). At a low magnification the colour scale indicates that these fibres are between 1 – 100 nm in height whilst the higher magnification revealed that the fibres are mostly between 5 – 30 nm in height (Figure 3.10 A and B respectively). The height range was similar across all 4 samples. The average roughness of the surface ($R_a$) was 6.94 ± 3.23 nm and the root mean square roughness ($R_q$) was 9.94 ± 4.99 nm (Table 3.4).

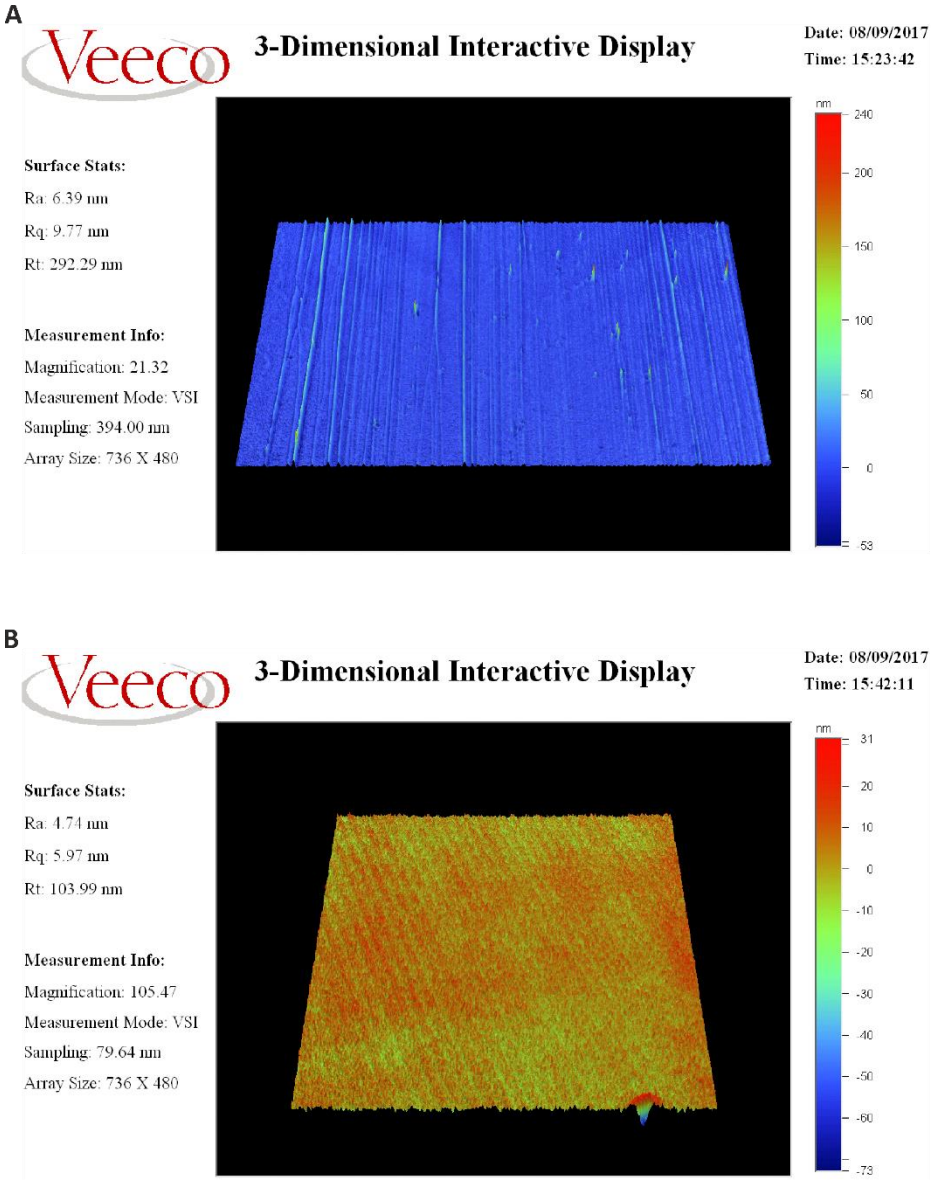


**Figure 3.10 Representative white light interferometry 3D plot of PTFE nanofibres coating a glass coverslip.** A: The nanofibres had an average roughness ($R_a$) of < 10 nm as observed at 21.32X magnification. B: Sample at 105.47X magnification. $R_a$, average roughness; $R_q$, root mean square roughness; $R_t$, maximum height of the profile.

**Table 3.4 Surface roughness values for PTFE nanofibres.**

| Roughness value[1] | PTFE nanofibres (nm)* |
|---|---|
| **$R_a$** | 6.94 ± 3.23 |
| **$R_q$** | 9.94 ± 4.99 |
| **$R_z$** | 144.39 ± 79.98 |

[1] $R_a$, average roughness; $R_q$, root mean square roughness; $R_z$, average maximum height of the profile.
* Data presented as mean ± SD from n = 4 samples.

#### 3.5.1.1.1 Polycarbonate Transwell membrane

Polycarbonate Transwell membranes have been used to culture corneal fibroblasts *in vitro* and have previously been shown to present parallel grooves across the surface (Guo *et al.*, 2007; Dimitrios Karamichos *et al.*, 2014). SEM was used to analyse the surface of the Transwell membranes and to investigate the presence of parallel grooves. FIJI analysis of the SEM images determined the average diameter of the pores to be 0.43 µm (SD = 0.01), slightly larger than the manufacturer reports (Table 3.5). The average number of pores per $cm^2$ was measured as $8.75 \times 10^7$ (SD = $8.21 \times 10^5$) and the pores covered approximately 12% of the membrane surface.

The random distribution of pores can be seen at relatively low magnification SEM images (Figure 3.11 A and B). These images also reveal a possible explanation for the increased pore diameter observed, several of the pores overlap and create one large pore. At higher magnifications parallel features were observed traversing patches of the membrane (Figure 3.11 C and D). These features were considerably smaller in width than the diameter of the pores and the increased magnification revealed small areas where these features were absent suggesting these were not consistent across the membrane.

**Table 3.5 Measured Transwell membrane properties from SEM micrographs.**

| | **Diameter of pore (µm)** | **Number of pores / $cm^2$** | **% area covered** |
|---|---|---|---|
| Reported by Corning | 0.4 | $1 \times 10^8$ | Data not supplied |
| Measured using FIJI * | 0.43 ± 0.01 | $8.75 \times 10^7 \pm 8.21 \times 10^5$ | 12.36 ± 0.58 |

* Data presented as mean ± SD from n = 4 fields of view.

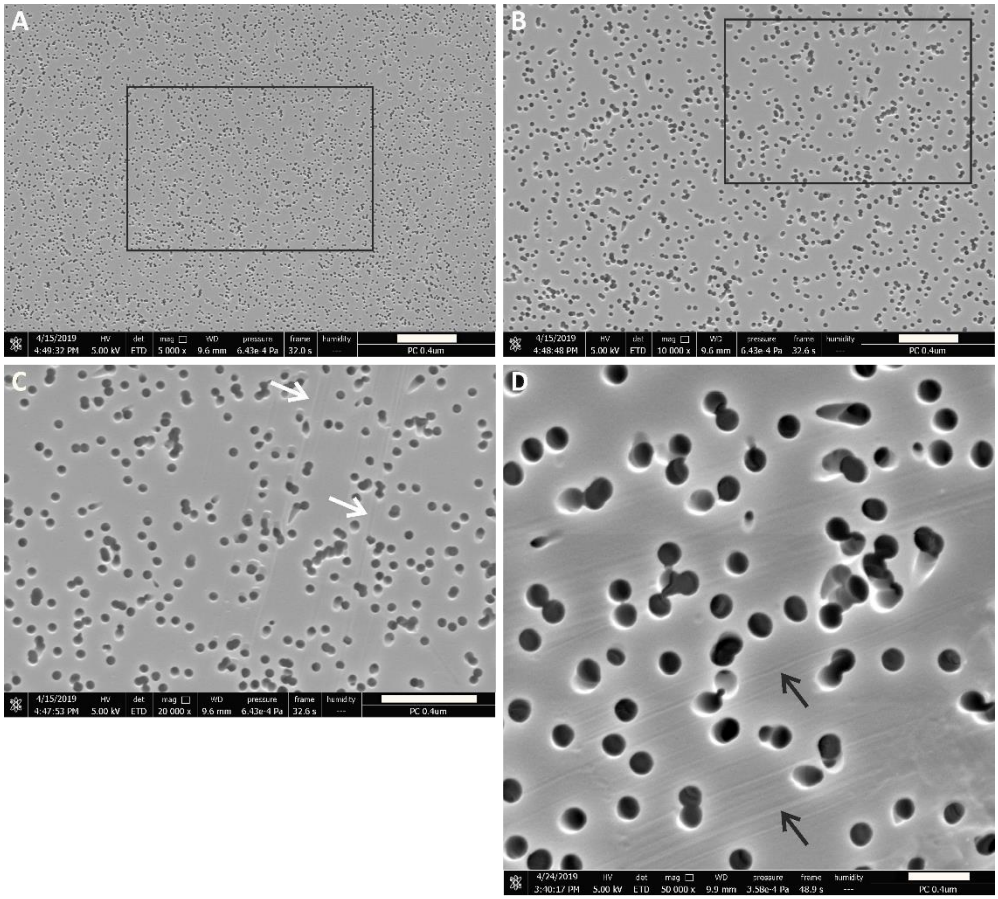


**Figure 3.11 Ultrastructure of a polycarbonate Transwell membrane.** A: Representative SEM image at 5000X view show the 0.4 µm pores in the Transwell membrane and the highlighted region (black box) is magnified in B. B: At 10,000X view the non-uniform distribution of the pores can be seen and the region within the black box is magnified in C. C: Faint lines can be seen on the surface of the membrane at 20,000X view (white arrows). D: A stitched image at an increased magnification of 50,000X shows the lines running across the surface of the membrane are visible (black arrows). Scale bars represent A: 10 µm; B: 5 µm; C: 4 µm; D: 1 µm.

### 3.5.2 hCFs in an *in vitro* model of the stroma

Three substrates were investigated for their suitability in a model of the corneal stroma: glass, PTFE-nf and Transwell membranes. A PicoGreen assay indicated that over 90% of cells that were seeded onto each substrate had attached after 2 h (Figure 3.12).

The effect of A2P supplementation on cell number and metabolic activity was also investigated using both a PicoGreen assay and a resazurin assay. Cells continued to proliferate with no significant change in cell number when A2P was added to the medium (A2PM) (Figure 3.13 A). Media type was shown to significantly affect metabolic activity ($p = 0.045$) however, when correcting for multiple comparisons, no significant differences were observed (Figure 3.13 B). A table of p values for each of these experiments can be found in (Appendix F).

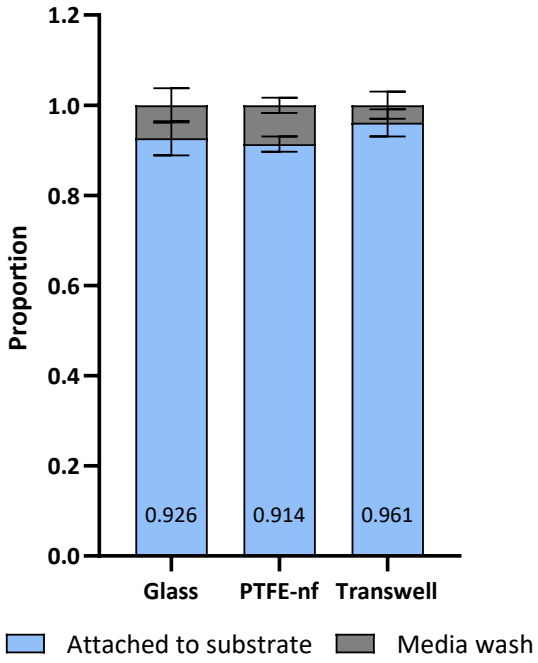


**Figure 3.12 Initial hCF attachment to substrates.** A PicoGreen assay was used to investigate the number of cells that attached to glass coverslips, PTFE-nfs or Transwell membranes. Cells were seeded onto each substrate and allowed to attach for 2 h prior to PicoGreen analysis on the substrates and on the media wash. n = 3 and error bars represent mean ± 1 SD. One-way ANOVA was performed on the fraction attached to the substrate. No significant differences were observed.

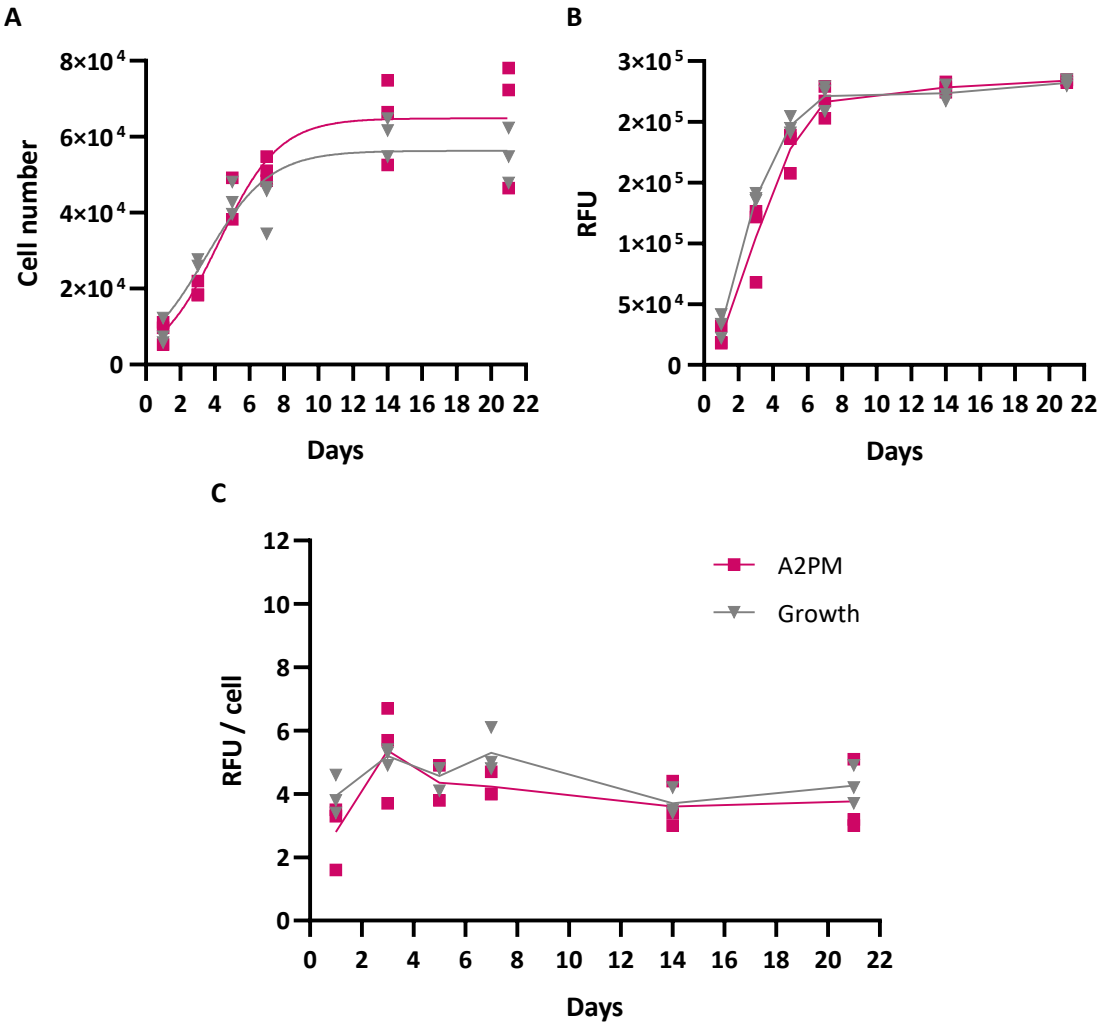


**Figure 3.13 Growth and metabolic activity of hCFs in normal (growth) and ascorbic acid supplemented (A2PM) conditions.** A: A PicoGreen assay was used to compare the proliferation of hCFs in A2PM (magenta) to normal, growth medium (grey). A logistic growth curve was applied where $R^2$ = 0.896 and 0.892 for Growth (as in Chapter 2, 2.5.1.2) and A2PM respectively. B: Cell metabolic activity was assessed using a resazurin sodium salt colorimetric assay over 21 days. C: To take into consideration the effect of an increase in cell number on the overall metabolic activity, the relative fluorescence was normalised to cell number. n = 3 biological replicates for all samples except for the cell number for A2PM at day 5 where n = 2; lines represent the mean in B and C. This experiment was performed on one occasion comparing growth, A2PM and FC with the same data being reported in Chapter 4 (4.5.4). Where data were normally distributed a two-way ANOVA was performed otherwise, a one-way ANOVA was performed with Tukey's *post hoc* test for multiple comparisons. No significant differences were observed.

### 3.5.2.1 hCFs aligned parallel to PTFE nanofibres

Phase contrast microscopy was used to visualise the hCFs growing over time (Figure 3.14). When cultured on the glass substrate hCFs were randomly oriented up to 24 h. By day 7 short range order was observed with areas of the fibroblasts appearing to align in different directions. By day 21 evidence of cell stratification could be seen with the hCFs forming a

layer of randomly oriented cells. In contrast, some hCFs could be seen aligning parallel to the PTFE-nf from as early as 3 h post-seeding. This continued as the cells proliferated however, by day 21 stratification was evident with cells orienting at different angles to the PTFE-nf.

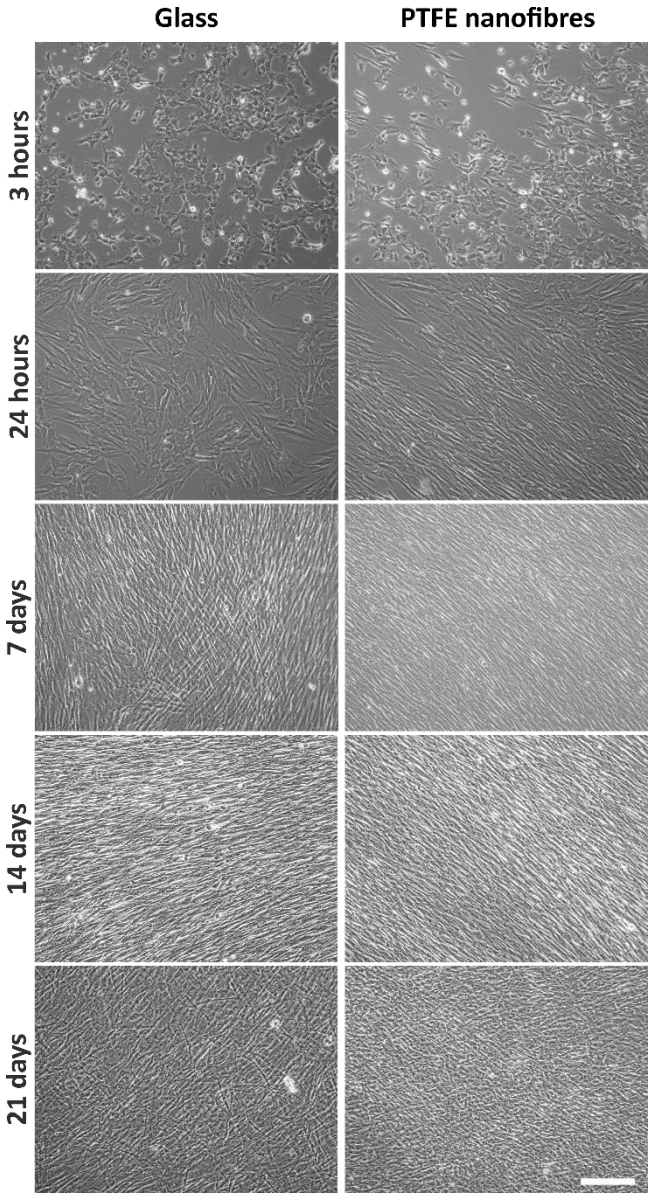


**Figure 3.14 Representative phase contrast images of hCFs cultured over time.** Cells were cultured on either control glass coverslips (left) or PTFE-nf (right) for 21 days. Scale bar represents 200 µm.

The alignment of hCFs on PTFE-nf was further investigated by analysing the orientation of the cytoskeleton using OrientationJ (Figure 3.15 & Figure 3.16). The normalised distributions of cells cultured on PTFE-nf showed a sharp peak at 0°, confirming that most cells are aligned in the dominant direction, running parallel to the nanofibres (Figure 3.15 A). Conversely, there is no sharp peak in the distribution when cultured on both

glass and Transwell membranes, indicating the cells are less aligned on these substrates (Figure 3.15 B and C, respectively). On Transwell membranes, a shallow broad peak is evident which suggests that whilst some alignment may be observed, this is not uniform across the sample. Investigating the deviation from the dominant direction revealed that 72.5% of pixels (representing filaments) were aligned within ± 10° of the dominant direction on PTFE-nf, three times greater than those on glass and two times greater than those on Transwell membranes (Figure 3.15 D) ($p = 0.0002$ and 0.0008 respectively). Few filaments are oriented between 40.1° – 50° from the dominant direction on PTFE-nf (0.3%) whereas on both glass and Transwell membranes this was greater than 5% (9.6% and 6.0% respectively) (Figure 3.15 E). Interestingly, only cultures on glass showed filaments oriented between 80.1° – 90° from the dominant direction (8.2%), significantly more than that observed on PTFE-nf ($p = 0.0485$) and Transwell membranes ($p = 0.0478$) (Figure 3.15 F).

OrientationJ was also used to analyse the change in orientation observed as cells stratify on each of the three substrates (Figure 3.16). When in contact with the PTFE-nf, the distribution of F-actin filament orientation was aligned with the nanofibres. The seventh donor appeared to maintain this alignment throughout the z-stack with minimal change in the distribution of F-actin filament. However, the other two donors displayed a decrease in alignment towards the middle of the cell construct, with a shallow broad peak observed. At the top of the cell construct, at least two separate distributions were observed suggesting that as the cells stratify they rotate and change orientation. The degree in which the cells rotated varied between 30° and 55°. The three donors behaved similarly when cultured on glass, with little alignment observed on any layer of the construct. However, the eighth donor also showed rotation by approximately 30° as the cells stratified. Broad, shallow peaks were observed on the substrate level of all donors on Transwell membranes suggesting that whilst there may be some alignment, this was not uniform across the sample. As with cultures on PTFE-nf, the cells rotated as they stratified but the distribution remained broad. The shift in the peak varied between donors and ranged from 18° to 77°.

The alignment of stratified cells appeared to be reduced but shifted when cultured on PTFE-nf. To quantify this, the alignment at each of the two main peaks in the top layer of cells was quantified (Figure 3.17). hCFs continued to align within ± 10° of the direction of the nanofibres (42.4%; Figure 3.17 A) but 36.1% of cells were aligned towards the second peak, suggesting that cells had rotated as they stratified. Few cells were oriented between ± 40-50° of either peak 1 (6.2%) or peak 2 (10.5%) (Figure 3.17 B). Less than 5% of cells were aligned within ± 80-90 ° of peak 1 (2.5%) and peak 2 (0.06%) (Figure 3.17 C).

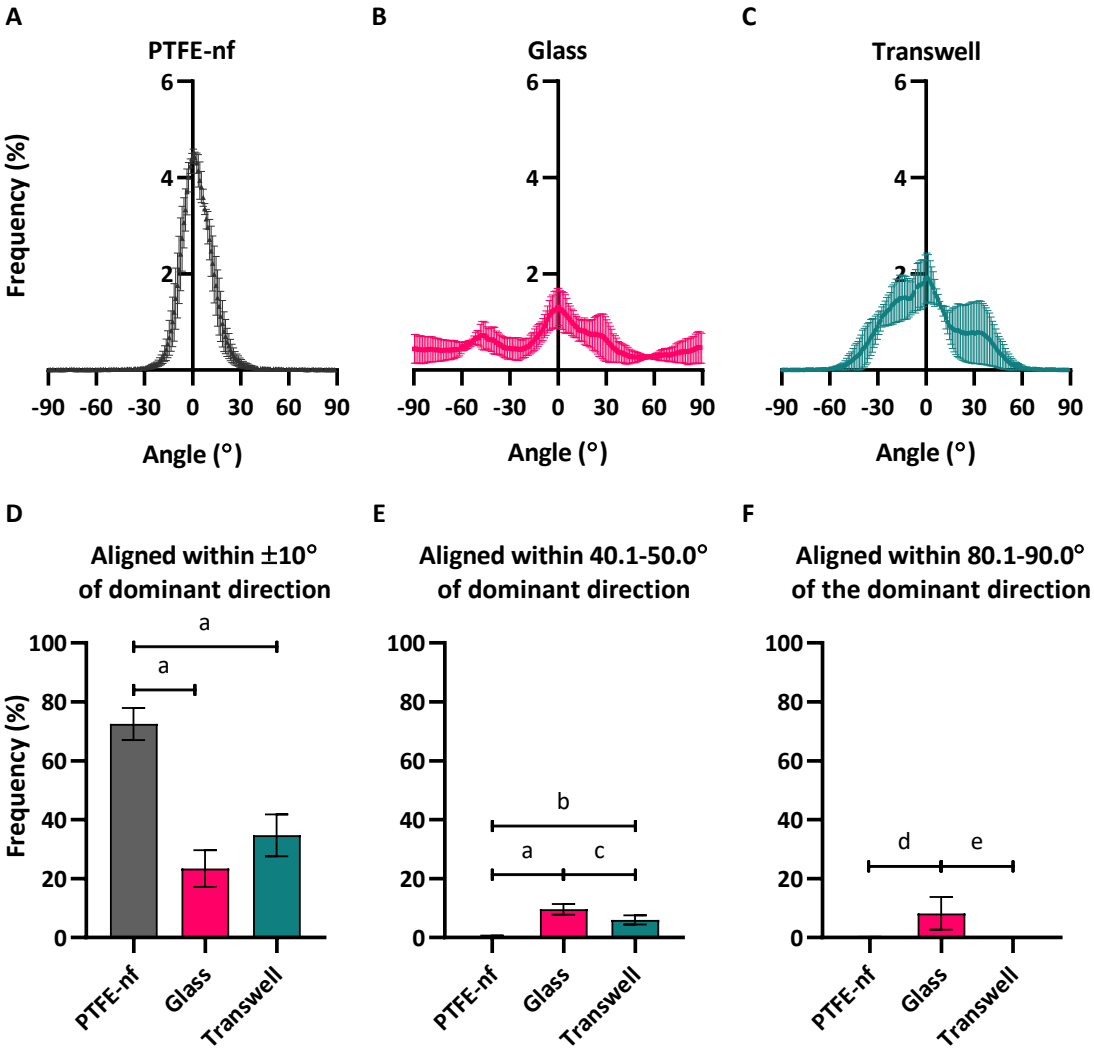


**Figure 3.15 OrientationJ analysis of F-actin distribution at the substrate level, normalised to the modal direction.** A: Distribution of cell orientation cultured on PTFE-nf (black). B: Distribution of cell orientation cultured on glass (magenta). C: Distribution of cell orientation cultured on Transwell membranes (teal). D-F: The alignment compared to the dominant direction was also investigated by grouping the distribution into 10° bins from the dominant direction. D: Quantification of the distribution aligned within ± 10° from the dominant direction on PTFE-nf (grey), glass (magenta) and on Transwell membranes (teal). E: Quantification of the distribution of actin filaments aligned between ± 40-50° of the dominant direction on PTFE-nf (grey), glass (magenta) and Transwell membranes (teal). F: Quantification of the distribution aligned within ± 80-90° of the dominant direction on PTFE-nf (grey), glass (magenta) and on Transwell membranes (teal). n = 3 biological replicates with the means ± 1 SD shown. A one-way ANOVA was performed on each 10° bin followed by Tukey's *post hoc* test for multiple comparisons; multiplicity adjusted p values: a = < 0.001; b = 0.0058; c = 0.0453; d = 0.0485; e = 0.0478.

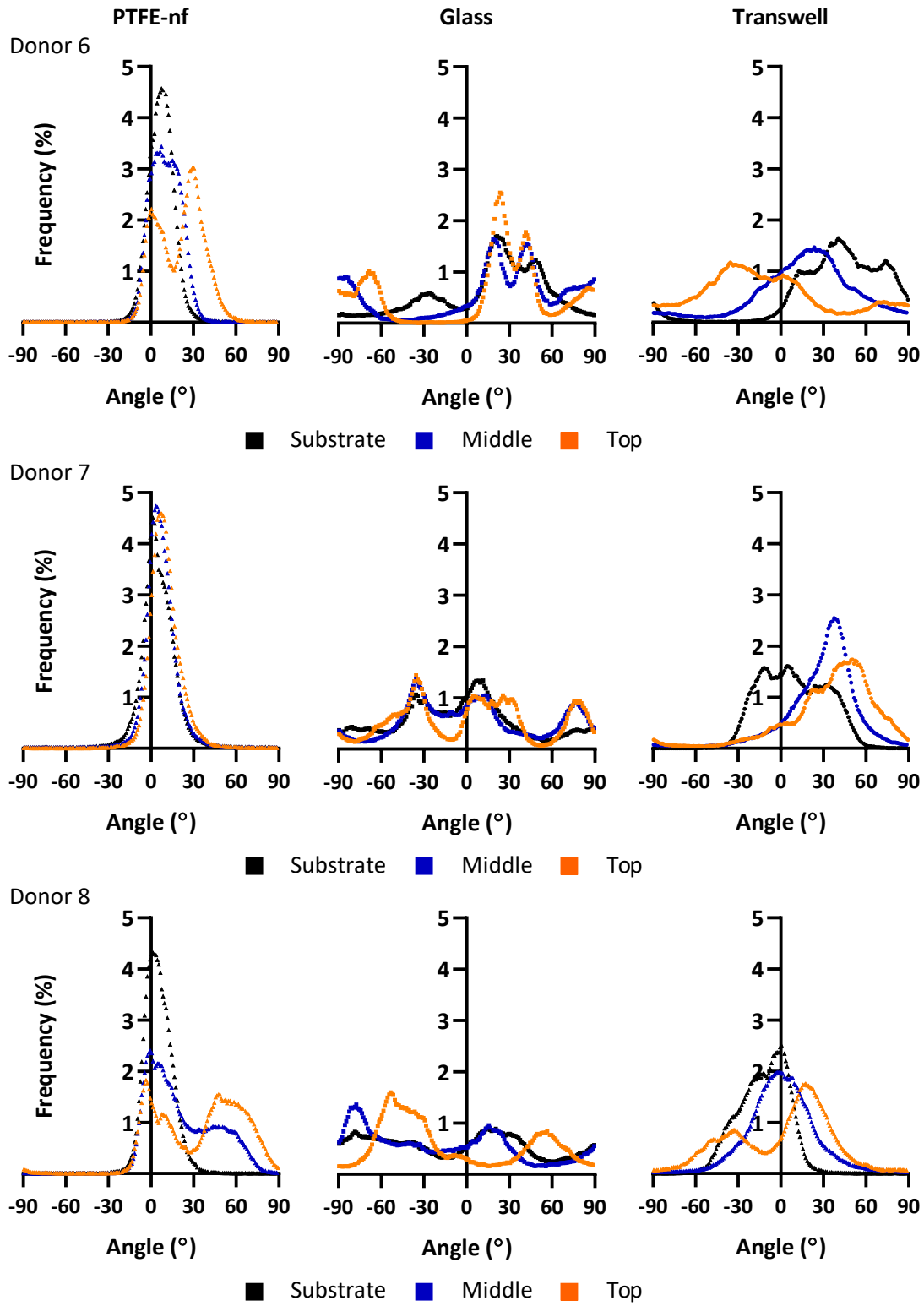


**Figure 3.16 Stratification of hCFs cultured on PTFE-nf, glass and a Transwell membrane for 30 days.** For each substrate, the distribution is split to show the alignment of cells on the substrate (black), those in the middle (blue) and those on top (orange) of the cell construct. Each donor has been shown separately (one donor per row; donors 6-8). The distributions of hCFs on PTFE-nf (left) show alignment on the substrate (same data as presented in Figure 3.15). The stratification of hCFs on glass (middle) and on Transwell membranes (right) are also shown.

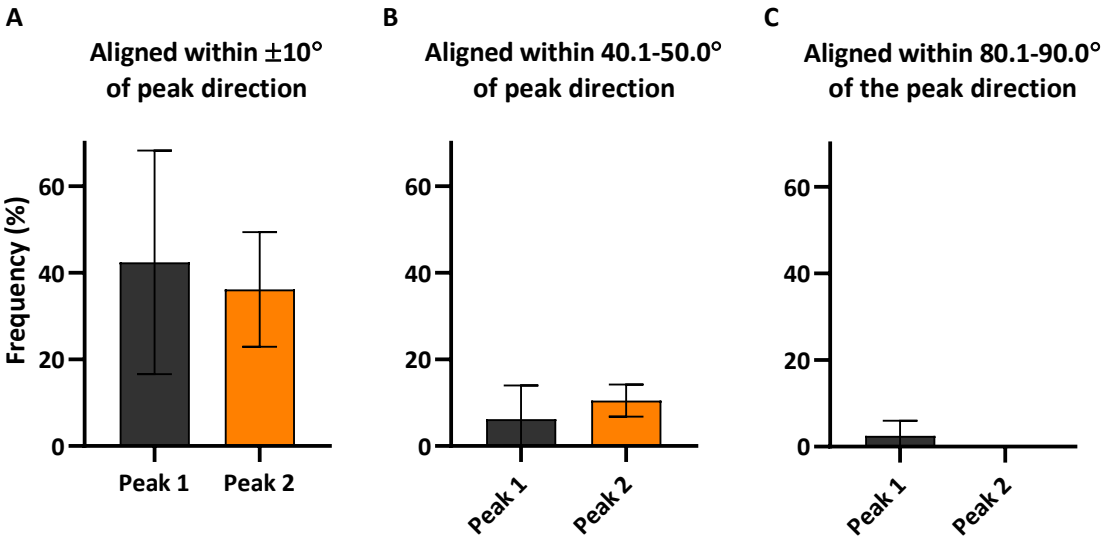


**Figure 3.17 Alignment of the top layer of stratified hCFs on PTFE-nf.** OrientationJ analysis of cell alignment on PTFE-nf showed that alignment is reduced but shifted as cells stratify. A: Quantification of the distribution aligned within ± 10° of the first (grey) and second (orange) peak (Figure 3.16). Peak 1 corresponds to the direction of the nanofibres. B: Quantification of the distribution aligned between ± 40-50° of peak 1 (grey) compared to peak 2 (orange). C: Quantification of the distribution aligned within ± 80-90° either peaks 1 and 2 (grey and orange, respectively). n = 3 for peak 1; n = 2 for peak 2, where a shift in angle was not observed for one donor.

### 3.5.2.2 hCFs deposit collagen types I, V and VI

ICC analysis was used to visualise collagen deposition by hCFs in media supplemented with 1 mM A2P (A2PM) on glass, PTFE-nf and on Transwell membranes. Initially, cells were permeabilised prior to the application of the primary antibody which revealed intracellular type I collagen expressed by hCFs cultured on PTFE-nf (Figure 3.18). Co-staining with phalloidin, which labels the F-actin of the cells, confirmed that the cells were aligned in the direction of the PTFE-nf.

As the deposition and alignment of extracellular collagens is of great importance when modelling the corneal stroma, hCFs were no longer permeabilised prior to the addition of the primary antibodies (Figure 3.19, Figure 3.20 and Figure 3.21). The maximum z-projections of hCFs show diffuse staining for type I collagen on all three substrates, which appears more aligned in cells cultured on PTFE-nf (59% aligned within ± 10° of the dominant direction; n = 3) than on either glass (30% aligned; n = 3) or the Transwell membrane (18% aligned; n = 13) (Figure 3.19). The staining of type I collagen on the Transwell membrane is diffuse but this is likely due to the higher cell number, and thus increase in deposited collagen. There is what appears to be intracellular staining of type III collagen on all substrates which is likely non-specific staining (Figure 3.20), although the staining observed is stronger than in the IgG control (Figure 3.22). Type V collagen was deposited by hCFs on

all substrates, with alignment again observed on PTFE-nf (72% aligned within ± 10° of the dominant direction; n = 2) but also on the glass substrate (42% aligned; n = 2). On the Transwell membranes type V collagen appears disorganised with little alignment (28% aligned; n = 3). Similarly, type VI collagen was deposited on all substrates (Figure 3.21) with that deposited by hCFs on PTFE-nf appearing the more aligned (67% aligned; n = 3) than the type VI collagen deposited on glass (29% aligned; n = 3) or the Transwell membrane (22% aligned; n = 3). A diffuse staining for α-SMA was observed with no actin fibrils evident, indicating non-specific staining in cells that were not permeabilised prior to ICC. A summary of collagen expression can be found in Table 3.6 at the end of the results section.

To further investigate the deposition of collagens, CTR and CNA35 were added to live cell cultures *in vitro*, prior to fixation (Figure 3.23 & Figure 3.24). The distribution of CNA35 labelled collagens showed some alignment with the cells (labelled with CTR) appearing to show short-range order when cultured on glass (Figure 3.23). Collagens can be seen in all layers as the cells stratify over 10 µm with the collagen orientation rotating by 25.3°. When cultured on PTFE-nf, the cells remained aligned along the nanofibres with the collagen orientation closely following the cells (Figure 3.24). Interestingly, as the cells stratified on PTFE-nf they also rotated 39.5° whilst still maintaining alignment.

Tiled images were acquired across an area covering approximately 3 $mm^2$ to assess the distribution of collagens across each sample after 30 days (Figure 3.25). The larger field of view confirms the random orientation of the deposited collagens when hCFs were cultured on glass, with there being no observable directionality. In contrast, when cultured on PTFE-nf the CNA35-labelled collagen can be seen following the direction of the nanofibres in the layer closest to the substrate. As also observed in Figure 3.24, there is a shift in the orientation of collagen in the subsequent layers yet this still appears aligned.

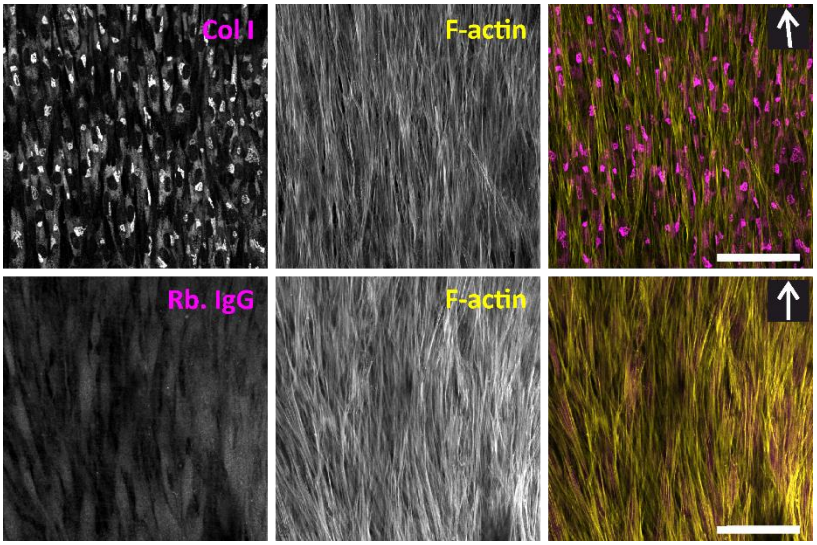


**Figure 3.18 Representative ICC analysis of intracellular type I collagen expressed by hCFs cultured on PTFE-nf for 24 days.** Intracellular expression of type I collagen (Col I; magenta) when hCFs were cultured in medium supplemented with 1 mM A2P and permeabilised prior to antibody staining. Cells were co-stained with phalloidin (F-actin; yellow). IgG control (magenta) is also shown. White arrows on merged images represents direction of PTFE-nf. n = 2 biological replicates. Scale bar represents 100 µm.

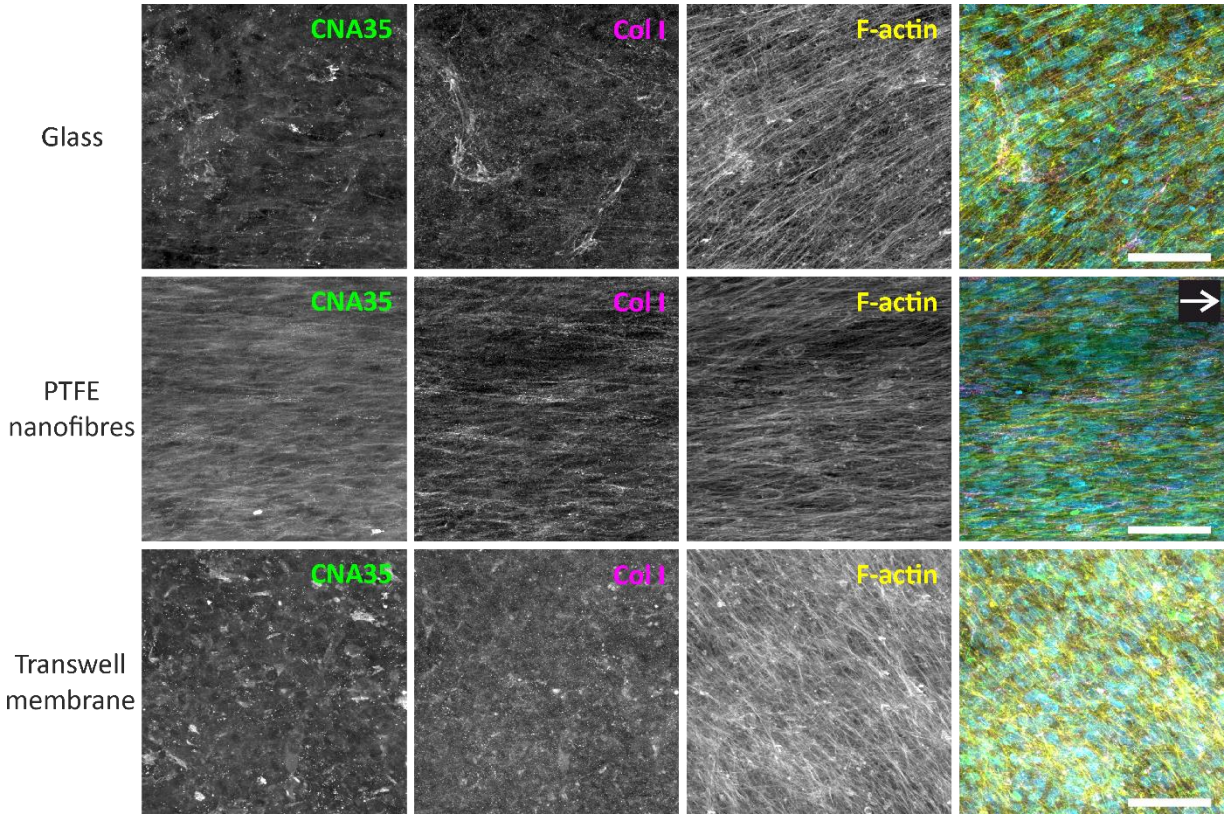


**Figure 3.19 Representative max. z-projections from ICC analysis of extracellular type I collagen expressed by hCFs cultured on glass, PTFE-nf and Transwell membranes for 30 days.** The extracellular expression of collagens (CNA35), specifically type I collagen (Col I; magenta) was analysed. Cells were co-stained with phalloidin (F-actin; yellow) and DAPI (blue) and the negative controls are shown in Figure 3.22. These same images were used for OrientationJ analysis (Figure 3.15) and as a comparison for macromolecular crowding (Chapter 4, 4.5.2). White arrow on merged image represents direction of PTFE-nf. n = 3 biological replicates. Scale bar represents 100 µm.

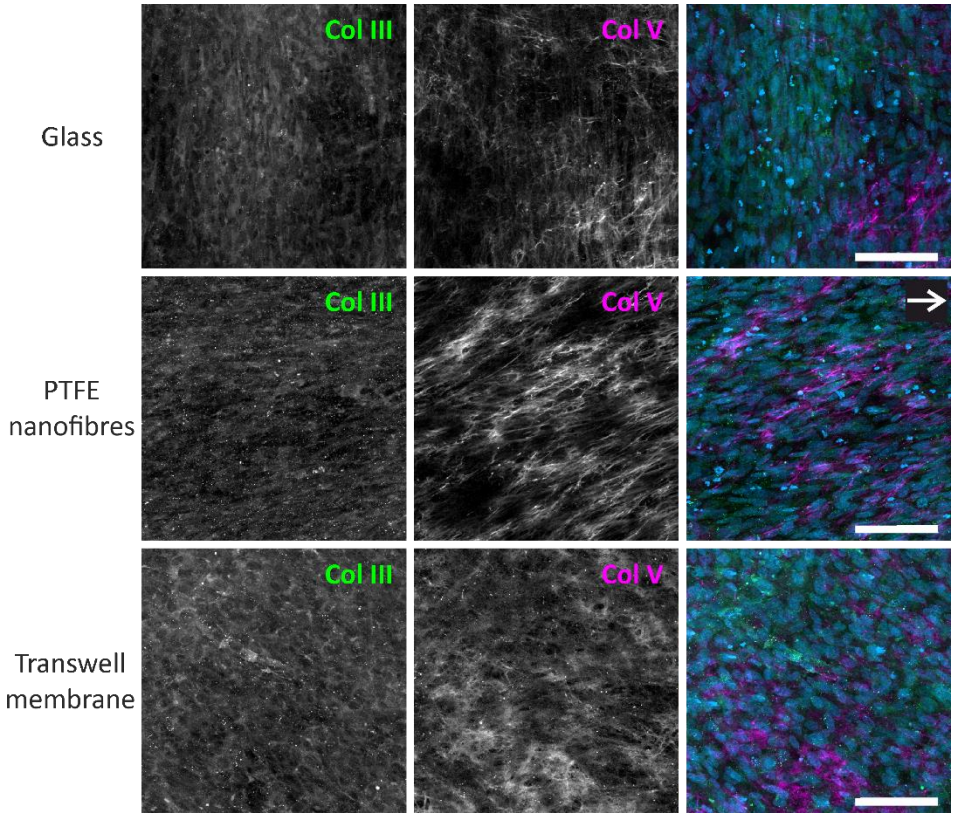


**Figure 3.20 Representative max. z-projections from ICC analysis of extracellular collagen types III and V expressed by hCFs cultured on glass, PTFE-nf and Transwell membranes for 30 days.** Collagen types III (Col III; green) and type V (Col V; magenta) are shown. These data were also used as a comparison for macromolecular crowding (Chapter 4, 4.5.2). Cells were co-stained with DAPI (blue) and the negative controls are shown in Figure 3.22. White arrow on merged image represents direction of PTFE-nf. n = 2 biological replicates except for on the Transwell membrane where n = 3. Scale bars represent 100 µm.

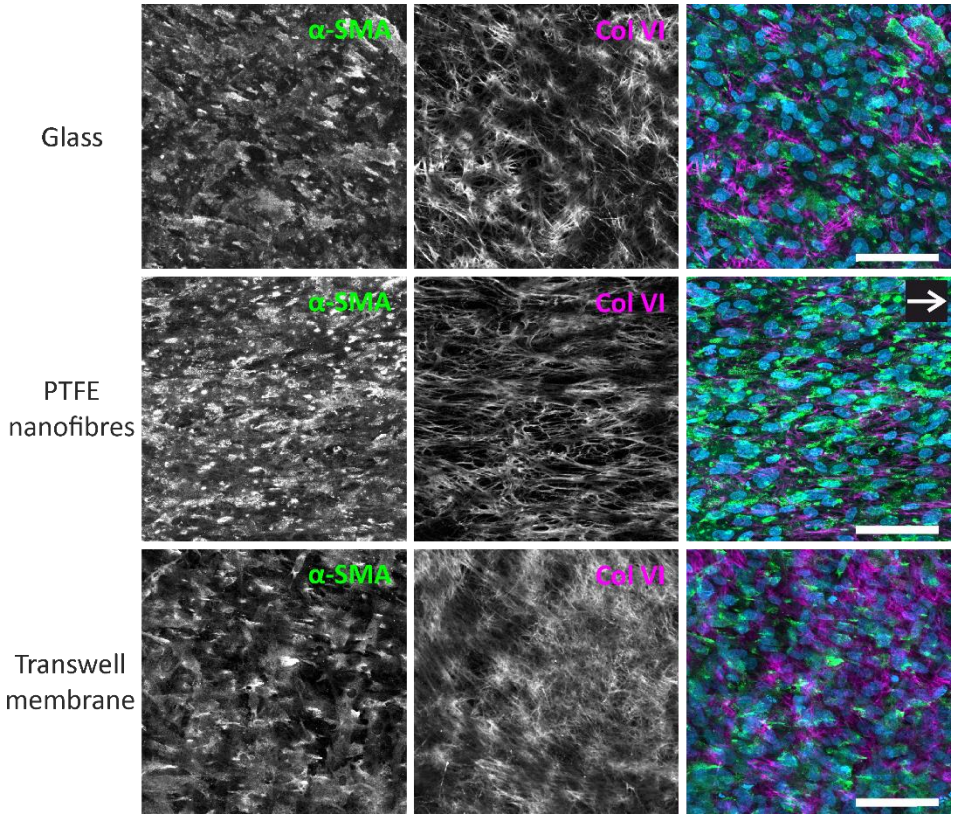


**Figure 3.21 Representative max. z-projections from ICC analysis of extracellular type VI collagen and α-SMA expressed by hCFs cultured on glass, PTFE-nf and Transwell membranes for 30 days.** α-SMA (green) and type VI collagen (Col VI; magenta) are shown. These data also were used as a comparison for macromolecular crowding (Chapter 4, 4.5.2). Cells were co-stained with DAPI (blue) and the negative controls are shown in Figure 3.22. White arrow on merged image represents direction of PTFE-nf. n = 3 biological replicates. Scale bars represent 100 µm**.**

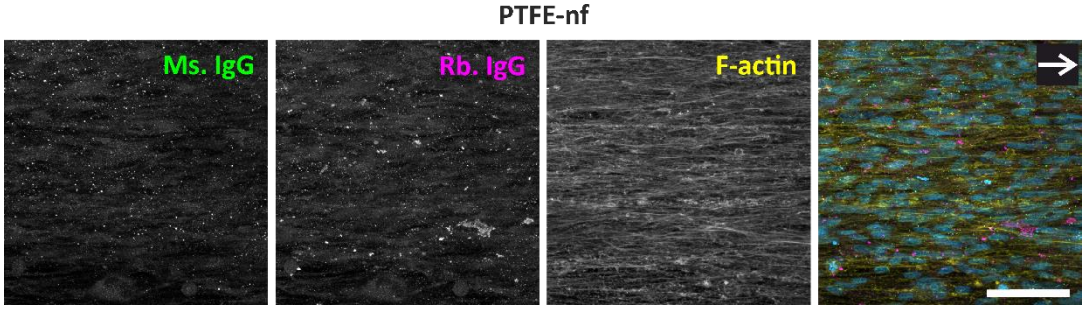


**Figure 3.22 IgG negative controls for mouse and rabbit primary antibodies.** Cells were co-stained with phalloidin (yellow) and DAPI (blue) with the merged images also shown. White arrow on merged image represents direction of PTFE-nf. n = 1 biological replicate. Scale bar represents 100 µm.

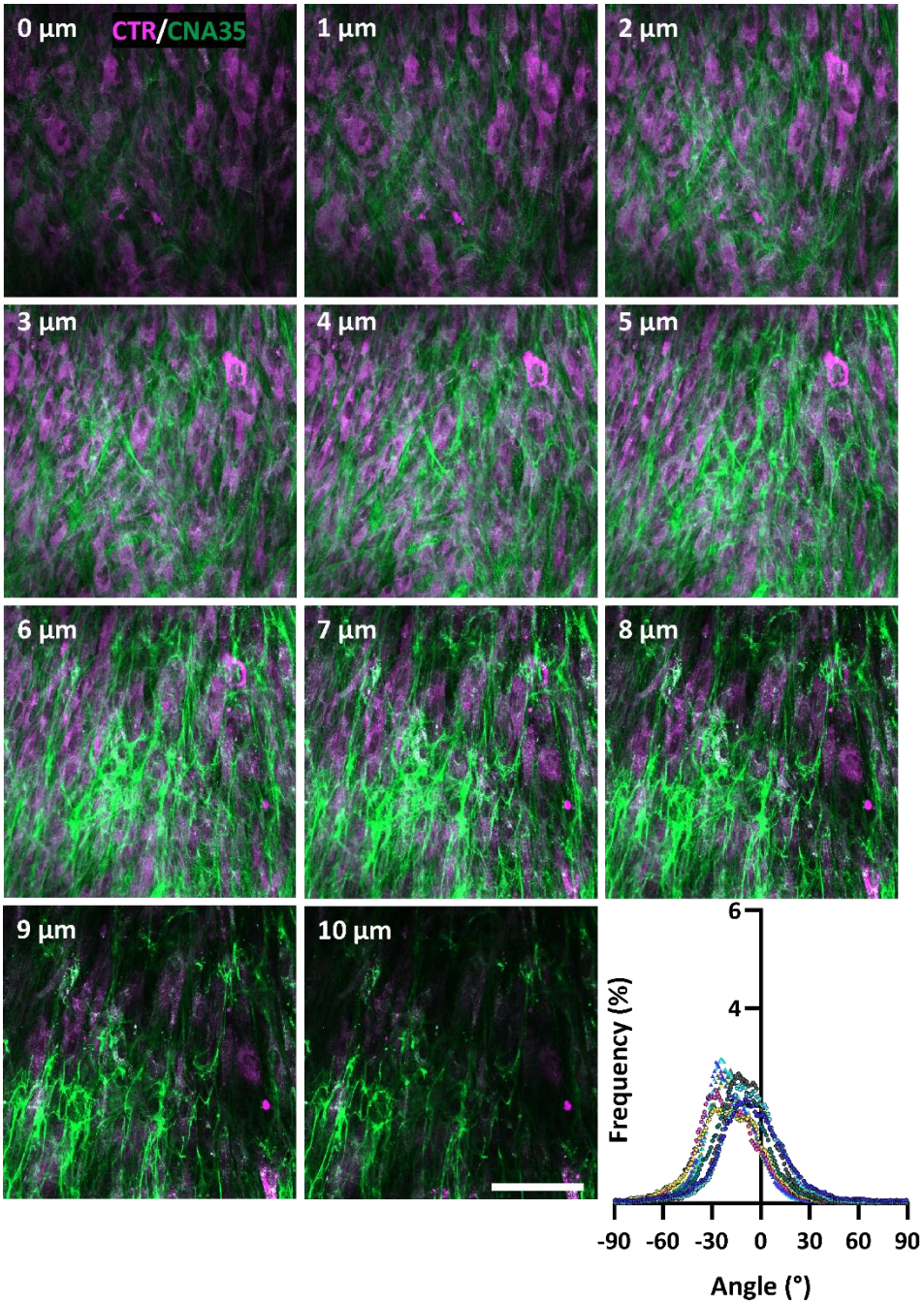


**Figure 3.23 Montage of 1 µm slices from a confocal Z-stack of hCFs cultured on glass for 28 days.** Cells were labelled with CTR (magenta) and collagen was labelled with CNA35 (green). 0 µm represents the cell layer closest to the glass substrate. Fibril orientation distribution of each layer normalised to the dominant direction at 0 µm is also shown. n = 1 biological replicate. Scale bar represents 100 µm.

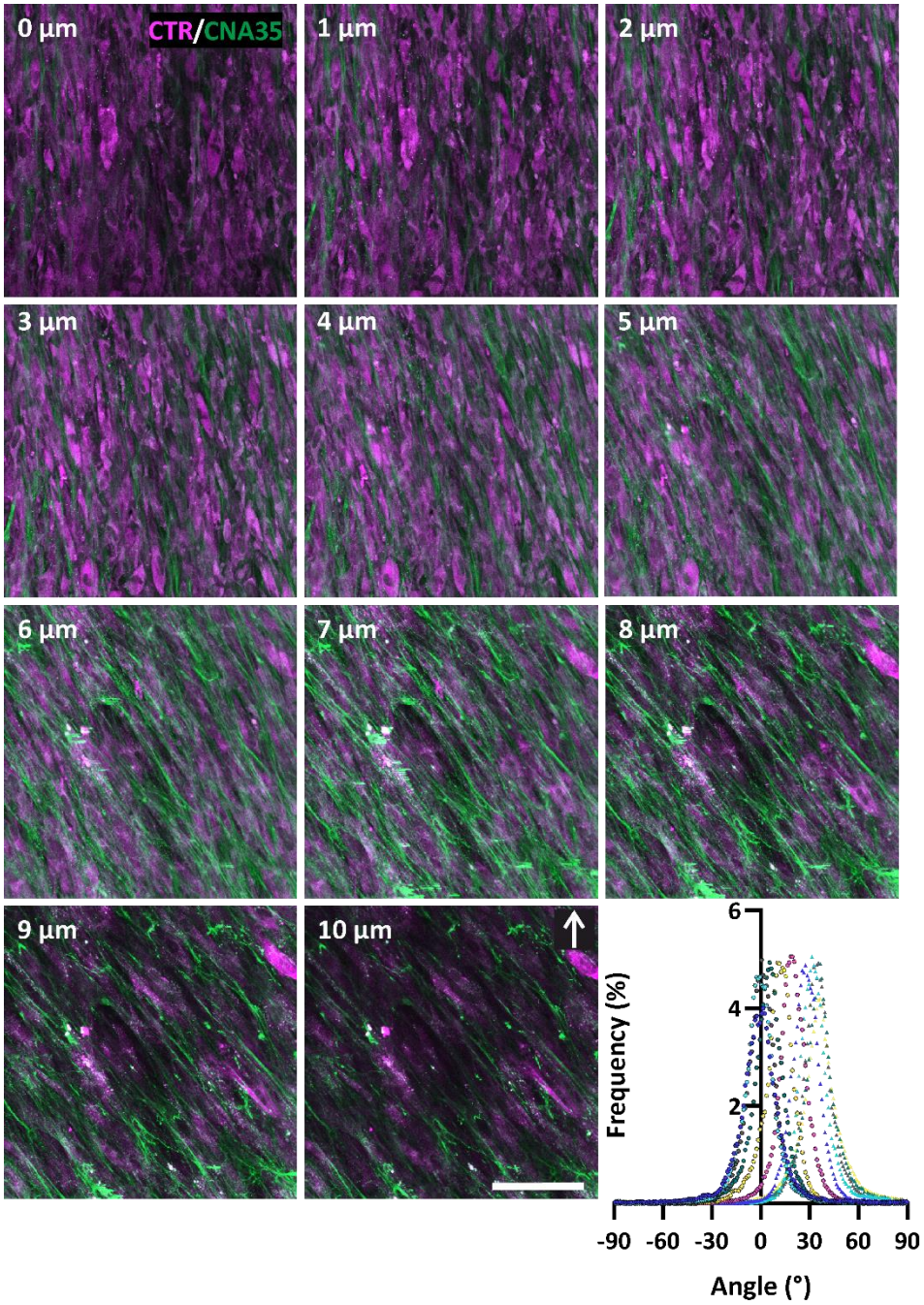


**Figure 3.24 Montage of 1 µm slices from a confocal Z-stack of hCFs cultured on PTFE-nf for 28 days and labelled with CTR (magenta) and CNA35 (green).** Images acquired show cells stratifying and depositing collagen with 0 µm representing the cell layer closest to the substrate. Fibril orientation distribution of each layer normalised to the direction of PTFE-nf is shown. White arrow represents direction of PTFE-nf. n = 1 biological replicate. Scale bar represents 100 µm.

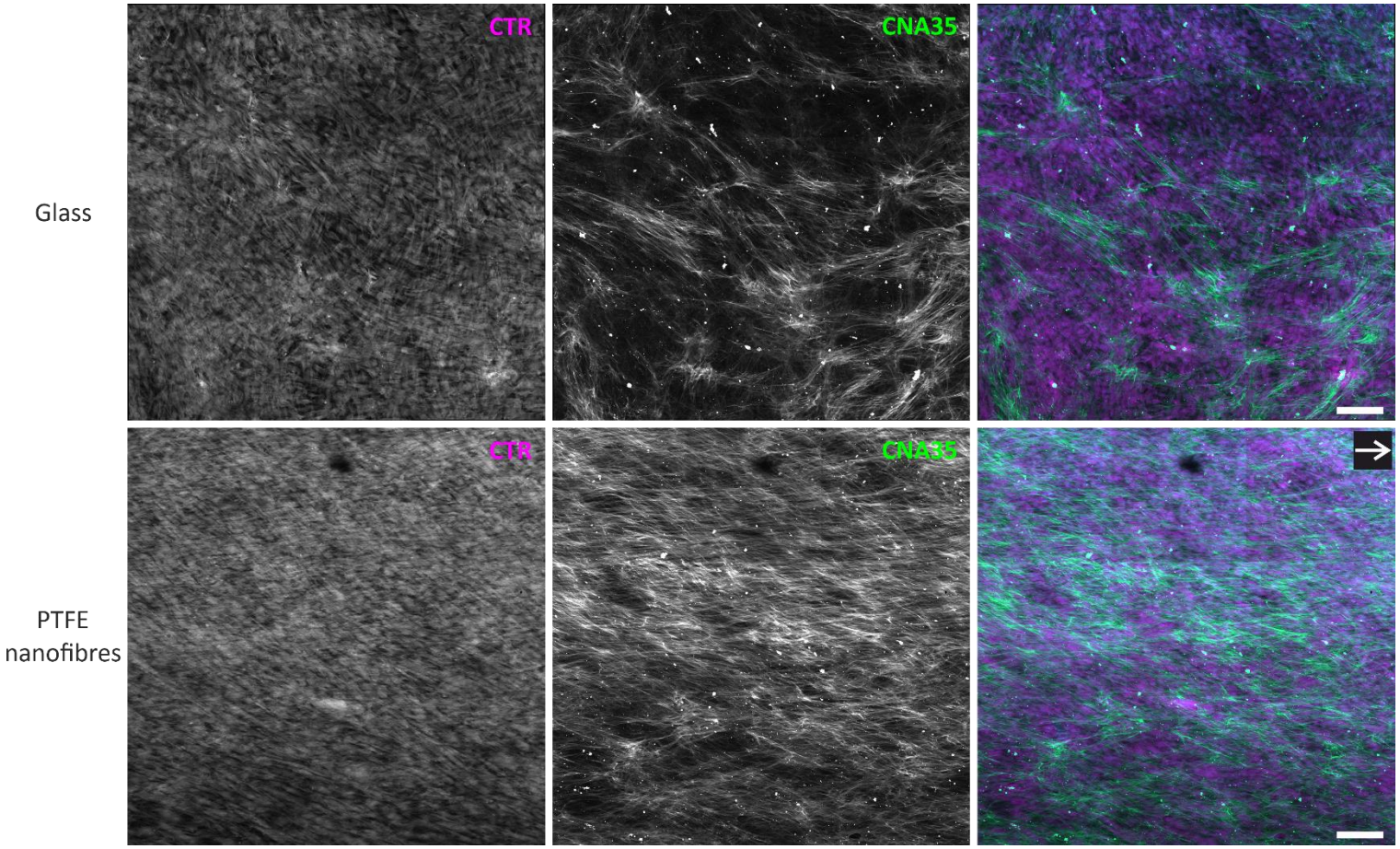


**Figure 3.25 ICC analysis of extracellular collagen deposited by hCFs cultured on glass and PTFE-nf for 30 days and labelled with CTR (magenta) and CNA35 (green).** Cells were co-stained with DAPI (blue) with the merged images also shown. Tiled images were acquired to show fibrillar collagen over a large field of view. White arrow on merged image represents the direction of the PTFE-nf. n = 1 biological replicate. Scale bars represent 200 µm.

### 3.5.3 Live cell imaging of collagen deposition

A model of the corneal stroma can be used for a variety of applications from evaluating the efficacy of drug treatments to understanding the mechanisms of wound healing. Live cell imaging of collagen deposition could enable the further understanding of collagen alignment and it was for this reason that PTFE-nf was selected as a substrate. Co-labelling hCFs with CTR and CNA35 enabled the visualisation of live cells, cultured on PTFE-nf, secreting collagen (Figure 3.26 A). At time point 0, there was no apparent collagen staining but hCFs had started to align parallel to the PTFE-nf. By hour 32, collagen could be clearly seen and this appeared to increase up to hour 64 (Figure 3.26 B). The distribution was normalised to the direction of the PTFE-nf and OrientationJ analysis showed a small, sharp peak around 0° which confirmed that the collagen was aligned at the start of imaging (Figure 3.26 C). As more collagen was deposited, alignment was maintained and appeared to slightly increase (Figure 3.26 D). The full time-series can be seen in Appendix G.

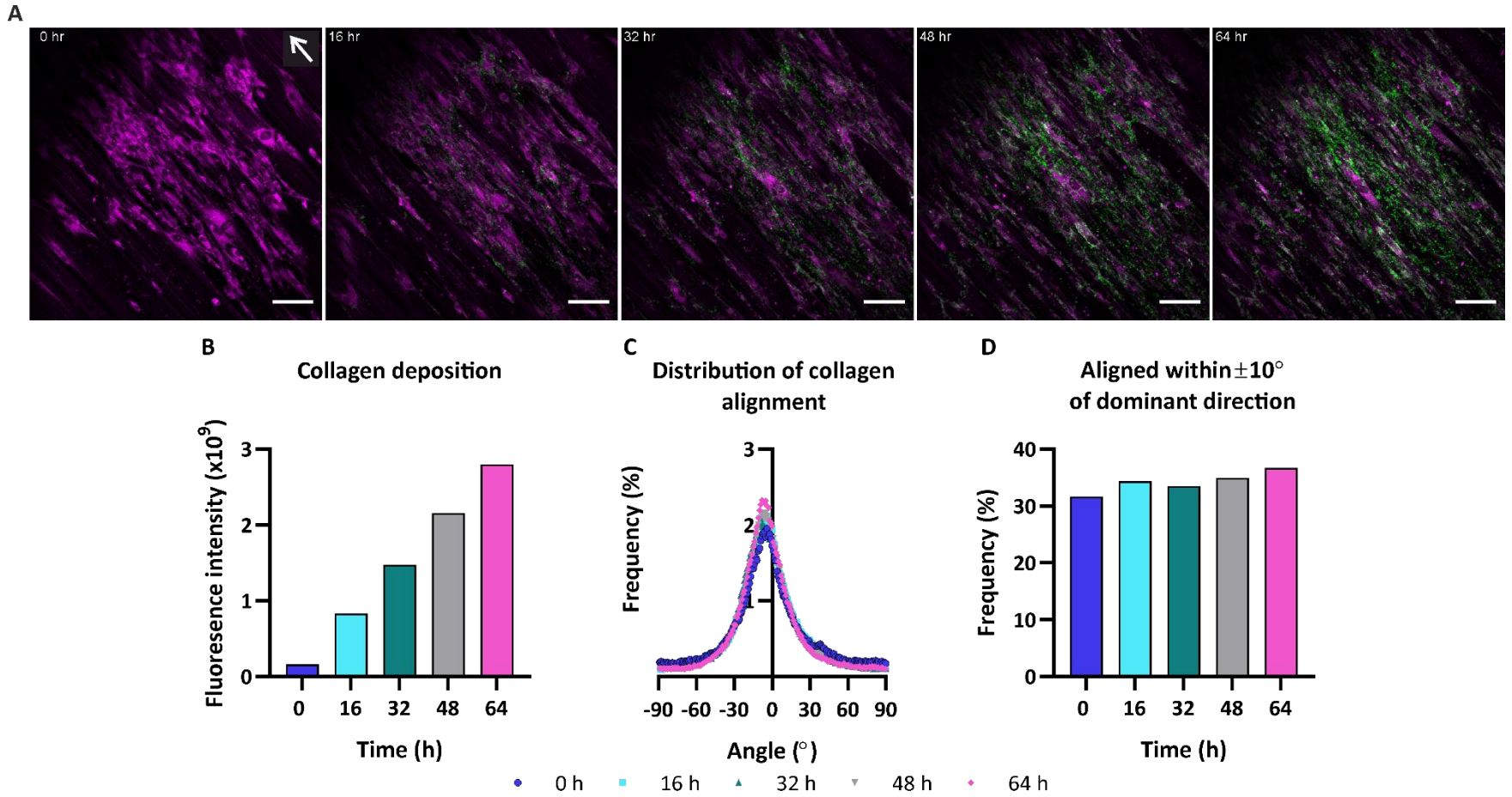


**Figure 3.26 Live cell imaging and analysis of hCFs cultured on PTFE-nf.** A: Images at 16-hour intervals are shown. Cytoplasm is labelled with CTR (magenta) and collagen is labelled with CNA35 (green). White arrow represents direction of PTFE-nf. Sale bars represent 100 µm. B: Fluorescence intensity shows that collagen increased with time. C: Normalised OrientationJ analysis shows collagen distribution over time. D: Distribution aligned within ± 10° of the PTFE-nf.

### 3.5.4 hMSCs in an *in vitro* model of the stroma

MSCs are a potential source of cells for corneal stroma engineering. Progenitor cells, such as hMSCs, can be differentiated into keratocytes and incorporated into *in vitro* models where they are reported to deposit an ECM that more accurately resembles the stroma (Du *et al.*, 2010; Syed-Picard *et al.*, 2015; Dos Santos *et al.*, 2019). Therefore, the potential of bone marrow-derived MSCs to differentiate into keratocytes and secrete an organised matrix were evaluated.

#### 3.5.4.1 hMSCs proliferated and expanded in both SCM and KDM

The growth and metabolic activity of hMSCs in differentiating medium was assessed and compared to cells cultured in SCM (Figure 3.27). There was no significant difference in cell number between media conditions at any of the time points, however there was greater variation between donors cultured in KDM (Figure 3.27 A). A logistic growth curve was applied to the data, this gave an $R^2$ value of 0.91 for the cells cultured in SCM but the variation between donors cultured in KDM resulted in a low $R^2$ value of 0.66.

No differences in the overall metabolic activity between the two culture conditions were observed across the 21-day period (Figure 3.27 B). The trend observed is similar to that seen in the growth curve with metabolic activity increasing up to day 14 before starting to plateau between days 14 and 21. To determine whether the observed increase in metabolic activity over time was because of the increase in cell numbers, the relative fluorescent units (RFU) per cell was calculated (Figure 3.27 C). No differences in the average metabolic activity per cell were observed however the variation between both donors and media conditions is reduced by day 7. The results here suggest that the average metabolic activity per cell is greatest at early time points, but varies between donors. However, because this is an average, and single cell metabolic activity was not assessed, it is not clear whether the increased metabolic activity at days 1 – 5 is as a result of a small sub-population of cells that are more metabolically active or if this is truly representative of the entire population.

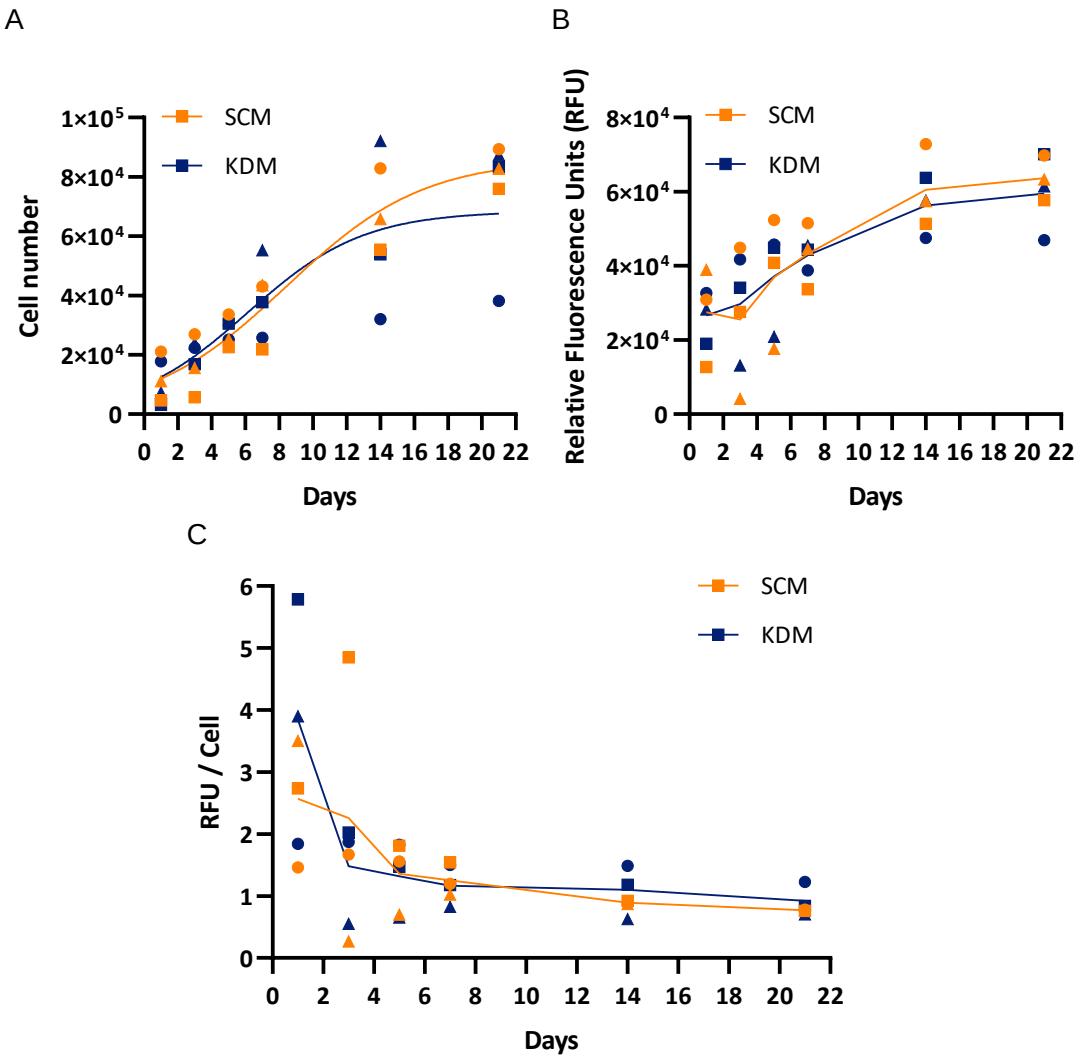


**Figure 3.27 Growth and metabolic activity of hMSCs over 21 days.** A: PicoGreen assay was used to compare the growth of hMSCs in KDM (blue) to those in SCM (orange). A logistic growth curve was applied. $R^2$ = 0.91 and 0.66 for SCM and KDM respectively. B: Cell metabolic activity was assessed using resazurin sodium salt colorimetric assay over 21 days. C: To take in to consideration the effect of an increase in cell number on the overall metabolic activity, the relative fluorescence was normalised to cell number. n = 3 biological replicates and the lines represent the mean. Where data were normally distributed a two-way ANOVA was performed otherwise a Kruskal-Wallis one-way ANOVA was performed. No significant differences were observed.

### 3.5.4.2 hMSCs formed spheres in KDM

The morphology of hMSCs undergoing differentiation in KDM was investigated via phase contrast microscopy (Figure 3.28). In both SCM and KDM, hMSCs cultured on glass appeared randomly oriented throughout the culture period whereas those cultured on PTFE-nf aligned parallel to the nanofibres. Interestingly, hMSCs cultured on PTFE-nf and in KDM started to detach from the substrate at day 7. This phenomenon progresses during the remaining 14 days of culture and areas with cell spheres are formed (Figure 3.28 inset).

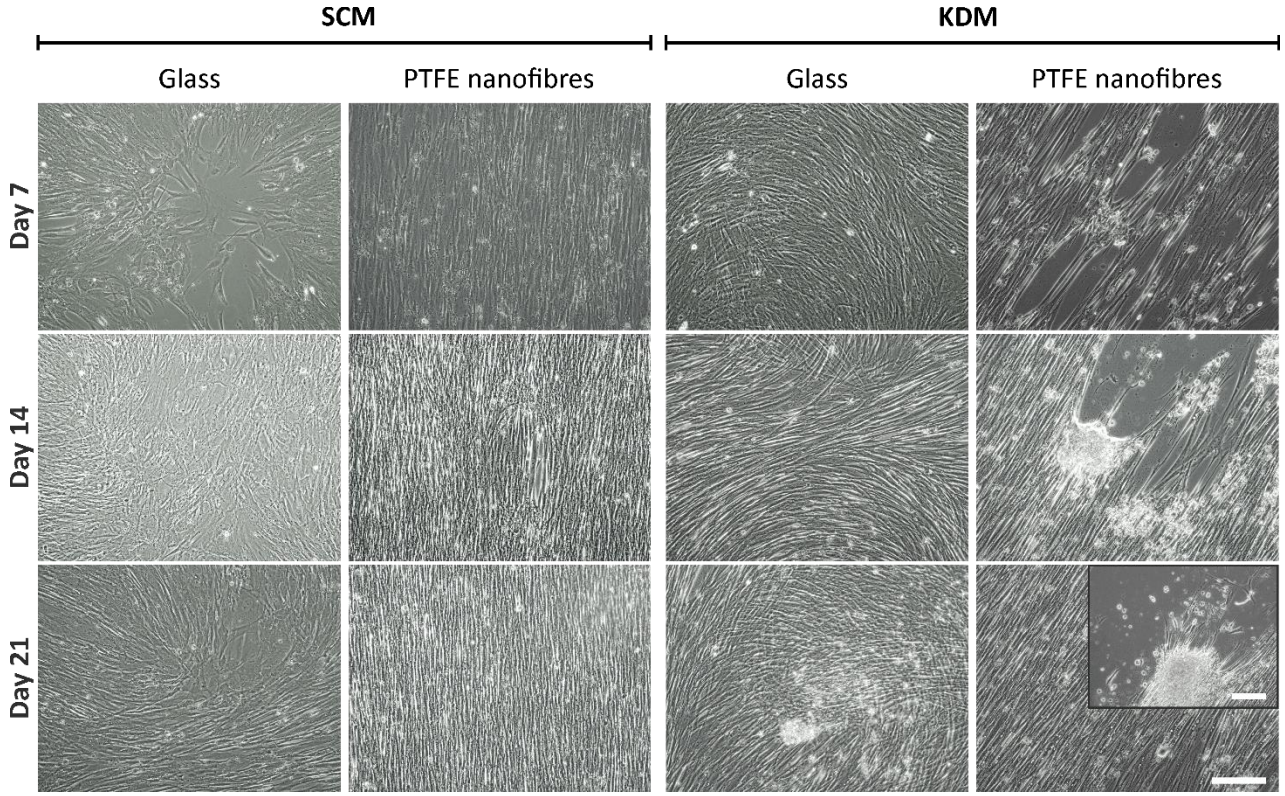


**Figure 3.28 Representative phase contrast images of hMSCs cultured in SCM or KDM.** Cells were cultured for 21 days on either glass coverslips or PTFE-nf. Cell contraction can be seen as early as day 7 with a cell cluster forming. This progresses throughout the culture period and amongst the aligned cells cell spheres can be seen at day 21 (inset). n = 2 biological donors. Scale bars represent 200 µm.

### 3.5.4.3 hMSCs cultured on Transwell membranes spontaneously formed cell spheres

In both media conditions hMSCs were observed forming spheres when cultured in Transwell membranes (Figure 3.29). These spheres were commonly observed when cells were cultured in KDM but sphere formation did occasionally occur when cultured in SCM.

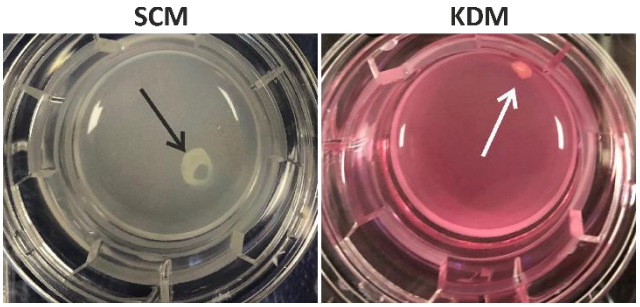


**Figure 3.29 Macroscopic image of hMSCs cultured on Transwell membranes for 7 days.** Cell spheres were occasionally formed when cultured in SCM (left; black arrow) and were often formed when cultured in KDM (right; white arrow).

### 3.5.4.4 hMSCs did not express keratocyte specific proteins

The expression of typical keratocyte markers (keratocan, lumican and CD34), in addition to proteins associated with fibroblasts (CD90) and myofibroblasts (α-SMA), were analysed using ICC. A summary of protein expression can be found in Table 3.6. On glass, hMSCs cultured in SCM showed little organisation (36%; n =3) (Figure 3.30). When cultured in differentiating medium (KDM), cells started to stratify and concentrate in small regions which again resulted in little alignment (38%; n = 3). F-actin staining revealed that as with hCFs, hMSCs cultured in SCM followed the topographical cues provided by the PTFE-nf and appeared to align accordingly (69%; n = 3) (Figure 3.31). However, the formation of pellets in KDM, as also observed in Figure 2.26, disrupted the alignment of hMSCs (42%; n = 3). Similar results were observed when cells were cultured on Transwell membranes with little alignment in both SCM (33%; n = 3) and KDM (30%; n = 3) (Figure 3.32).

hMSCs in KDM did not appear to express keratocan, with only diffuse staining observed in cells cultured on PTFE-nf, glass coverslips and on Transwell membranes (Figure 3.31, Figure 3.30 & Figure 3.32 respectively). A similar observation was made for CD34 when cultured on PTFE-nf and glass. Lumican was expressed ubiquitously on all substrates in both conditions; interestingly the expression appeared to be predominantly intracellular with little colocalization with collagens (CNA35; Figure 3.31 & Figure 3.30). IgG controls showed minimal non-specific staining (Figure 3.33).

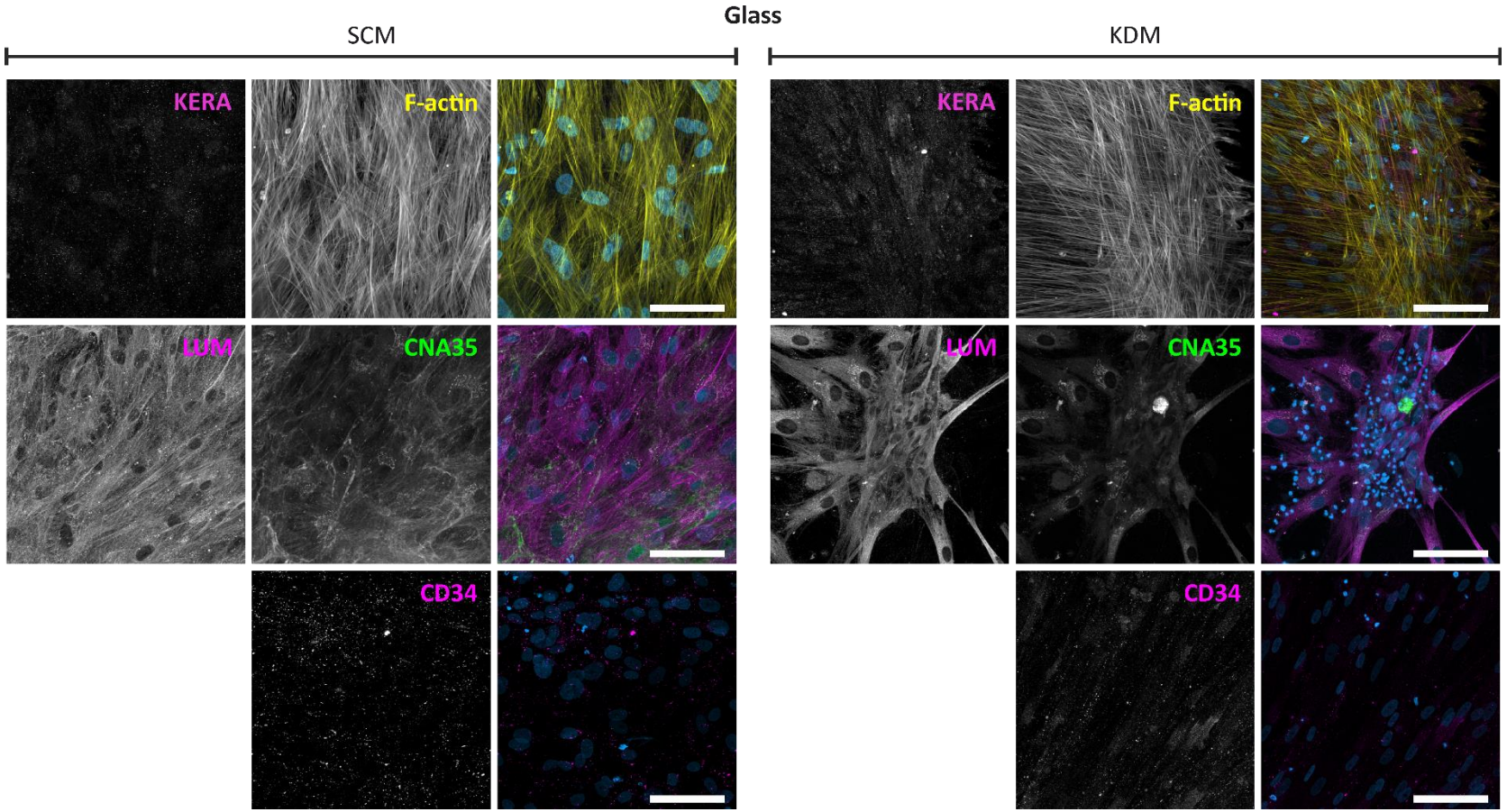


**Figure 3.30 Representative max. z-projections from ICC analysis of keratocyte markers expressed by hMSCs cultured on glass in differentiating (KDM) and control (SCM) media for 21 days.** Keratocyte markers: keratocan (KERA; magenta), lumican (LUM; magenta) and CD34 (magenta). Collagens were also labelled (CNA35; green). Cells were co-stained with phalloidin (F-actin; yellow) and DAPI (blue) and the negative controls are shown in (Figure 3.33). n = 3 biological replicates for all except CD34 where n = 2. Scale bar represents 100 µm.

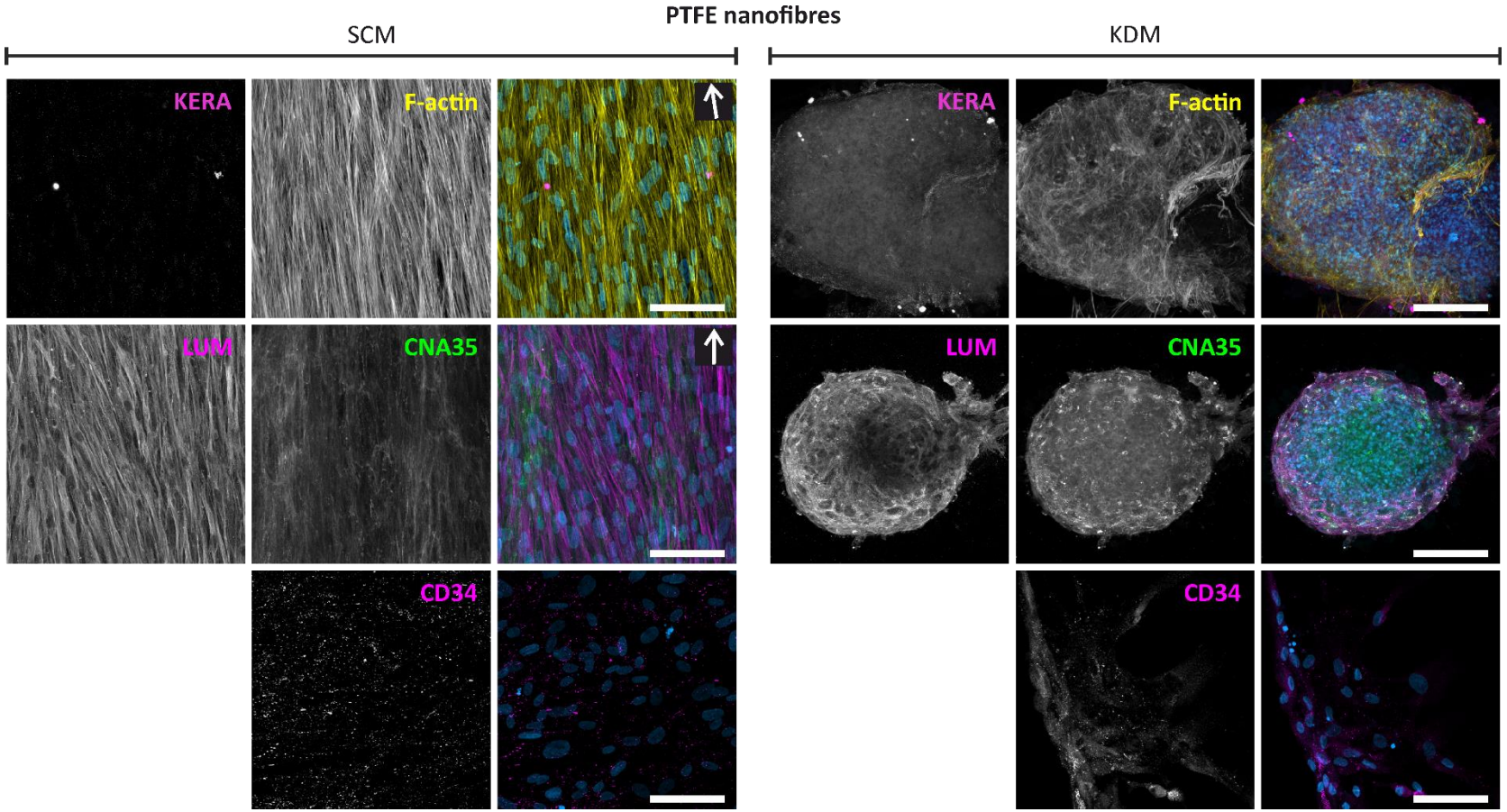


**Figure 3.31 Representative max. z-projections from ICC analysis of keratocyte markers expressed by hMSCs cultured on PTFE-nf in differentiating (KDM) and control (SCM) media for 21 days.** Keratocyte markers: keratocan (KERA; magenta), lumican (LUM; magenta) and CD34 (magenta). Collagens were also labelled (CNA35; green). Cells were co-stained with phalloidin (F-actin; yellow) and DAPI (blue) and the negative controls are shown in (Figure 3.33). n = 3 biological replicates for all except CD34 where n = 2. Scale bars represent 100 µm.

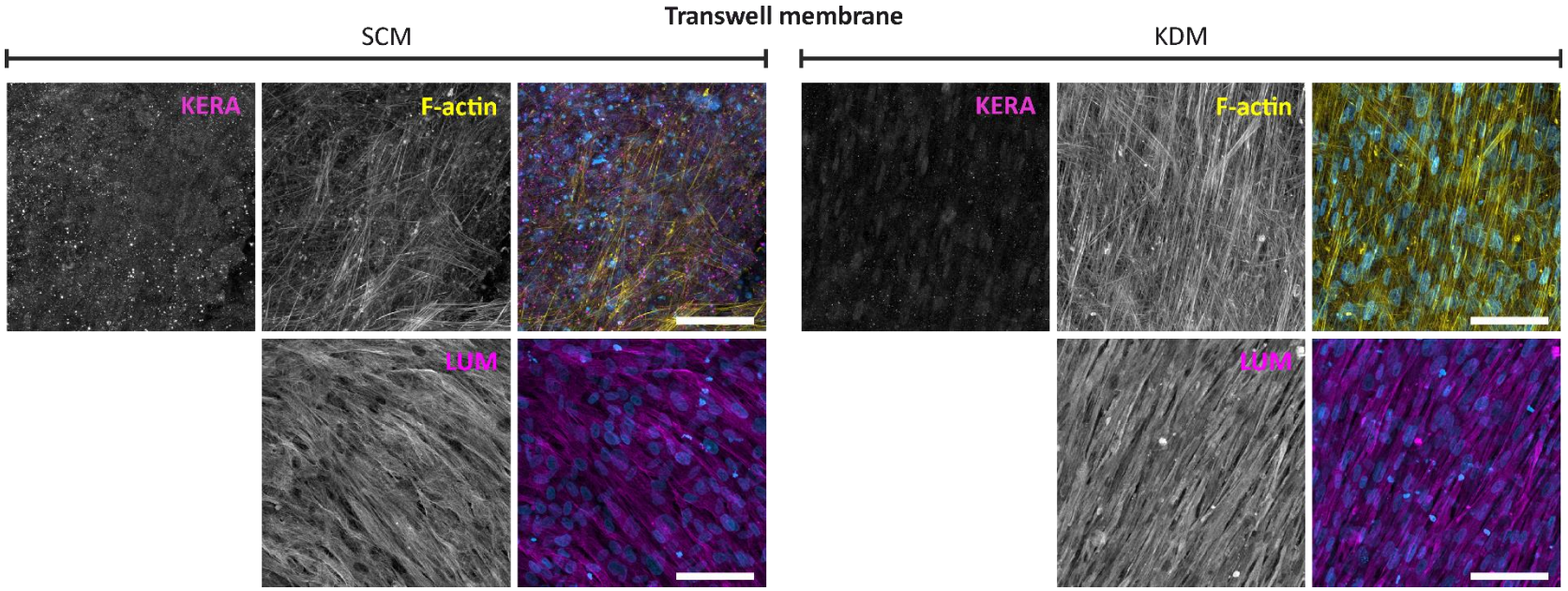


**Figure 3.32 Representative max. z-projections from ICC analysis of keratocyte markers expressed by hMSCs cultured on Transwell membranes in differentiating (KDM) and control (SCM) media for 21 days**. Keratocyte markers: keratocan (KERA; magenta) and lumican (LUM; magenta). Cells were co-stained with phalloidin (F-actin; yellow) and DAPI (blue) and the negative controls are shown in (Figure 3.33). n = 3 biological replicates. Scale bar represents 100 µm.

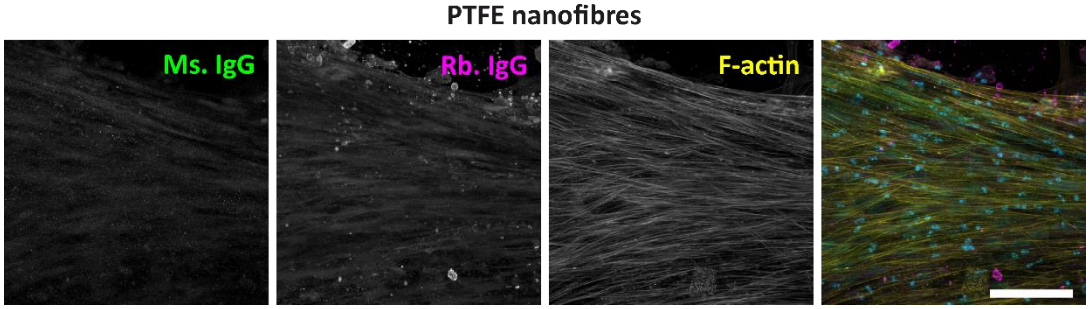


**Figure 3.33 IgG negative controls for mouse and rabbit primary antibodies on hMSCs cultured in KDM.** Cells were counterstained with phalloidin (yellow) and DAPI (blue) with the merged images also shown. n = 1 biological replicate. Scale bar represents 100 µm.

### 3.5.4.5 hMSCs exhibited varied deposition of collagens found in the stroma

Type I collagen was consistently expressed by hMSCs cultured in both SCM and KDM on all three substrates (Figure 3.34, Figure 3.35, Figure 3.36). A summary of collagen expression can be found in Table 3.6. Collagen types III and VI were also observed in hMSCs cultured in KDM on glass as the cells started to form pellets (Figure 3.34). Unfortunately, some pellets were lost during sample processing, leaving behind few remaining cells which may explain the absence of type V collagen. No expression of α-SMA was evident, with only non-specific staining observed but a low expression of CD90 could be seen. These findings differ to those cultured in SCM on glass where type V collagen expression was observed, alongside α-SMA. There was little deposition of type III collagen when hMSCs were cultured in SCM on glass. A-SMA is a marker for myofibroblasts, the wound repair phenotype found in corneal wounds, and is often expressed in conjunction with type III collagen, but this was not observed here.

hMSC pellets formed on PTFE-nf (in KDM) expressed collagen types I, V and VI but not type III collagen (Figure 3.35). There also appears to be expression of both CD90, a fibroblast marker, and α-SMA, a protein associated with myofibroblasts. Given the pelleted nature of the cells, it is hard to distinguish actin filaments and the apparent expression of α-SMA may be non-specific staining. hMSCs cultured in SCM displayed expression of collagen types I and V but not collagens type III and VI. A-SMA expression was also observed in SCM, with SMA fibres clearly distinguishable.

Cultures on Transwell membranes displayed similar expression to those on glass, with no type V collagen expression observed in KDM, but diffuse staining of the other collagens (Figure 3.36). Positive α-SMA expression was observed in hMSCs cultured in both KDM and SCM on Transwell membranes. As with cultures on glass, hMSCs in SCM on Transwell membranes expressed collagen types I, V and VI with diffuse type III collagen and were positive for CD90.

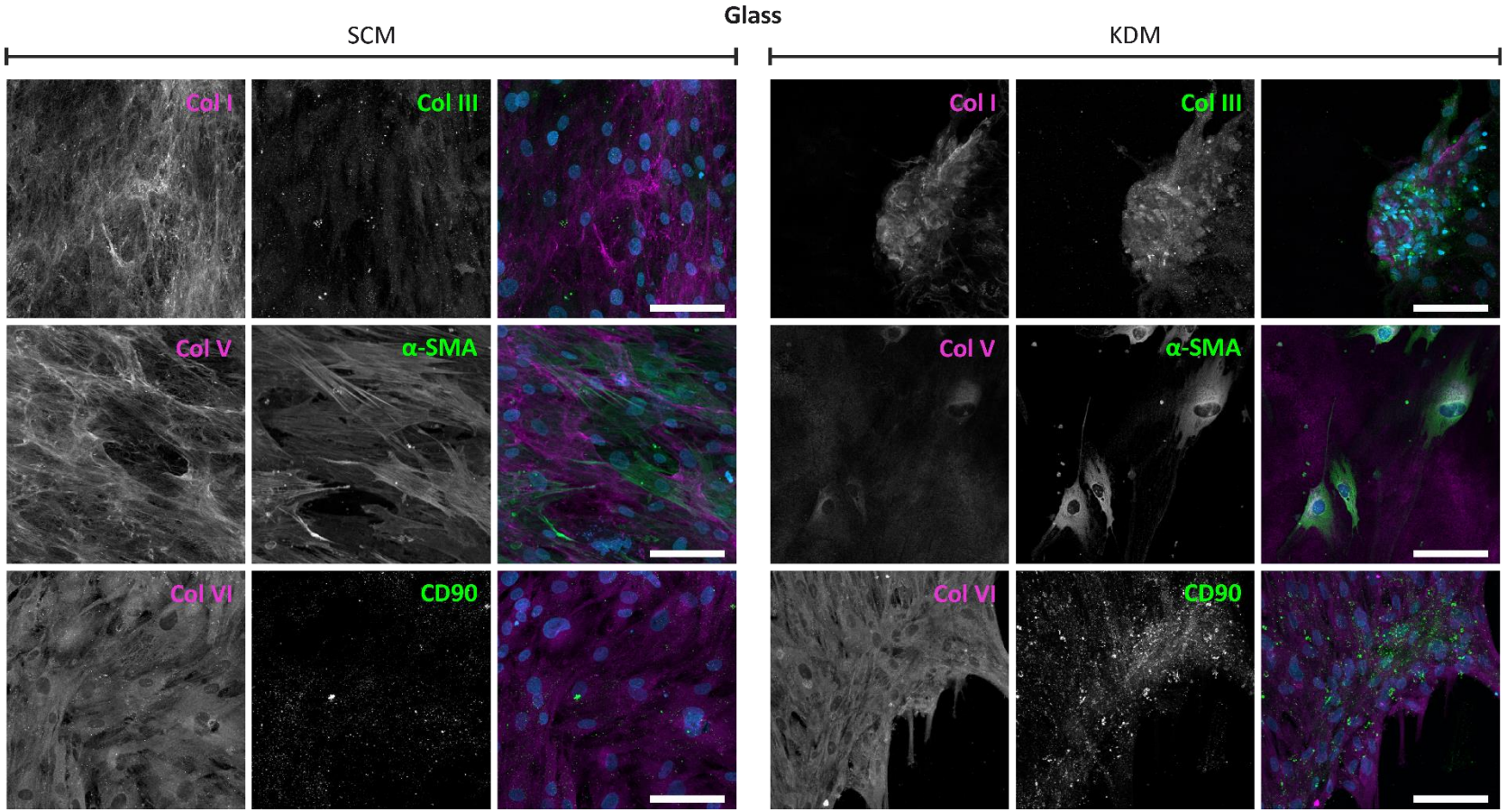


**Figure 3.34 Representative max. z-projections from ICC analysis of collagens and fibroblast markers expressed by hMSCs cultured on glass in differentiating (KDM) and control (SCM) media.** Cornea-specific collagen types I (Col I; magenta), V (Col V; magenta) and VI (Col VI; magenta). The expression of fibroblast and myofibroblast markers CD90 (green), type III collagen (Col III; green) and α-SMA (green) was also analysed. Cells were co-stained with DAPI (blue) and the negative controls are shown in (Figure 3.33). n = 2 biological replicates except for Col V, α-SMA and CD90 where n = 1. Scale bars represent 100 µm.

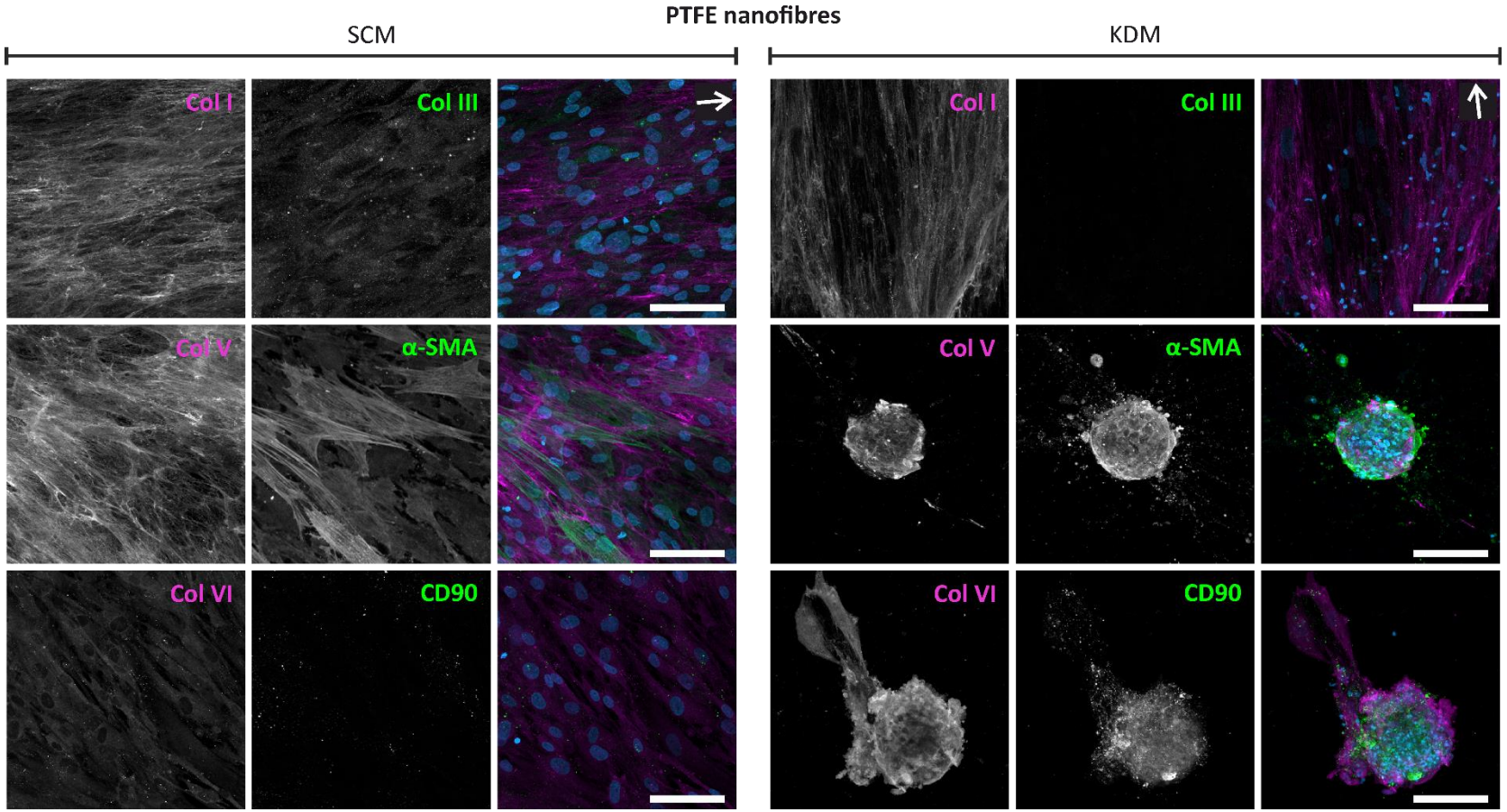


**Figure 3.35 Representative max. z-projections from ICC analysis of collagens and fibroblast markers expressed by hMSCs cultured on PTFE-nf in differentiating (KDM) and control (SCM) media.** Cornea-specific collagen types I (Col I; magenta), V (Col V; magenta) and VI (Col VI; magenta). The expression of fibroblast and myofibroblast markers CD90 (green), type III collagen (Col III; green) and α-SMA (green) was also analysed. Cells were co-stained with DAPI (blue) and the negative controls are shown in (Figure 3.33). n = 2 biological replicates except for Col V, α-SMA and CD90 where n = 1. Scale bar represents 100 µm.

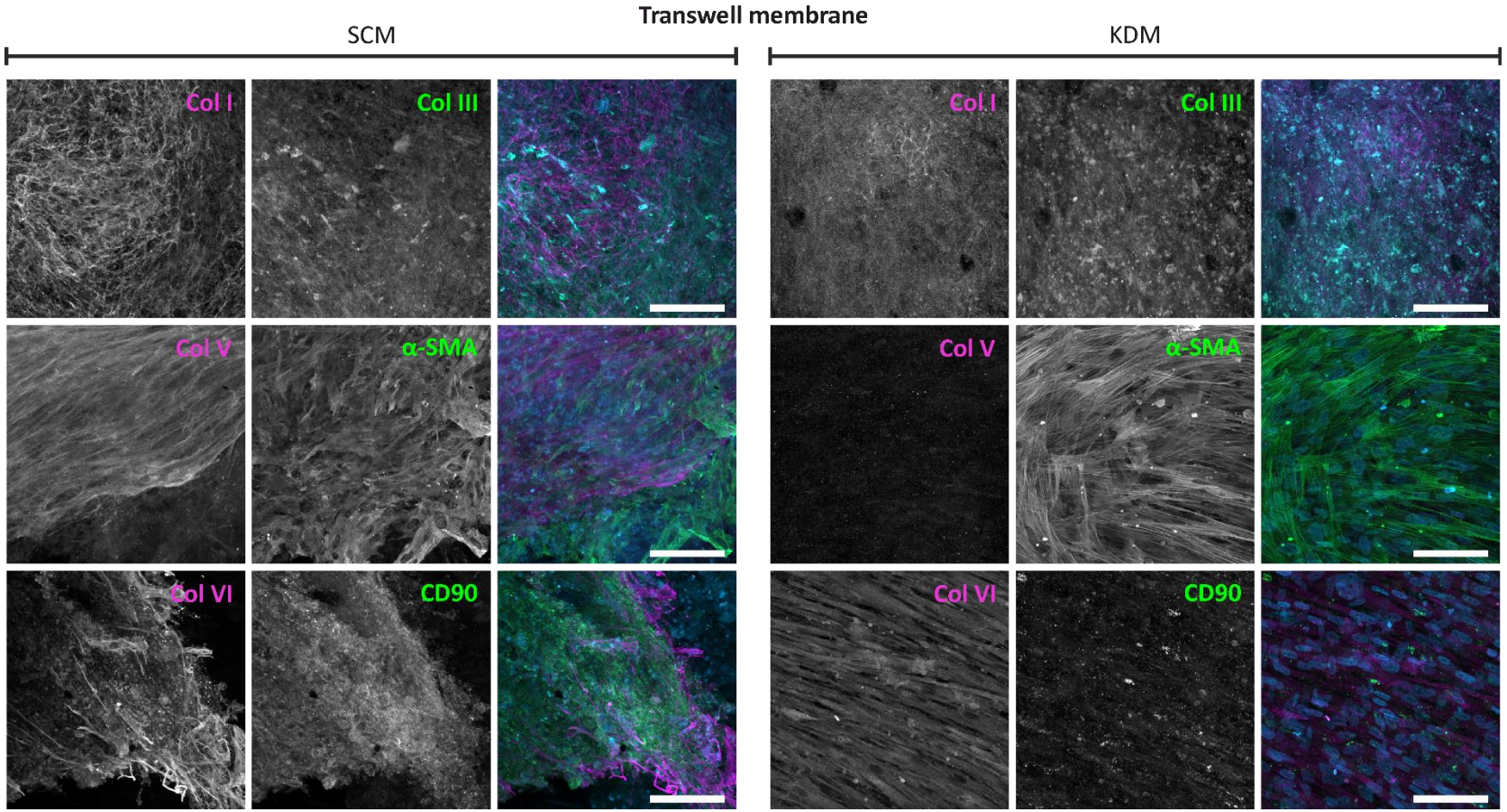


**Figure 3.36 Representative max. z-projections from ICC analysis of collagens and fibroblast markers expressed by hMSCs cultured on Transwell membranes in differentiating (KDM) and control (SCM) media.** Cornea-specific collagen types I (Col I; magenta), V (Col V; magenta) and VI (Col VI; magenta). The expression of fibroblast and myofibroblast markers CD90 (green), type III collagen (Col III; green) and α-SMA (green) was also analysed. Cells were co-stained with DAPI (blue) and the negative controls are shown in (Figure 3.33). n = 2 biological replicates. Scale bars represent 100 µm.

#### 3.5.4.6 hMSCs did not show an increase in keratocyte marker gene expression

Keratocytes are typically characterised by their expression of keratocan and lumican, as shown in the ICC data, but also their expression of aldehyde dehydrogenase (ALDH), prostaglandin D2 synthase (PTGDS), carbohydrate sulfotransferase 6 (CHST6) and aquaporin 1 (AQP1). To further characterise the hMSCs and to determine if hMSCs had the potential to differentiate towards the keratocyte lineage, gene expression analysis was used. RT-qPCR revealed that the expression of genes typically associated with keratocytes was not increased in hMSCs in KDM compared to those in SCM (Figure 3.37 A). The following, where Ct values exceeded 35 or were not obtained at all, have an n of 2: (SCM (Glass): LUM and COL3A1; KDM (Glass): ALDH3A1 and CHST6; SCM (PTFE-nf): COL6A1; and KDM (Transwell): ALDH3A1 and AQP1). For the majority of the keratocyte markers, no significant changes were observed between media nor between substrates. The expression of ALDH1A1 was reduced between hMSCs cultured in SCM on glass and Transwell membranes ($p = 0.0468$). The expression of collagens typically associated with the stroma (types I, V and VI) did not change much between media and substrate. Only the expression of COL5A1 increased between hMSCs cultured on PTFE-nf in SCM and those on Transwell membranes in KDM ($p = 0.0048$) (Figure 3.37 B). COL3A1 expression, a collagen associated with scar tissue within the stroma, was increased in cultures on Transwell membranes in KDM compared to hMSCs on glass in SCM ($p = 0.0317$), on PTFE-nf in SCM ($p = 0.0114$) and on PTFE-nf in KDM ($p = 0.0466$).

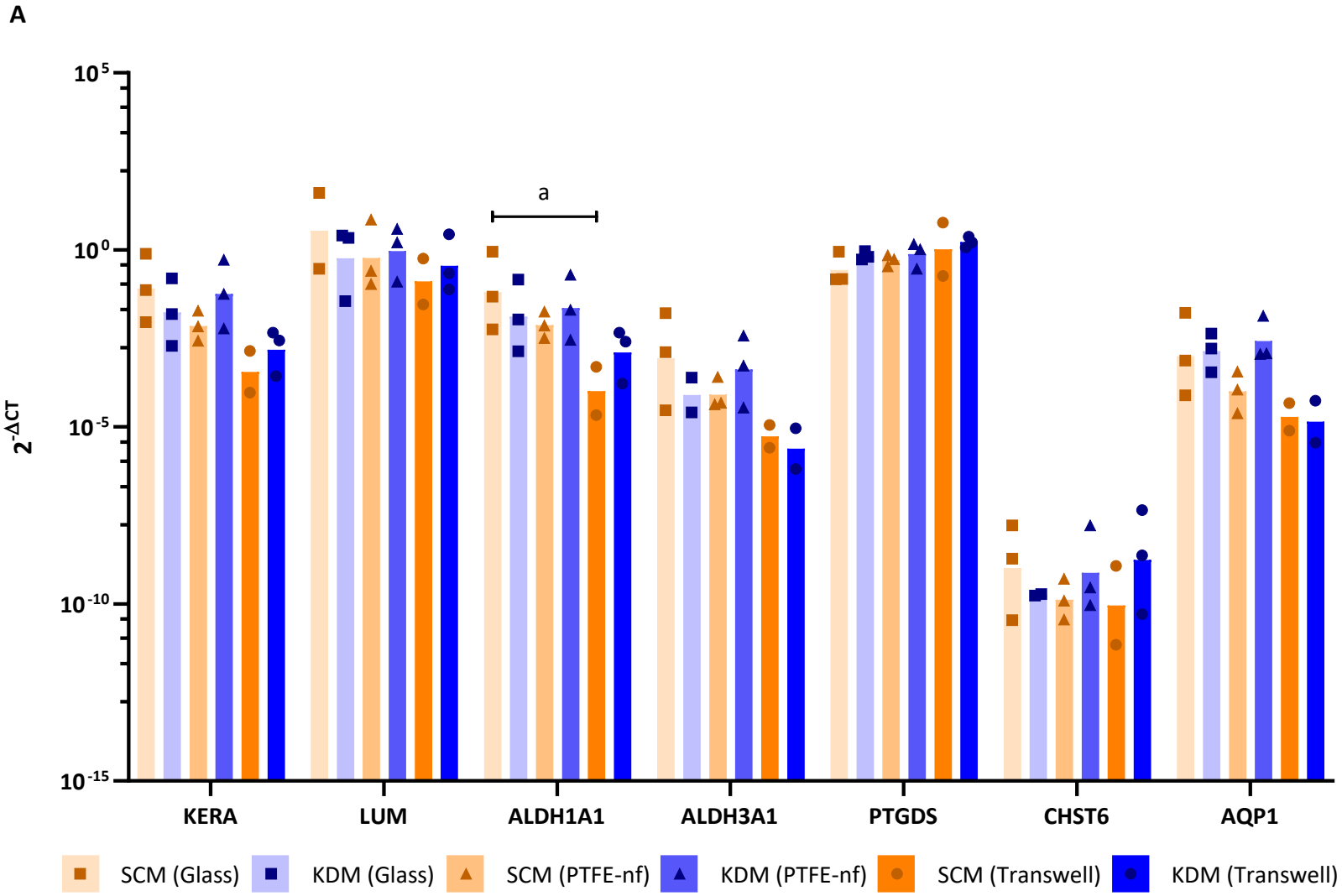
A
$10^5$
$10^0$
$10^{-5}$
$10^{-10}$
$10^{-15}$
$2^{-\Delta CT}$
a
KERA
LUM
ALDH1A1
ALDH3A1
PTGDS
CHST6
AQP1
SCM (Glass)
KDM (Glass)
SCM (PTFE-nf)
KDM (PTFE-nf)
SCM (Transwell)
KDM (Transwell)

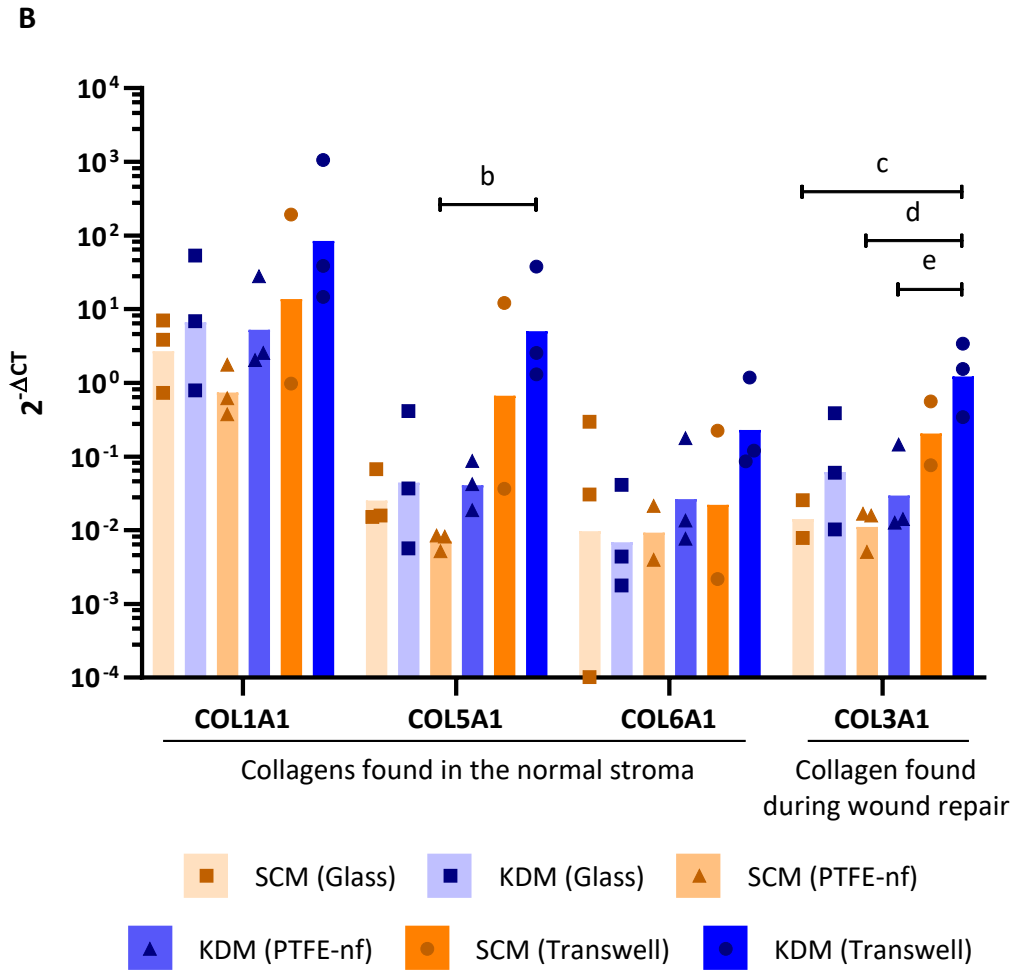


**Figure 3.37 Gene expression analysis of keratocyte markers and collagens in hMSCs.** hMSCs were cultured on glass coverslips (squares), PTFE-nf (triangles) or on Transwell membranes (circles) in either SCM (orange) or KDM (blue) for 21 days. A: The expression of typical keratocyte markers were analysed via qPCR. B: Expression of collagens were also analysed. Values are shown on a logarithmic scale and normalised to GAPDH. n = 3 biological replicates except for hMSCs in SCM on Transwell membranes, where n = 2. In some samples expression was undetectable and so n = 2 for the following: SCM (Glass): LUM and COL3A1; KDM (Glass): ALDH3A1 and CHST6; SCM (PTFE-nf): COL6A1; and KDM (Transwell): ALDH3A1 and AQP1. Bar represents the geometric mean. 2-way ANOVAs were performed on each gene after Box-Cox transformations. Multiplicity adjusted p values are reported: a = 0.0468; b = 0.0048; c = 0.0317; d = 0.0114; e = 0.0466.

**Table 3.6 Summary of results obtained from ICC analysis on hCFs and hMSCs. Protein expression (+ or -), % cells aligned, and comments are shown.**

| | Substrate | Col I | Col V | Col VI | Col III | Kera | Lum | CD34 | α-SMA | CD90 | % alignment* | Comments |
|---|---|---|---|---|---|---|---|---|---|---|---|---|
| **hCF** | Glass | + | + | + | - | N/A | N/A | N/A | - | N/A | 23 | |
| | PTFE-nf | + | + | + | - | N/A | N/A | N/A | - | N/A | 73 | Second alignment peak indicates rotation |
| | Transwell membrane | + | + | + | - | N/A | N/A | N/A | - | N/A | 35 | Broad distribution of orientations suggests some short-range alignment |
| **hMSC (SCM)** | Glass | + | + | + | - | - | + | - | + | - | 36‡ | |
| | PTFE-nf | + | + | - | - | - | + | - | + | - | 69‡ | |
| | Transwell membrane | + | + | + | + | - | + | N/A | + | + | 33‡ | Formed pellets |
| **hMSC (KDM)** | Glass | + | - | + | + | - | + | - | - | + | 38‡ | Formed pellets |
| | PTFE-nf | + | + | + | - | - | + | - | +† | + | 42‡ | Formed pellets |
| | Transwell membrane | + | - | + | + | - | + | N/A | + | - | 30‡ | Formed pellets |

*alignment within ± 10°; N/A, not assessed; †expression likely non-specific staining; ‡average alignment based on 1 ROI per donor.

## 3.6 Discussion

The aim of this chapter was to determine a suitable cell type and substrate for creation of an *in vitro* model of the corneal stroma. The results obtained in this study suggest that hCFs are a more suitable cell choice than hMSCs for the *in vitro* model. hCFs aligned parallel to the PTFE-nf, with the cells rotating as they stratify, mimicking the architecture of the stroma. hCFs were also shown to deposit collagen types I, V and VI whereas hMSCs did not consistently express type V collagen across all substrates. In addition, hMSCs cultured in KDM had the tendency to form cell pellets, despite the provision of topographical cues, thus losing the structure that resembled the stroma. Furthermore, differentiated hMSCs did not express the proteins nor proteoglycans that are used to characterise keratocytes, signifying that their differentiation was unsuccessful.

### 3.6.1 hCFs in an *in vitro* model

The corneal stroma is composed of aligned collagen fibrils which form lamellae that are oriented roughly orthogonally throughout. An ideal model of the stroma would be composed of an organised and aligned ECM, a result of cellular alignment which can be influenced by substrate nanotopography. There are a range of topographical cues that can be employed in tissue engineering, from pillars and pits to aligned grooves and fibres (Bettinger *et al.*, 2009; Nikkhah *et al.*, 2012). Topographical cues have been shown to influence the behaviour of cells from cell morphology and alignment to cell phenotype and gene expression (Myrna *et al.*, 2012; Nguyen *et al.*, 2016). The alignment of corneal stromal cells on an aligned microgrooved substrate has been shown to result in the deposition of aligned collagen fibrils, a result not always seen with other cell types (Guillemette *et al.*, 2009). The deposited matrix has a structure that more closely resembles that found *in situ*, compared to those cultured on randomly oriented substrates (Wu *et al.*, 2012). The structure and organisation of the matrix has been shown to affect the transparency of the constructs too, with a more organised ECM being more transparent (Guillemette *et al.*, 2009; Phu *et al.*, 2011). In this study three materials, glass, PTFE-nf and polycarbonate Transwell membranes, were compared to identify which could be used as a substrate for cells to emulate the stroma. Analysis of the PTFE coated coverslips created for the study confirmed the presence of nanofibres 5 – 30 nm in height whilst SEM of the Transwell membranes revealed the presence of parallel grooves, both of which could provide cues to the hCFs, as previously described (Gouveia *et al.*, 2013; Dimitrios Karamichos *et al.*, 2014). hCFs cultured on PTFE-nf were more aligned (72% within ± 10° of the dominant direction) than both those on Transwell

membranes (35%) and those on the glass coverslip control (23%). Furthermore, the deposited collagen types I, V and VI were all most aligned on PTFE-nf. The analysis of collagen alignment was performed on a single ROI on each biological sample and therefore does not consider the variability across each sample. Interestingly, the SEM images of Transwell membranes in this study suggests that these grooves were not consistent across the membrane, with small areas either absent of grooves or with a random, textured topography. This could explain the non-uniform alignment of hCFs cultured on Transwell membranes observed in this study. Pore size is also known to influence cell behaviour. The 0.4 µm pores in the Transwell membrane are approximately less than 0.1% the size of cells and the pores should, therefore, prevent transmigration (Chung *et al.*, 2018). Providing hCFs with aligned, linear nanotopography has previously been shown to prevent the transdifferentiation of hCFs to myofibroblasts, as characterised by the expression of a-SMA (Myrna *et al.*, 2012). In the present study, α-SMA filaments were not observed via ICC and so it was concluded that the staining was non-specific. However, to better image the deposited collagen, as opposed to intracellular collagen, the cells had not been permeabilised prior to ICC analysis. Although there have been reports of successful staining with the anti-α-SMA antibody without permeabilisation, there is a small possibility that if the cells were first permeabilised the staining would reveal more specific expression of α-SMA.

Ascorbic acid is thought to be essential for the deposition of collagen as it is an essential cofactor for both prolyl- and lysyl hydroxylases, required for the conversion of proline and lysine to hydroxyproline and hydroxylysine respectively (Gelse *et al.*, 2003). In the absence of hydroxyproline, the collagen triple helix cannot be formed and hydroxylysine is required for the cross-linking of collagen fibrils (Canty and Kadler, 2005; Eyre and Wu, 2005). Therefore, to stimulate the production of collagen, culture medium was supplemented with 1 mM of A2P as previously described (Guo *et al.*, 2007; Ren *et al.*, 2008; Gouveia *et al.*, 2013, 2017b; Foster *et al.*, 2015). Mammalian cells are typically exposed to concentrations in the range of 10 – 70 µM *in vivo* (Padayatty and Levine, 2016) yet, for the purpose of expanding cells, hCFs were not supplemented with ascorbic acid (Guo *et al.*, 2007; Gouveia *et al.*, 2017a). Whilst the absence of ascorbic acid is non-fatal, it is possible that these cells were not representative of normal, healthy corneal fibroblasts. 1 mM of ascorbic acid was used in this study as it approximates the ascorbic acid concentration in the cornea (0.22 mg/g, equivalent to 0.76 mM) (Ringvold *et al.*, 2000). The addition of ascorbic acid when hCFs were seeded into the *in vitro* model may have rescued the cells, returning them to a normal phenotype, or irreversible epigenetic alterations may have occurred. A resazurin

assay was used to confirm that the supraphysiologic concentration of ascorbic acid did not result in any cytotoxic effects, as has been previously reported (Clément *et al.*, 2001; Padayatty and Levine, 2016).

In the centre of the stroma, collagen lamellae are oriented roughly orthogonally. In the present study fibroblast layers formed an angle shift between 30° – 55° on PTFE-nf and between 18° – 77° on Transwell membranes, relative to the first layer of cells. The rotation of hCFs was observed as the cells stratified and is important not only for recapitulating the structure but, it may also provide mechanical support to the construct (Quantock *et al.*, 2015). This rotation has been reported before in hCFs but was not observed in dermal fibroblasts and it is thought to be an intrinsic characteristic of corneal stromal cells, involving cell-cell contact guidance (Guillemette *et al.*, 2009; Then *et al.*, 2011). The first layer of cells aligns along the topographical cues and it is likely that these cues are somehow propagated through the cell and result in multi-layered cell orientation. One possibility is that there is a change in the expression of integrins and cadherins in the first layer of cells that results in the subsequent alignment of the matrix and the second layer of cells (Le Saux *et al.*, 2020).

The degree of collagen alignment within the cornea varies depending on the depth (anterior or posterior) and nasal-temporal position. Collagen fibrils in the centre of the cornea are oriented roughly orthogonally whilst the shift in angle is reduced at the periphery (Aghamohammadzadeh *et al.*, 2004). In this study, hCFs were isolated from the corneoscleral rims, after a corneal button had been removed for transplantation. Here, in the peripheral cornea, the preferred direction of collagen fibrils has been shown to be circumferential at the limbal region. It may, therefore, be possible that stromal cells isolated from this region behave differently to those from the centre of the cornea, where collagen fibrils are oriented roughly orthogonally. Perhaps, if stromal cells were isolated from the centre of the cornea, the shift in angle would have been closer to 90°. Incorporating an aligned biological matrix as a positive control would help to confirm the observations made in this study. An aligned matrix, such as that found in tendon or the corneal stroma, would allow for comparisons to be drawn between the ECM deposited on PTFE-nf and Transwell membranes and that found *in vivo.* Furthermore, the alignment and rotation of hCFs on PTFE-nf could be directly compared to these tissues to determine the degree of alignment necessary to recapitulate the tissue. For example, if a decellularised corneal stroma were used as a control, it would be possible to determine the shift in angle necessary to recapitulate the centre/periphery of the cornea.

The results discussed here suggest that PTFE-nf is the superior substrate for the growth of a stroma equivalent, with the cells more strongly aligned (73%) than when cultured on Transwell membranes (35%). Furthermore, PTFE-nf supported the rotation of cells as they stratified, resembling the lamellae of the stroma.

#### 3.6.1.1 Comparison to other corneal stroma models

The hCF Transwell model was first established by (Guo *et al.*, 2007). It has since been used, with minor modifications, for several purposes from modelling a keratoconic cornea to investigating the stroma-nerve interaction in a diabetic corneal model (Karamichos *et al.*, 2012; Priyadarsini *et al.*, 2017b). In previous Transwell-based models, hCFs have been shown to stratify and create roughly orthogonal lamellae when supplemented with ascorbic acid (Guo *et al.*, 2007). Furthermore, hCFs in the Transwell model have been shown to deposit collagen types V and VI, which the data in the present study also supports (Guo *et al.*, 2007; Karamichos *et al.*, 2010). The deposition of type III collagen is typically associated with corneal fibroblasts cultured in media supplemented with 10% serum (as in the present study) and is upregulated when compared to keratocytes cultured in 1% serum (Karamichos *et al.*, 2013; Dimitrios Karamichos *et al.*, 2014). In the present study, the staining of type III collagen appears to be intracellular and is likely to be non-specific staining given that the hCF constructs were not permeabilised prior to ICC analysis. The staining is also of a similar level to the background staining seen in the IgG controls. This is further supported by a study which found little secretion of type III collagen by hCFs, unless stimulated with TGF-β1 (Karamichos *et al.*, 2010). As mentioned above, α-SMA fibrils were not observed in the Transwell model in this study. These data combined suggest that hCFs can be cultured long-term at a high cell density whilst maintaining their phenotype and not transdifferentiating into myofibroblasts.

The human corneal stroma is typically between 461.8 – 465.4 µm thick (Reinstein *et al.*, 2009). Although not measured in this study, the Transwell model typically ranges between 20 – 40 µm in thickness at 4 weeks, just a fraction of the thickness of the human corneal stroma (Guo *et al.*, 2007; Karamichos *et al.*, 2010; Dimitrios Karamichos *et al.*, 2014). Constructs cultured on Transwell membranes can be peeled and stacked to create a thicker construct, more representative of the entire corneal stroma (Priyadarsini *et al.*, 2017a). This technique has the potential to be a useful method for generating 3D constructs greater than 300 µm thick in under 4 weeks. However, when employed in the present study this method failed with the cell sheet breaking and contracting, showing it to be a particularly technically

challenging methodology. Other groups have reported the successful stacking of sheets of fibroblasts for the formation of a corneal model (Carrier *et al.*, 2009; Couture *et al.*, 2016). However, these models tend to focus on the formation of a construct that macroscopically resembles the cornea, with a stratified epithelium and minimal haze, and neglect mimicking the alignment of cells and ECM (Proulx *et al.*, 2010). The fibroblast sheets first used in the model of Carrier *et al.* were cultured in flasks prior to stacking, which would suggest that both the cells and the deposited collagen are randomly oriented, although the microarchitecture was not analysed. The stacking of corneal stromal cells adhered to electrospun nanofibres has also been used to model the stroma (Wilson *et al.*, 2012). Here, stromal cells were cultured on aligned nanofibres which were subsequently stacked at 90° to one another, with a filter paper ring acting as a spacer between the layers and a collagen hydrogel cast into the construct. The addition of nanofibres, providing topographical cues, improved the alignment of stromal cells. Stromal cells were also found to have a reduced expression of fibroblast and myofibroblast markers CD90 and α-SMA when cultured in this construct compared to those cultured on tissue culture plastic. However, collagen hydrogels typically have larger collagen fibrils and thus the microarchitecture of the corneal stroma would not be captured making it an unsuitable model (Saeidi *et al.*, 2012a).

PTFE-nf have previously been used as substrate for corneal stromal cells but with the addition of a peptide amphiphile coating (Gouveia *et al.*, 2013). Interestingly, despite the authors finding that the addition of a peptide amphiphile coating covered the PTFE-nf, creating an irregular topography, they found that cells successfully aligned. The present study not only confirmed the deposition of aligned collagen types I and V, as reported by Gouveia *et al.*, but revealed that PTFE-nf can support a shift in the alignment of collagen fibres (Gouveia *et al.*, 2017a). Gouveia *et al*. also showed that the sheets of aligned stromal cells could support the attachment of epithelial cells (Gouveia et al., 2017a). Whist not investigated in the present study, these previous findings suggest that hCFs cultured on PTFE-nf would support the growth of epithelial cells if the corneal model were to be developed further. The shift in alignment of collagen fibrils as hCFs stratify on PTFE-nf has not previously been reported and this model better resembles the corneal stroma.

Other attempts at creating a construct that can recapitulate the corneal stroma have focused on the use of hCSSCs. In the present study, isolation of hCSSCs was unsuccessful (Chapter 1) but others have reported that stimulating CSSCs cultured on aligned electrospun poly(ester urethane) urea with TGF-β3 results in the secretion of collagen with orthogonal orientation (Wu *et al.*, 2013). Simultaneously differentiating hCSSCs in KDM supplemented

with FGF-2 and TGF-β3 resulted in a construct approximately 70 µm thick, approximately 15% of the thickness of the human stroma (Wu *et al.*, 2013). Wu *et al.* directly compared hCSSCs and hCFs and their ability to create a structure that mimicked the corneal stroma (Wu *et al.*, 2014a). The authors showed the successful differentiation of hCSSCs to keratocytes and used ICC and histology to show that hCSSCs secreted more ECM and created thicker constructs. Second harmonic generation microscopy and TEM revealed the orthogonal orientation of collagen deposited by hCSSCs (Wu *et al.*, 2014a). This could suggest that perhaps the *in vitro* culture conditions of hCFs are not optimal for an *in vitro* model and that differentiating progenitor cells into keratocytes would be preferable.

### 3.6.2 Live cell imaging of collagen deposition

To date, the most common method of analysing collagen fibrillogenesis is through the use of fixed models. This often involves the fixation of cells (or tissue) and using electron microscopy, particularly transmission electron microscopy (TEM), to study collagen fibril secretion and formation (Kadler *et al.*, 1996). This, however, means that much of what is currently known about the secretion and deposition of collagen is based on static images which may only show part of the process. In order to look at fibrillogenesis dynamically Krahn *et al.* created a probe using a collagen binding domain (CNA) isolated from *Staphylococcus aureus* which binds to fibrillar collagens (Krahn *et al.*, 2006). This probe, CNA35, has been used to observe the initial secretion of collagen up to 52 h (Boerboom *et al.*, 2007). Here, the culture time was extended to 64 h and hCFs were cultured on PTFE-nf to induce the alignment of cells and collagen. Over time, the deposition of collagen continued to increase and was somewhat aligned in the direction of the nanofibres. The percentage of aligned collagen fibrils did not greatly increase over the 64 hours but this, combined with the ICC analysis of hCF alignment suggests that as the cells proliferate it remodels and aligns the deposited collagen. The use of CNA35 in the corneal stroma model can provide further insight in to the mechanisms behind collagen fibrillogenesis. This method is a much simpler technique than other reported methods for the live cell imaging of collagen fibrillogenesis, such as the tagging of type I collagen using GFP-tagging or tagging with a photoswitchable protein Dendra2; though, the photoswitchable nature of Dendra2 does enable the differentiation of old and new fibrils (Pickard *et al.*, 2018). Although not investigated in this study, the stroma model could also be used to investigate cell stratification and to reveal at what point the shift in cell orientation occurs.

### 3.6.3 hMSCs in an *in vitro* model

The potential of stem/progenitor cells to differentiate into keratocytes has been explored for both tissue engineering (Du *et al.*, 2010; Wu *et al.*, 2013) and wound healing purposes (Du *et al.*, 2009). Along with CSSCs (Syed-Picard *et al.*, 2016), adipose-derived MSCs (Du *et al.*, 2010), bone marrow-derived MSCs (Dos Santos *et al.*, 2019), umbilical cord stem cells (Dos Santos *et al.*, 2019) and dental pulp stem cells (Syed-Picard *et al.*, 2015) have all shown some potential to differentiate into keratocytes after culture in KDM.

Bone marrow-derived MSCs have previously been used in corneal stroma research and have shown the potential to differentiate into keratocytes both *in vitro* and *in vivo,* hence their use in the present study (Liu *et al.*, 2012; Park *et al.*, 2012; Dos Santos *et al.*, 2019). Bone marrow-derived MSCs have been intrastromally transplanted into keratocan-null mouse corneas where they differentiated into keratocytes, expressing keratocan with a dendritic cell body (Liu *et al.*, 2012). *In vitro* studies have included the culturing of MSCs in keratocyte-conditioned culture media which resulted in an increased expression of lumican and ALDH1A1 (Park *et al.*, 2012). Recently, bone marrow-derived MSCs differentiated in KDM, media supplemented with TGF-β3 and FGF-2, showed an increase in the gene expression of CHST6 (involved in keratan sulphate biosynthesis) compared to undifferentiated cells (Dos Santos *et al.*, 2019). The growth factors FGF-2 and TGF- β3 have both been used to differentiate corneal stromal stem and stem-like cells into keratocytes (Wu *et al.*, 2013; Sidney and Hopkinson, 2018). FGF-2 reportedly stimulates cells to secrete aligned collagen fibrils in a single direction and TGF-β3 induces stratification and orthogonal rotation of cells (Wu *et al.*, 2013; Sidney and Hopkinson, 2018). However, it is important to remember that bone marrow-derived MSCs are progenitors of skeletal tissue such as bone, cartilage and adipocytes and they may be susceptible to differentiating down one of those three lineages (Bianco *et al.*, 2001). FGF-2 can, in fact, enhance the osteogenic differentiation potential of bone marrow-derived MSCs, which may explain the pellet formation observed in this chapter (Zellin and Linde, 2000; Luong *et al.*, 2012).

Previously, progenitor cells have been pelleted or cultured in a fibrin gel prior to keratocyte differentiation (Du *et al.*, 2010; Syed-Picard *et al.*, 2015; Yam *et al.*, 2018). The differentiation of MSCs to keratocytes was successful in a 3D system but alignment was not assessed (nor evident) in these models. In order to mimic the highly organised structure of the corneal stroma the cells require topographical cues to induce alignment. Therefore, the present study investigated culturing hMSCs on PTFE-nf and polycarbonate Transwell membranes to induce the deposition of an aligned and organised matrix. hMSCs were

observed to form spheres when cultured in KDM on both PTFE-nf and Transwell membranes, although pellets were also formed in SCM on Transwell membranes. The formation of spheres on a substrate prepared with topographical cues is unusual, with previous studies reporting the successful differentiation of stem cells and the creation of a cell sheet, representative of a lamella within the stroma (Karamichos *et al.*, 2011; Syed-Picard *et al.*, 2015). Bovine keratocytes can form spheres under adherent conditions unlike human keratocytes where spheres only tend to form in low attachment conditions (Scott *et al.*, 2011). Moreover, the phenotype of bovine keratocytes can be enhanced when cultured as a sphere, as assessed by the expression of keratan sulphate (Funderburgh *et al.*, 2008). Whilst these results may suggest that the formation of a sphere is indicative of a keratocyte phenotype *in vitro*, both protein and gene expression analysis suggest differentiation was unsuccessful. An alternative explanation is that as the cells in KDM proliferated they contracted, resulting in detachment from the substrate. As there was no significant difference between the number of cells cultured in SCM compared to those in KDM, the detachment of cells may not be solely influenced by cell proliferation. It is worth noting, however, that cell pellets may have been lost during media changes resulting in a reportedly lower cell number. The addition of a Rho-associated coiled-coil kinase (ROCK) protein inhibitor to the culture of bone marrow-derived MSCs has been shown to inhibit the detachment of cell sheets *in vitro* (Nakamura *et al.*, 2014). Furthermore, ROCK-inhibitors have been shown to decrease the number of focal adhesions formed (Nakamura *et al.*, 2014). It could be possible that the culturing of hMSCs in KDM increased the number of focal adhesions. This would increase the contractile force, resulting in the detachment of the cell sheet and the formation of cell spheres. Although not investigated in the present study, the number of focal adhesions may have been greater in KDM cultures. The main hypothesis here is a combination of the above-mentioned suggestions. The hMSCs attached to the substrate, forming focal adhesions whilst continuing to proliferate. As the cells increased in number, a large concentration of sticky matrix molecules such as glycoproteins and GAGs were secreted. At the same time, contractile forces (arising from α-SMA) were exerted by the cell and resulted in the detachment of the cell sheet from the substrate below. Once the cell sheet had detached, the cells bound to the matrix molecules and formed pellets. The addition of a ROCK-inhibitor (Y-27632) has been shown to reduce the TGF-β1-induced expression of α-SMA in corneal keratocytes, suggesting supplementing the medium with Y-27632 could also prevent the differentiation of cells to a myofibroblast phenotype (J. Chen

*et al.*, 2009). ROCK inhibitors may prevent pellet formation and alter the phenotype of the differentiated hMSCs from myofibroblasts to a more keratocyte-like phenotype.

Keratocytes are typically characterised based on their dendritic morphology and the expression of genes, including keratocan (KERA), lumican (LUM), aldehyde dehydrogenase 3A1 (ALDH3A1), carbohydrate sulfotransferase (CHST6) and prostaglandin D2 synthase (PTGDS) (Wu *et al.*, 2013). The protein expression of keratan sulphate and collagen types I, V and VI are also used to characterise keratocytes (Carlson *et al.*, 2005; Pei *et al.*, 2006; Wu *et al.*, 2012). The positive expression of the above-mentioned proteins and proteoglycans along with negligible expression of α-SMA and type III collagen would suggest that the hMSCs had been successfully differentiated in the present study. Unfortunately, both ICC analysis and RT-qPCR revealed that keratocan was not expressed by hMSCs in KDM. Similarly, ALDH1A1 and ALDH3A1 were not expressed, as determined by RT-qPCR. Lumican was expressed by cells in both KDM and SCM, but this may be explained by bone marrow-derived MSCs also expressing lumican (Friedl *et al.*, 2007). The lack of evidence for hMSCs differentiating into keratocytes in the present study may be due to several factors. One such explanation may be that as the hMSCs were not used at very low passages (P4) they may have undergone phenotypic drift and started to differentiate down another lineage. Lumican is also associated with chondrocytes and chondrogenic differentiation (Friedl *et al.*, 2007). Furthermore, collagen types III and VI contribute to the matrix within cartilage, with ICC analysis suggesting both of these proteins are expressed in the control (SCM) cultures on Transwell membranes (Eyre, 2001). It is possible that hMSCs differentiated into another cell type, such as chondrocytes. What is unclear is whether this occurred prior to the start of the experiment, or if the long culture period of confluent cells in SCM resulted in the differentiation of MSCs. The characterisation studies in Chapter 2 (2.5.3.3) showed that at a later passage (P3 – 4) the cells were far outside the criteria set out by the ISCT, but they still displayed trilineage differentiation potential. If the hMSCs had started to differentiate, it could explain why the treatment with KDM was unsuccessful and why lumican was expressed, as this is expressed by chondrocytes. Interestingly, when cultured on the Transwell membrane, type III collagen and α-SMA were expressed by hMSCs in both KDM and SCM, indicative of myofibroblast formation (Funderburgh *et al.*, 2003). It has been shown that bone marrow derived-MSCs applied to a corneal wound model differentiate into myofibroblasts, characterised by the expression of α-SMA (Ye *et al.*, 2006). Given the positive expression of α-SMA and type III collagen observed, it could be suggested that the

environment within the Transwell cultures mimicked that of a wound environment resulting in myofibroblast differentiation of hMSCs, but not hCFs.

#### 3.6.3.1 The role of stiffness on keratocyte phenotype

Substrate stiffness is another material property that, along with topographical cues, can regulate cell phenotype (Chen *et al.*, 2020). Corneal stromal cells cultured on stiff substrates, such as tissue culture plastic (> $10^6$ kPa), have a decreased expression of ALDH3A1, ALDH1A1, CD34 and lumican when compared to a substrate with a stiffness similar to the corneal stroma (25 kPa) (Chen *et al.*, 2020). Moreover, an increase in α-SMA expression is seen when corneal fibroblasts are cultured on tissue culture plastic compared to those on more compliant substrates (Dreier *et al.*, 2013b). With the PTFE-nf used in this study being coated on a glass coverslip, the stiffness of the substrate is much greater than the physiological stiffness of the human corneal stroma. It is, therefore, possible that the stiffness of the glass substrate may have hindered the ability of the MSCs to differentiate into keratocytes. Furthermore, the stiffness of the substrate may contribute to the formation of cell spheres as opposed to the creation of a cell sheet. Cells form larger, more stable focal adhesions on stiffer matrices resulting in an increase in contractile forces exerted by the cell onto the surrounding matrix (Wells, 2008). These forces can ultimately lead to the detachment of the cell sheet and a reorganisation of the deposited matrix, resulting in the formation of a sphere (Fukamizu and Grinnell, 1990; Nakamura *et al.*, 2014). This also applies to the Transwell membranes and the same explanation can be used for the inability to differentiate hMSCs on the Transwell membranes. Whilst the stiffness of the polycarbonate Transwell membrane was not measured in this study, polycarbonate has been reported to have a similar stiffness to glass ( > $10^6$ kPa) (Jee and Lee, 2010; Lauridsen and Gonzalez, 2017). This effect may have been enhanced by the initial high cell number used in this experiment; more cells exert contractile forces on the deposited ECM resulting in the detachment of the cell sheet.

## 3.7 Conclusions

In this study, hCFs and hMSCs were cultured on two substrates (PTFE-nf and polycarbonate Transwell membranes), and assessed for their use in an *in vitro* model of the corneal stroma. hCFs aligned parallel to PTFE-nf, depositing an organised matrix which resembled the corneal stroma. Furthermore, a shift in the orientation of hCFs was observed as the cells stratified, further mimicking the ECM of the corneal stroma. Although there was evidence of some cell alignment on the Transwell membranes, this was not uniform across the sample, as shown

by the broad distribution of angles. hMSCs could not be successfully differentiated into keratocytes, perhaps because cells were not used at very low passages in this study. The formation of cell pellets on all three substrates when cultured in KDM is likely a result of the unsuccessful differentiation but a less stiff substrate may support the growth of differentiated cells.

The data presented in this chapter suggest that hCFs cultured on PTFE-nf is the most suitable combination for bioengineering the corneal stroma. The cells and the collagens deposited were highly aligned, mimicking the lamellae of the corneal stroma.

## 3.8 Limitations and future work

The limitations of this study include the use of hMSCs beyond P1 when attempting keratocyte differentiation. The expansion of hMSCs was necessary due to the high cell number required for seeding cells on to both substrates. To further understand why the differentiation was unsuccessful it could be attempted with hMSCs from an earlier passage, where they have retained their MSC phenotype. As discussed, culture media could be supplemented with a ROCK-inhibitor to decrease the number of focal adhesions formed and preventing the detachment of cell sheets (Nakamura *et al.*, 2014). Furthermore, a ROCK-inhibitor could prevent the differentiation of cells to a myofibroblast phenotype (J. Chen *et al.*, 2009). The combination of a ROCK-inhibitor and early-passage hMSCs could be key to the successful use of bone marrow-derived MSCs in an *in vitro* model of the stroma.

A second limitation is the use of fibroblasts over keratocytes within the model. It is well known that keratocytes outperform hCFs with their ability to secrete ECM that resembles that found in the stroma. Whilst the use of keratocytes would have been preferable, cultured keratocytes are prone to phenotypic drift and becoming fibroblastic. Additionally, all attempts at isolating stem cells and inducting keratocyte differentiation were unsuccessful in this study. A study has shown that isolated stromal cells can be propagated in media supplemented with ROCK inhibitor Y27632, insulin-like growth factor-1, amnion stromal extract and low serum concentrations (Yam *et al.*, 2015). Once the cells were expanded, the deprival of serum resulted in the stromal cells regaining markers associated with keratocytes. Similarly, switching stromal cells to low-glucose, serum-free media after expansion can result in the rescuing of the keratocyte phenotype (Foster *et al.*, 2015). Future developments of the model would involve comparing both of these conditions to hCFs to evaluate their performance in recapitulating the stroma.

Future work for improving the hCF *in vitro* model would focus on methods to increase the rate of ECM deposition, either by supplementing media with a growth factor such as TGF-β or by incorporating macromolecules to accelerate matrix deposition, investigated in Chapter 4. To further investigate the deposited ECM, the construct could be denuded of cells using ammonia hydroxide. This would allow for the analysis of extracellular proteins without the risk of interference from cellular proteins and cellular autofluorescence. Live cell imaging of the hCF model revealed the beginning of collagen deposition over 64 h, becoming visible after approximately 8 h. A longer culture period would enable the observation of hCF stratification in combination with their shift in orientation. The fluorescent labelling of proteins associated with focal adhesions, such as paxillin, may also allow the visualisation of cell alignment via contact guidance, enabling the study of the interaction between substrate, matrix and the cell. The stable transfection of red fluorescent protein tagged-paxillin comes with the caveat that several passages would be required. Therefore, both the 30-day culture and the live cell imaging using just CNA35 should first be performed using hCFs at a greater passage, such as P10, to determine that the observations of cell alignment and collagen expression are unchanged. Alternatively, collagen could be labelled with CNA35 followed by a medium change and live cell imaging. This may allow for collagen fibril remodelling to be observed and could contribute to the understanding of collagen fibrillogenesis.

# Chapter 4. Macromolecular crowding

## 4.1 Overview

Bottom-up engineering approaches can take a long period of time to create a construct that resembles the native tissue (Griffith and Harkin, 2014). To reduce the necessary culture period, macromolecular crowding (MMC) of cell culture media has been employed to accelerate the *in vitro* deposition of ECM components such as collagen (Lareu *et al.*, 2007b; Kumar *et al.*, 2015a). This chapter focuses on the use of mono-MMC with carrageenan (Kumar *et al.*, 2015b, 2018), a mucopolysaccharide derived from red algae, and mixed-MMC with two different molecular weights of Ficoll (Kumar *et al.*, 2015a), a neutral polysaccharide. Both PTFE-nf and Transwell membranes were used as substrates in this chapter. Transwell membranes were included due to previous characterisation of fibril deposition and organisation, analysed using transmission electron microscopy (TEM) (Guo *et al.*, 2007). It is possible that the collagen deposited on PTFE-nf is not assembled in the same way and so both substrates were evaluated.

## 4.2 Aims and Objectives

**The aim of this chapter was to use macromolecular crowding to accelerate the deposition of collagen in the *in vitro* corneal stroma model.**

The objectives of this chapter were:

1. To use dynamic light scattering to quantify the fractional volume occupancy;
2. To analyse the collagen deposited by hCFs on PTFE-nf and Transwell membranes via ICC and TEM;
3. To determine the effect of long-term MMC on cell viability.

## 4.3 Materials

**Sigma/Merck (Germany):** Carrageenan (C1013); Ficoll PM 70 (F2878); Ficoll PM 400 (F4375)

**TAAB (England):** Medium premix resin kit (T028); Formvar solution in chloroform (0.25%; F145/035); Gilder grid G200HEX CU-100 (GG017/C); Reynolds lead citrate (L037); Sodium cacodylate (S008)

**Agar Scientific (England):** Glutaraldehyde 25% EM grade 10 (AGR1020); Osmium tetroxide 4% solution (AGR1024); Uranyl acetate (AGR1260A)

**Malvern Panalytical (England):** 12 mm polystyrene cuvette (DTS0012); Polycarbonate folded capillary zeta cell disposable cuvette (DTS1070)

**Diatome (USA):** Diamond knife

## 4.4 Methods

### 4.4.1 Dynamic light scattering

Carrageenan, at a concentration of 75 µg/ml, and a Ficoll cocktail (37.5 mg/ml Ficoll PM 70 and 25 mg/ml Ficoll PM 400) were dispersed in PBS at room temperature (Kumar *et al.*, 2015a, 2015b). The solution was then transferred to a polystyrene cuvette and dynamic light scattering (DLS) measurements were read at 20°C and 37°C using Zetasizer Nano ZS90 to obtain the average hydrodynamic diameter (Z-Ave.). Alternatively, the solution was transferred to a polycarbonate folded capillary cuvette and the zeta potential measured at 37°C. Results were analysed using the Zetasizer software v 7.13 (Malvern).

Fractional volume occupancy (FVO) was calculated using (Eq. 4.4.1.1) to (Eq. 4.4.1.3), as described by (Chen *et al.*, 2011):

$$Volume\ of\ crowder\ molecule = \frac{4}{3}\pi r^3 \qquad \text{(Eq. 4.4.1.1)}$$

Where r = hydrodynamic radius;

$$Number\ of molecules\ in\ X\ mg = \frac{(X \times 10^{-3}) \times (6.022 \times 10^{23})}{MW} \qquad \text{(Eq. 4.4.1.2)}$$

Where X = mass of crowder added per ml; 6.022 x $10^{23}$ is the Avogadro number and MW = molecular weight of crowder. The MW of CAR was assumed to be was 550 kDa (Uno *et al.*, 2001).

$$FVO\ (\%) = \frac{Volume\ of\ crowder\ molecule}{Number\ of\ molecules\ in\ X\ mg} \times 100 \qquad \text{(Eq. 4.4.1.3)}$$

### 4.4.2 Macromolecular crowding of hCFs

hCFs at P4 – 6 were seeded onto PTFE-nf and glass coverslips at a seeding density of 5 x $10^3$ cells/cm$^2$ or onto a 6-well polycarbonate Transwell membrane at a density of 1.06 x $10^5$ cells/cm$^2$ and allowed to attach for 2.5 h before being topped up with hCF growth medium and incubated overnight. Carrageenan, Ficoll PM 70 and Ficoll PM 400 were sterilised under UV light in a class II biosafety cabinet for 1 h (NuAire). Following a 24 h incubation period in growth medium, cells were switched to either A2PM (Table 4.1) supplemented with 75 µg/ml carrageenan (CAR) (Satyam *et al.*, 2014) or A2PM with a Ficoll cocktail consisting of 37.5 mg/ml Ficoll PM 70 and 25 mg/ml Ficoll PM 400 (FC) (Kumar *et al.*, 2015a). hCFs cultured in A2PM alone were used as a control. Media were replaced every 2 – 3 days and cells were cultured for up to 30 days.

**Table 4.1 Media and supplements used for MMC of hCFs.**

| Crowder | Basal media | Supplements |
|---|---|---|
| None (A2PM) | DMEM high glucose GlutaMAX | 10% FBS, 100 U/ml penicillin, 100 µg/ml streptomycin, 2.5 µg/ml amphotericin B and 1 mM A2P. |
| Carrageenan (CAR) | DMEM high glucose GlutaMAX | 10% FBS, 100 U/ml penicillin, 100 µg/ml streptomycin, 2.5 µg/ml amphotericin B, 1 mM A2P and 75 µg/ml carrageenan |
| Ficoll cocktail (FC) | DMEM high glucose GlutaMAX | 10% FBS, 100 U/ml penicillin, 100 µg/ml streptomycin, 2.5 µg/ml amphotericin B, 1 mM A2P, 37.5 mg/ml Ficoll PM 70 and 25 mg/ml Ficoll PM 400. |

### 4.4.3 Immunocytochemistry

hCFs were fixed in 10% NBF for 10 – 15 min at room temp. Samples were subjected to an immunocytochemistry staining procedure as described in Chapter 2 (2.4.4), however cells were not permeabilised. Primary antibodies used were: anti-collagen I, anti-collagen III, anti-collagen V, anti-α-SMA (Table 2.2) and anti-collagen VI (Table 3.1). Where co-staining with CNA35 was performed, 0.5 µM CNA35 was added in conjunction with the primary antibody. Alternatively, CTR and CNA35 were added to live cells prior to fixation as previously described (Chapter 3, 3.4.3.4). Images were processed as described in Chapter 3 (3.4.3.5). OrientationJ was performed on 1 representative ROI to quantify the alignment of collagens and CNA35 on slices corresponding to the substrate. The percent of collagen alignment at ± 10° is reported in the text.

### 4.4.4 Transmission electron microscopy

Cells were seeded onto PTFE-nf or into polycarbonate Transwell membranes as described in Chapter 3, 3.4.3. Cells were subsequently cultured in A2PM, CAR or FC for 30 days. The Biomedical Electron Microscopy unit (University of Liverpool) then fixed the samples in 2.5% (w/v) glutaraldehyde in 0.1 M cacodylate buffer (pH 7.4) in a Pelco Biowave®Pro (Ted Pella Inc., USA) at 100 W, 20" Hg for 3 min followed by 30 min at room temperature. Samples were post-fixed with 2% (w/v) osmium tetroxide in double distilled $H_2O$ followed by 2% (w/v) aqueous uranyl acetate overnight at 4°C. To prevent precipitation artefacts, cells were washed with double distilled $H_2O$ between each staining step. Samples were dehydrated in a graded ethanol series (30, 50, 70 and 90% followed by 2 x 100% each for 5 min) before filtration (2 x 30 min 1:1 ethanol:resin) and embedding in a medium premix resin.

For transmission electron microscopy, 70 – 74 nm sections were taken perpendicular to the substrate surface (parallel to the nanofibres on PTFE-nf as shown in Figure 4.1), using

a U6 ultra microtome (Leica Microsystems, Germany) and a diamond knife and collected on Formvar (0.25% (w/v) in chloroform) coated 200 mesh copper grids. Grids were post-stained with 4% aqueous uranyl acetate followed by 2.66% lead nitrate in Reynolds' lead citrate before images were acquired on a 120 kV Tecnai G2 Spirit BioTWIN (FEI, USA) using a RIO16 camera (Gatan, USA) and GMS3 software.

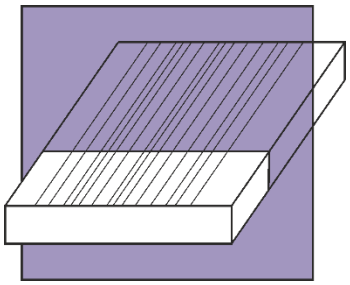

**Figure 4.1 Diagrammatic representation of the sectioning plane used to section samples cultured on PTFE-nf.** Sections were taken perpendicular to the substrate surface and approximately parallel to the PTFE-nf.

### 4.4.5 Cell growth and metabolic activity

To determine the metabolic activity of the hCFs during culture in crowded media, cells were seeded in to a 48-well plate at a density of 5 x $10^3$ cells/$cm^2$. Following overnight incubation in growth medium, media were switched to either A2PM, CAR or FC with media changed every 2 – 3 days. A resazurin assay was used as described in Chapter 3 (3.4.3.3). Following the resazurin assay, the cell number was also determined. The quantification of DNA per well using a PicoGreen assay was used to calculate the cell number as described in Chapter 3 (3.4.3.3). This experiment was performed on one occasion with growth, A2PM and FC media with the same data reported in both Chapter 2 and Chapter 3.

### 4.4.6 Transparency

hCFs cultured in crowded conditions on glass or PTFE-nf for 28 days were gently rinsed thrice with PBS. Samples were kept submerged in PBS (1 ml) and the absorbance was measured at wavelengths between 350 – 650 nm using a SPECTROstar Nano microplate reader (BMG, Germany). Three technical repeats were performed and averaged and the results were normalised to the absorbance of a plain glass coverslip. Percentage transmission was calculated using (Eq. 4.4.6.1):

$$\%\, Transmission = 10^{(2-A)} \qquad \text{(Eq. 4.4.6.1)}$$

Where A = absorbance measured.

### 4.4.7 Statistical analysis

All statistical analyses were performed using SigmaPlot software (v 14.0) and GraphPad Prism 9 software (v 9.0.0). A significance level of $p < 0.05$ was set for all experiments. Data were reported as mean ± 1 standard deviation (SD). To ensure all data were normally distributed, a Shapiro-Wilk test was performed. Where there were three or more groups with one factor a one-way ANOVA with Tukey's *post hoc* test for multiple comparisons was used, otherwise where there were just two variables a t-test was performed. A Brown-Forsythe test was used to ensure equal variance. For comparing three or more groups with two factors, a two-way ANOVA was performed and a Spearman's test for heteroscedasticity was used to ensure equal variances. If the residuals after fitting the model were not normally distributed and data could not be suitably transformed, either a one-way ANOVA (where data were normally distributed) or a Kruskal-Wallis one-way ANOVA was performed. Multiplicity adjusted p values are reported.

## 4.5 Results

### 4.5.1 CAR and FC are polydisperse polysaccharides

DLS was used to assess the size distribution of CAR and FC particles suspended in PBS at 20°C (Figure 4.2). The cumulants mean hydrodynamic diameter (Z-average) of carrageenan and carrageenan passed through a 0.75 µm filter (CAR filt.) were significantly different ($p < 0.0001$), confirming the presence of large particles or aggregates when unfiltered (Figure 4.2 A). This was further supported by the significant decrease in the polydispersity index after filtration, which formed a more monodisperse solution (Figure 4.2 C). The Z-average of FC was significantly smaller than both carrageenan solutions ($p < 0.0001$). However, as FC is a cocktail formed using two molecules with different molecular weights, distribution analysis was also reported which revealed particles with significantly different hydrodynamic diameters (10.13 nm and 65.95 nm respectively; $p = 0.0001$; Figure 4.2 B). The cocktail of two differently sized polysaccharides created a solution with a polydispersity index similar to carrageenan (Figure 4.2 C).

The hydrodynamic diameter of both carrageenan and the Ficoll cocktail were also measured at 37°C, to replicate cell culture conditions. Both macromolecules appeared to form aggregates, which ultimately resulted in a measurement error due to the increase in polydispersity. Although the sample became too polydisperse to obtain reliable readings, initial results showed an increase in the Z-average of carrageenan to 1423 ± 677 nm and the polydispersity index increased to 0.861 ± 0.140 ($n = 2$) (Table 4.2). Similarly, the Z-average of the Ficoll cocktail increased to 365.23 ± 242.91 whilst the polydispersity index increased to 0.586 ± 0.164. The zeta potential, measured at 37°C, confirmed that CAR was negatively charged (-8.94 ± 1.30 mV), whereas the Ficoll cocktail could be considered neutral (-2.68 ± 0.38 mV) (Table 4.2).

The measured hydrodynamic diameter at 20°C (Table 4.2) was used to approximate the fractional volume occupied (FVO) by the crowder. Unfiltered CAR was calculated as occupying 41.34% of the total volume of medium. Owing to the fact that a Ficoll cocktail was used, approximating the FVO of FC was not possible (see Discussion, section 4.6.2.1).

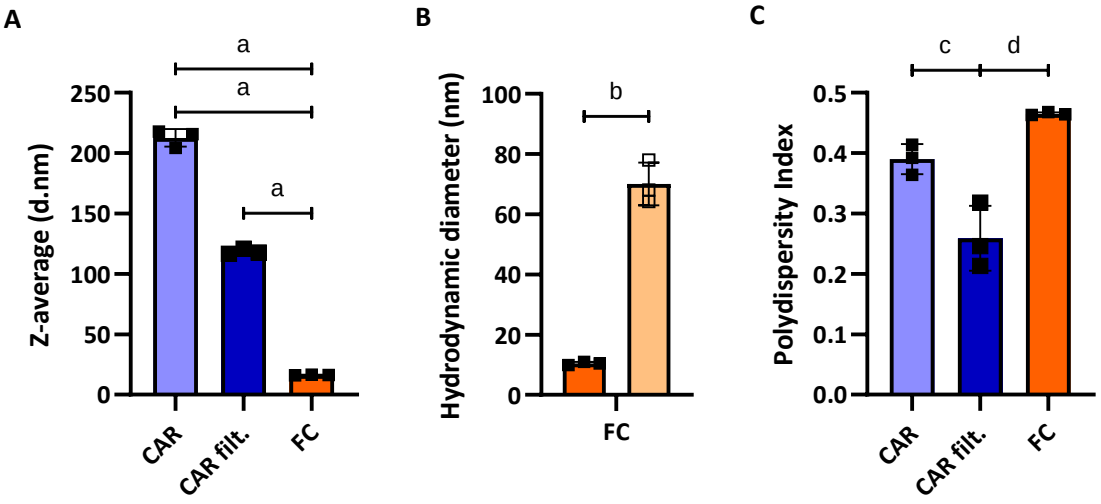


**Figure 4.2 DLS measurements of CAR and FC at 20°C.** A: The cumulants mean hydrodynamic diameter (Z-average) of carrageenan (CAR), CAR passed through a 0.75 µm filter (CAR filt.) and FC. B: FC is composed of two polymers with different molecular weights and hydrodynamic diameters, shown by the dark and light orange. C: The polydispersity index of CAR, CAR filt. and FC is shown. n = 3 and error bars show SD. Where there are three variables a one-way ANOVA was performed with Tukey's *post hoc* test for multiple comparisons, otherwise a t-test was performed: a = < 0.0001; b = 0.0001; c = 0.008; d = 0.0008.

**Table 4.2 DLS measurements of CAR and FC at 20°C and 37°C.**

| Sample | Z-average (d.nm) | Polydispersity Index | Zeta Potential (mV) |
|---|---|---|---|
| CAR (20°C) | 212.6 ± 6.0$^{\dagger}$ | 0.390 ± 0.020$^{\dagger}$ | - |
| CAR (37°C) | 1423 ± 677$^{*\P}$ | 0.861 ± 0.140$^{*\P}$ | - 8.94 ± 1.30$^{\dagger}$ |
| FC (20°C) | 16.23 ± 0.19$^{\dagger}$ | 0.465 ± 0.002$^{\dagger}$ | - |
| FC (37°C) | 365.23 ± 242.91$^{\S\P}$ | 0.586 ± 0.164$^{\S\P}$ | -2.68 ± 0.38$^{\ddagger}$ |

Results presented as mean ± *SD*. $^{*}$n = 2; $^{\dagger}$n = 3; $^{\ddagger}$n = 4; $^{\S}$n = 9; $^{\P}$sample too polydisperse for accurate cumulant analysis but data reported for comparison.

### 4.5.2 ICC analysis suggests collagen aggregates when cells are crowded with a negatively charged crowder

ICC analysis was used to visualise the collagen deposited after culture in non-crowded (control) and crowded conditions on glass, PTFE-nf and on Transwell membranes. From as early as day 2, an apparent increase in the deposition of Col I was observed when crowded with CAR (Figure 4.3). The collagen deposited in crowded conditions appeared to align with the hCFs after both 2 and 7 days, and CAR did not seem to affect cell alignment along PTFE-nf. The IgG negative control did not show any fluorescence suggesting that the secondary antibody is not non-specifically binding to residual carrageenan. To determine whether the collagen I antibody was non-specifically binding to residual carrageenan, and thus incorrectly

appearing as if there is an increase in collagen deposition, the collagen probe (CNA35) was used to visualise collagens (Figure 4.4). Medium that was not supplemented with A2P was also used as a control, as ascorbic acid is thought to be essential for the synthesis of collagen (Pinnell, 1985; Canty and Kadler, 2005). hCFs cultured for 7 days in uncrowded medium without A2P showed minimal collagen deposition. Conversely, cells cultured in crowded conditions, in the absence of A2P, appeared to deposit collagen. When supplemented with A2P cells in both normal and crowded conditions deposited collagen. Interestingly, under crowded conditions, the collagen appears to align to what could be carrageenan aggregates in media both with and without A2P supplementation with large structures present. CNA35 was added to CAR medium in a cell-free system to determine if carrageenan was non-specifically labelled by CNA35 (Figure 4.5). The lack of staining suggests that CNA35 does not bind to carrageenan. The areas of intense fluorescence are likely to be dust or serum aggregates.

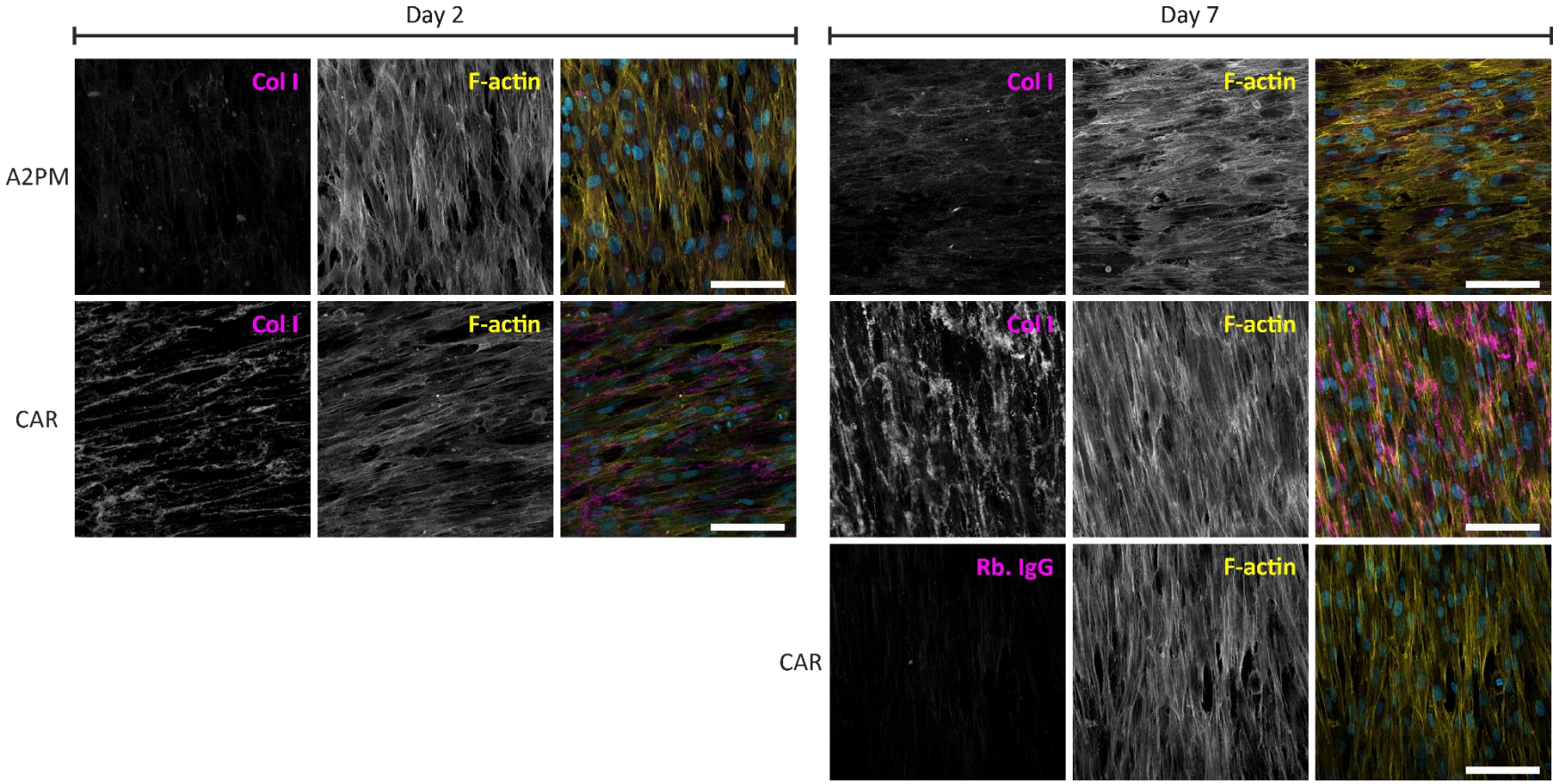


**Figure 4.3 ICC analysis of deposited type I collagen by hCFs cultured on PTFE-nf in uncrowded and crowded (CAR) conditions.** The deposition of type I collagen (magenta) in uncrowded (A2PM) and carrageenan-crowded (CAR) conditions at days 2 and 7 is shown. Cells were co-stained with phalloidin (F-actin; yellow) and DAPI (blue). n = 1 biological replicate. Scale bars represent 100 µm.

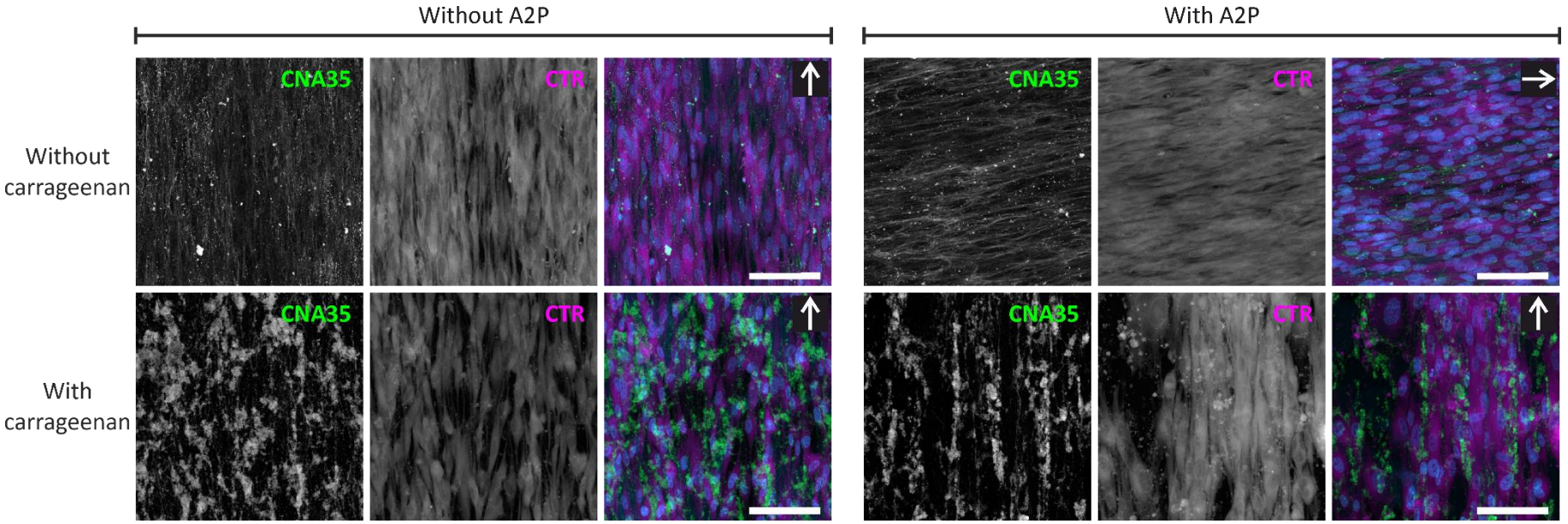


**Figure 4.4 Max. z-projection from ICC analysis of deposited collagen by hCFs cultured on PTFE-nf in uncrowded and crowded (carrageenan) conditions.** The deposition of collagens (CNA35; green) in uncrowded and crowded conditions are shown. The hCFs (CTR; magenta) were cultured both with and without ascorbic acid supplementation to stimulate collagen deposition. Cells were co-stained with DAPI (blue). White arrows on merged images represents direction of PTFE-nf. n = 1 biological replicate. Scale bars represent 100 µm.

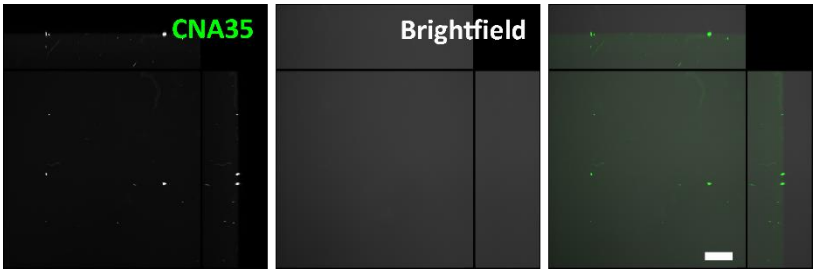


**Figure 4.5 Orthogonal max. z-projections of cell-free CAR medium with CNA35.** CNA35 (green) did not appear to bind to carrageenan in CAR medium where cells were not present. The small areas of intense fluorescence are likely autofluorescence from dust particles on top of the medium. Scale bar represents 100 µm.

The deposition of collagens type I, III, V and VI were also analysed after 30 days of culture. As reported in Chapter 3, the staining for type I collagen was diffuse and showed little organisation when cultured on glass in A2PM (30%, n = 3) (Figure 4.6). The deposition of collagens appeared to increase with MMC. Interestingly, when crowded with Ficoll type I collagen resembled that deposited under normal (uncrowded) (46%; n = 2) whereas cultures in CAR appeared to form collagen aggregates with little alignment (32%; n = 3). This phenotype was also observed with CNA35 labelling, with only 18% (n = 2) of labelled collagens aligning within ± 10°, less than that of cultures in A2PM (37%; n =3) and FC (47%; n = 3). When cultured on PTFE-nf, hCFs in A2PM aligned parallel to the nanofibres, following topographical cues and depositing aligned type I collagen (59%; n = 3) (Figure 4.7). Again, there was an apparent increase in type I collagen deposited in FC (50% alignment; n = 2) whilst aggregates disrupted collagen alignment in CAR cultures (34%; n = 3). Aggregated collagen was also observed on the Transwell membrane using CNA35 labelling in the CAR culture (24%; n = 3), but staining was diffuse in control conditions (18%; n = 3) (Figure 4.8).

The deposition of type III collagen was only enhanced when hCFs were cultured in CAR – this also appeared to be in an aggregated form and typical fibrils were not observed (Figure 4.9 & Figure 4.10). However, this may be non-specific binding of the antibody to residual carrageenan. The staining observed on samples cultured on Transwell membranes isn't as defined as those on glass or on PTFE and this is likely due to the higher cell number, and thus increase in deposited collagen (Figure 4.11). Type V collagen also appeared to be aggregated when cultured in CAR and this was most evident on PTFE-nf, disrupting alignment (44%; n = 3) (Figure 4.10). There was an apparent increase of type V collagen cultured on PTFE-nf in medium crowded with the Ficoll cocktail although alignment was reduced (58%; n = 3) when compared to A2PM cultures (72%; n =2) (Figure 4.10).

α-SMA expression was investigated to determine if the hCFs transitioned into myofibroblasts after crowding. No α-SMA expression was observed when hCFs were cultured on glass and PTFE-nf, independent of media condition (Figure 4.12 & Figure 4.13). An apparent decrease in the expression of α-SMA was observed when hCFs were cultured on a Transwell membrane in CAR compared to the A2PM control; however, actin filaments are not evident and this is likely non-specific staining (Figure 4.14). Crowding appeared to result in the increase of type VI collagen on all substrates but aggregates were again observed when cells were cultured in CAR. Cultures on glass showed little alignment whether cultured in A2PM (29%; n = 3), CAR (44%; n = 3) or FC (25%; n = 3) (Figure 4.12). Crowding with Ficoll maintained the alignment of type VI collagen deposited by hCFs cultured on PTFE-nf (78%; n = 2) whereas aggregates disrupted alignment in CAR cultures (38%; n = 3). To quantify collagen content, a hydroxyproline assay was trialled in uncrowded and carrageenan-crowded samples but the assay did not detect any collagen.

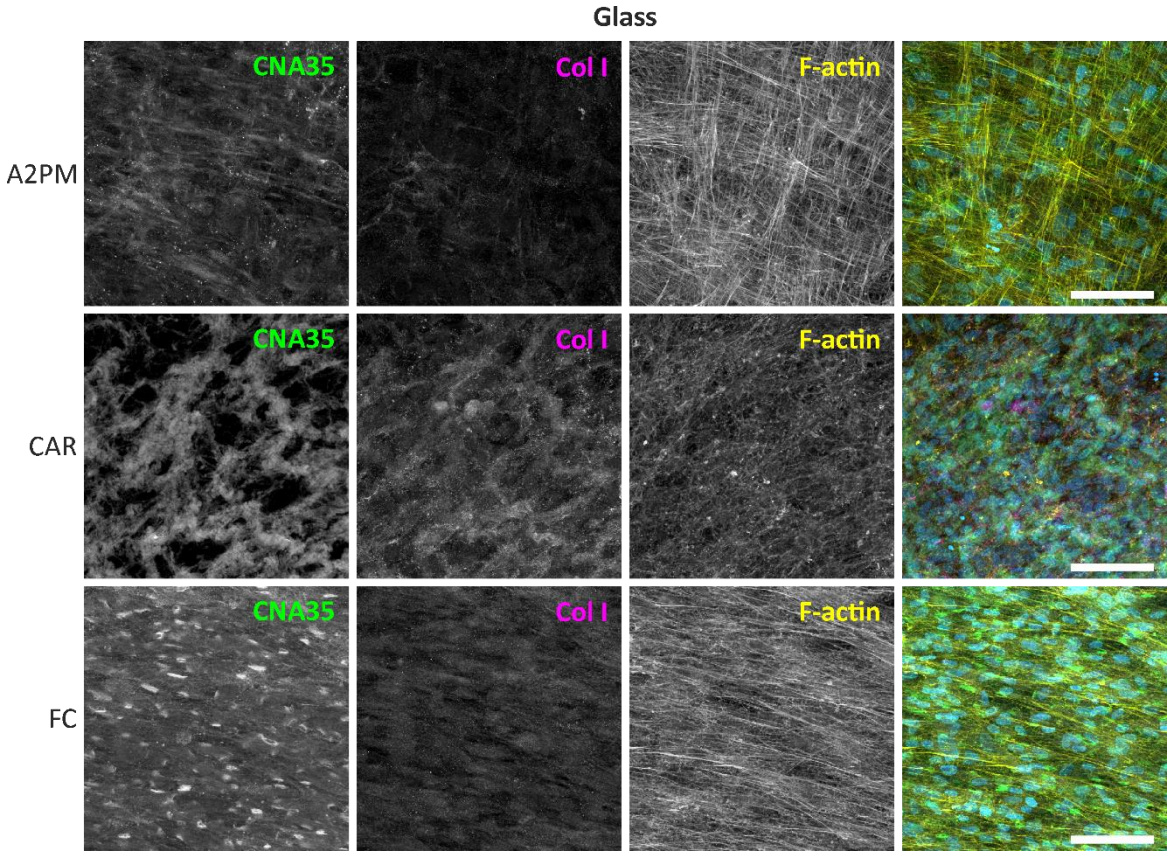


**Figure 4.6 Representative max. z-projections from ICC analysis of deposited type I collagen by hCFs cultured on glass in uncrowded (A2PM) or crowded (CAR or FC) media for 30 days.** The deposition of collagens (CNA35; green) and, specifically, type I collagen (Col I; magenta) was analysed. Cells were co-stained with phalloidin (F-actin; yellow) and DAPI (blue). Merged images are also shown. n = 3 biological replicates except for FC, where n =2. Scale bar represents 100 µm.

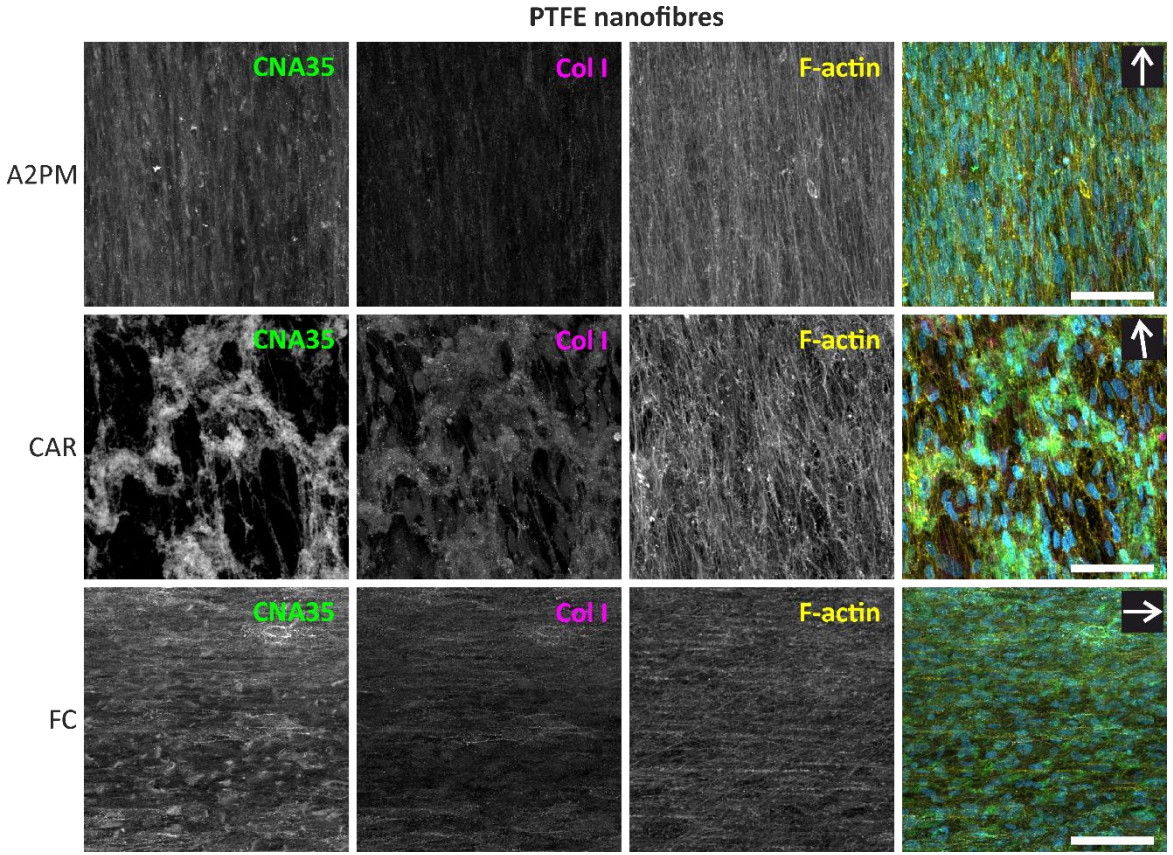


**Figure 4.7 Representative max. z-projections from ICC analysis of deposited type I collagen by hCFs cultured on PTFE-nf in uncrowded (A2PM) or crowded (CAR and FC) media for 30 days.** The deposition of collagens (CNA35; green) and, specifically, type I collagen (Col I; magenta) was analysed. Cells were co-stained with phalloidin (F-actin; yellow) and DAPI (blue). Merged images are also shown. White arrows on merged images represents direction of PTFE-nf. n = 3 biological replicates except for FC, where n =2. Scale bar represents 100 µm.

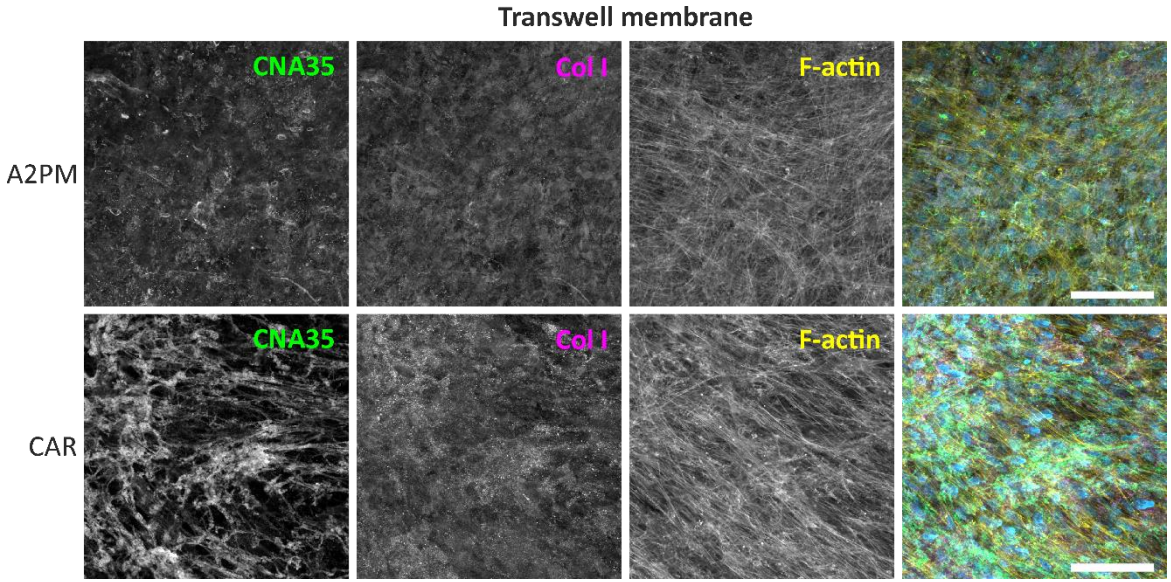


**Figure 4.8 Representative images from ICC analysis of deposited type I collagen by hCFs cultured on Transwell membranes in uncrowded (A2PM) or crowded (CAR) media for 30 days.** The deposition of collagens (CNA35; green) and, specifically, type I collagen (Col I; magenta) was analysed. Cells were co-stained with phalloidin (F-actin; yellow) and DAPI (blue). Merged images are also shown. n = 3 biological replicates. Scale bars represent 100 µm.

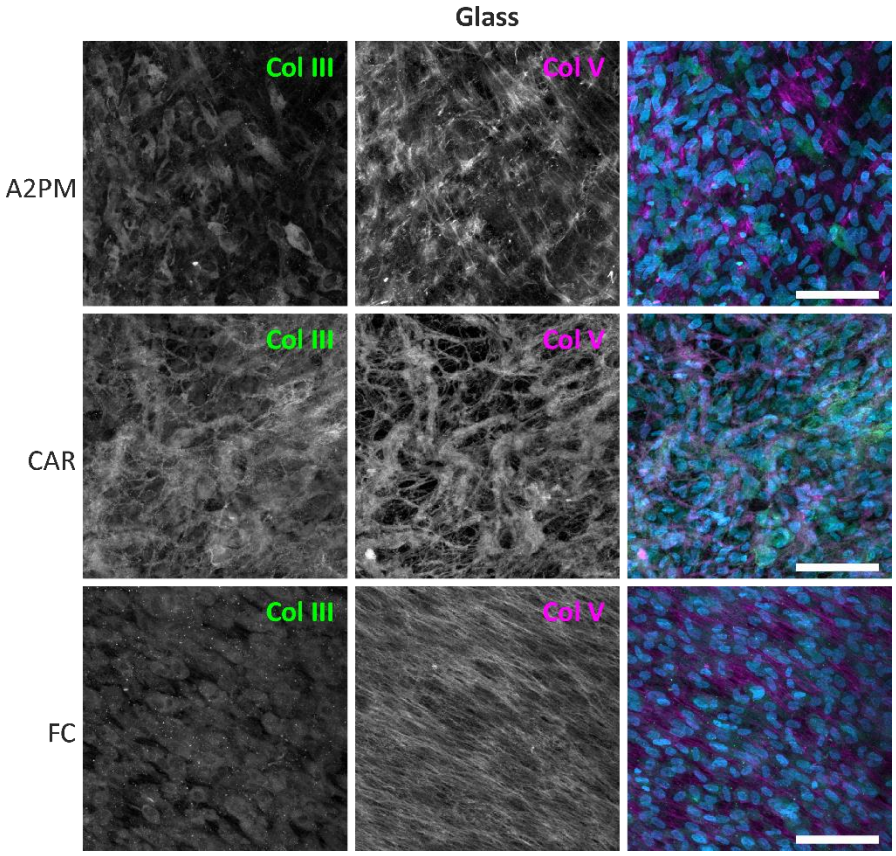


**Figure 4.9 Representative max. z-projections from ICC analysis of deposited collagen types III and V by hCFs cultured on glass in uncrowded (A2PM) or crowded (CAR and FC) media for 30 days.** Collagen types III (Col III; green) and type V (Col V; magenta) are shown. Merged images with DAPI-stained nuclei (blue) are also shown. n = 3 biological replicates except for A2PM, where n =2. Scale bar represents 100 µm.

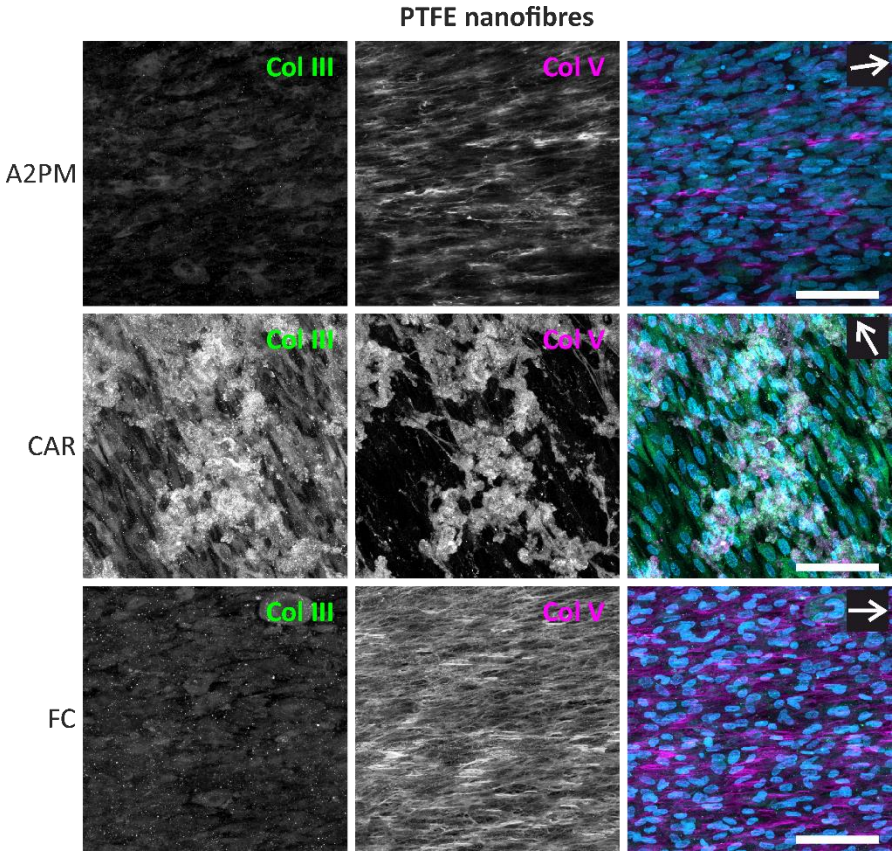


**Figure 4.10 Representative max. z-projections from ICC analysis of deposited collagen types III and V by hCFs cultured on PTFE-nf in uncrowded (A2PM) or crowded (CAR and FC) media for 30 days.** Collagen types III (Col III; green) and type V (Col V; magenta) are shown. Merged images with DAPI-stained nuclei (blue) are also shown. White arrows on merged images represents direction of PTFE-nf. n = 3 biological replicates except for A2PM, where n =2. Scale bar represents 100 µm.

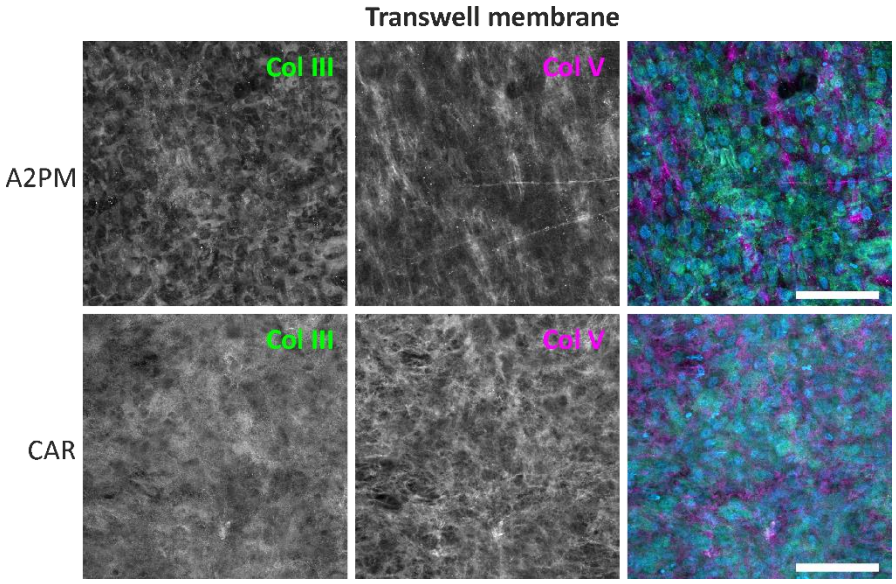


**Figure 4.11 Representative images from ICC analysis of deposited collagen types III and V by hCFs cultured on Transwell membranes in uncrowded (A2PM) or crowded (CAR) media for 30 days.** Collagen types III (Col III; green) and type V (Col V; magenta) are shown. Merged images with DAPI-stained nuclei (blue) are also shown. n = 3 biological replicates. Scale bars represent 100 µm.

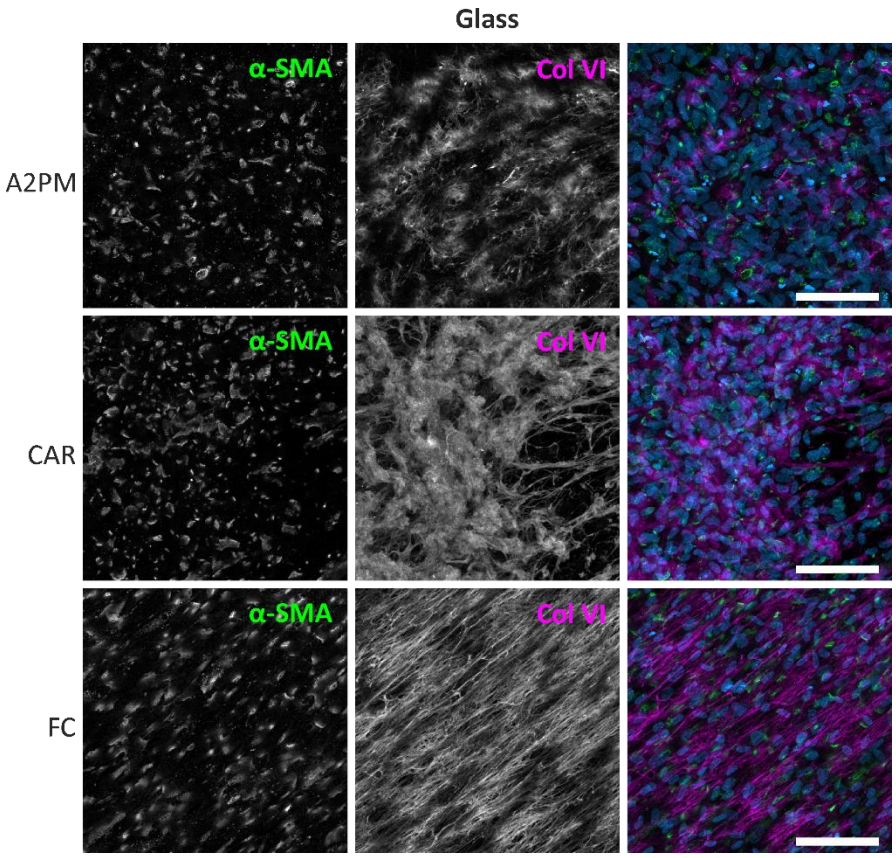


**Figure 4.12 Representative max. z-projections from ICC analysis of deposited type VI collagen and α-SMA expression in hCFs cultured on glass in uncrowded (A2PM) or crowded (CAR and FC) media for 30 days.** α-SMA (green) and type VI collagen (Col VI; magenta) are shown. Merged images with DAPI-stained nuclei (blue) are also shown. n = 3 biological replicates. Scale bars represent 100 µm.

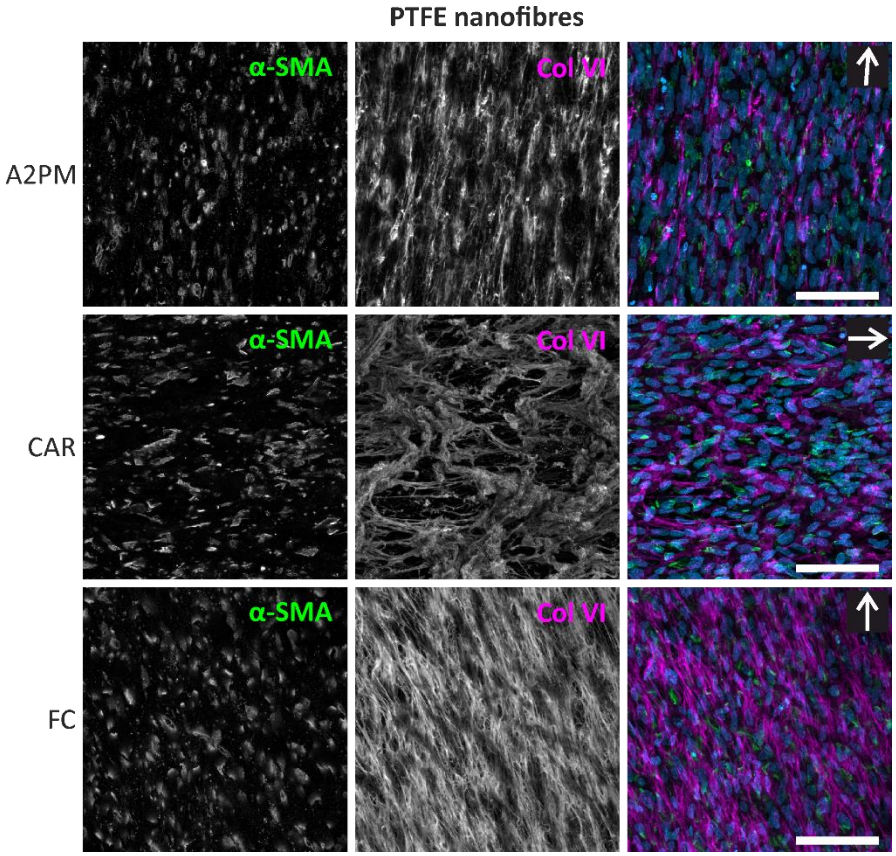


**Figure 4.13 Representative max. z-projections from ICC analysis of deposited type VI collagen and α-SMA expression in hCFs cultured on PTFE-nf in uncrowded (A2PM) or crowded (CAR and FC) media for 30 days.** α-SMA (green) and type VI collagen (Col VI; magenta) are shown. Merged images with DAPI-stained nuclei (blue) are also shown. White arrows on merged images represents direction of PTFE-nf. n = 3 biological replicates. Scale bars represent 100 µm.

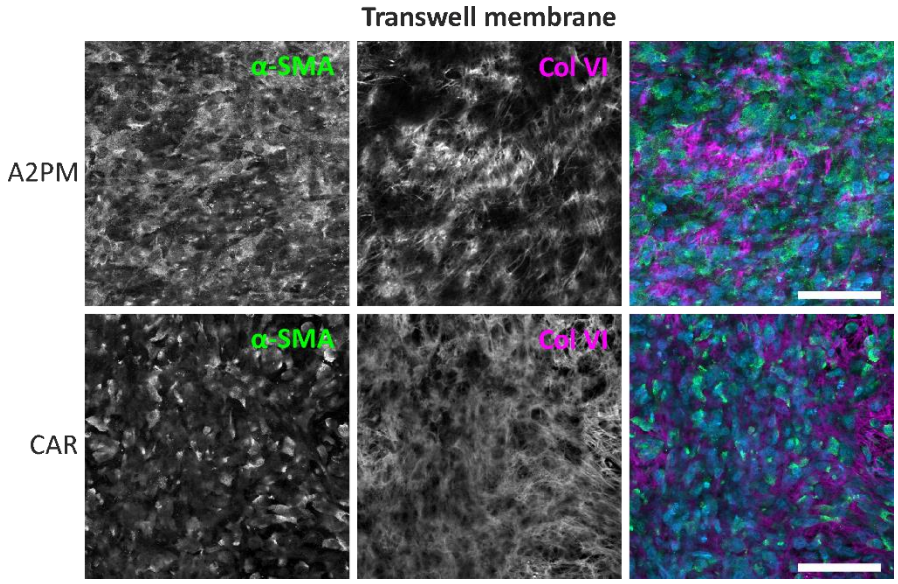


**Figure 4.14 Representative images from ICC analysis of deposited type VI collagen and α-SMA expression in hCFs cultured on Transwell membranes in uncrowded (A2PM) or crowded (CAR) media for 30 days.** α-SMA (green) and type VI collagen (Col VI; magenta) are shown. Merged images with DAPI-stained nuclei (blue) are also shown. n = 3 biological replicates. Scale bar represents 100 µm.

### 4.5.3 MMC with CAR appears to change ultrastructure of deposited collagen

TEM was employed to evaluate the ultrastructure of collagen fibrils deposited by hCFs after 30 days in culture on PTFE-nf (Figure 4.15) and on Transwell membranes (Figure 4.16). Culturing of hCFs on PTFE-nf in uncrowded medium showed minimal ECM deposition with no evident collagen fibrils visible. Conversely, crowding with CAR appeared to produce an amorphous ECM again with no evidence of typical collagen fibrils (Figure 4.15). Large fibrillar structures with an unusual banding pattern were observed in areas both adjacent to the cell and between cell layers in carrageenan-crowded cultures. Collagen-like fibrils, identified by the distinct periodic banding pattern, could be seen when hCFs were crowded with FC. These fibrils could be seen orienting parallel and perpendicular to the plane of sectioning. Interestingly, the hCFs cultured in FC exhibited large vacuoles within the cell, a phenotype not observed in the control A2PM cultures or those in CAR.

Dues to the increased cell seeding density, more hCFs and thus more ECM was observed in the Transwell cultures even without crowding (Figure 4.16). Collagen fibrils, characterised by the periodic banding, could be seen running parallel and perpendicular to the hCFs. Loose, lamellar-like structures were observed, with the orientation of collagen appearing to change direction in the control A2PM culture, consistent with previous studies (Guo *et al.*, 2007; Karamichos *et al.*, 2010). The amorphous matrix seen in samples cultured in CAR on PTFE-nf was also found in the CAR Transwell samples. Here, however, the large

fibrillar structures with the unusual banding pattern were more apparent and were seen spanning the space between cells. Collagen-like fibrils were observed in the FC culture however the lamellar-like architecture was not apparent. Similar to the PTFE-nf FC culture, the hCFs in FC culture possessed large vacuoles (Figure 4.16 inset).

To further investigate the fibrillar structures observed in CAR the boxed areas of each image in Figure 4.17 were magnified and rotated to allow for a direct comparison. The distinct banding pattern seen in A2PM is the same as that observed in FC cultures, suggesting that these are the same fibrillar structures, likely type I collagen. The structures seen in CAR not only seem to aggregate laterally and span approximately 600 nm but the banding pattern differs. The distinct banding observed in A2PM and FC samples was lost in CAR samples and the periodicity appeared to increase. Comparing the bands observed in CAR cultures to those found in cultured dermis, fibroblasts and in pathologic Bruch's membrane (Figure 4.18 A – C) show similarities between the banding patterns and periodicity.

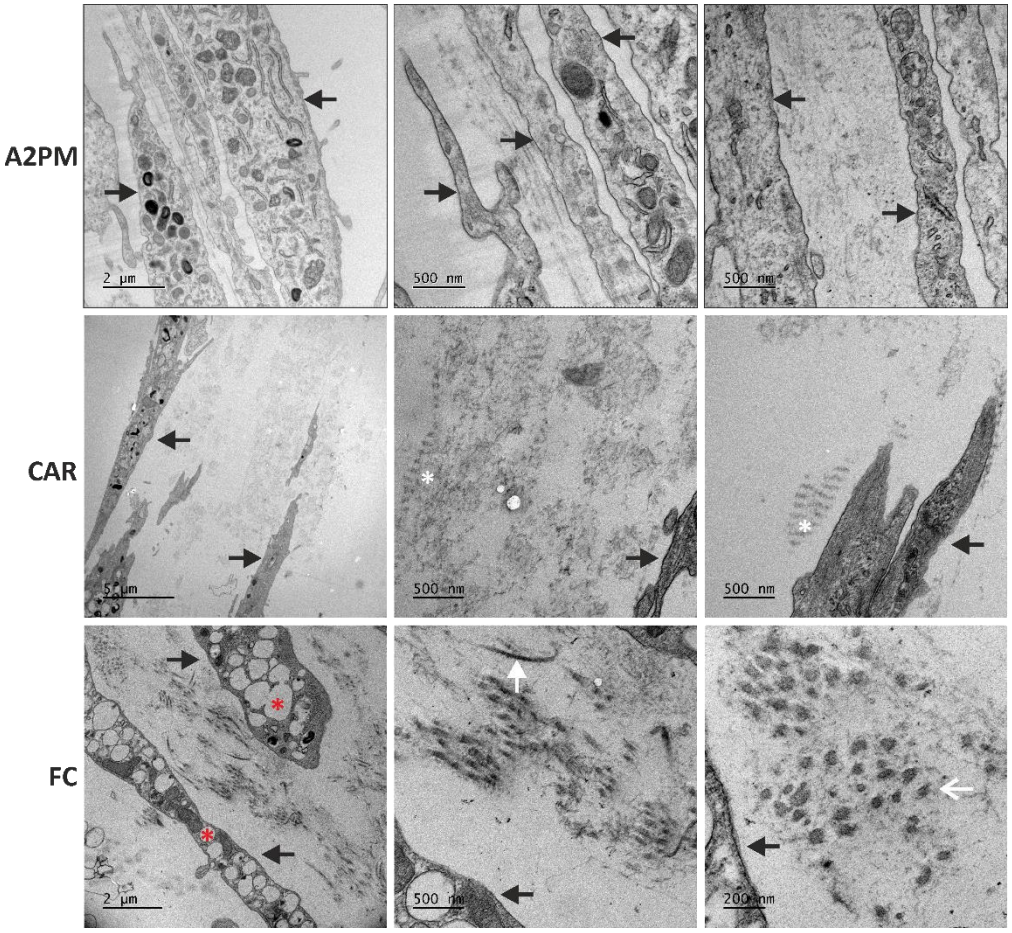


**Figure 4.15 TEM of hCFs cultured on PTFE-nf for 30 days.** hCFs were cultured on PTFE-nf in uncrowded medium (A2PM; top), medium crowded with carrageenan (CAR; middle), or medium crowded with Ficoll (FC; bottom). The hCFs (black arrow) cultured in FC have a large number of vacuoles (red asterisks). Collagen is evident in FC with collagen fibrils orienting both parallel (closed white arrow) and perpendicular (open white arrow) to the section. The ECM deposited by hCFs in CAR (white asterisks) is unusual with large banded structure. Three different magnifications are shown for each condition with scale bars indicated on the images.

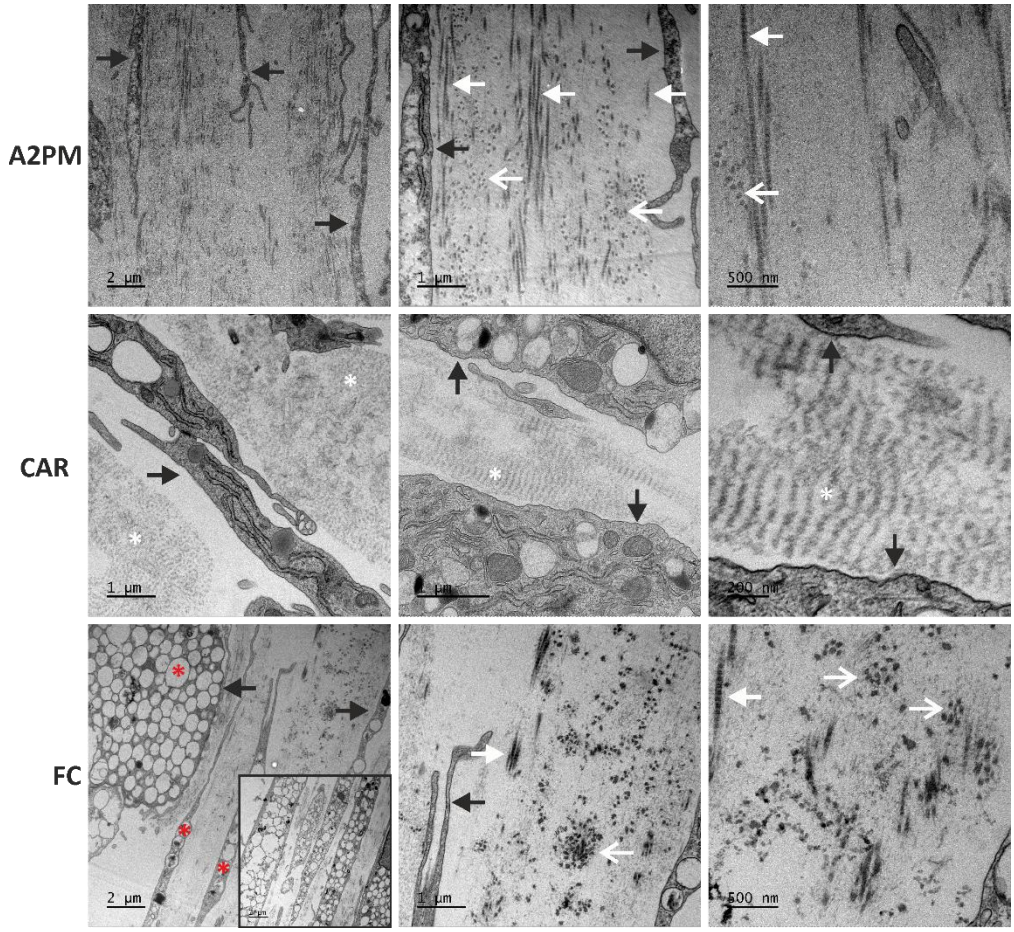


**Figure 4.16 TEM of hCFs cultured on Transwell membranes for 30 days.** hCFs were cultured on Transwell membranes in uncrowded medium (A2PM; top), medium crowded with carrageenan (CAR; middle), or medium crowded with Ficoll (FC; bottom). hCFs (black arrows) can be seen adjacent to collagen fibrils which are oriented both parallel (closed white arrows) and perpendicular (open white arrows) to the section in A2PM and FC. The hCFs cultured in FC have a large number of vesicles (red asterisks and inset). The ECM deposited by hCFs in CAR (white asterisks) appears amorphous. Three different magnifications are shown for each condition with scale bars indicated on the images.

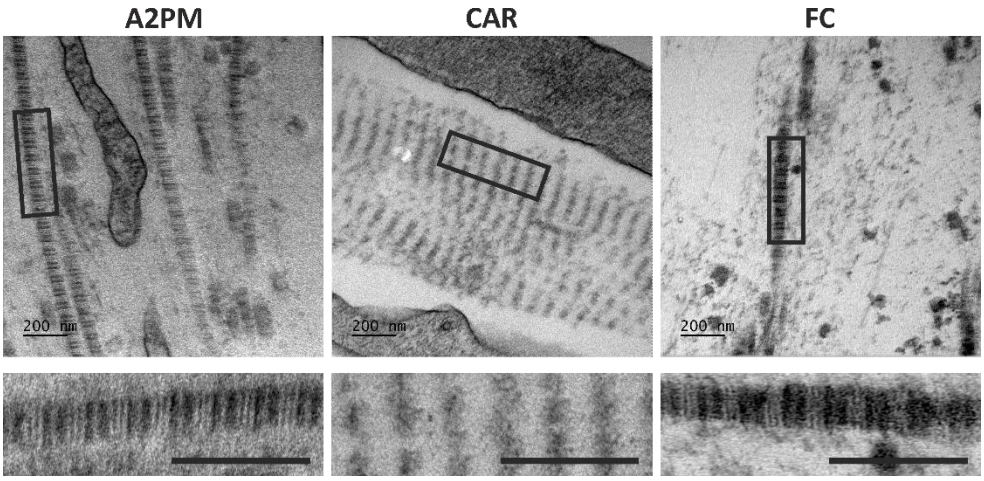


**Figure 4.17 TEM of fibrillar structures from hCFs cultured on Transwell membranes for 30 days.** hCFs were cultured on Transwell membranes in uncrowded medium (A2PM; left), medium crowded with carrageenan (CAR; middle), or medium crowded with Ficoll (FC; right). Banded fibrils (boxed regions) were magnified and images rotated for direct comparison. Scale bars represent 200 nm.

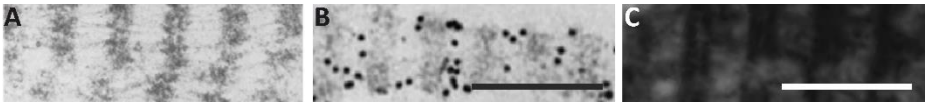


**Figure 4.18 TEM of different collagen aggregates observed in the literature.** A: Filamentous aggregate observed in cultured dermis. Image adapted from Kobayasi *et al.* (1985) and the scale bar was absent from the figure (Kobayasi *et al.*, 1985). B: Human skin fibroblast cultures were immunolabelled with anti-type VI collagen where the secondary antibodies were conjugated to colloidal gold particles. Image adapted from (Bruns *et al.*, 1986). C: Double-banded aggregate found in the Bruch's membrane of a patient with age-related macular degeneration. Image adapted from (Knupp *et al.*, 2006). Scale bars represent 200 nm (B and C).

### 4.5.4 Cell number is not affected by MMC with FC

Given the ultrastructural appearance of hCFs cultured in FC, a PicoGreen and resazurin assay were carried out on cells cultured in a 48-well plate to investigate the effect of MMC on cell number and cellular metabolic activity respectively (Figure 4.19). Culturing hCFs in medium supplemented with A2P did not affect cell number when compared to those cultured in growth medium (Figure 4.19 A). Similarly, the addition of FC as a crowder exhibited no effect on cell number (Figure 4.19 A). Media type was shown to significantly affect metabolic activity ($p = 0.045$) however, when correcting for multiple comparisons, no significant differences were observed (Figure 4.19 B). A table of p values for each of these experiments can be found in Appendix F. To determine whether the rise in metabolic activity observed was likely due to the increase in cell number the relative fluorescent units (RFU) per cell were calculated (Figure 4.19 C). These results show that there may be a small increase in the

metabolic activity at day 3 in both media conditions. After this initial peak, metabolic activity decreased to levels similar to day 1 and remains consistent across the measured time frame. Surprisingly, crowding with carrageenan resulted in cell death and so data were not obtained. This phenomenon was only observed when hCFs were cultured in CAR in a 48-well plate. When cultured on substrates with a greater surface area (coverslips and the Transwell membranes in 6-well plates) cell death did not occur. No other differences were observed.

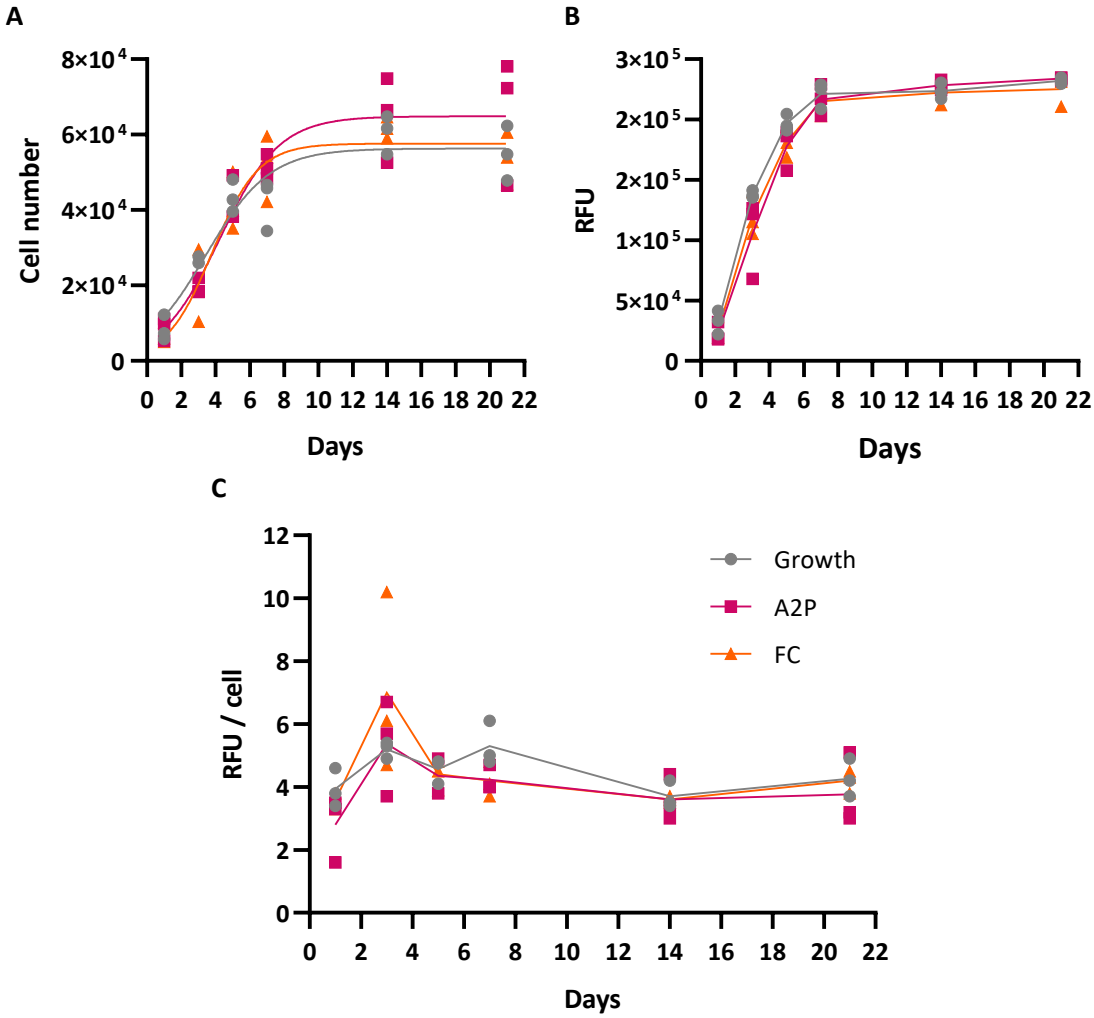


**Figure 4.19 Growth and metabolic activity of hCFs in normal (A2PM) and crowded (FC) conditions.** A: PicoGreen assay was used to compare the growth of hCFs in growth (grey; Chapter 2, 2.5.1.2) A2PM (magenta; Chapter 3, 3.5.2) and FC (orange) media. hCFs cultured in CAR at low cell numbers did not survive beyond day 1 and thus data was not included. A logistic growth curve was applied where $R^2$ = 0.896, 0.892 and 0.908 for growth, A2PM and FC respectively. B: Cell metabolic activity was assessed using resazurin sodium salt colorimetric assay over 21 days. C: To take into consideration the effect of an increase in cell number on the overall metabolic activity, the relative fluorescence was normalised to cell number. n = 3 biological replicates for all samples except for the cell number for A2PM at day 5 where n = 2; lines represent the mean. This experiment was performed on one occasion with growth, A2PM and FC with the same data being reported in Chapter 3. Where data were normally distributed a two-way ANOVA was performed otherwise, a one-way ANOVA was performed with Tukey's *post hoc* test for multiple comparisons. No significant differences were observed.

### 4.5.5 Macromolecular crowding affects transparency of *in vitro* stroma model after 30 days in culture

The corneal stroma must maintain transparency to allow the transmittance, and subsequent refraction, of light on to the retina. Along with the epithelium, the keratocytes within the corneal stroma protect the eye against potential UV damage. In particular, corneal crystallins such as ALDH3A1 can metabolise the toxic by-products of UV-induced oxidative stress (Abedinia *et al.*, 1990; Estey *et al.*, 2007).To give an indication of how amorphous collagen deposition affected transparency, and thus the function of the *in vitro* model, the transparency of hCF constructs was assessed at wavelengths from 300 – 650 nm (Figure 4.20 A). The data were normalised to a glass coverslip and the cell-free PTFE-nf substrate was comparable with plain glass, indicating that the nanofibres do not interfere with the transmission of light. As the transparency of each hCF culture varies with wavelength, a wavelength within the ultraviolet range (UV; 350 nm) and one in the middle of the visible range (560 nm) were selected for comparison. In the UV spectrum no difference was observed between uncrowded (A2PM) and crowded (CAR and FC) samples (Figure 4.20 B). Similarly, no significant difference was observed between the glass and PTFE-nf substrates. However, in the middle of the visible range, at 560 nm, there was a reduction in transmission between hCFs cultured on glass in A2PM and those cultured in FC ($p = 0.0266$) (Figure 4.20 C). There was also a decrease in transmission between hCFs in A2PM on glass and those in FC cultured on PTFE-nf, but this was not statistically significant ($p = 0.0507$). Interestingly, there was no difference between hCFs cultured in A2PM on glass compared to those cultured on PTFE-nf at 350 and 560 nm. Equally, no significant differences were observed between hCFs cultured on PTFE-nf in A2PM and those in crowded conditions at these two wavelengths.

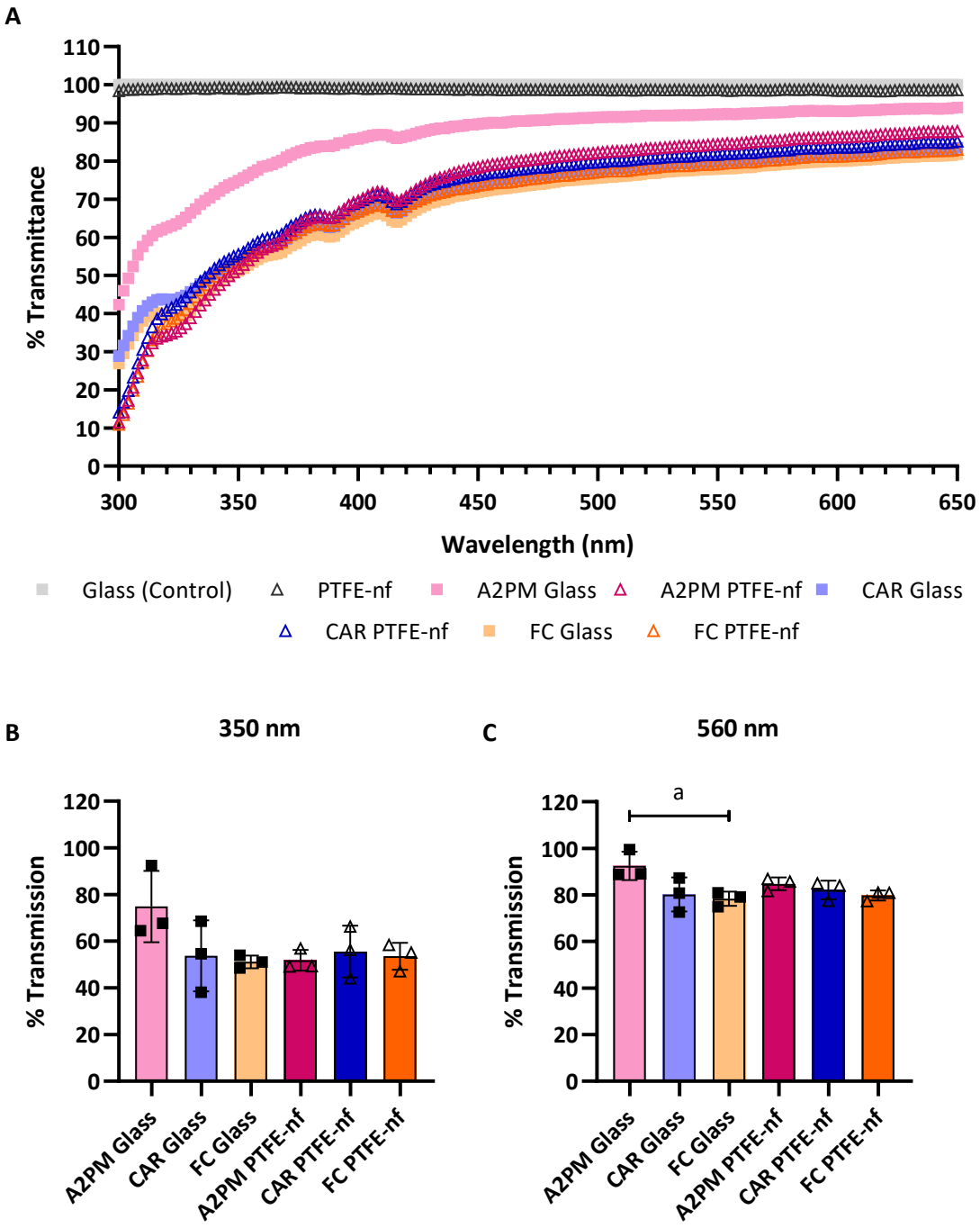


**Figure 4.20 Transparency of hCFs cultured in normal (A2PM) and crowded (CAR and FC) conditions for 30 days on glass or PTFE-nf.** A: The average transmittance of samples measured at wavelengths from 300 to 650 nm normalised to glass (control). B: Transmittance at wavelength of 350 nm (UV) was compared. C: Transmittance at 560 nm was also compared. n = 3 biological replicates and SD error bars are shown. One-way ANOVA was performed with Tukey's *post hoc* test for multiple comparisons; a = 0.0266.

## 4.6 Discussion

The aim of this chapter was to use macromolecular crowding to amplify the production of the ECM, specifically collagens type I, V and VI. The results obtained in this study suggest that although MMC may increase the deposition of collagen, supporting previously published data, the ultrastructure can also be affected. Long-term crowding with carrageenan appears to result in the aggregation of collagens. Conversely, the use of the neutrally charged Ficoll cocktail does not result in protein aggregates, but the cellular uptake of Ficoll may affect cell transparency – a potential issue should this model be adapted for clinical use. Although the ultrastructure of the ECM was not investigated in short-term cultures, ICC of hCFs cultured in medium crowded with carrageenan suggest that similar aggregates may be seen but on a much smaller scale.

### 4.6.1 Carrageenan

Carrageenans are polysaccharides derived from red seaweed that are used as thickening agents in the food industry. As previously mentioned, they can be distinguished by the number of sulphates per disaccharide unit (Carneiro-Da-Cunha *et al.*, 2011). In this study the carrageenan source was predominantly κ-carrageenan with some λ-carrageenan, with κ-carrageenan having one sulphate group and λ-carrageenan having three.

#### 4.6.1.1 Characterisation of carrageenan source

It has been reported that the optimal concentration of carrageenan, for increasing collagen deposition, is 75 µg/ml and that at this concentration carrageenan has a hydrodynamic diameter of approximately 1600 nm (Satyam *et al.*, 2014). Although this optimal concentration was determined using WS-1 fibroblasts (a cell line derived from human skin), the same trend was observed in human tenocytes and osteoblasts and 75 µg/ml carrageenan was later used with human corneal fibroblasts (Satyam *et al.*, 2014; Kumar *et al.*, 2015b, 2018). The reported hydrodynamic diameter of carrageenan varies from approximately 200 nm to 1600 nm and has been shown to increase with concentration (Satyam *et al.*, 2014; Gaspar *et al.*, 2019a). Where the larger diameter (approximately 1600 nm) was reported, carrageenan was dispersed in distilled water at 25°C (Satyam *et al.*, 2014). However, smaller diameters have been recorded when carrageenan is dispersed in Hank's Balanced Salt Solution (approximately 260 nm at 100 µg/ml), although the temperature, which is likely to be a key factor, was unreported (Gaspar *et al.*, 2019a). In this study, when dispersed in PBS at 20°C, the hydrodynamic diameter of carrageenan was 212.6 nm which is comparable to

the literature. Although unreliable due to measurement uncertainty (likely a result of the sample being too polydisperse), when dispersed in distilled water the hydrodynamic radius of carrageenan was 422 nm, almost double that measured when dispersed in PBS. This is further supported by Carneiro-da-Cunha *et al.* who found that increasing the ionic strength of the solvent, through the addition of sodium chloride, resulted in a lower reported hydrodynamic radius of κ-carrageenan (Carneiro-Da-Cunha *et al.*, 2011). The variation in results highlights the importance of mimicking physiological conditions to understand the effect of MMC in cell culture.

The polydispersity of carrageenan has previously been reported with nanoparticle tracking analysis, demonstrating that a solution of 75 µg/ml carrageenan contains molecules with sizes ranging from 10 nm – 2000 nm, although the solvent used was not stated (Satyam *et al.*, 2014). In the present study the polydispersity index was 0.39; lower than the 0.6 that has been found elsewhere (Gaspar *et al.*, 2019a). To investigate the potential presence of large aggregates when dispersed in PBS a carrageenan solution was passed through a 0.75 µm filter and both the hydrodynamic diameter and the polydispersity index were significantly reduced. These results suggest that when dispersed in PBS large molecules are present in carrageenan solutions which could have an effect on the crowding within culture media. In this study, and in previously published reports, the media supplemented with carrageenan was not filtered, therefore these large carrageenan aggregates are expected (Satyam *et al.*, 2014; Kumar *et al.*, 2015b). The presence of larger aggregates explains the increased the polydispersity index of unfiltered carrageenan when compared to the filtered version. The polydispersity of the carrageenan solution increased when measurements were recorded at 37°C, again highlighting the importance of mimicking physiological conditions. Although a measurement error was reported when the temperature was increased, the results suggest that carrageenan aggregates at physiologic temperatures. The effect of potential carrageenan aggregates on macromolecular crowding has not previously been discussed but this may have deleterious effects on collagen deposition. If it is assumed that aggregation can increase the effect of MMC, the excluded volume effect may be greater than originally expected for cells grown at 37°C. It is possible that increasing the excluded volume effect beyond an optimal level can result in over-crowding which may segregate procollagen from C-/N-proteinases. This could prevent the cleavage of procollagen and thus reduce the amount of type I collagen that is deposited.

The zeta potential at 37°C showed that CAR is negatively charged, as expected, and agrees with published data (Gaspar *et al.*, 2019a). Given that proteins such as procollagen

are negatively charged at physiological pH, this can result in a larger excluded volume effect with carrageenan repelling procollagen. A greater excluded volume effect is thought to accelerate the rate of collagen deposition *in vitro*, however, as discussed above, there is likely a limit before solutions become over-crowded (Lareu *et al.*, 2007a).

The FVO of carrageenan at 20°C in this study was calculated following conventional methods (Chen *et al.*, 2011). In the present study the FVO was reported to be approximately 40% however this is based on several assumptions: that the macromolecule has a well-defined molecular weight; that macromolecules are perfect spheres; that the macromolecule is electroneutral; and that there is only a single macrosolute present (Hall and Minton, 2003; Chen *et al.*, 2011). In the case of carrageenan, many of these assumptions are unlikely to be valid. The weight average molecular weight ranges from 450 – 650 kDa, with 550 kDa being used in this study (Uno *et al.*, 2001). Serum is used in the cultures described in this study and therefore the macromolecule albumin will also be present (Lareu *et al.*, 2007a). Despite these assumptions, the FVO is commonly reported when macromolecular crowding is employed, with the accepted caveat that it is a crude estimate (Rashid *et al.*, 2014; Gaspar *et al.*, 2019a; Gonzalez-Molina *et al.*, 2019). However, the assumptions can lead to unrealistic values greater than 100% being reported and thus should be used with caution (Gaspar *et al.*, 2019a; Gonzalez-Molina *et al.*, 2019).

#### 4.6.1.2 Short-term crowding with carrageenan

MMC has been used in cell culture to accelerate the deposition of collagen by cells cultured *in vitro* (Satyam *et al.*, 2014; Kumar *et al.*, 2015b). Carrageenan has been used as a crowder in cultures with dermal fibroblasts (Satyam *et al.*, 2016; Gaspar *et al.*, 2019a, 2019b), bone marrow stromal cells (Cigognini *et al.*, 2016; Gaspar *et al.*, 2019b), corneal fibroblasts (Kumar *et al.*, 2015b, 2018) and tenocytes (Satyam *et al.*, 2014; Gaspar *et al.*, 2019b) at concentrations ranging from 1 to 500 µg/ml. In this study, ICC revealed that crowding with carrageenan enhanced deposition of type I collagen from as early as day 2, supporting previously published data (Kumar *et al.*, 2015b; Cigognini *et al.*, 2016). As previously discussed, ascorbic acid is thought to be essential for the deposition of collagen as it is an essential cofactor for the hydroxylation of proline and lysine (Gelse *et al.*, 2003). To further investigate the effect of carrageenan on collagen deposition, hCFs were cultured without A2P supplementation for 7 days. Interestingly, enhanced collagen deposition was again observed in cultures crowded with carrageenan but this time without A2P supplementation. In the absence of ascorbic acid, it has been shown that small amounts of collagen can be

secreted into the culture media by fibroblasts *in vitro* however, little is integrated into the cell layer (Lareu *et al.*, 2007a). The successful deposition of collagens in the absence of A2P may be due to alternative reducing agents enabling the hydroxylation of proline *in vitro* (Evans and Peterkofsky, 1976; Chauhan *et al.*, 1985). It is, therefore, possible that macromolecular crowding enhanced the conversion of procollagen to collagen fibrils which could then be incorporated into the cell layer. For example, crowding may encourage the interaction of C-/N-proteinases with procollagen thus resulting in accelerated collagen fibrillogenesis. However, if ascorbic acid is necessary for the hydroxylation of proline, it is likely that the collagen protein will be incorrectly folded here, in the absence of A2P. Given that misfolded proteins cannot easily leave the endoplasmic reticulum, the apparent increase in collagen could be a result of the collagen antibodies and CNA35 binding directly to carrageenan (Canty and Kadler, 2005). To see if this was true, CNA35 was added to culture medium with carrageenan in the cell-free system. CNA35 was shown not to bind to carrageenan suggesting that the staining is specific to collagens. Perhaps, in the absence of A2P, misfolded collagens can still be secreted but form gelatin-like aggregates which the collagen antibodies can bind to. This could explain the unusual morphology of collagen observed.

#### 4.6.1.3 Long-term crowding with carrageenan

Typically, MMC has been used in short-term cultures with few extending beyond 15 days (Ang *et al.*, 2014; Graceffa and Zeugolis, 2019; Assunção *et al.*, 2020). In this study, the culture period was extended to 30 days in an attempt to promote the thickening of the matrix to mimic the corneal stroma. Crowding for 30 days with carrageenan resulted in the detection of aggregates using antibodies for collagens type I, III, V and VI, and aggregates were also detected using the CNA35 collagen probe. These aggregates disrupted the alignment of collagen, particularly when compared to hCFs cultured in A2PM on PTFE-nf. There is the caveat that the analysis of collagen alignment was only performed on one region of interest on each biological replicate, although the observation that aggregates disrupt collagen alignment is likely a true result. The lack of technical repeats is of more importance when comparing the alignment between substrates, particularly with glass and Transwell membranes where alignment may vary over the substrate. Aggregation has not been explicitly described in relation to crowding with carrageenan but has been observed when 500 kDa dextran sulphate was used (Lareu *et al.*, 2007a, 2007b; C. Chen *et al.*, 2009; Assunção *et al.*, 2020). Dextran sulphate is a negatively charged polymer that has been used to enhance

ECM deposition in tissue engineering and to create a rapid *in vitro* model of scar tissue (C. Chen *et al.*, 2009). At 100 µg/ml dextran sulphate has a reported FVO of 5.2% (Lareu *et al.*, 2007b), however as little as 10 µg/ml is sufficient to enhance collagen deposition which equates to an FVO of 0.52% (Assunção *et al.*, 2020). Given that this is such a low value, the authors proposed that the increase in ECM observed isn't the result of MMC alone. Assunção *et al.* used Alcian blue staining to observe dextran sulphate deposits in a cell-free system and found that they colocalised with type I collagen and fibronectin aggregates (Assunção *et al.*, 2020). Dextran sulphate did not form deposits in the absence of proteins, suggesting that the crowder interacted with the proteins supporting previously published data (Ruoslahti *et al.*, 1979). It is possible that carrageenan may interact with proteins in a similar way, leading to their co-deposition and aggregation. Similar observations have been made when using the negatively charged 200 kDa polysodium-4-styrene sulfonate (PSS) (Peng and Raghunath, 2010). Here, type I collagen and fibronectin were both observed to aggregate after 2 days of fibroblast culture when crowded with PSS. Given that the formation of collagen aggregates has been reported with the use of other negatively charged crowders, it is likely that the apparent aggregation observed in this study was as a result of carrageenan's negative charge.

The increase in type III collagen observed here has previously been reported with MMC using carrageenan in media supplemented with 0.5% new born calf serum and 0.5% human serum (Kumar *et al.*, 2015b). Type III collagen is associated with myofibroblasts and scar tissue within the stroma. The presence of type III collagen may suggest that the hCFs had started to transition into myofibroblasts but, the lack of α-SMA expression in CAR cultures contradicts this. However, to better image the deposited collagen, as opposed to intracellular collagen, the cells were not permeabilised prior to ICC. Although there have been reports of successful staining with the anti-α-SMA antibody without permeabilisation, there is a small possibility that if the cells were first permeabilised the staining would reveal specific expression of α-SMA filaments.

#### 4.6.1.3.1 Ultrastructural analysis of collagen deposited in a carrageenan-crowded system

The impact that MMC has on the ultrastructure of collagen deposited by cells is rarely investigated. Given the unusual staining observed at the light microscopy level when cells are crowded with carrageenan, TEM was employed to gain a better understanding of the effect that MMC has on collagen. Under normal culture conditions (A2PM) very little collagen could be found when cells were cultured on PTFE-nf, likely due to the relatively low seeding

density used. However, when cultured at a higher cell density on Transwell membranes, collagen fibrils were observed. These collagen fibrils formed lamellar-like structures with fibril orientation changing direction, similar to the arrangement within the native corneal stroma, as has been previously shown (Guo *et al.*, 2007).

The addition of carrageenan showed an increase in large, fibrillar extracellular components, which was seen in hCFs cultured on both PTFE-nf and on Transwell membranes. It is possible that the large banded structures observed are residual carrageenan that has bound to the cell layer and remained post-washing. TEM studies of carrageenan gels have revealed aggregates that can form fine networks but whose structure differs from the ECM seen in this study (Walther *et al.*, 2006). It may also be possible that the observed matrix is as a result of the co-deposition of carrageenan and matrix proteins, as discussed previously. A 2007 study by Lareu *et al.* used TEM to view the pericellular matrix 48 hours after culture with dextran sulphate (Lareu *et al.*, 2007b). Cell layers were pelleted and embedded in agarose prior to EM where aggregates with cross-striation resembling collagen were found (Lareu *et al.*, 2007b). However, given the short culture period and the differences in sample processing, the results cannot be directly compared. Immuno-electron microscopy, the labelling of structures with gold particles prior to TEM, could reveal whether or not the structures observed in this study are ECM proteins.

#### 4.6.1.3.1.1 Collagen aggregates may be fibrous long-spacing collagen

The banding pattern of the aggregates observed indicated a periodicity greater than that observed in most fibrillar collagens (67 nm). Fibrous long-spacing (FLS) collagens are collagens with a periodicity greater than 67 nm, although typically the periodicity exceeds 100 nm (Paige *et al.*, 1998). They have been found in pathologic tissues (when found in neural tissues these are referred to as Luse bodies (Luse, 1960)) and *in vitro* (Hashimoto and Ohyama, 1974). There are believed to be four different morphologies that the FLS collagen can present, dependent on the banding pattern observed via TEM (Paige and Goh, 2001). The different morphologies are characterised by the number and the width of bands evident after being negatively stained and imaged via TEM (Chapman and Armitage, 1972). FLS I has a periodicity of 250 nm with one narrow overlap band per period; FLS II has a periodicity of 250 nm but possesses two narrow overlap bands that are close together; FLS III (periodicity of 100 nm) contains four narrow overlap bands with interbands of a comparable size and FLS IV (periodicity of 170 nm) has one broad overlap band (Chapman and Armitage, 1972; Paige and Goh, 2001). The composition of the FLS collagen is somewhat unknown with research

suggesting it could be derived from the basement membrane and be composed of laminin and type VI collagen (Miki *et al.*, 1993). However, FLS collagen can also be prepared *in vitro* by dialysing an acidic type I collagen solution mixed with a glycoprotein (Paige and Goh, 2001; Wen and Goh, 2006).

FLS collagens have also been referred to as filamentous collagen aggregates that have been described in pathological tissues and have been found in collagenase-treated tissues (Figure 4.21 A-C) (Kobayasi *et al.*, 1985; Miki *et al.*, 1993; Paige *et al.*, 1998). Based on the observation of aggregates in collagenase-treated tissues, it can be hypothesised that the fibrillar aggregates found in this study are as a result of collagen degradation. MMC with carrageenan can increase the activity of MMPs, specifically MMP-2 (Cigognini *et al.*, 2016; Satyam *et al.*, 2016; Tsiapalis *et al.*, 2020) and MMP-9 (Tsiapalis *et al.*, 2020), in cultures up to 14 days. Beyond 14 days MMP activity may increase further in crowded conditions and result in consistent collagenolysis causing the aggregates observed in this study. However, MMC has also been shown to increase the expression of procollagen C proteinase enhancer 1 (PCPE1) (Lareu *et al.*, 2007b). PCPE1 is a protein that not only enhances the activity of C-proteinases, and thus the deposition of collagen, but also inhibits MMP-2 (Mott *et al.*, 2000; Löffek *et al.*, 2011). Further work into the effect that crowding has on MMP expression and ECM remodelling is required to understand the cause of the aggregates observed in this study. Specifically, monitoring the activity of MMPs and their inhibitors, TIMPs, over time could reveal if there is an imbalance between the degradation and synthesis rate of collagen.

Similar aggregate structures have also been found in the Descemet's membrane of diabetic rats (Akimoto *et al.*, 2008) and in the corneal stroma of diabetic patients (Rehany *et al.*, 2000; Kowalczuk *et al.*, 2013). It has been proposed that excessive glycation may result in the presence of FLS collagen however, the mechanism behind this is unknown. It may be possible that MMC with carrageenan results in pockets of concentrated media and supplements, such as glucose, resulting in excess glycation.

#### 4.6.1.3.1.2 Collagen aggregate may be aggregates of type VI collagen

Type VI collagen is a beaded-filament found within the corneal stroma with a beaded repeat of 105 nm (Cescon *et al.*, 2015). A 2002 study compared the structures of banded aggregates, found in the Bruch's membrane of pathologic retinas, with type VI collagen using electron microscopy (Knupp *et al.*, 2002). The banded aggregates found in the Bruch's membrane had a periodicity of 80 – 110 nm and both single and double banded structures were observed (Figure 4.21 D). The single bands were the same width as the double bands suggesting that

the gaps could somehow be filled with a protein. Sorsby's fundus dystrophy, a disease that affects the Bruch's membrane, is characterised by a mutation of TIMP-3. Although the mutation does not affect the ability of TIMP-3 to inhibit MMPs, the mutated TIMP-3 is more resistant to degradation and thus an accumulation occurs (Knupp *et al.*, 2002). Knupp *et al.* hypothesise that the protein interacting with type VI collagen and filling the gaps in the double banded structure is the mutated TIMP-3 (Knupp *et al.*, 2006). These aggregates were seen adjacent to typical 105 nm type VI collagen beaded-filaments which led the authors to hypothesise that beaded-filaments are a precursor to the aggregates. Knupp *et al.* also showed that intermediates exist where secondary banding is evident, possibly showing the interaction of proteins filling the gap in double banded aggregates (Knupp *et al.*, 2006). Knupp *et al.* suggests that the banded structures previously termed fibrous long-spacing collagen may in fact be type VI collagen aggregates. This is supported by earlier research by Bruns and colleagues who used immuno-EM to confirm that fibrils with a 100 nm periodicity are type VI collagen (Bruns *et al.*, 1986). Here, adenosine triphosphate was added to fibroblast cultures to induce aggregation of thin filaments (Bruns *et al.*, 1986). Of particular interest is their observation of these fibrils coating type I collagen fibrils in rat tail tendons (Figure 4.21 E). In this study, TEM did not reveal any typical type I collagen fibrils in carrageenan-supplemented cultures despite ICC suggesting the presence of type I collagen deposits. If type VI collagen aggregates can cover type I fibrils this may explain the apparent absence of type I collagen in EM micrographs.

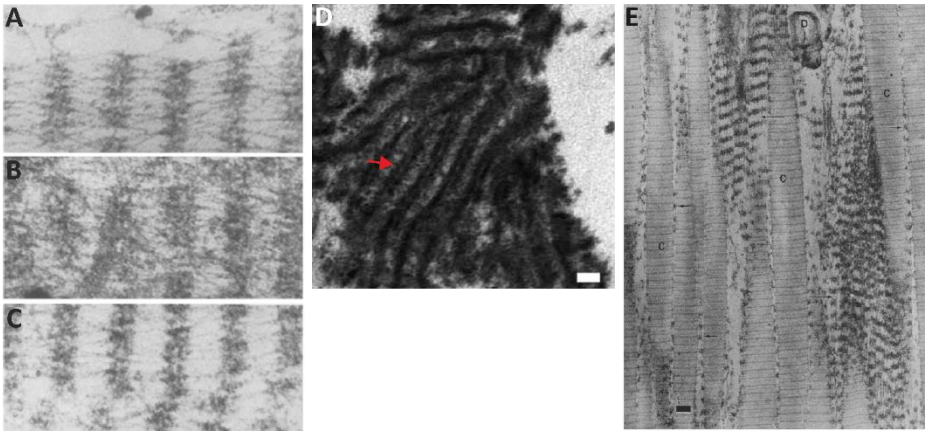


**Figure 4.21 A comparison of the different collagen aggregates observed.** A: Filamentous aggregates have been observed in collagenase-treated dermis; B: in the dermis of morphea; C: in cultured dermis. Images from (Kobayasi *et al.*, 1985). Scale bars were absent from these images. D: Single- and double-banded aggregates have also been found in the retina of patients with Sorsby's fundus dystrophy and these are likely type VI collagen aggregates. Red arrow indicates area where double-banded aggregates can be seen. Figure adapted from (Knupp *et al.*, 2006). E: Similar aggregates were found by Bruns *et al.* in rat tail tendon after treatment with adenosine triphosphate (Bruns *et al.*, 1986). The aggregates are thought to be type VI collagen which partially coat type I collagen fibrils. Scale bars represent 100 nm (D and E).

#### 4.6.1.3.1.3 Collagen aggregates may be a result of anomalous diffusion and increased fibril nucleation sites

Anomalous diffusion is defined as diffusion in which the mean squared displacement does not increase linearly with time (Dix and Verkman, 2008). MMC with larger molecules can result in the anomalous subdiffusion of molecules of interest, such as procollagens, resulting in them being restricted to a reduced area (Chau *et al.*, 2020). Whilst this can be beneficial, and result in the increased cleavage of procollagens by C-/N-proteinases, it may also have a detrimental effect. One model of collagen fibrillogenesis suggests that the process of collagen fibril formation is based on diffusion limited aggregation (Parkinson *et al.*, 1995). By reducing the rate of diffusion via MMC with large molecules, such as carrageenan, it is possible that collagen fibrillogenesis is halted and thus shorter, incomplete fibrils are formed. Given that carrageenan has a large hydrodynamic radius and is negatively charged (and thus repels procollagen molecules), it is possible that the available area for procollagen molecules and proteinases is restricted beyond an optimal level. The aggregates could, therefore, be incomplete collagen fibrils which antibodies can also bind to.

*In vivo* collagen fibrillogenesis is dependent on the formation of fibronectin, a matrix protein that serves as a template for collagens (Kadler *et al.*, 2008). Along with other matrix proteins, macromolecular crowding has also been shown to increase fibronectin deposition

which, in turn, corresponds to an increase in potential collagen nucleation sites (Kumar *et al.*, 2015b, 2018; Graham *et al.*, 2019). When Graham *et al.* limited the amount of accessible fibronectin, by cross-linking a fibronectin coating to a substrate prior to cell seeding, they found that crowding with a Ficoll cocktail no longer increased the deposition of type I collagen. This highlights the importance of fibronectin in collagen nucleation and fibrillogenesis and MMC (Graham *et al.*, 2019). By increasing the number of nucleation sites, it is possible that collagen fibrillogenesis begins but that the fibrils cannot elongate either as a result of anomalous subdiffusion limiting fibril growth or, simply, because the procollagen molecules are incorporated into fibrils at a faster rate than they are secreted by the cells. This could result in incomplete collagen fibrils which may resemble those seen in cultures crowded with carrageenan.

#### 4.6.1.3.2 The effect of crowding with carrageenan on construct transparency

Perhaps unexpectedly, the disruption to collagen did not have a detectable impact on the transparency of the *in vitro* model. At both 350 and 560 nm there was no significant decrease in light transmission. As the ICC analysis shows, the collagen aggregates are not consistent across the sample. There is a small possibility that the light transmission was measured in an area adjacent to a collagen aggregate, allowing light to pass through. This may offer a potential explanation as to why there was no significant decrease in transmission but, the averaging of the technical and biological replicates should have corrected for this. It is also interesting that whilst not significantly different, the transmission of light through cultures in A2PM on glass compared to those on PTFE-nf was not identical. As a hydrophobic material, PTFE-nf restricts the attachment area to some extent which may result in areas of a higher cell density and cause a decrease in light transmission (Kearns *et al.*, 2010). Corneal fibroblasts are associated with corneal haze and a loss of transparency, compared to keratocytes (Jester *et al.*, 1999), specifically the expression of corneal crystallin ALDH3A1 is decreased in corneal fibroblasts (Pei *et al.*, 2006). The knockout of ALDH3A1 in mice has been linked to an increase in light scattering and corneal haze and therefore, a high cell density of fibroblasts may result in a further decrease in transparency (Chen *et al.*, 2017). An alternative explanation relates to the orientation of hCFs on each substrate. When cultured on PTFE-nf, the cells follow topographical cues to align parallel to the nanofibres and create a structure resembling a lamella within the corneal stroma. On glass, where there are no topographical cues, hCFs have shown short-range order where they can produce roughly orthogonal layers (Figure 4.6). Absorbance measurements taken in areas of short-range order are likely to be

less than those taken where cells are randomly oriented, resulting in greater light transmission. This could explain the high transmittance values of cultures cultured in A2PM on glass (92.4% at 560 nm) compared to those on PTFE-nf (84.8% at 560 nm) and why there is no significant difference between uncrowded cultures.

#### 4.6.1.3.3 The effect of crowding with carrageenan on cell viability

Surprisingly, at low cell numbers, crowding with carrageenan resulted in the death of hCFs and so the effect on metabolic activity over time could not be studied. This has not been reported in the literature and contrasts the earlier results of this study, where cells survived up to day 30 on Transwell membranes and PTFE-nf, when seeded at higher number. For the metabolic activity study, cells were seeded on a smaller substrate, and thus at a lower cell number, it is possible that seeding more cells provided some sort of protection against crowding as they increase in number. To further understand the cytotoxic effects observed at a lower cell number, the relative proportion of carrageenan in each culture can be calculated. In the main cell culture experiments, carried out in a 6-well plate, carrageenan was added to the cells at a concentration of 11.25 ng/cell. In the growth and metabolic activity assay, which was conducted in a 48-well plate, carrageenan was added at a concentration of 7.8 ng/cell. Although this does not explain the apparent cytotoxicity of carrageenan at low cell numbers, similar findings of cell death after crowding with carrageenan have been observed elsewhere with hCFs (Ebraheim Ismail, personal communication at ARVO, 2019).

### 4.6.2 Ficoll cocktail

In this study mixed-MMC was employed using a Ficoll cocktail composed of Ficoll 70 kDa and Ficoll 400 kDa.

#### 4.6.2.1 Characterisation of Ficoll cocktail source

Two particle sizes of approximately 10 nm and 65 nm were found in the Ficoll cocktail at 20°C. Similar sizes have been reported by Gaspar *et al.* at approximately 10 nm and 70 nm. However, the reported values differ to those obtained when Ficoll 70 and Ficoll 400 were measured separately (approximately 10 nm and 25 nm respectively) (Gaspar *et al.*, 2019a). The authors suggest that particle aggregation may occur when these molecules are mixed together in a compound thus increasing polydispersity (Gaspar *et al.*, 2019a). Furthermore, the results of the present study suggest that aggregates also form at temperatures of 37°C.

The polydispersity index of the Ficoll cocktail in this study was around 0.5, which agrees with previously published data (approximately 0.46). This has been shown to roughly equate to the sum of the individual polydispersity indices for Ficoll 70 plus Ficoll 400 (Gaspar *et al.*, 2019a). Other reported values for the size of Ficoll 70 and Ficoll 400 are 8 nm and 16 nm respectively (Chen *et al.*, 2011). Using these values, the authors estimate that that the respective FVOs would be 8.7% and 8% and so the cocktail would have an FVO of 17% (Chen *et al.*, 2011). Based on the particle sizes observed in this study, 10 and 65 nm, the respective FVOs would be 16.9% and 541.2% and so the cocktail would have an estimated FVO of 558%. This large value highlights the limitations of FVO and why it should be used with caution when studying systems with more than one macromolecule present. It is hard to predict how the aggregates would interact with the other Ficoll particles and the macromolecules found within cell culture medium, such as albumin, but it is likely to alter the calculated FVO. DLS measurements of nanoparticles in cell culture medium supplemented with 10% FBS, as used in this study, have been shown to be unreliable thus making it harder to predict the interactions between macromolecular crowders and cell culture medium (Gollwitzer *et al.*, 2016).

Ficoll is a neutral polysaccharide and this is thought to result in a weaker volume excluding effect, which is supported by the fact that molecules which are similar in molecular weight (MW) can have very different hydrodynamic diameters. Harve *et al.* observed that negatively charged dextran sulphate (MW 500 kDa) had a hydrodynamic diameter three times greater than Ficoll 400 (MW 400 kDa) (Harve *et al.*, 2006). Charged molecules will experience intramolecular electrostatic repulsion resulting in a more open structure, thus appearing to have a much greater hydrodynamic diameter. A molecule with a larger hydrodynamic diameter will occupy more space (greater FVO). To overcome this Ficoll is often combined with a molecule of a different size to create a cocktail with a greater FVO than mono-MMC with Ficoll 400, as described in this chapter (Zeiger *et al.*, 2012; Ang *et al.*, 2014).

#### 4.6.2.2 Long-term crowding with Ficoll cocktail

Mixed-MMC with a Ficoll cocktail has been used to accelerate collagen deposition in cultures of dermal (Gaspar *et al.*, 2019a) and corneal fibroblasts (Kumar *et al.*, 2015a) but has had variable effects in bone marrow stromal cell cultures (Zeiger *et al.*, 2012; Cigognini *et al.*, 2016). In the present study, an apparent increase in type I collagen deposition was observed when hCFs were crowded with the Ficoll cocktail and the collagen appeared to have a similar

arrangement to the control samples, with little difference in alignment. Unlike crowding with carrageenan, the Ficoll cocktail did not appear to increase type III collagen deposition. Type III collagen is associated with myofibroblasts and scar tissue within the stroma, the absence of which suggests that the hCFs have not transitioned into myofibroblasts. This is further confirmed by the apparent absence of α-SMA staining in FC cultures. However, as previously mentioned, the cells were not permeabilised prior to ICC and it is possible that permeabilisation would reveal more specific α-SMA expression. Previously published data has reported that the crowding of hCFs with a Ficoll cocktail does result in an increase in type III collagen deposition at days 2, 4 and 6 (Kumar *et al.*, 2015a). The differences observed between this study and that reported by Kumar *et al.* may be caused by the different sources and concentrations of sera used. In this study, 10% FBS was used to culture the hCFs whereas Kumar *et al.* used 0.5% human serum to reduce exogenous MMP-2 (Kumar *et al.*, 2015a). Serum-free media supplemented with FGF-2 has been shown to increase the expression of COL3A1 whilst maintaining low α-SMA expression (Lynch *et al.*, 2016). The additional supplementation of insulin-like growth factor 1 (IGF-1) can decrease the expression of COL3A1 without increasing α-SMA expression (Lynch *et al.*, 2016). Therefore, it is possible that the increased type III collagen deposition observed by Kumar *et al.* was as a result of the low concentration of serum, and growth factors, used. The results of the present study indicate that use of a Ficoll cocktail suitably accelerate the production of an *in vitro* corneal stroma model when used in sera containing media.

#### 4.6.2.2.1 Ultrastructural analysis of collagen deposited in a Ficoll-crowded system

Ultrastructural analysis was used to analyse the orientation of the collagen deposited. It was shown that MMC with the Ficoll cocktail appeared to increase the amount of collagen deposited by hCFs on PTFE-nf, supporting ICC analysis. However, the hCFs contained many large vesicles within each cell, a phenotype not observed when cells were cultured in uncrowded or carrageenan-crowded media. This became more apparent when cells were cultured at a higher cell density on Transwell membranes and multiple cells could be seen in one field of view. These vesicles may be evidence of the uptake of Ficoll by the fibroblasts (Zeiger *et al.*, 2012). Following a 24 hour incubation period with fluorescently labelled Ficoll 400 and Ficoll 70, Zeiger *et al.* reported that bone marrow derived-MSCs displayed punctate intracellular staining, suggesting that Ficoll can be endocytosed by MSCs (Zeiger *et al.*, 2012). Zeiger *et al.* deduced that only minor uptake of Ficoll was observed over 24 hours and this was unlikely to increase crowding within the cell. However, the results of the present study

suggest that the long-term culture of hCFs with Ficoll can result in large uptake of the polysaccharide. The process through which Ficoll is taken up by the cell is through caveolae-dependent pinocytosis (a form of endocytosis where particles in the extracellular fluid are taken up by the cell) (Rashid *et al.*, 2014). Both Ficoll 400 and Ficoll 70 have been shown to co-localise with lysosomes post-pinocytosis (Rashid *et al.*, 2014). It is possible that once inside the acidic environment found within lysosomes that Ficoll is degraded into sucrose moieties. From here the sucrose may act osmotically and draw water into the lysosome, resulting in the swelling of the lysosome, which can now be termed a 'sucrosome'. The large vesicles observed in the TEM micrographs in this study may be these swollen sucrosomes. If hCFs secrete sucrase, the sucrose can be hydrolysed into glucose and fructose which can then be released into the cytosol. As the media were replaced every 2 – 3 days, there will be a constant uptake of Ficoll which will result in the constant formation of sucrosomes. Although these vesicles were not observed in the carrageenan-crowded hCFs, it is likely that the cells also took up carrageenan. The presence of the vesicles in the Ficoll-crowded system is not unexpected given the high concentration of particles added – 1000 times greater than carrageenan. Unlike crowding with carrageenan, hCFs cultured with a Ficoll cocktail deposited collagen fibrils with the typical banding pattern, comparable to those observed in uncrowded conditions. Similarly, the collagen fibrils can be seen to change direction when cultured on Transwell membranes although these lamellae do not appear to extend over the same distance that was observed in uncrowded samples.

#### 4.6.2.2.2 The effect of crowding with a Ficoll cocktail on construct transparency

Crowding with Ficoll did have a small effect on the transparency of the hCF constructs at 560 nm. Although no distinguishable differences were observed between hCFs cultured on PTFE-nf in A2PM compared to constructs cultured in FC, there was a small decrease in transmission between hCFs cultured on glass in A2PM and crowded samples. In short-term cultures of 6 days no differences in transparency have previously been reported with crowded and uncrowded samples both exhibiting transmittance close to a PBS control (Kumar *et al.*, 2015a). The extended culture period used in the present study may account for the differences in transparency observed, with a prolonged culture period resulting in an increase in cell number. The endocytosis of Ficoll is likely to have directly affected cellular transparency by causing a change in the refractive index within the cell. Similarly, the uptake of Ficoll may also impact the expression of corneal crystallins. Although not investigated in this study, as the expression is typically reduced in corneal fibroblasts, corneal crystallins

help to maintain cellular transparency by creating short-range order within the cell thus reducing any fluctuations in the refractive index, reviewed in (Jester, 2008). It is possible that intracellular Ficoll may reduce the expression of corneal crystallins and further affect cell transparency. Furthermore, the fibrils seen in the TEM images of hCFs crowded with Ficoll do not seem to be as homogeneous in diameter as those in the control. This may be an artefact of sample sectioning and not a true phenotype of MMC with Ficoll – serial sectioning of the sample, along with an increase in the number of replicates may help to confirm this. If, however, this is a true phenotype and crowding with the Ficoll cocktail results in misshapen and irregular collagen fibrils, this will further affect the transparency of the culture (Chakravarti *et al.*, 2000).

#### 4.6.2.2.3 The effect of crowding with a Ficoll cocktail on cell viability

Surprisingly, despite the ultrastructural appearance of the hCFs when cultured in FC, there were no differences in either cell number or metabolic activity of the cells compared to those cultured in A2PM. This data supports previous findings which report that the metabolic activity of cells cultured in the presence of a Ficoll cocktail does not change after 6 days (Satyam *et al.*, 2014; Kumar *et al.*, 2015a). These results imply that the abundance of vesicles within the hCFs does not have a detrimental effect on cell proliferation, metabolic activity or collagen synthesis. Nevertheless, the vesicles may be having an effect on a variable that was not measured in this study.

## 4.7 Conclusions

In this study two macromolecular crowders were assessed for their potential to accelerate collagen deposition within the *in vitro* model of the corneal stroma. Both carrageenan and the Ficoll cocktail appeared to increase the deposition of collagen but the qualitative nature of ICC meant that this could not be quantified. Ultrastructural analysis of collagen revealed that lamellar-like structures were formed when hCFs were cultured on Transwell membranes in uncrowded media, as previously described, suggesting that this substrate is best suited to the creation of an *in vitro* stroma model (Guo *et al.*, 2007). Ultrastructural analysis also revealed that crowding with carrageenan resulted in large collagen aggregates, whilst crowding with a Ficoll cocktail resulted in the uptake of Ficoll within vesicles that slightly reduced transparency.

The data presented in this chapter suggest that carrageenan is not a suitable crowder for corneal stroma tissue engineering. Uniform collagen, with a small fibril diameter and

regular intrafibrillar spacing, is a key component in maintaining stroma transparency and this is disrupted by large aggregates when crowding with carrageenan. Although transparency was disrupted, the Ficoll cocktail may suitably accelerate collagen deposition. The possible deleterious effects of intracellular Ficoll uptake requires further investigation prior to its use in tissue engineering. Alternatively, the use of a cocktail containing other neutrally charged macromolecular crowders could be considered. Polyethylene glycol (PEG) is a neutral polymer that has previously been used to accelerate the conversion of procollagen to collagen in dermal fibroblast cultures (Bateman *et al.*, 1986). More recently, PEG with a molecular weight of 600 kDa has been shown to increase collagen deposition in an adenocarcinoma cell line (Gonzalez-Molina *et al.*, 2019). The calculated (supraphysiologic) FVO (300%) achieved through crowding with PEG also induced cell alignment. Given that cell and matrix alignment is essential when trying to recapitulate the corneal stroma, PEG may prove to be a useful macromolecular crowder.

MMC with both dextran sulphate and a Ficoll cocktail has been used with TGF-β1 to create *in vitro* models of lung and skin fibrosis (C. Chen *et al.*, 2009; Juhl *et al.*, 2020). These models have been used as screening tools for anti-fibrotic therapies by companies such as GlaxoSmithKline and Nordic Bioscience (Juhl *et al.*, 2020; Rønnow *et al.*, 2020). The approach described here can be adapted to create a model of a corneal scar by stimulating the cells with TGF-β1, inducing myofibroblast differentiation and further stimulating collagen deposition. The stromal scar model would be useful to test anti-fibrotic therapies, targeting corneal haze, such as human recombinant decorin (Hill *et al.*, 2018).

## 4.8 Limitations and Future work

The limitations of this study include the low number of biological replicates, particularly with the TEM analysis. TEM has its own limitations such as the small field of view which can provide a challenge when trying to draw conclusions about the gross effect of crowding, cell viability and collagen deposition. However, as the described phenotypes were observed in constructs cultured on both PTFE-nf and on Transwell membranes, it is likely that these observations are representative of each culture condition.

Future work would include the fluorescent labelling of Ficoll prior to cell culture and subsequent live cell imaging. This would allow for the tracking of Ficoll particles after they are endocytosed to see how long they remain within the cell, if they are eventually released or accumulate indefinitely, using a pulse-chase protocol. Equally, if a specific antibody becomes available, the labelling of constructs with an anti-carrageenan antibody may help

to determine whether residual carrageenan remains after processing or if carrageenan is incorporated into the ECM. The live cell imaging of collagen deposition using CNA35 and CTR, as described in Chapter 3, in carrageenan-crowded media would enable the visualisation of aggregate formation which could help to understand their formation. Similarly, the use of correlative light-electron microscopy, can be used to identify the time point at which aggregation occurs. This, combined with immuno-EM, may reveal whether or not the aggregates do coat type I collagen fibrils and confirm if the aggregates are, at least in some part, formed of type VI collagen.

# Chapter 5. General discussion

## 5.1 General discussion

The corneal stroma is composed of heterotypic type I/V collagen fibrils which are small in diameter to maintain corneal transparency. These fibrils form lamellae which are arranged roughly orthogonally throughout and provide the cornea with its mechanical strength. An *in vitro* model of the stroma could be used to investigate stroma wound healing and collagen fibrillogenesis whilst also reducing the number of animal models used in research. An ideal model would be composed of an ECM that resembles the microarchitecture of the corneal stroma. The main aim of this thesis was to identify a suitable cell source and substrate for the development of an *in vitro* corneal stroma model, as well as employing macromolecular crowding to increase the deposition of collagen.

A suitable cell source is one that is easily obtained, readily expanded and can deposit an ECM with a similar composition as the native stroma. Substrates can modulate cell behaviour and the provision of topographical cues can induce cell alignment which can lead to the deposition of an organised matrix. However, cells cultured *in vitro* are removed from their typical microenvironments that are crowded with macromolecules. Here, the conversion of procollagen to collagen can be slow. The addition of inert macromolecules to aqueous culture media can increase the rate of collagen deposition, thus reducing the culture time necessary to create a stroma model.

Human corneal stromal stem cells (hCSSCs) have been shown to differentiate into keratocytes and deposit an organised ECM, suggesting these cells have great potential for use in a stroma model (Wu *et al.*, 2012, 2013). In this study, however, the isolated population of hCSSCs was heterogeneous resulting in both inter- and intra-donor variability in the expression of stem cell markers. The isolated populations also transitioned into cells with a fibroblast-like morphology by passage 2, indicative of a phenotype change. These cells were difficult to culture and, as a result, hMSCs were considered as an alternative cell type. Despite also displaying inter-donor variability, hMSCs were capable of trilineage differentiation and, when cultured in keratocyte differentiating medium (KDM), expressed two proteoglycans commonly associated with keratocytes – keratocan and lumican (Carlson *et al.*, 2005). A cell sphere was formed when the medium was switched to KDM and so substrates with topographical cues were used to encourage cell alignment. Human corneal fibroblasts (hCFs) were easily isolated and readily expanded, which may explain their widespread use in corneal tissue engineering (Guo *et al.*, 2007; Proulx *et al.*, 2010; Priyadarsini *et al.*, 2016b). For these reasons, hCFs and hMSCs were incorporated into *in vitro* stroma models.

The ideal model of the stroma would consist of an organised ECM, which can be achieved by aligning cells – a compromise between the natural morphology of keratocytes and the deposition of an organised ECM. *In vivo* keratocytes are dendritic-like cells with interconnecting lamellipodia. Providing cells with aligned, topographical cues can result in the cells becoming polarised and their processes unable to extend perpendicular to the topographical features. This would prevent keratocytes from exhibiting their characteristic dendritic morphology but would allow for the deposition of an aligned matrix. However, this is less of an issue with hCFs, which are inherently spindle-shaped. Two substrates with aligned, linear nanotopographical features were investigated in this study: PTFE nanofibres (PTFE-nf) and polycarbonate Transwell membranes. The high seeding density used in the Transwell model meant that there was an apparent increase in collagen deposition when compared to those cultured on PTFE-nf. However, the topographical cues provided by the PTFE-nf resulted in a significant increase in hCF alignment which translates to the alignment of the deposited ECM. Furthermore, hCFs cultured on PTFE-nf formed an angle shift between 30° – 55°, relative to the first layer. hCFs on Transwell membranes did also shift in angle between the first and top layers but the distribution of angles was still broad, likely a result of the non-uniform distribution of grooves found on the Transwell membranes. Whilst both substrates appeared to support the growth of hMSCs in KDM, neither were successful in supporting keratocyte differentiation. The addition of topographical cues did not prevent the formation of cell spheres and α-SMA expression was observed in cultures on Transwell membranes, indicative of a myofibroblast phenotype. Both substrates were further investigated, as each had its own benefits, with PTFE-nf increasing cell alignment and the Transwell membrane, with the large cell number, appearing to deposit more collagen.

To increase collagen deposition, macromolecular crowding was incorporated into the corneal stroma models. The polydispersity and charge of crowders is known to affect collagen deposition. Two commonly used crowders were trialled – carrageenan, a negatively charged polysaccharide, and a Ficoll cocktail of neutral charge. At an early timepoint, carrageenan appeared to increase type I collagen deposition however, labelling with CNA35 suggested that the collagen formed aggregates. Longer time points confirmed this, with ICC analysis showing aggregates of collagen at day 30, whereas the Ficoll cocktail resulted in an apparent increase of fibrillar collagen. The ultrastructural analysis of collagens in a crowded system is under-investigated, with few studies investigating the ultrastructure of the deposited ECM (Lareu *et al.*, 2007b). TEM of the deposited collagen revealed that crowding with carrageen resulted in the formation of large banded structures, possibly the aggregated

form of type VI collagen, typically seen in pathological tissues. TEM also revealed the apparent uptake of Ficoll by the hCFs, evidenced by the presence of large vesicles. This supports the previous finding by Zeiger *et al.* who observed the uptake of Ficoll by bone marrow-derived MSCs (Zeiger *et al.*, 2012). Despite this, no cytotoxic effects were observed when crowding with the Ficoll cocktail and its use in the stroma model may suitably accelerate collagen deposition. Alternatively, other neutrally charged crowders could be investigated to avoid the cellular uptake of the macromolecules.

## 5.2 Summary of main findings

This study demonstrated:

1. hCFs are readily available cells that can be easily incorporated into an *in vitro* model
2. PTFE nanofibres provide topographical cues which result in the alignment of hCFs and deposited collagens (more so than cultures on Transwell membranes)
3. Long-term culture (up to 30 days) of hCFs on PTFE-nf can result in cell stratification and a shift in alignment between 30 – 55°
4. Ultrastructural analysis of hCFs cultured on Transwell membranes showed the formation of loose lamellar-like collagen
5. Crowding with carrageenan resulted in the formation of collagen aggregates with an ultrastructure resembling that of fibrous long-spacing collagen and type VI collagen aggregates
6. Macromolecular crowding with Ficoll appeared to increase collagen deposition by hCFs on PTFE-nf, although ultrastructural analysis revealed cellular uptake

## 5.3 Suggestions for future work

To further optimise the hCF stroma model, the culture media could be switched to a low-glucose, serum-free medium which may rescue the keratocyte phenotype. Other cell sources could be investigated, such as iPSCs or early-passage MSCs, and differentiated into keratocytes. The alternative compositions of KDM could also be investigated, as described by Bray *et al.* (Bray *et al.*, 2012). Alternatively, corneal stromal cells could be expanded in a low-serum medium, as described by Yam *et al.*, and then serum-starved to induce an activated keratocyte phenotype prior to incorporation into the model (Yam *et al.*, 2015). Identifying and comparing other macromolecular crowders, such as polyethylene glycol (PEG), to the Ficoll cocktail used in this study may also improve the model. It is possible that

other neutrally charged crowder (e.g. PEG) may increase the rate of collagen deposition without the potentially deleterious effects of intracellular Ficoll uptake

To further understand the effect that crowding with carrageenan has on collagens ultrastructural analysis of collagen deposited after a shorter timeframe (e.g. 7 days) could be undertaken. Immunocytochemistry suggested that type I collagen was not as aggregated at day 7 when compared to day 30. Performing TEM at an earlier timepoint may show the formation of the protein aggregates and could show the early stages of type VI collagen aggregates covering type I collagen fibrils. Additionally, using immuno-EM to label the aggregates would reveal if type I collagen fibrils are present or if the aggregates are formed purely of type VI collagen. Finally, ultrastructural analysis of collagens deposited when crowded with other negatively charged crowders can be used to see if the results observed in this study are specific to carrageenan or are an attribute of the negative charge.

If an ideal cell line were to be produced it would be one where the ECM deposited could be fine-tuned with ease. For example, the addition of a certain combination of growth factors (e.g. TGF-β3, FGF-2 etc.) would result in the deposition of heterotypic type I/V collagen fibrils with a diameter of around 30 nm, similar to that produced by keratoblasts. By being able to perfectly control the components of the matrix that is deposited, one could use the collagen probe to investigate mammalian stromal development. To speculate further, if the cell line could be manipulated so that it suddenly resembled a myofibroblast (perhaps by changing the growth factors), the deposition of collagens during wound healing could also be explored.

## 5.4 Applications of a corneal stroma model

An *in vitro* model of the corneal stroma has many applications. To date, stroma models are used to model different disease states, from keratoconus to diabetic neuropathy and fibrosis (Karamichos *et al.*, 2010, 2012). Adapting the model to include the co-culture of other corneal cells, such as the endothelium, epithelium and nerve cells, would allow for the modelling of more complex diseases. Modelling these diseases, such as keratoconus and diabetic neuropathy, will enable the exploration of treatments and therapies. For example, mutations in CHST6 are responsible for some cases of the genetic condition macular corneal dystrophy (Klintworth, 2009). A stroma model could be created using corneal cells isolated from donors with this condition. This disease model can then be used to test treatments such as the application of small activating RNAs to upregulate the expression CHST6 (Kwok *et al.*, 2019).

### 5.4.1 Understanding mechanisms of tissue development

How the stroma forms during development is still being investigated, with most research focusing on chick models (Funderburgh *et al.*, 1986; Koudouna *et al.*, 2018; Young *et al.*, 2019). However, it is known that avian corneas first form a primary stroma, an event not seen in mammalian corneas (Espana and Birk, 2020). The stroma model could be used to further understand the mechanisms behind tissue development. In particular, the model could be used to study collagen fibril alignment and cell stratification. Live cell imaging of cells cultured on substrates with aligned nanotopography, and labelling collagen with CNA35, may reveal how collagen is aligned. Future research could focus on how collagen fibrils maintain alignment once cells stratify and they are no longer in contact with the cues provided by the substrate. Imaging cells as they stratify and as their orientation rotates may reveal key events, necessary for the formation of lamellar tissues. Understanding tissue development can assist in understanding disease.

### 5.4.2 Understanding wound healing

Corneal stroma models are currently being used to investigate matrix metalloproteinase expression during wound healing (Couture *et al.*, 2016). During wound healing, growth factors and cytokines such as IL-1 and TNFα are released by epithelial cells and enter the stroma to recruit myofibroblasts. The addition of epithelial cells to the model may allow for the modelling of wound healing. By further understanding would healing, research into treatments for corneal scars can take place, perhaps by identifying signalling pathways to target.

## 5.5 Applications of a lamellar collagen model

The stroma model could be adapted to research other lamellar collagen tissues. One example is the annulus fibrosus (AF) of the intervertebral disc. With adaptation, such as changing the cell type, the *in vitro* model used in the present study may also be used to model the lamellar collagen of the AF. Here, the tissue is composed of aligned collagen fibrils, lamellae, which are oriented at 30° to adjacent layers (Shamsah *et al.*, 2019). The stratification and rotation observed as hCFs were cultured on PTFE-nf may also be useful in tissue engineering the AF, assuming AF cells behave similarly. The alignment of cells is also a design requirement in other areas of regenerative medicine, such as tendon healing and the generation of nerve guides. In fact, a recent study by Foolen *et al.* suggests that tendon-derived cells cultured in

an aligned, organised matrix possessed a greater ability to remodel the ECM than cells in a disorganised (scar) matrix (Foolen *et al.*, 2018). The stroma model could be adapted to create both a 2D model of both healthy and scarred tendons, using PTFE-nf and glass substrates respectively.

## 5.6 Modelling other diseases

Incorporating macromolecular crowding with carrageenan into the model used in the present study resulted in the formation of collagen aggregates which resembled aggregates observed in pathological tissues (Kobayasi *et al.*, 1985; Knupp *et al.*, 2006). Crowding with carrageenan may, therefore, offer a disease model for conditions such as Sorsby's fundus dystrophy (condition affecting the Bruch's membrane) and morphea (condition affecting the skin) (Kobayasi *et al.*, 1985; Knupp *et al.*, 2002). Being able to model these diseases *in vitro* may lead to the development of drug treatments and possibly reduce the use of animal models.

## 5.7 Concluding remarks

The original hypothesis of this study was that cells residing in the limbal stroma can be influenced by nanotopography to deposit an organised matrix that resembled the microarchitecture of the corneal stroma. Further, it was hypothesised that macromolecular crowding would increase matrix deposition without disrupting the organisation of the matrix. This study has shown that that corneal fibroblasts can deposit oriented collagen when cultured on PTFE-nf. It was also shown that hCFs and, consequently, the ECM also remained oriented as the cells stratified, most likely through cell-cell contact guidance. Macromolecular crowding appeared to increase the deposition of collagen, with Ficoll maintaining matrix alignment. The stroma model presented here meets the minimum design requirements for studying collagen fibrillogenesis and this is the proposed use of this model. It is expected that the stroma model can be easily adapted with the addition of a stratified epithelium, to meet the design criteria for both a corneal wound healing model and for drug testing.

# Chapter 6. Appendices

## 6.1 Appendix A

### 6.1.1 Positive control for primary antibodies used to characterise keratocytes

A human corneal stroma was collagenase-digested and subjected to cytospinning as a way of isolating keratocytes prior to them transitioning into fibroblasts. The cytospin preparations were then used as a positive control for the primary antibodies specific to corneal keratocytes: collagens type I, V and VI, CD34, ALDH1A1, ALDH3A1, keratocan and lumican. Fibroblast marker, CD90, and myofibroblast marker, α-SMA were also used as a control.

Collagens type V and VI were expressed in cytospin preparations; collagen type I staining was relatively diffuse but this may be as a result of the low cell number (Figure 6.1). All keratocyte markers, with the exception of ALDH1A1 were expressed in cytospin preparations and so this antibody was not used in further experiments (Figure 6.2). As expected, both CD90 and α-SMA were not expressed.

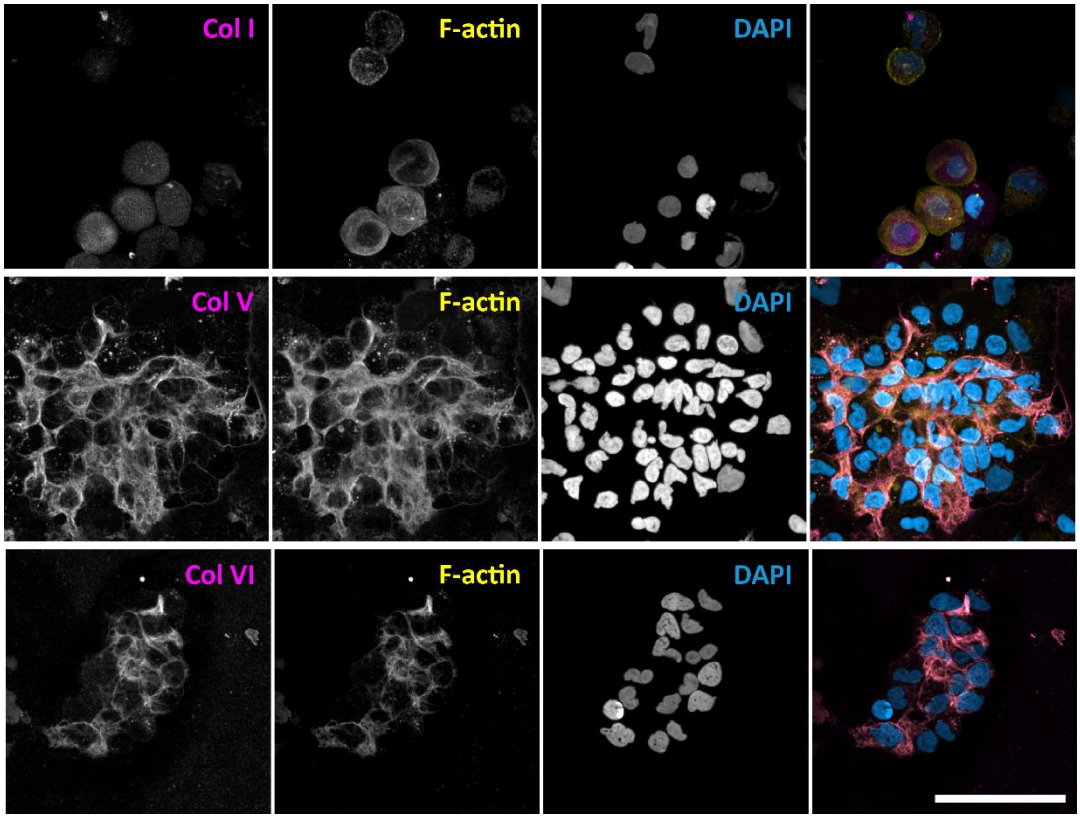


**Figure 6.1 Max. z-projection from ICC of collagens in human corneal stroma cytospin preparations.** Cytospin preparations displayed positive expression of collagens type V and VI (magenta) but staining of collagen type I was diffuse and may be non-specific. Preparations were also stained with Phalloidin to visualise F-actin (yellow) and DAPI (blue). Merge images are also shown. n = 1 biological replicate. Scale bar represents 50 µm.

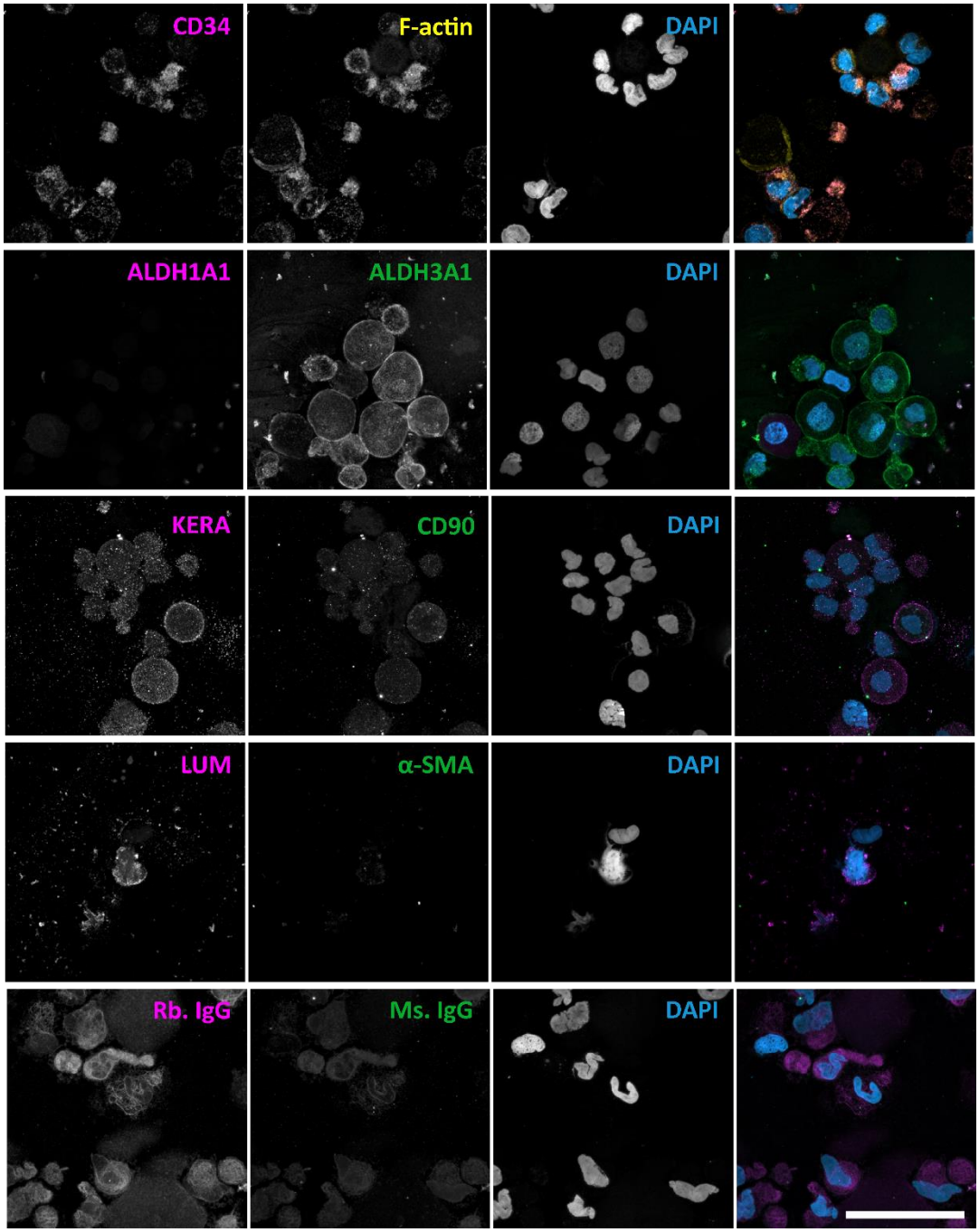


**Figure 6.2 ICC of keratocyte-, fibroblast- and myofibroblast-markers in human corneal stroma cytospin preparations.** Cytospin preparations displayed positive expression of CD34, keratocan and lumican (magenta) but not ALDH1A1. Positive expression of ALDH3A1 (green) was also shown. Fibroblast marker CD90 was not expressed, neither was myofibroblast marker α-SMA (green). One preparation was also stained with Phalloidin to visualise F-actin (yellow). All preparations were co-stained with DAPI (blue). Merged images are also shown. IgG negative controls are shown for comparison. n = 1 biological replicate. Scale bar represents 50 µm.

## 6.2 Appendix B

### 6.2.1 Selection of housekeeping gene using GeNorm

Analysis of housekeeping genes for both hCSSCs compared with hCFs (Table 6.1) and hMSCs compared with differentiated hMSCs (Table 6.2) using geNorm analysis revealed that GAPDH and ACTB were equally stable. GAPDH was chosen as the housekeeping gene for all future experiments.

**Table 6.1 Stepwise elimination of least stable housekeeping genes for hCSSCs and hCFs.**

| | GAPDH | 18S RNA | ACTB | B2M |
|---|---|---|---|---|
| **hCFs** | 1.00E+00 | 1.00E+00 | 1.00E+00 | 8.50E-01 |
| **hCSSCs** | 7.39E-03 | 2.07E-01 | 1.87E-03 | 1.00E+00 |
| 1) M < 1.5[1] | **3.325** | **3.325** | **4.260** | **4.508** |
| 2) M < 1.5[1] | **2.401** | **4.099** | **3.103** | - |
| 3) M < 1.5[1] | **1.404** | - | **1.404** | - |

[1] At each step, the gene expression stability measure (M) is calculated and the gene with the highest M value (magenta) is excluded until just two genes remain (green).

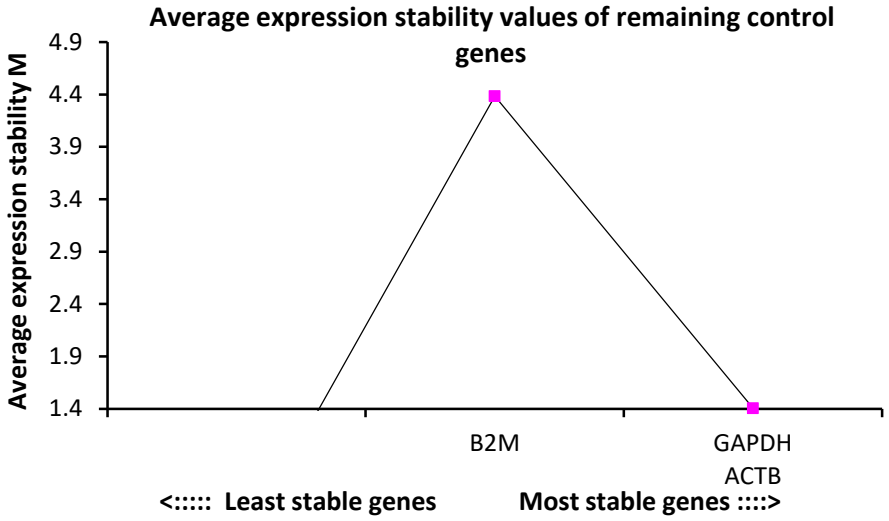


**Figure 6.3 Graphical representation of the average expression stability value of the remaining housekeeping genes identified using geNorm for hCSSCs.**

**Table 6.2 Stepwise elimination of least stable housekeeping genes for hMSCs.**

| | GAPDH | 18S RNA | ACTB | B2M |
|---|---|---|---|---|
| **hMSC (SCM)** | 1.37E-01 | 3.41E-02 | 1.18E-01 | 3.33E-01 |
| **hMSC (KDM)** | 1.00E+00 | 1.00E+00 | 1.00E+00 | 1.00E+00 |
| 1) M < 1.5[1] | **0.827** | **1.671** | **0.827** | **1.431** |
| 2) M < 1.5[1] | **0.530** | - | **0.608** | **0.983** |
| 3) M < 1.5[1] | **0.156** | - | **0.156** | - |

[1] At each step, the gene expression stability measure (M) is calculated and the gene with the highest M value (magenta) is excluded until just two genes remain (green).

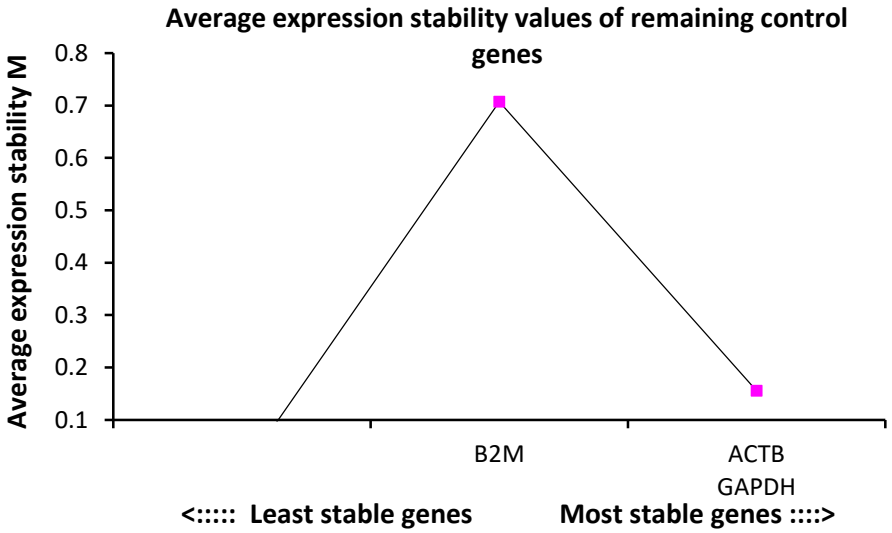


**Figure 6.4 Graphical representation of the average expression stability value of the remaining housekeeping genes identified using geNorm for hMSCs.**

## 6.3 Appendix C

### 6.3.1 Program for paraffin embedding chondrocyte pellets

Chondrocyte pellets were embedded in paraffin using the program outlined in Table 6.3.

**Table 6.3 Paraffin embedding program used to embed chondrocyte pellets.**

| Reagent | Duration (min) |
|---|---|
| 70% ethanol | 30 |
| 90% ethanol | 30 |
| 100% ethanol | 5 |
| 100% ethanol | 10 |
| 100% ethanol | 10 |
| 100% ethanol | 20 |
| Xylene | 10 |
| Xylene | 20 |
| Xylene | 30 |
| Paraffin wax | 30 |
| Paraffin wax | 60 |
| Paraffin wax | 150 |

## 6.4 Appendix D

### 6.4.1 Details for hCSSC isolation attempts

The length of time between donor death and CSSC isolation may have had an effect on the success of cell isolation. The average length of time between donor death and cell isolation was 41.6 ± 16.3 days (Table 6.4). However, for donors isolated using Method 1, this assumes that the tissue was stored in organ culture medium for no more than 3 weeks prior to supplementing the medium with dextran (Pels, 1997).

**Table 6.4 Length of time between date of death and cell isolation from donor tissue.**

| Donor number | Age (sex) ‡ | Number of days between date of death* and cell isolation |
|---|---|---|
| **Method 1** | | |
| Donor A (HCR025) | Unknown | 6* |
| Donor B (HCR043) | 74 | 16* |
| **Method 2** | | |
| Donor 1 (IEB012) | 61 | 49 |
| Donor 2 (IEB015) | 65 | 43 |
| Donor 3 (IEB024_025) | 49 (M) | 67 |
| Donor 4 (NHS021) | Unknown | 33 |
| Donor 5 (NHS025_026) | Unknown | 25 and 34† |

*Where date of death was not provided, date corneas were placed into dextran was used; †two donors were combined to improve cell numbers; ‡where the sex of the donor was known it is included in parentheses – M, male; F, female.

## 6.5 Appendix C

### 6.5.1 pQE-30 vector for CNA35

For the expression of CNA35, a microbial surface component recognising adhesive matrix molecules, a pQE30CNA35 plasmid (Figure 6.5) was transformed into single competent cells (Chapter 3, 3.4.2).

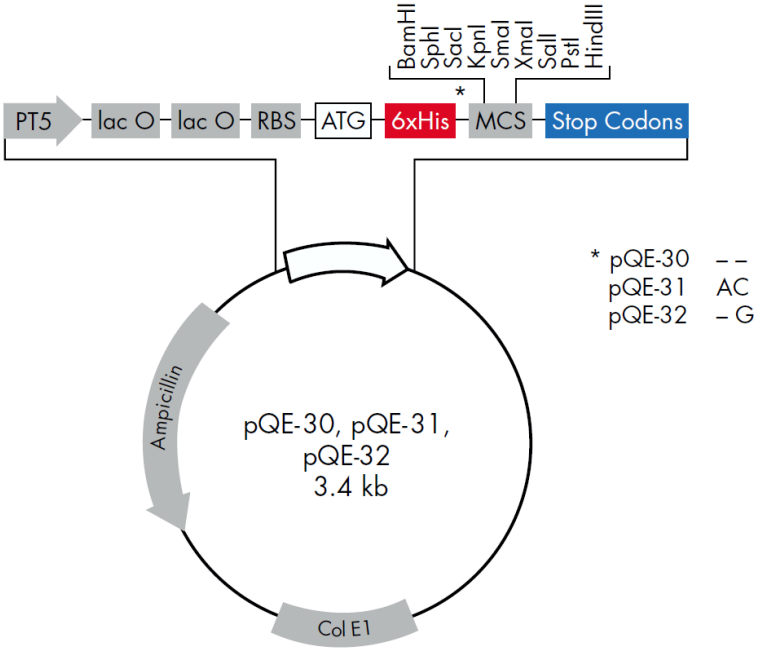


**Figure 6.5 Vector pQE-30 coding for the collagen binding part of the A domain of *S. aureus.* The plasmid was kindly gifted to Dr. Elizabeth Canty-Laird (supervisor) by Magnus Höök.**

## 6.6 Appendix E

### 6.6.1 Confirming OrientationJ Distribution

To confirm that the OrientationJ Distribution plugin performed as expected, an image was digitally rotated within FIJI prior to running the plugin. The distribution shifted 20°, as expected, however the frequency at the dominant orientation decreased (Figure 6.6). This can be explained by the loss of image corners that occurred when rotating the image and can be seen in Figure 6.7. Surprisingly, a new peak was also formed at 75° and so the OrientationJ Analysis plugin was used to create a colour survey where Hue represents the angle of orientation; Saturation represents coherency; and Brightness is the same as the input image. The colour survey revealed an artefact at the edge of the rotated images where a band of a singular colour could be seen which was absent from the original images. This has been magnified in the boxed region of the third image and the circular colour map confirms that this colour is at 75°.

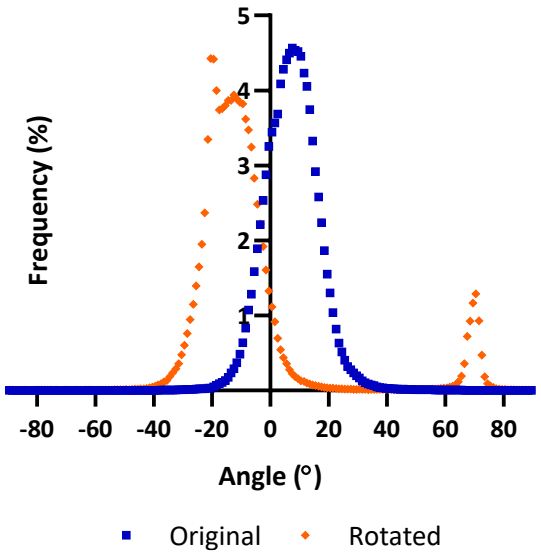


**Figure 6.6 OrientationJ analysis of the cumulative distribution of one donor which has been digitally rotated by 20 degrees.** When the image is digitally rotated by 20° using FIJI, the peak of the distribution shifts to the left by 20°. The peak isn't as large as the original distribution and a new peak has been formed at 75°, caused by image artefacts shown below.

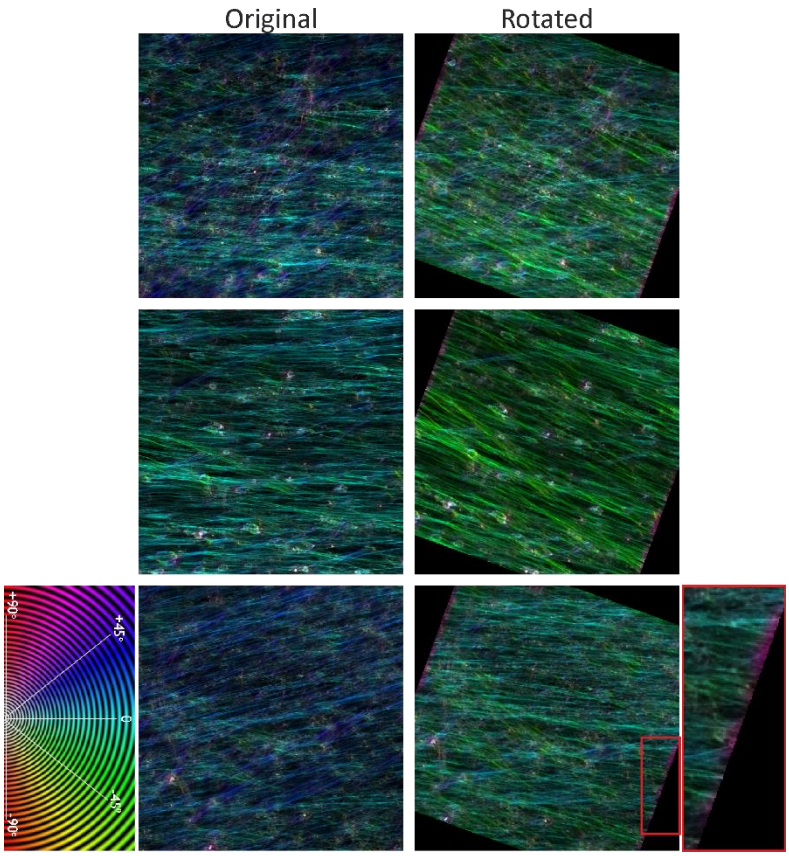


**Figure 6.7 OrientationJ Colour Survey of both the original and the rotated images.** When the original image was digitally rotated by 20°, the corners of the image are lost. There is also an edge artefact in the rotated images showing a magenta streak (magnified in the bottom right image) which corresponds to 75° as shown in the circular colour map (bottom left).

## 6.7 Appendix F

### 6.7.1 P values for growth curves, resazurin assay and RFU/cell for hCFs

Cell number and metabolic activity were assessed to compare media treatments (growth, A2PM and FC) of hCFs , with the same data being reported in both Chapter 3 (3.5.2) and Chapter 4 (4.5.4). A two-way ANOVA was performed on cell number (Table 6.5), metabolic activity (Table 6.6) and relative fluorescence per cell (Table 6.8), and a Tukey's *post hoc* test for multiple comparisons was performed (Table 6.7).

**Table 6.5 Results from two-way ANOVA performed on hCF cell number data with growth, A2PM and FC.**

| Source of variation | SS (Type III) | DF | MS | F (DFn, DFd) | p value |
|---|---|---|---|---|---|
| Time | 173534 | 5 | 34707 | F (5, 35) = 104.8 | p < 0.0001 |
| Media | 493.5 | 2 | 246.7 | F (2, 35) = 0.7449 | p = 0.4822 |
| Interaction | 2874 | 10 | 287.4 | F (10, 35) = 0.8678 | p = 0.5705 |
| Residual | 11593 | 35 | 331.2 | | |

**Table 6.6 Results from one-way ANOVA performed on metabolic activity data with growth, A2PM and FC where media and time variables were concatenated.**

| Source of variation | SS (Type III) | DF | MS | F (DFn, DFd) | p value |
|---|---|---|---|---|---|
| Between groups | 290774336406 | 17 | 17104372730 | F (17, 36) = 107.3 | p < 0.0001 |
| Residual | 5740627154 | 36 | 159461865 | | |

**Table 6.7 Tukey's pairwise multiple comparisons. Comparisons of interest are shown.**

| Comparison | Diff. of means | q | p value |
|---|---|---|---|
| Growth1 vs. A2PM1 | 9374 | 1.286 | >0.9999 |
| Growth1 vs. FC1 | 7115 | 0.9759 | >0.9999 |
| A2PM1 vs. FC1 | -2260 | 0.3099 | >0.9999 |
| Growth3 vs. A2PM3 | 32639 | 4.477 | 0.1839 |
| Growth3 vs. FC3 | 17805 | 2.442 | 0.948 |
| A2PM3 vs. FC3 | -14834 | 2.035 | 0.9901 |
| Growth5 vs. A2PM5 | 19128 | 2.624 | 0.9101 |
| Growth5 vs. FC5 | 15633 | 2.144 | 0.9834 |
| A2PM5 vs. FC5 | -3496 | 0.4795 | >0.9999 |
| Growth7 vs. A2PM7 | 4684 | 0.6425 | >0.9999 |
| Growth7 vs. FC7 | 5912 | 0.8109 | >0.9999 |
| A2PM7 vs. FC7 | 1228 | 0.1684 | >0.9999 |
| Growth14 vs. A2PM14 | -4978 | 0.6827 | >0.9999 |
| Growth14 vs. FC14 | 1114 | 0.1528 | >0.9999 |
| A2PM14 vs. FC14 | 6092 | 0.8356 | >0.9999 |
| Growth21 vs. A2PM21 | -1760 | 0.2414 | >0.9999 |
| Growth21 vs. FC21 | 7032 | 0.9646 | >0.9999 |
| A2PM21 vs. FC21 | 8792 | 1.206 | >0.9999 |

**Table 6.8 Results from two-way ANOVA performed on hCF fluorescence per cell (RFU/cell) data with growth, A2PM and FC.**

| Source of variation | SS (Type III) | DF | MS | F (DFn, DFd) | P value |
|---|---|---|---|---|---|
| Time | 0.2992 | 5 | 0.05985 | F (5, 35) = 7.772 | p < 0.0001 |
| Media | 0.03494 | 2 | 0.01747 | F (2, 35) = 2.269 | p = 0.1184 |
| Interaction | 0.06133 | 10 | 0.006133 | F (10, 35) = 0.7965 | p = 0.6326 |
| Residual | 0.2695 | 35 | 0.007700 | | |

## 6.8 Appendix G

### 6.8.1 hCFs imaged over time show the secretion of collagen

The *in vitro* model of the corneal stroma was used to visualise collagen deposition over time. hCFs were seeded onto PTFE-nf in a chamber slide and allowed to rest for 24 hours. The cells were then labelled with CellTracker Red (CTR) and collagen was labelled with the collagen probe (CNA35) before imaging hourly over 64 hours on a Zeiss LSM 700 (Figure 6.8). The images show the migration of cells over time as they move adjacent to the PTFE-nf and the increased secretion of collagen. Magnified images at time points: 0, 16, 32, 48 and 64 hours are shown in Chapter 3 (Figure 3.26).

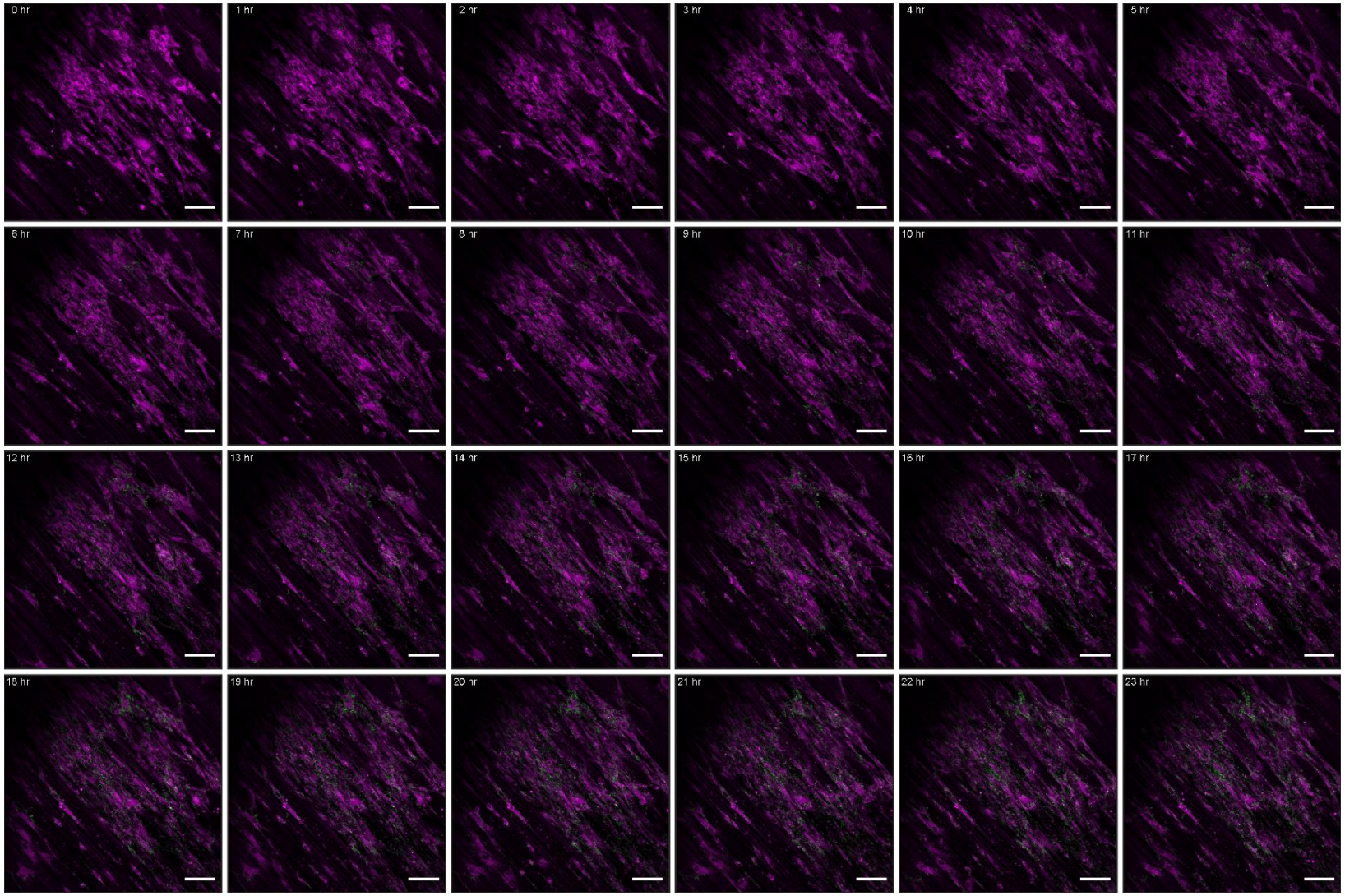
0 hr
1 hr
2 hr
3 hr
4 hr
5 hr
6 hr
7 hr
8 hr
9 hr
10 hr
11 hr
12 hr
13 hr
14 hr
15 hr
16 hr
17 hr
18 hr
19 hr
20 hr
21 hr
22 hr
23 hr

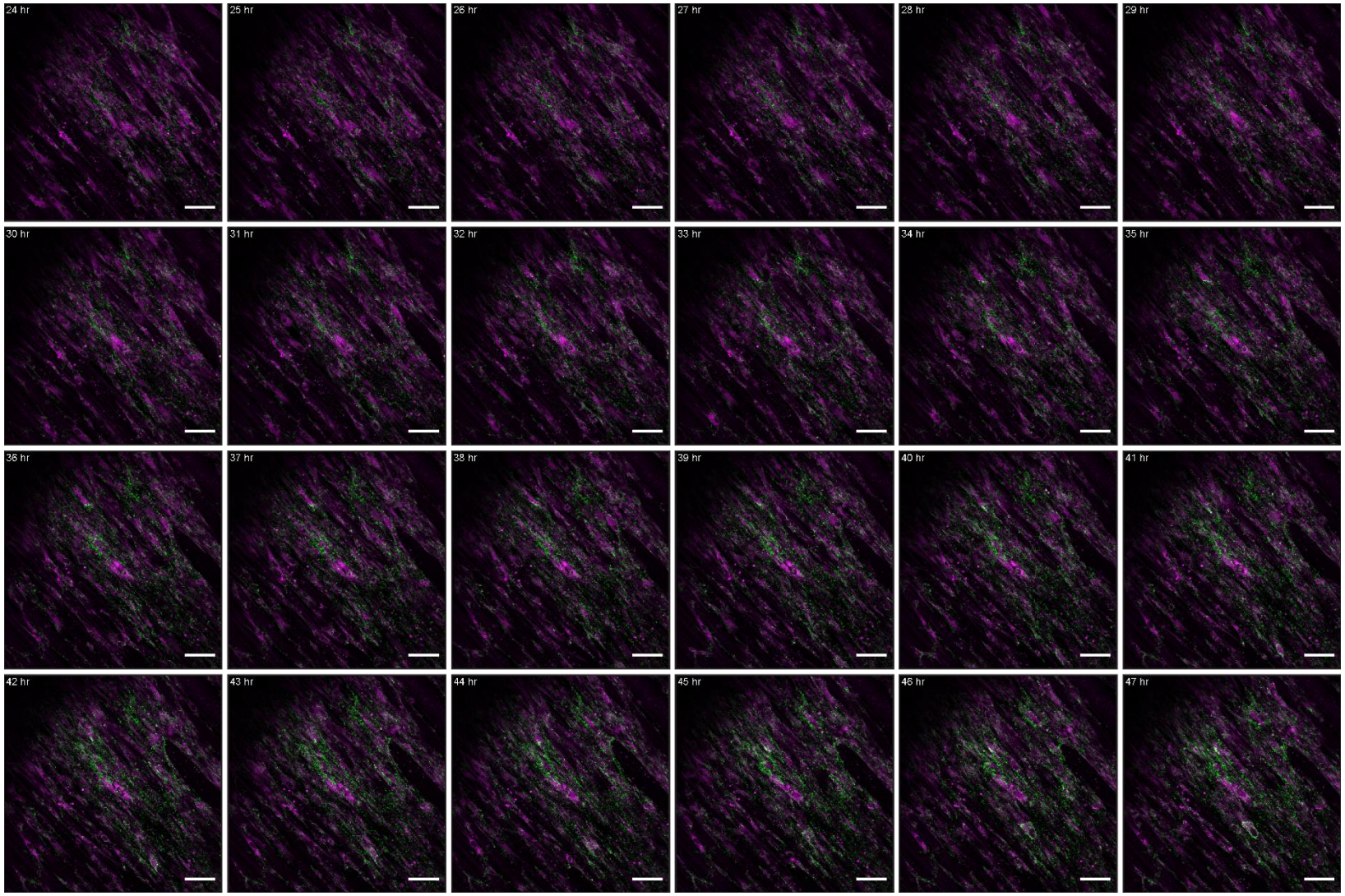
24 hr
25 hr
26 hr
27 hr
28 hr
29 hr
30 hr
31 hr
32 hr
33 hr
34 hr
35 hr
36 hr
37 hr
38 hr
39 hr
40 hr
41 hr
42 hr
43 hr
44 hr
45 hr
46 hr
47 hr

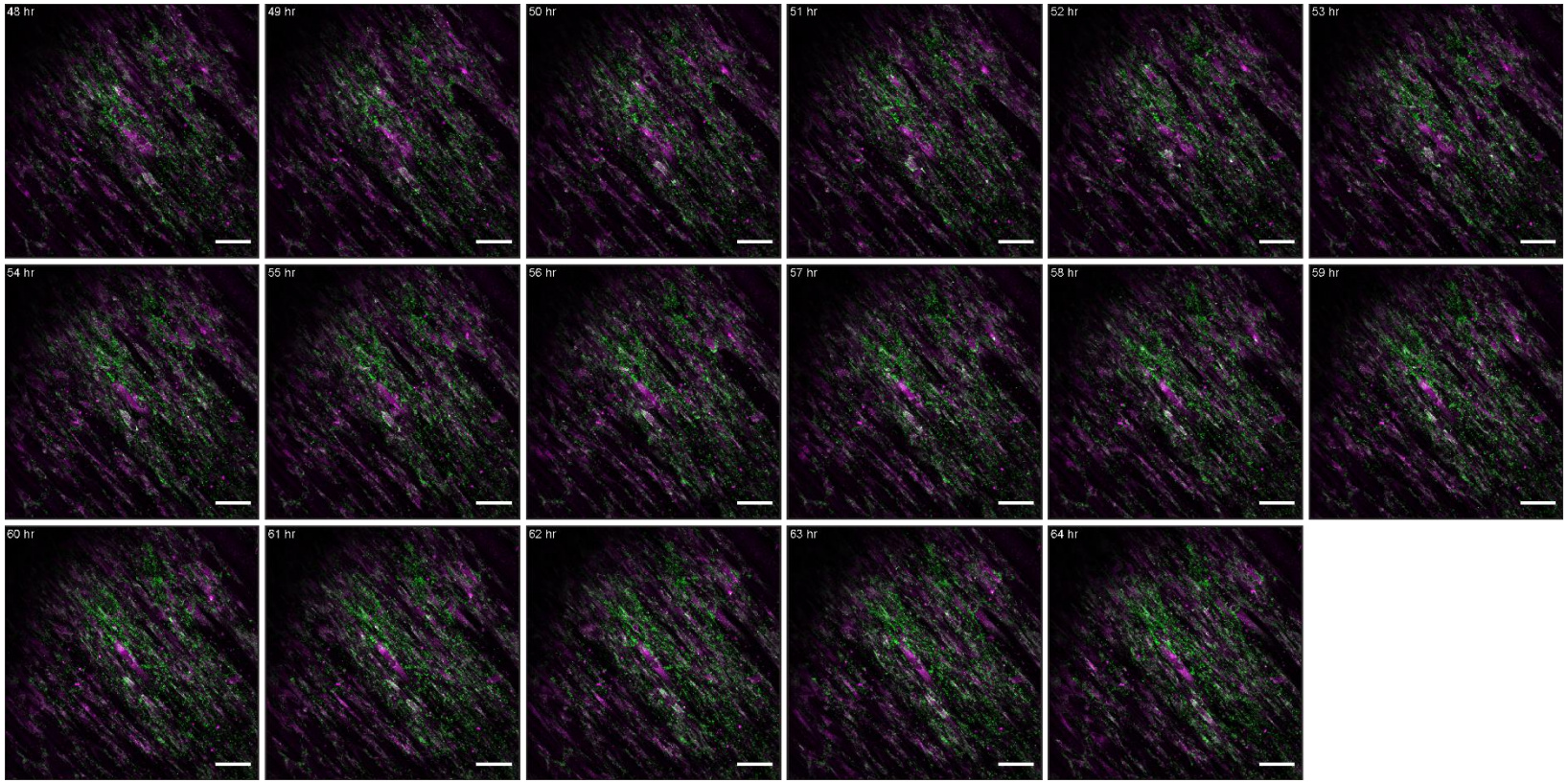


**Figure 6.8 Live cell imaging of hCFs cultured in magnetic chamber slide on PTFE-nf were imaged every hour for 64 hours.** Images at 1-hour intervals are shown above with the cytoplasm labelled with CTR (magenta) and collagen labelled with CNA35 (green). Scale bars represent 100 µm.

# References

Abahussin, M., Hayes, S., Cartwright, N.E.K., Kamma-Lorger, C.S., Khan, Y., Marshall, J., Meek, K.M. (2009). 3D collagen orientation study of the human cornea using X-ray diffraction and femtosecond laser technology. *Investig. Ophthalmol. Vis. Sci.* 50 (11), 5159–5164.

Abedinia, M., Pain, T., Algar, E.M., Holmes, R.S. (1990). Bovine corneal aldehyde dehydrogenase: The major soluble corneal protein with a possible dual protective role for the eye. *Exp. Eye Res.* 51 (4), 419–426.

Achilleos, A., Trainor, P.A. (2012). Neural crest stem cells: discovery, properties and potential for therapy. *Cell Res. 2012 222*. 22 (2), 288–304.

Adewumi, O., Aflatoonian, B., Ahrlund-Richter, L., Amit, M., Andrews, P.W., Beighton, G., Bello, P.A., Benvenisty, N., Berry, L.S., Bevan, S., Blum, B., Brooking, J., Chen, K.G., Choo, A.B.H., Churchill, G.A., Corbel, M., Damjanov, I., Draper, J.S., Dvorak, P., Emanuelsson, K., Fleck, R.A., Ford, A., Gertow, K., Gertsenstein, M., Gokhale, P.J., Hamilton, R.S., Hampl, A., Healy, L.E., Hovatta, O., Hyllner, J., Imreh, M.P., Itskovitz-Eldor, J., Jackson, J., Johnson, J.L., Jones, M., Kee, K., King, B.L., Knowles, B.B., Lako, M., Lebrin, F., Mallon, B.S., Manning, D., Mayshar, Y., McKay, R.D.G., Michalska, A.E., Mikkola, M., Mileikovsky, M., Minger, S.L., Moore, H.D., Mummery, C.L., Nagy, A., Nakatsuji, N., O'Brien, C.M., Oh, S.K.W., Olsson, C., Otonkoski, T., Park, K.Y., Passier, R., Patel, H., Patel, M., Pedersen, R., Pera, M.F., Piekarczyk, M.S., Pera, R.A.R., Reubinoff, B.E., Robins, A.J., Rossant, J., Rugg-Gunn, P., Schulz, T.C., Semb, H., Sherrer, E.S., Siemen, H., Stacey, G.N., Stojkovic, M., Suemori, H., Szatkiewicz, J., Turetsky, T., Tuuri, T., Van Den Brink, S., Vintersten, K., Vuoristo, S., Ward, D., Weaver, T.A., Young, L.A., Zhang, W. (2007). Characterization of human embryonic stem cell lines by the International Stem Cell Initiative. *Nat. Biotechnol.* 25 (7), 803–816.

Aghamohammadzadeh, H., Newton, R.H., Meek, K.M. (2004). X-Ray Scattering Used to Map the Preferred Collagen Orientation in the Human Cornea and Limbus. *Structure*. 12 (2), 249–256.

Ahearne, M., Lysaght, J., Lynch, A.P. (2014). Combined influence of basal media and fibroblast growth factor on the expansion and differentiation capabilities of adipose-derived stem cells. *Cell Regen.* 3 (1), 3:13.

Ahmad, S. (2012). Concise Review: Limbal Stem Cell Deficiency, Dysfunction, and Distress. *Stem Cells Transl. Med.* 1 (2), 110–115.

Ainscough, S.L., Linn, M.L., Barnard, Z., Schwab, I.R., Harkin, D.G. (2011). Effects of fibroblast origin and phenotype on the proliferative potential of limbal epithelial progenitor cells. *Exp. Eye Res.* 92 (1), 10–19.

Akimoto, Y., Sawada, H., Ohara-Imaizumi, M., Nagamatsu, S., Kawakami, H. (2008). Change in long-spacing collagen in Descemet's membrane of diabetic Goto-Kakizaki rats and its suppression by antidiabetic agents. *Exp. Diabetes Res.* 2008, 818341.

Altman, G.H., Diaz, F., Jakuba, C., Calabro, T., Horan, R.L., Chen, J., Lu, H., Richmond, J., Kaplan, D.L. (2003). Silk-based biomaterials. *Biomaterials*. 24 (3), 401–16.

Andrzejewska, A., Catar, R., Schoon, J., Qazi, T.H., Sass, F.A., Jacobi, D., Blankenstein, A., Reinke, S., Krüger, D., Streitz, M., Schlickeiser, S., Richter, S., Souidi, N., Beez, C., Kamhieh-Milz, J., Krüger, U., Zemojtel, T., Jürchott, K., Strunk, D., Reinke, P., Duda, G., Moll, G., Geissler, S. (2019). Multi-Parameter Analysis of Biobanked Human Bone Marrow Stromal Cells Shows Little Influence for Donor Age and Mild Comorbidities on Phenotypic and Functional Properties. *Front. Immunol.* 10 (November), 1–24.

Ang, X.M., Lee, M.H.C., Blocki, A., Chen, C., Ong, L.L.S., Asada, H.H., Sheppard, A., Raghunath, M. (2014). Macromolecular crowding amplifies adipogenesis of human bone marrow-derived mesenchymal stem cells by enhancing the pro-adipogenic microenvironment. *Tissue Eng. - Part A*. 20 (5–6), 966–981.

Assunção, M., Wong, C.W., Richardson, J.J., Tsang, R., Beyer, S., Raghunath, M., Blocki, A. (2020). Macromolecular dextran sulfate facilitates extracellular matrix deposition by electrostatic interaction independent from a macromolecular crowding effect. *Mater. Sci. Eng. C*. 106, 110280.

Bajpai, V.K., Mistriotis, P., Andreadis, S.T. (2012). Clonal multipotency and effect of long-term in vitro expansion on differentiation potential of human hair follicle derived mesenchymal stem cells. *Stem Cell Res.* 8 (1), 74–84.

Barbosa, F.L., Chaurasia, S.S., Cutler, A., Asosingh, K., Kaur, H., de Medeiros, F.W., Agrawal, V., Wilson, S.E. (2010). Corneal myofibroblast generation from bone marrow-derived cells. *Exp. Eye Res.* 91 (1), 92–96.

Barthes, J., Özçelik, H., Hindié, M., Ndreu-Halili, A., Hasan, A., Vrana, N.E. (2014). Cell Microenvironment Engineering and Monitoring for Tissue Engineering and Regenerative Medicine: The Recent Advances. *Biomed Res. Int.* 2014 (Article ID 921905), 18.

Basu, S., Hertsenberg, A.J., Funderburgh, M.L., Burrow, M.K., Mann, M.M., Du, Y., Lathrop, K.L., Syed-Picard, F.N., Adams, S.M., Birk, D.E., Funderburgh, J.L. (2014). Human limbal biopsy-derived stromal stem cells prevent corneal scarring. *Sci. Transl. Med.* 10 (6), 266ra172.

Bateman, J.F., Cole, W.G., Pillow, J.J., Ramshaw, J.A.M. (1986). Induction of procollagen

processing in fibroblast cultures by neutral polymers. *J. Biol. Chem.* 261 (9), 4198–4203.

Bateman, J.F., Golub, S.B. (1990). Assessment of procollagen processing defects by fibroblasts cultured in the presence of dextran sulphate. *Biochem. J.* 267 (3), 573–577.

Beales, M.P., Funderburgh, J.L., Jester, J. V., Hassell, J.R. (1999). Proteoglycan synthesis by bovine keratocytes and corneal fibroblasts: Maintenance of the keratocyte phenotype in culture. *Investig. Ophthalmol. Vis. Sci.* 40 (8), 1658–1663.

Beamson, G., Clark, D.T., Deegan, D.E., Hayes, N.W., Law, D.S.L., Rasmusson, J.R., Salaneck, W.R. (1996). Characterization of PTFE on Silicon Wafer Tribological Transfer Films by XPS, Imaging XPS and AFM. *Surf. Interface Anal.* 24 (3), 204–210.

Benedek, G.B. (1971). Theory of Transparency of the Eye. *Appl. Opt.* 10 (3), 459.

Berryhill, B.L., Beales, M.P., Hassell, J.R. (2001). Production of prostaglandin D synthase as a keratan sulfate proteoglycan by cultured bovine keratocytes. *Investig. Ophthalmol. Vis. Sci.* 42 (6), 1201–1207.

Berryhill, B.L., Kader, R., Kane, B., Birk, D.E., Feng, J., Hassell, J.R. (2002). Partial restoration of the keratocyte phenotype to bovine keratocytes made fibroblastic by serum. *Investig. Ophthalmol. Vis. Sci.* 43 (11), 3416–3421.

Bettinger, C.J., Langer, R., Borenstein, J.T. (2009). Engineering substrate topography at the Micro- and nanoscale to control cell function. *Angew. Chemie - Int. Ed.* 48 (30), 5406–5415.

Bianco, P., Riminucci, M., Gronthos, S., Robey, P.G. (2001). Bone Marrow Stromal Stem Cells: Nature, Biology, and Potential Applications. *Stem Cells*. 19 (3), 180–192.

Birk, D.E., Fitch, J.M., Babiarz, J.P., Linsenmayer, T.F. (1988). Collagen type I and type V are present in the same fibril in the avian corneal stroma. *J. Cell Biol.* 106 (3), 999–1008.

Birk, D.E., Trelstad, R.L. (1986). Extracellular compartments in tendon morphogenesis: Collagen fibril, bundle, and macroaggregate formation. *J. Cell Biol.* 103 (1), 231–240.

Birk, D.E., Trelstad, R.L. (1984). Extracellular compartments in matrix morphogenesis: Collagen fibril, bundle, and lamellar formation by corneal fibroblasts. *J. Cell Biol.* 99 (6), 2024–2033.

Boerboom, R.A., Krahn, K.N., Megens, R.T.A., van Zandvoort, M.A.M.J., Merkx, M., Bouten, C.V.C. (2007). High resolution imaging of collagen organisation and synthesis using a versatile collagen specific probe. *J. Struct. Biol.* 159 (3), 392–399.

Bonanno, J.A. (2012). Molecular mechanisms underlying the corneal endothelial pump. *Exp. Eye Res.* 95 (1), 2–7.

Branch, M.J., Hashmani, K., Dhillon, P., Jones, D.R.E., Dua, H.S., Hopkinson, A. (2012).

Mesenchymal Stem Cells in the Human Corneal Limbal Stroma. *Invest. Ophthalmol. Vis. Sci.* 53 (9), 5109–5116.

Bray, L.J., Heazlewood, C.F., Atkinson, K., Hutmacher, D.W., Harkin, D.G. (2012). Evaluation of methods for cultivating limbal mesenchymal stromal cells. *Cytotherapy*. 14 (8), 936–947.

Bray, L.J., Heazlewood, C.F., Munster, D.J., Hutmacher, D.W., Atkinson, K., Harkin, D.G. (2014). Immunosuppressive properties of mesenchymal stromal cell cultures derived from the limbus of human and rabbit corneas. *Cytotherapy*. 16 (1), 64–73.

Brookes, N.H., Loh, I.P., Clover, G.M., Poole, C.A., Sherwin, T. (2003). Involvement of corneal nerves in the progression of keratoconus. *Exp. Eye Res.* 77 (4), 515–524.

Brown, M.E., Montgomery, M.L., Kamath, M.M., Nicholas, S., Liu, Y., Karamichos, D., Fuller, K.K. (2021). A novel 3D culture model of fungal keratitis to explore host-pathogen interactions within the stromal environment. *Exp. Eye Res.* 207, 108581.

Brunette, I., Roberts, C.J., Vidal, F., Harissi-Dagher, M., Lachaine, J., Sheardown, H., Durr, G.M., Proulx, S., Griffith, M. (2017). Alternatives to eye bank native tissue for corneal stromal replacement. *Prog. Retin. Eye Res.* 59, 97–130.

Bruns, R.R., Press, W., Engvall, E., Timpl, R., Gross, J. (1986). Type VI collagen in extracellular, 100-nm periodic filaments and fibrils: Identification by immunoelectron microscopy. *J. Cell Biol.* 103 (2), 393–404.

Builles, N., Janin-Manificat, H., Malbouyres, M., Justin, V., Rovère, M.R., Pellegrini, G., Torbet, J., Hulmes, D.J.S., Burillon, C., Damour, O., Ruggiero, F. (2010). Use of magnetically oriented orthogonal collagen scaffolds for hemi-corneal reconstruction and regeneration. *Biomaterials*. 31 (32), 8313–8322.

Buznyk, O., Pasyechnikova, N., Islam, M.M., Iakymenko, S., Fagerholm, P., Griffith, M. (2015). Bioengineered Corneas Grafted as Alternatives to Human Donor Corneas in Three High-Risk Patients. *Clin. Transl. Sci.* 8 (5), 558–562.

Canty, E.G., Kadler, K.E. (2005). Procollagen trafficking, processing and fibrillogenesis. *J. Cell Sci.* 118 (7), 1341–1353.

Canty, E.G., Lu, Y., Meadows, R.S., Shaw, M.K., Holmes, D.F., Kadler, K.E. (2004). Coalignment of plasma membrane channels and protrusions (fibropositors) specifies the parallelism of tendon. *J. Cell Biol.* 165 (4), 553–563.

Carlson, E.C., Liu, C.Y., Chikama, T.I., Hayashi, Y., Kao, C.W.C., Birk, D.E., Funderburgh, J.L., Jester, J. V., Kao, W.W.Y. (2005). Keratocan, a cornea-specific keratan sulfate proteoglycan, is regulated by lumican. *J. Biol. Chem.* 280 (27), 25541–25547.

Carneiro-Da-Cunha, M.G., Cerqueira, M.A., Souza, B.W.S., Teixeira, J.A., Vicente, A.A. (2011). Influence of concentration, ionic strength and pH on zeta potential and mean hydrodynamic diameter of edible polysaccharide solutions envisaged for multinanolayered films production. *Carbohydr. Polym.* 85 (3), 522–528.

Carrier, P., Deschambeault, A., Audet, C., Talbot, M., Gauvin, R., Giasson, C.J., Auger, F.A., Guérin, S.L., Germain, L. (2009). Impact of cell source on human cornea reconstructed by tissue engineering. *Invest. Ophthalmol. Vis. Sci.* 50 (6), 2645–2652.

Carrier, P., Deschambeault, A., Talbot, M., Giasson, C.J., Auger, F.A., Guérin, S.L., Germain, L. (2008). Characterization of wound reepithelialization using a new human tissue-engineered corneal wound healing model. *Investig. Ophthalmol. Vis. Sci.* 49 (4), 1376–1385.

Cescon, M., Gattazzo, F., Chen, P., Bonaldo, P. (2015). Collagen VI at a glance. *J. Cell Sci.* 128 (19), 3525–3531.

Chakravarti, S., Magnuson, T., Lass, J.H., Jepsen, K.J., LaMantia, C., Carroll, H. (1998). Lumican regulates collagen fibril assembly: Skin fragility and corneal opacity in the absence of lumican. *J. Cell Biol.* 141 (5), 1277–1286.

Chakravarti, S., Petroll, W.M., Hassell, J.R., Jester, J. V., Lass, J.H., Paul, J., Birk, D.E. (2000). Corneal opacity in lumican-null mice: Defects in collagen fibril structure and packing in the posterior stroma. *Investig. Ophthalmol. Vis. Sci.* 41 (11), 3365–3373.

Chakravarti, S., Zhang, G., Chervoneva, I., Roberts, L., Birk, D.E. (2006). Collagen fibril assembly during postnatal development and dysfunctional regulation in the lumican-deficient murine cornea. *Dev. Dyn.* 235 (9), 2493–2506.

Chapman, J.A., Armitage, P.M. (1972). An analysis of fibrous long spacing forms of collagen. *Connect. Tissue Res.* 1 (1), 31–37.

Chau, C.C., Hewitt, E.W., Actis, P. (2020). The role of macromolecular crowding in single-entity electrochemistry: friend or foe? *Curr. Opin. Electrochem.* 100654.

Chauhan, U., Assad, R., Peterkofsky, B. (1985). Cysteinyl-Cysteine and the Microsomal Protein From Which it is Derived Act as Reducing Cofactor For Prolyl Hydroxylase. *Biochem. Biophys. Res. Commun.* 131 (1), 277–283.

Chaurasia, S., Lim, R., Lakshminarayanan, R., Mohan, R. (2015). Nanomedicine Approaches for Corneal Diseases. *J. Funct. Biomater.* 6 (2), 277–298.

Chaurasia, S.S., Kaur, H., de Medeiros, F.W., Smith, S.D., Wilson, S.E. (2009). Reprint of "Dynamics of the expression of intermediate filaments vimentin and desmin during myofibroblast differentiation after corneal injury." *Exp. Eye Res.* 89 (4), 590–596.

Chen, C., Loe, F., Blocki, A., Peng, Y., Raghunath, M. (2011). Applying macromolecular crowding to enhance extracellular matrix deposition and its remodeling in vitro for tissue engineering and cell-based therapies. *Adv. Drug Deliv. Rev.* 63 (4), 277–290.

Chen, C., Peng, Y., Wang, Z.B., Fish, P. V., Kaar, J.L., Koepsel, R.R., Russell, A.J., Lareu, R.R., Raghunath, M. (2009). The Scar-in-a-Jar: Studying potential antifibrotic compounds from the epigenetic to extracellular level in a single well. *Br. J. Pharmacol.* 158 (5), 1196–1209.

Chen, J., Backman, L.J., Zhang, W., Ling, C., Danielson, P. (2020). Regulation of Keratocyte Phenotype and Cell Behavior by Substrate Stiffness. *ACS Biomater. Sci. Eng.* 6 (9), 5162–5171.

Chen, J., Guerriero, E., Sado, Y., Sundarraj, N. (2009). Rho-mediated regulation of TGF-β1- and FGF-2-induced activation of corneal stromal keratocytes. *Investig. Ophthalmol. Vis. Sci.* 50 (8), 3662–3670.

Chen, S., Mienaltowski, M.J., Birk, D.E. (2015). Regulation of corneal stroma extracellular matrix assembly. *Exp. Eye Res.* 133, 69–80.

Chen, S., Oldberg, A., Chakravarti, S., Birk, D.E. (2010). Fibromodulin regulates collagen fibrillogenesis during peripheral corneal development. *Dev. Dyn.* 239 (3), 844–854.

Chen, S., Young, M.F., Chakravarti, S., Birk, D.E. (2014). Interclass small leucine-rich repeat proteoglycan interactions regulate collagen fibrillogenesis and corneal stromal assembly. *Matrix Biol.* 35, 103–111.

Chen, Y., Jester, J. V., Anderson, D.M., Marchitti, S.A., Schey, K.L., Thompson, D.C., Vasiliou, V. (2017). Corneal haze phenotype in Aldh3a1-null mice: In vivo confocal microscopy and tissue imaging mass spectrometry. *Chem. Biol. Interact.* 276, 9–14.

Cho, H., Covington, H.I., Cintron, C. (1990). Immunolocalization of type VI collagen in developing and healing rabbit cornea. *Investig. Ophthalmol. Vis. Sci.* 31 (6), 1096–1102.

Choong, P.-F., Mok, P.-L., Cheong, S.-K., Then, K.-Y. (2007). Mesenchymal stromal cell-like characteristics of corneal keratocytes. *Cytotherapy*. 9 (3), 252–8.

Chung, H.H., Mireles, M., Kwarta, B.J., Gaborski, T.R. (2018). Use of porous membranes in tissue barrier and co-culture models. *Lab Chip*.

Cigognini, D., Gaspar, D., Kumar, P., Satyam, A., Alagesan, S., Sanz-Nogués, C., Griffin, M., O'Brien, T., Pandit, A., Zeugolis, D.I. (2016). Macromolecular crowding meets oxygen tension in human mesenchymal stem cell culture - A step closer to physiologically relevant in vitro organogenesis. *Sci. Rep.* 6 (April), 1–11.

Clément, M. V., Ramalingam, J., Long, L.H., Halliwell, B. (2001). The in vitro cytotoxicity of

ascorbate depends on the culture medium used to perform the assay and involves hydrogen peroxide. *Antioxidants Redox Signal.* 3 (1), 157–163.

Corpuz, L.M., Dunlevy, J.R., Hassell, J.R., Conrad, A.H., Conrad, G.W. (2000). Molecular cloning and relative tissue expression of keratocan and mimecan in embryonic quail cornea. *Matrix Biol.* 19 (7), 693–698.

Corpuz, L.M., Funderburgh, J.L., Funderburgh, M.L., Bottomley, G.S., Prakash, S., Conrad, G.W. (1996). Molecular cloning and tissue distribution of keratocan: Bovine corneal keratan sulfate proteoglycan 37A. *J. Biol. Chem.* 271 (16), 9759–9763.

Cournil-Henrionnet, C., Huselstein, C., Wang, Y., Galois, L., Mainard, D., Decot, V., Netter, P., Stoltz, J.F., Muller, S., Gillet, P., Watrin-Pinzano, A. (2008). Phenotypic analysis of cell surface markers and gene expression of human mesenchymal stem cells and chondrocytes during monolayer expansion. *Biorheology*. 45 (3–4), 513–526.

Couture, C., Zaniolo, K., Carrier, P., Lake, J., Patenaude, J., Germain, L., Guérin, S.L. (2016). The tissue-engineered human cornea as a model to study expression of matrix metalloproteinases during corneal wound healing. *Biomaterials*. 78, 86–101.

Craig, A.S., Parry, D.A.D. (1981). Collagen fibrils of the vertebrate corneal stroma. *J. Ultrasructure Res.* 74 (2), 232–239.

Curtis, A.S.G., Clark, P. (1990). The effects of topographic and mechanical properties of materials on cell behavior. *Crit. Rev. Biocompat.* 5 (4), 343–362.

Danielson, K.G., Baribault, H., Holmes, D.F., Graham, H., Kadler, K.E., Iozzo, R. V. (1997). Targeted disruption of decorin leads to abnormal collagen fibril morphology and skin fragility. *J. Cell Biol.* 136 (3), 729–743.

Daxer, A., Misof, K., Grabner, B., Ettl, A., Fratzl, P. (1998). Collagen fibrils in the human corneal stroma: Structure and aging. *Investig. Ophthalmol. Vis. Sci.* 39 (3), 644–648.

DelMonte, D.W., Kim, T. (2011). Anatomy and physiology of the cornea. *J. Cataract Refract. Surg.* 37 (3), 588–598.

Diab, M., Wu, J.J., Eyre, D.R. (1996). Collagen type IX from human cartilage: A structural profile of intermolecular cross-linking sites. *Biochem. J.* 314 (1), 327–332.

Ding, X., Wu, J., Jiang, C. (2010). ABCG2: A potential marker of stem cells and novel target in stem cell and cancer therapy. *Life Sci.* 86 (17–18), 631–637.

Dix, J.A., Verkman, A.S. (2008). Crowding Effects on Diffusion in Solutions and Cells. *Annu. Rev. Biophys.* 37 (1), 247–263.

Dominici, M., Le Blanc, K., Mueller, I., Slaper-Cortenbach, I., Marini, F., Krause, D., Deans, R., Keating, A., Prockop, D., Horwitz, E. (2006). Minimal criteria for defining multipotent

mesenchymal stromal cells. The International Society for Cellular Therapy position statement. *Cytotherapy*. 8 (4), 315–7.

Dos Santos, A., Balayan, A., Funderburgh, M.L., Ngo, J., Funderburgh, J.L., Deng, S.D. (2019). Differentiation capacity of human mesenchymal stem cells into keratocyte lineage. *Investig. Ophthalmol. Vis. Sci.* 60 (8), 3013–3023.

Doutch, J., Quantock, A.J., Smith, V.A., Meek, K.M. (2008). Light transmission in the human cornea as a function of position across the ocular surface: Theoretical and experimental aspects. *Biophys. J.* 95 (11), 5092–5099.

Dravida, S., Pal, R., Khanna, A., Tipnis, S.P., Ravindran, G., Khan, F. (2005). The transdifferentiation potential of limbal fibroblast-like cells. *Dev. Brain Res.* 160 (2), 239–251.

Dreier, B., Gasiorowski, J.Z., Morgan, J.T., Nealey, P.F., Russell, P., Murphy, C.J. (2013a). Early responses of vascular endothelial cells to topographic cues. *Am. J. Physiol. Physiol.* 305 (3), C290–C298.

Dreier, B., Thomasy, S.M., Mendonsa, R., Raghunathan, V.K., Russell, P., Murphy, C.J. (2013b). Substratum compliance modulates corneal fibroblast to myofibroblast transformation. *Investig. Ophthalmol. Vis. Sci.* 54 (8), 5901–5907.

Du, Y., Carlson, E.C., Funderburgh, M.L., Birk, D.E., Pearlman, E., Guo, N., Kao, W.W.-Y., Funderburgh, J.L. (2009). Stem Cell Therapy Restores Transparency to Defective Murine Corneas. *Stem Cells*. 27 (7), 1635–1642.

Du, Y., Funderburgh, M.L., Mann, M.M., SundarRaj, N., Funderburgh, J.L. (2005). Multipotent stem cells in human corneal stroma. *Stem Cells*. 23 (9), 1266–75.

Du, Y., Roh, D.S., Funderburgh, M.L., Mann, M.M., Marra, K.G., Rubin, J.P., Li, X., Funderburgh, J.L. (2010). Adipose-derived stem cells differentiate to keratocytes in vitro. *Mol. Vis.* 16 (September), 2680–2689.

Du, Y., SundarRaj, N., Funderburgh, M.L., Harvey, S.A., Birk, D.E., Funderburgh, J.L. (2007). Secretion and organization of a cornea-like tissue in vitro by stem cells from human corneal stroma. *Invest. Ophthalmol. Vis. Sci.* 48 (11), 5038–5045.

Dua, H.S., Faraj, L.A., Branch, M.J., Yeung, A.M., Elalfy, M.S., Said, D.G., Gray, T., Lowe, J. (2014). The collagen matrix of the human trabecular meshwork is an extension of the novel pre-Descemet's layer (Dua's layer). *Br. J. Ophthalmol.* 98 (5), 691–697.

Dua, H.S., Faraj, L.A., Said, D.G., Gray, T., Lowe, J. (2013). Human corneal anatomy redefined: A novel pre-descemet's layer (Dua's Layer). *Ophthalmology*. 120 (9), 1778–1785.

Dua, H.S., Said, D.G. (2016). Clinical evidence of the pre-Descemets layer (Dua's layer) in

corneal pathology. *Eye*.

Duarte Campos, D.F., Rohde, M., Ross, M., Anvari, P., Blaeser, A., Vogt, M., Panfil, C., Yam, G.H.-F., Mehta, J.S., Fischer, H., Walter, P., Fuest, M. (2019). Corneal bioprinting utilizing collagen-based bioinks and primary human keratocytes. *J. Biomed. Mater. Res. - Part A*. 107 (9), 1945–1953.

Dunlevy, J.R., Beales, M.P., Berryhill, B.L., Cornuet, P.K., Hassell, J.R. (2000). Expression of the Keratan Sulfate Proteoglycans Lumican, Keratocan and Osteoglycin/Mimecan During Chick Corneal Development. *Exp. Eye Res.* 70 (3), 349–362.

Dunn, G.A., Heath, J.P. (1976). A new hypothesis of contact guidance in tissue cells. *Exp. Cell Res.* 101 (1), 1–14.

Eghrari, A.O., Riazuddin, S.A., Gottsch, J.D. (2015). Overview of the Cornea: Structure, Function, and Development, 1st ed, Progress in Molecular Biology and Translational Science. Elsevier Inc.

Ellis, R.J. (2001). Macromolecular crowding: Obvious but underappreciated. *Trends Biochem. Sci.*

Elsheikh, A., Brown, M., Alhasso, D., Rama, P., Campanelli, M., Garway-Heath, D. (2008). Experimental assessment of corneal anisotropy. *J. Refract. Surg.* 24 (2), 178–187.

Eroshenko, N., Ramachandran, R., Yadavalli, V.K., Rao, R.R. (2013). Effect of substrate stiffness on early human embryonic stem cell differentiation. *J. Biol. Eng.* 7 (1), 7.

Espana, E.M., Birk, D.E. (2020). Composition, structure and function of the corneal stroma. *Exp. Eye Res.* 198, 108137.

Espana, E.M., Kawakita, T., Liu, C.Y., Tseng, S.C.G. (2004). CD-34 expression by cultured human keratocytes is downregulated during myofibroblast differentiation induced by TGF-β1. *Investig. Ophthalmol. Vis. Sci.* 45 (9), 2985–2991.

Estey, T., Piatigorsky, J., Lassen, N., Vasiliou, V. (2007). ALDH3A1: a corneal crystallin with diverse functions. *Exp. Eye Res.* 84 (1), 3–12.

Evans, C.A., Peterkofsky, B. (1976). Ascorbate-independent proline hydroxylation resulting from viral transformation of balb 3T3 cells and unaffected by dibutyryl camp treatment. *J. Cell. Physiol.* 89 (3), 355–367.

Eyre, D. (2001). Collagen of articular cartilage. *Arthritis Res. Ther.* 4 (30), 30–35.

Eyre, D.R., Wu, J.J. (2005). Collagen cross-links. *Top. Curr. Chem.* 247, 207–229.

Faraghat, S.A., Hoettges, K.F., Steinbach, M.K., Veen, D.R. van der, Brackenbury, W.J., Henslee, E.A., Labeed, F.H., Hughes, M.P. (2017). High-throughput, low-loss, low-cost, and label-free cell separation using electrophysiology-activated cell enrichment. *Proc.*

*Natl. Acad. Sci.* 114 (18), 4591–4596.

Feneck, E.M., Lewis, P.N., Meek, K.M. (2019). Three-dimensional imaging of the extracellular matrix and cell interactions in the developing prenatal mouse cornea. *Sci. Rep.* 9 (1), 11277.

Fernández-Pérez, J., Kador, K.E., Lynch, A.P., Ahearne, M. (2020a). Characterization of extracellular matrix modified poly(ε-caprolactone) electrospun scaffolds with differing fiber orientations for corneal stroma regeneration. *Mater. Sci. Eng. C*. 108 (November 2019), 0–8.

Fernández-Pérez, J., Madden, P.W., Ahearne, M. (2020b). Engineering a Corneal Stromal Equivalent Using a Novel Multilayered Fabrication Assembly Technique*. *Tissue Eng. Part A*. 60 (9), 152–160.

Fini, M.E. (1999). Keratocyte and fibroblast phenotypes in the repairing cornea. *Prog. Retin. Eye Res.* 18 (4), 529–551.

Fini, M.E., Stramer, B.M. (2005). How the cornea heals: cornea-specific repair mechanisms affecting surgical outcomes. *Cornea*. 24 (8 Suppl), S2–S11.

Foolen, J., Wunderli, S.L., Loerakker, S., Snedeker, J.G. (2018). Tissue alignment enhances remodeling potential of tendon-derived cells - Lessons from a novel microtissue model of tendon scarring. *Matrix Biol.* 65, 14–29.

Foster, J.W., Gouveia, R.M., Connon, C.J. (2015). Low-glucose enhances keratocyte-characteristic phenotype from corneal stromal cells in serum-free conditions. *Sci. Rep.* 5 (April), 10839.

Foster, J.W., Wahlin, K., Adams, S.M., Birk, D.E., Zack, D.J., Chakravarti, S. (2017). Cornea organoids from human induced pluripotent stem cells. *Sci. Rep.* 7 (January), 41286.

Franco-Barraza, J., Beacham, D.A., Amatangelo, M.D., Cukierman, E. (2016). Preparation of Extracellular Matrices Produced by Cultured and Primary Fibroblasts. *Curr. Protoc. Cell Biol.* 71 (June), 10.9.1-10.9.34.

Friedl, G., Schmidt, H., Rehak, I., Kostner, G., Schauenstein, K., Windhager, R. (2007). Undifferentiated human mesenchymal stem cells (hMSCs) are highly sensitive to mechanical strain: transcriptionally controlled early osteo-chondrogenic response in vitro. *Osteoarthr. Cartil.* 15 (11), 1293–1300.

Fukamizu, H., Grinnell, F. (1990). Spatial organization of extracellular matrix and fibroblast activity: Effects of serum, transforming growth factor β, and fibronectin. *Exp. Cell Res.* 190 (2), 276–282.

Funderburgh, J.L., Caterson, B., Conrad, G.W. (1986). Keratan sulfate proteoglycan during

embryonic development of the chicken cornea. *Dev. Biol.* 116 (2), 267–277.

Funderburgh, J.L., Funderburgh, M.L., Du, Y. (2016). Stem Cells in the Limbal Stroma. *Ocul. Surf.* 14 (2), 113–120.

Funderburgh, J.L., Funderburgh, M.L., Mann, M.M., Corpuz, L., Roth, M.R. (2001). Proteoglycan Expression during Transforming Growth Factor β-induced Keratocyte-Myofibroblast Transdifferentiation. *J. Biol. Chem.* 276 (47), 44173–44178.

Funderburgh, J.L., Hevelone, N.D., Roth, M.R., Funderburgh, M.L., Rodrigues, M.R., Nirankari, V.S., Conrad, G.W. (1998). Decorin and biglycan of normal and pathologic human corneas. *Investig. Ophthalmol. Vis. Sci.* 39 (10), 1957–1964.

Funderburgh, J.L., Mann, M.M., Funderburgh, M.L. (2003). Keratocyte phenotype mediates proteoglycan structure: A role for fibroblasts in corneal fibrosis. *J. Biol. Chem.* 278 (46), 45629–45637.

Funderburgh, M.L., Du, Y., Mann, M.M., SundarRaj, N., Funderburgh, J.L. (2005). PAX6 expression identifies progenitor cells for corneal keratocytes. *FASEB J.* 19 (10), 1371–1373.

Funderburgh, M.L., Mann, M.M., Funderburgh, J.L. (2008). Keratocyte phenotype is enhanced in the absence of attachment to the substratum. *Mol. Vis.* 14 (January), 308–317.

Gain, P., Jullienne, R., He, Z., Aldossary, M., Acquart, S., Cognasse, F., Thuret, G. (2016). Global Survey of Corneal Transplantation and Eye Banking. *JAMA Ophthalmol.* 134 (2), 167.

Galiacy, S.D., Fournié, P., Massoudi, D., Ancèle, E., Quintyn, J.-C., Erraud, A., Raymond-Letron, I., Rolling, F., Malecaze, F. (2011). Matrix metalloproteinase 14 overexpression reduces corneal scarring. *Gene Ther.* 18, 462–468.

Gaspar, D., Fuller, K.P., Zeugolis, D.I. (2019a). Polydispersity and negative charge are key modulators of extracellular matrix deposition under macromolecular crowding conditions. *Acta Biomater.* 88, 197–210.

Gaspar, D., Ryan, C.N.M., Zeugolis, D.I. (2019b). Multifactorial bottom-up bioengineering approaches for the development of living tissue substitutes. *FASEB J.* 33 (4), 5741–5754.

Gelse, K., Pöschl, E., Aigner, T. (2003). Collagens - Structure, function, and biosynthesis. *Adv. Drug Deliv. Rev.* 55 (12), 1531–1546.

Gerardo, H., Lima, A., Carvalho, J., Ramos, J.R.D., Couceiro, S., Travasso, R.D.M., Pires das Neves, R., Grãos, M. (2019). Soft culture substrates favor stem-like cellular phenotype and facilitate reprogramming of human mesenchymal stem/stromal cells (hMSCs) through mechanotransduction. *Sci. Rep.* 9 (1), 1–18.

Ghezzi, C.E., Marelli, B., Omenetto, F.G., Funderburgh, J.L., Kaplan, D.L. (2017). 3D functional corneal stromal tissue equivalent based on corneal stromal stem cells and multi-layered silk film architecture. *PLoS One*. 12 (1), 1–18.

Gipson, I.K., Spurr-Michaud, S.J., Tisdale, A.S. (1987). Anchoring fibrils from a complex network in human and rabbit cornea. *Investig. Ophthalmol. Vis. Sci.* 28 (2), 212–220.

Gollwitzer, C., Bartczak, D., Goenaga-Infante, H., Kestens, V., Krumrey, M., Minelli, C., Pálmai, M., Ramaye, Y., Roebben, G., Sikora, A., Varga, Z. (2016). A comparison of techniques for size measurement of nanoparticles in cell culture medium. *Anal. Methods*. 8 (26), 5272–5282.

Gonzalez-Molina, J., Mendonça da Silva, J., Fuller, B., Selden, C. (2019). The extracellular fluid macromolecular composition differentially affects cell-substrate adhesion and cell morphology. *Sci. Rep.* 9 (1), 1–12.

Gouveia, R.M., Castelletto, V., Alcock, S.G., Hamley, I.W., Connon, C.J. (2013). Bioactive films produced from self-assembling peptide amphiphiles as versatile substrates for tuning cell adhesion and tissue architecture in serum-free conditions. *J. Mater. Chem. B*. 1 (44), 6157–6169.

Gouveia, R.M., González-Andrades, E., Cardona, J.C., González-Gallardo, C., Ionescu, A.M., Garzon, I., Alaminos, M., González-Andrades, M., Connon, C.J. (2017a). Controlling the 3D architecture of Self-Lifting Auto-generated Tissue Equivalents (SLATEs) for optimized corneal graft composition and stability. *Biomaterials*. 121, 205–219.

Gouveia, R.M., Hamley, I.W., Connon, C.J. (2015). Bio-fabrication and physiological self-release of tissue equivalents using smart peptide amphiphile templates. *J. Mater. Sci. Mater. Med.* 26 (10), 1–9.

Gouveia, R.M., Koudouna, E., Jester, J., Figueiredo, F., Connon, C.J. (2017b). Template Curvature Influences Cell Alignment to Create Improved Human Corneal Tissue Equivalents. *Adv. Biosyst.* 1700135.

Graceffa, V., Zeugolis, D.I. (2019). Carrageenan enhances chondrogenesis and osteogenesis in human bone marrow stem cell culture. *Eur. Cell. Mater.* 37, 310–332.

Graham, J., Raghunath, M., Vogel, V. (2019). Fibrillar fibronectin plays a key role as nucleator of collagen I polymerization during macromolecular crowding-enhanced matrix assembly. *Biomater. Sci.* 7 (11), 4519–4535.

Griffith, M., Harkin, D.G. (2014). Recent advances in the design of artificial corneas. *Curr. Opin. Ophthalmol.* 25 (3), 240–7.

Guillemette, M.D., Cui, B., Roy, E., Gauvin, R., Giasson, C.J., Esch, M.B., Carrier, P.,

Deschambeault, A., Dumoulin, M., Toner, M., Germain, L., Veres, T., Auger, F.A. (2009). Surface topography induces 3D self-orientation of cells and extracellular matrix resulting in improved tissue function. *Integr. Biol.* 1 (2), 196–204.

Guo, X., Hutcheon, A.E.K., Melotti, S.A., Zieske, J.D., Trinkaus-Randall, V., Ruberti, J.W. (2007). Morphologic characterization of organized extracellular matrix deposition by ascorbic acid-stimulated human corneal fibroblasts. *Investig. Ophthalmol. Vis. Sci.* 48 (9), 4050–4060.

Haack-Sørensen, M., Hansen, S.K., Hansen, L., Gaster, M., Hyttel, P., Ekblond, A., Kastrup, J. (2013). Mesenchymal Stromal Cell Phenotype is not Influenced by Confluence during Culture Expansion. *Stem Cell Rev. Reports*. 9 (1), 44–58.

Hall, D., Minton, A.P. (2003). Macromolecular crowding: Qualitative and semiquantitative successes, quantitative challenges. *Biochim. Biophys. Acta - Proteins Proteomics*. 1649 (2), 127–139.

Hanna, C., Bicknell, D.S., O'brien, J.E. (1961). Cell Turnover in the Adult Human Eye. *Arch. Ophthalmol.* 65 (5), 695–698.

Harkin, D.G., Foyn, L., Bray, L.J., Sutherland, A.J., Li, F.J., Cronin, B.G. (2015). Concise reviews: can mesenchymal stromal cells differentiate into corneal cells? A systematic review of published data. *Stem Cells*. 33 (3), 785–791.

Hart, R.W., Farrell, R.A. (1969). Light scattering in the cornea. *J. Opt. Soc. Am.* 59 (6), 766–774.

Harve, K.S., Raghunath, M., Lareu, R.R., Rajagopalan, R. (2006). Macromolecular Crowding in Biological Systems: Dynamic Light Scattering (DLS) To Quantify the Excluded Volume Effect (EVE). *Biophys. Rev. Lett.* 01 (03), 317–325.

Harwood, R., Grant, M.E., Jackson, D.S. (1975). Studies on the glycosylation of hydroxylysine residues during collagen biosynthesis and the subcellular localization of collagen galactosyltransferase and collagen glucosyltransferase in tendon and cartilage cells. *Biochem. J.* 152 (2), 291–302.

Hashimoto, K., Ohyama, H. (1974). Cross banded filamentous aggregation in the human dermis. *J. Invest. Dermatol.* 62 (2), 106–112.

Hassell, J.R., Birk, D.E. (2010). The molecular basis of corneal transparency. *Exp. Eye Res.* 91 (3), 326–335.

Hata, R.-I., Senoo, H. (1989). L-ascorbic acid 2-phosphate stimulates collagen accumulation, cell proliferation, and formation of a three-dimensional tissuelike substance by skin fibroblasts. *J. Cell. Physiol.* 138 (1), 8–16.

Hayes, S., Lewis, P., Islam, M.M., Doutch, J., Sorensen, T., White, T., Griffith, M., Meek, K.M. (2015). The structural and optical properties of type III human collagen biosynthetic corneal substitutes. *Acta Biomater.* 25, 121–30.

Hertsenberg, A.J., Funderburgh, J.L. (2015). Stem Cells in the Cornea, 1st ed, Progress in Molecular Biology and Translational Science. Elsevier Inc.

Hill, L.J., Moakes, R.J.A., Vareechon, C., Butt, G., Ng, A., Brock, K., Chouhan, G., Vincent, R.C., Abbondante, S., Williams, R.L., Barnes, N.M., Pearlman, E., Wallace, G.R., Rauz, S., Logan, A., Grover, L.M. (2018). Sustained release of decorin to the surface of the eye enables scarless corneal regeneration. *npj Regen. Med. 2018 31*. 3 (1), 1–12.

Honn, K. V., Singley, J.A., Chavin, W. (1975). Fetal Bovine Serum: A Multivariate Standard. *Exp. Biol. Med.* 149 (2), 344–347.

Hopfer, U., Fukai, N., Hopfer, H., Wolf, G., Joyce, N., Li, E., Olsen, B.R. (2005). Targeted disruption of Col8a1 and Col8a2 genes in mice leads to anterior segment abnormalities in the eye. *FASEB J.* 19 (10), 1232–1244.

Iftimia-Mander, A., Hourd, P., Dainty, R., Thomas, R.J. (2013). Mesenchymal stem cell isolation from human umbilical cord tissue: Understanding and minimizing variability in cell yield for process optimization. *Biopreserv. Biobank.* 11 (5), 291–298.

Iozzo, R. V (1999). The biology of the small leucine-rich proteoglycans. Functional network of interactive proteins. *J. Biol. Chem.* 274 (27), 18843–6.

Isaacson, A., Swioklo, S., Connon, C.J. (2018). 3D bioprinting of a corneal stroma equivalent. *Exp. Eye Res.* 173 (March), 188–193.

Islam, M.M., Buznyk, O., Reddy, J.C., Pasyechnikova, N., Alarcon, E.I., Hayes, S., Lewis, P., Fagerholm, P., He, C., Iakymenko, S., Liu, W., Meek, K.M., Sangwan, V.S., Griffith, M. (2018). Biomaterials-enabled cornea regeneration in patients at high risk for rejection of donor tissue transplantation. *npj Regen. Med.* 3 (1).

Javidan, Y., Schilling, T.F. (2004). Development of cartilage and bone. *Methods Cell Biol.*

Jee, A.Y., Lee, M. (2010). Comparative analysis on the nanoindentation of polymers using atomic force microscopy. *Polym. Test.* 29 (1), 95–99.

Jester, J. V. (2008). Corneal Crystallins and the Development of Cellular Transparency. *Semin. Cell Dev. Biol.* 19 (2), 82–93.

Jester, J. V., Barry, P.A., Lind, G.J., Petroll, W.M., Garana, R., Cavanagh, H.D. (1994). Corneal keratocytes: In situ and in vitro organization of cytoskeletal contractile proteins. *Investig. Ophthalmol. Vis. Sci.* 35 (2), 730–743.

Jester, J. V., Murphy, C.J., Winkler, M., Bergmanson, J.P.G., Brown, D., Steinert, R.F., Mannis,

M.J. (2013). Lessons in corneal structure and mechanics to guide the corneal surgeon. *Ophthalmology*.

Jester, J. V., Petroll, W.M., Barry, P.A., Cavanagh, H.D. (1995). Expression of α-smooth muscle (α-SM) actin during corneal stromal wound healing. *Investig. Ophthalmol. Vis. Sci.* 36 (5), 809–819.

Jester, J. V, Moller-Pedersen, T., Huang, J., Sax, C.M., Kays, W.T., Cavangh, H.D., Petroll, W.M., Piatigorsky, J. (1999). The cellular basis of corneal transparency: evidence for "corneal crystallins." *J. Cell Sci.* 112 ( Pt 5, 613–622.

Jones, R.R., Mi, S., Chen, B., Hamley, I.W., Connon, C.J. (2011). Investigating The Mechanical Properties Of Collagen Substrates & Their Influence On The Ex Vivo Expansion Of Limbal Epithelial Cells. *Investig. Ophthalmol. Vis. Sci.* 52 (14), 312.

Joseph, A., Hossain, P., Jham, S., Jones, R.E., Tighe, P., McIntosh, R.S., Dua, H.S. (2003). Expression of CD34 and L-Selectin on Human Corneal Keratocytes. *Investig. Ophthalmol. Vis. Sci.* 44 (11), 4689–4692.

Joseph, R., Srivastava, O.P., Pfister, R.R. (2016). Modeling keratoconus using induced pluripotent stemcells. *Investig. Ophthalmol. Vis. Sci.* 57 (8), 3685–3697.

Juhl, P., Bondesen, S., Hawkins, C.L., Karsdal, M.A., Bay-Jensen, A.-C., Davies, M.J., Siebuhr, A.S. (2020). Dermal fibroblasts have different extracellular matrix profiles induced by TGF-β, PDGF and IL-6 in a model for skin fibrosis. *Sci. Reports 2020 101*. 10 (1), 1–10.

Kadler, K.E., Baldock, C., Bella, J., Boot-Handford, R.P. (2007). Collagens at a glance. *J. Cell Sci.* 120 (12), 1955–1958.

Kadler, K.E., Hill, A., Canty-Laird, E.G. (2008). Collagen fibrillogenesis: fibronectin, integrins, and minor collagens as organizers and nucleators. *Curr. Opin. Cell Biol.* 20 (5), 495–501.

Kadler, K.E., Holmes, D.F., Trotter, J.A., Chapman, J.A. (1996). Collagen fibril formation. *J. Biochem.* 316 (Pt 1), 1–11.

Kaluzhny, Y., Kinuthia, M.W., Plotkin, A., Hayden, P., Klausner, M. (2016). Molecular mechanism of ocular surface damage: Applications to dry eye and wound healing models on in vitro reconstructed human corneal tissues. *Investig. Ophthalmol. Vis. Sci.* 57 (12), 4380.

Kaluzhny, Y., Kinuthia, M.W., Truong, T., Lapointe, A.M., Hayden, P., Klausner, M. (2018). New human organotypic corneal tissue model for ophthalmic drug delivery studies. *Investig. Ophthalmol. Vis. Sci.* 59 (7), 2880–2898.

Kao, W.W.-Y., Liu, C.-Y. (2003). Roles of lumican and keratocan on corneal transparency. *Glycoconj. J.* 19 (4–5), 275–85.

Karamichos, Dimitrios, Funderburgh, M.L., Hutcheon, A.E.K., Zieske, J.D., Du, Y., Wu, J., Funderburgh, J.L. (2014). A role for topographic cues in the organization of collagenous matrix by corneal fibroblasts and stem cells. *PLoS One*. 9 (1), e86260.

Karamichos, D., Guo, X.Q., Hutcheon, A.E.K., Zieske, J.D. (2010). Human corneal fibrosis: An in vitro model. *Investig. Ophthalmol. Vis. Sci.* 51 (3), 1382–1388.

Karamichos, D., Hutcheon, A.E.K., Zieske, J.D. (2014). Reversal of fibrosis by TGF-β3 in a 3D invitro model. *Exp. Eye Res.* 124, 31–36.

Karamichos, D., Rich, C.B., Hutcheon, A.E.K., Ren, R., Saitta, B., Trinkaus-Randall, V., Zieske, J.D. (2011). Self-Assembled Matrix by Umbilical Cord Stem Cells. *J. Funct. Biomater.* 2 (4), 213–229.

Karamichos, D., Rich, C.B., Zareian, R., Hutcheon, A.E.K., Ruberti, J.W., Trinkaus-Randall, V., Zieske, J.D. (2013). TGF-β3 stimulates stromal matrix assembly by human corneal keratocyte-like cells. *Investig. Ophthalmol. Vis. Sci.* 54 (10), 6612–6619.

Karamichos, D., Zareian, R., Guo, X., Hutcheon, A.E.K., Ruberti, J.W., Zieske, J.D. (2012). Novel in Vitro Model for Keratoconus Disease. *J. Funct. Biomater.* 3 (4), 760–775.

Kaufman, H.E., Beuerman, R.W., Steinemann, T.L., Thompson, H.W., Varnell, E.D. (1991). Optisol Corneal Storage Medium. *Arch. Ophthalmol.* 109 (6), 864–868.

Kearns, V.R., Doherty, P.J., Beamson, G., Martin, N., Williams, R.L. (2010). Friction transfer of polytetrafluoroethylene (PTFE) to produce nanoscale features and influence cellular response in vitro. *J. Mater. Sci. Mater. Med.* 21 (7), 2213–2226.

Kearns, V.R., Williams, R.L., Mirvakily, F., Doherty, P.J., Martin, N. (2013). Guided gingival fibroblast attachment to titanium surfaces: An in vitro study. *J. Clin. Periodontol.* 40 (1), 99–108.

Kern, P., Menasche, M., Robert, L. (1991). Relative rates of biosynthesis of collagen type I, type V and type VI in calf cornea. *Biochem. J*. 274, 615–617.

Kessler, E., Adar, R. (1989). Type I procollagen C-proteinase from mouse fibroblasts: Purification and demonstration of a 55-kDa enhancer glycoprotein. *Eur. J. Biochem.* 186 (1–2), 115–121.

Kilic Bektas, C., Hasirci, V. (2020). Cell loaded 3D bioprinted GelMA hydrogels for corneal stroma engineering. *Biomater. Sci.* 8 (1), 438–449.

Kim, H., Jang, J., Park, J., Lee, K.P., Lee, S., Lee, D.M., Kim, K.H., Kim, H.K., Cho, D.W. (2019). Shear-induced alignment of collagen fibrils using 3D cell printing for corneal stroma tissue engineering. *Biofabrication*. 11 (3).

Kimura, S., Kobayashi, M., Nakamura, M., Hirano, K., Awaya, S., Hoshino, T. (1995).

Immunoelectron Microscopic Localization of Decorin in Aged Human Corneal and Scleral Stroma, Electron Microsc.

Klintworth, G.K. (2009). Corneal dystrophies. *Orphanet J. Rare Dis.* 4 (1), 7.

Knupp, C., Chong, N.H.V., Munro, P.M.G., Luthert, P.J., Squire, J.M. (2002). Analysis of the collagen VI assemblies associated with Sorsby's fundus dystrophy. *J. Struct. Biol.* 137 (1–2), 31–40.

Knupp, C., Pinali, C., Munro, P.M., Gruber, H.E., Sherratt, M.J., Baldock, C., Squire, J.M. (2006). Structural correlation between collagen VI microfibrils and collagen VI banded aggregates. *J. Struct. Biol.* 154 (3), 312–326.

Kobayasi, T., Asboe-Hansen, G., Tsurufuji, S. (1985). Filamentous aggregates of collagen. Ultrastructural evidence for collagen-fibril degradation in situ. *Arch. Dermatol. Res.* 277 (3), 214–219.

Komai, Y., Ushiki, T. (1991). The three-dimensional organisation of collagen fibrils in the human cornea and sclera. *Investig. Ophthalmol. Vis. Sci.* 32 (8), 2244–2258.

Koopman, R., Schaart, G., Hesselink, M.K. (2001). Optimisation of oil red O staining permits combination with immunofluorescence and automated quantification of lipids. *Histochem. Cell Biol.* 116 (1), 63–68.

Koudouna, E., Mikula, E., Brown, D.J., Young, R.D., Quantock, A.J., Jester, J. V. (2018). Cell regulation of collagen fibril macrostructure during corneal morphogenesis. *Acta Biomater.* 79, 96–112.

Kowalczuk, L., Latour, G., Bourges, J.-L., Savoldelli, M., Jeanny, J.-C., Plamann, K., Schanne-Klein, M.-C., Behar-Cohen, F. (2013). Multimodal Highlighting of Structural Abnormalities in Diabetic Rat and Human Corneas. *Transl. Vis. Sci. Technol.* 2 (2), 3.

Krahn, K.N., Bouten, C.V.C., Van Tuijl, S., Van Zandvoort, M.A.M.J., Merkx, M. (2006). Fluorescently labeled collagen binding proteins allow specific visualization of collagen in tissues and live cell culture. *Anal. Biochem.* 350 (2), 177–185.

Kumar, P., Satyam, A., Cigognini, D., Pandit, A., Zeugolis, D.I. (2018). Low oxygen tension and macromolecular crowding accelerate extracellular matrix deposition in human corneal fibroblast culture. *J. Tissue Eng. Regen. Med.* 12 (March 2017), 6–18.

Kumar, P., Satyam, A., Fan, X., Collin, E., Rochev, Y., Rodriguez, B.J., Gorelov, A., Dillon, S., Joshi, L., Raghunath, M., Pandit, A., Zeugolis, D.I. (2015a). Macromolecularly crowded in vitro microenvironments accelerate the production of extracellular matrix-rich supramolecular assemblies. *Sci. Rep.* 5, 8729.

Kumar, P., Satyam, A., Fan, X., Rochev, Y., Rodriguez, B.J., Gorelov, A., Joshi, L., Raghunath,

M., Pandit, A., Zeugolis, D.I. (2015b). Accelerated Development of Supramolecular Corneal Stromal-Like Assemblies from Corneal Fibroblasts in the Presence of Macromolecular Crowders. *Tissue Eng. Part C*. 21 (7), 660–70.

Kureshi, A.K., Funderburgh, J.L., Daniels, J.T. (2014). Human corneal stromal stem cells exhibit survival capacity following isolation from stored organ-culture corneas. *Investig. Ophthalmol. Vis. Sci.* 55 (11), 7583–7588.

Kwok, A., Raulf, N., Habib, N. (2019). Developing small activating RNA as a therapeutic: Current challenges and promises. *Ther. Deliv.*

Lagali, N., Germundsson, J., Fagerholm, P. (2009). The role of Bowman's layer in corneal regeneration after phototherapeutic keratectomy: A prospective study using in vivo confocal microscopy. *Investig. Ophthalmol. Vis. Sci.* 50 (9), 4192–4198.

Lai, J.Y., Tu, I.H. (2012). Adhesion, phenotypic expression, and biosynthetic capacity of corneal keratocytes on surfaces coated with hyaluronic acid of different molecular weights. *Acta Biomater.* 8 (3), 1068–1079.

Lareu, R.R., Arsianti, I., Subramhanya, H.K., Yanxian, P., Raghunath, M. (2007a). In Vitro Enhancement of Collagen Matrix Formation and Crosslinking for Applications in Tissue Engineering : A Preliminary Study. *Tissue Eng.* 13 (2).

Lareu, R.R., Subramhanya, K.H., Peng, Y., Benny, P., Chen, C., Wang, Z., Rajagopalan, R., Raghunath, M. (2007b). Collagen matrix deposition is dramatically enhanced in vitro when crowded with charged macromolecules: The biological relevance of the excluded volume effect. *FEBS Lett.* 581 (14), 2709–2714.

Lassen, N., Pappa, A., Black, W.J., Jester, J. V., Day, B.J., Min, E., Vasiliou, V. (2006). Antioxidant function of corneal ALDH3A1 in cultured stromal fibroblasts. *Free Radic. Biol. Med.* 41 (9), 1459–1469.

Last, J.A., Thomasy, S.M., Croasdale, C.R., Russell, P., Murphy, C.J. (2012). Compliance profile of the human cornea as measured by atomic force microscopy. *Micron*. 43 (12), 1293–1298.

Lauridsen, H.M., Gonzalez, A.L. (2017). Biomimetic, ultrathin and elastic hydrogels regulate human neutrophil extravasation across endothelial-pericyte bilayers. *PLoS One*. 12 (2), e0171386.

Le Saux, G., Wu, M.C., Toledo, E., Chen, Y.Q., Fan, Y.J., Kuo, J.C., Schvartzman, M. (2020). Cell-Cell Adhesion-Driven Contact Guidance and Its Effect on Human Mesenchymal Stem Cell Differentiation. *ACS Appl. Mater. Interfaces*. 12 (20), 22399–22409.

Lee, A., Karamichos, D., Onochie, O.E., Hutcheon, A.E.K., Rich, C.B., Zieske, J.D., Trinkaus-

Randall, V. (2018). Hypoxia modulates the development of a corneal stromal matrix model. *Exp. Eye Res.* 170 (November 2017), 127–137.

Levis, H.J., Brown, R.A., Daniels, J.T. (2010). Plastic compressed collagen as a biomimetic substrate for human limbal epithelial cell culture. *Biomaterials*. 31 (30), 7726–7737.

Li, G.-G., Zhu, Y.-T., Xie, H.-T., Chen, S.-Y., Tseng, S.C.G. (2012). Mesenchymal Stem Cells Derived from Human Limbal Niche Cells. *Invest. Ophthalmol. Vis. Sci.* 53 (9), 5686–5697.

Li, J., Chen, M., Fan, X., Zhou, H. (2016). Recent advances in bioprinting techniques: Approaches, applications and future prospects. *J. Transl. Med.* 14 (1), 271.

Liang, Y., Yu, D., Perez-Soler, R., Klostergaard, J., Zou, Y. (2017). TRIB2 contributes to cisplatin resistance in small cell lung cancer. *Oncotarget*. 8 (65), 109596–109608.

Lim, M., Goldstein, M.H., Tuli, S., Schultz, G.S. (2003). Growth factor, cytokine and protease interactions during corneal wound healing. *Ocul. Surf.* 1 (2), 53–65.

Lindstrom, R.L., Kaufman, H.E., Skelnik, D.L., Laing, R.A., Lass, J.H., Musch, D.C., Trousdale, M.D., Reinhart, W.J., Burris, T.E., Sugar, A., Davis, R.M., Hirokawa, K., Smith, T., Gordon, J.F. (1992). Optisol corneal storage medium. *Am. J. Ophthalmol.* 114 (3), 345–356.

Liu, C.Y., Birk, D.E., Hassell, J.R., Kane, B., Kao, W.W.Y. (2003). Keratocan-deficient mice display alterations in corneal structure. *J. Biol. Chem.* 278 (24), 21672–21677.

Liu, C.Y., Shiraishi, A., Kao, C.W.C.., Converse, R.L., Funderburgh, J.L., Corpuz, L.M., Conrad, G.W., Kao, W.W.Y. (1998). The cloning of mouse keratocan cDNA and genomic DNA and the characterization of its expression during eye development. *J. Biol. Chem.* 273 (35), 22584–22588.

Liu, H., Zhang, J., Liu, C.-Y., Hayashi, Y., Kao, W.W.-Y. (2012). Bone marrow mesenchymal stem cells can differentiate and assume corneal keratocyte phenotype. *J. Cell. Mol. Med.* 16 (5), 1114–1124.

Liu, W., Merrett, K., Griffith, M., Fagerholm, P., Dravida, S., Heyne, B., Scaiano, J.C., Watsky, M.A., Shinozaki, N., Lagali, N., Munger, R., Li, F. (2008). Recombinant human collagen for tissue engineered corneal substitutes. *Biomaterials*. 29 (9), 1147–1158.

Lizarraga-Valderrama, L.R., Taylor, C.S., Claeyssens, F., Haycock, J.W., Knowles, J.C., Roy, I. (2019). Unidirectional neuronal cell growth and differentiation on aligned polyhydroxyalkanoate blend microfibres with varying diameters. *J. Tissue Eng. Regen. Med.* 13 (9), 1581–1594.

Löffek, S., Schilling, O., Franzke, C.W. (2011). Biological role of matrix metalloproteinases: A critical balance. *Eur. Respir. J.* 38 (1), 191–208.

Long, C.J., Roth, M.R., Tasheva, E.S., Funderburgh, M.L., Smit, R., Conrad, G.W., Funderburgh,

J.L. (2000). Fibroblast growth factor-2 promotes keratan sulfate proteoglycan expression by keratocytes in vitro. *J. Biol. Chem.* 275 (18), 13918–13923.

Lorenzo-Martín, E., Gallego-Muñoz, P., Mar, S., Fernández, I., Cidad, P., Martínez-García, M.C. (2019). Dynamic changes of the extracellular matrix during corneal wound healing. *Exp. Eye Res.* 186.

Luong, L.N., Ramaswamy, J., Kohn, D.H. (2012). Effects of osteogenic growth factors on bone marrow stromal cell differentiation in a mineral-based delivery system. *Biomaterials*. 33 (1), 283–294.

Luse, S.A. (1960). Electron microscopic studies of brain tumors. *Neurology*. 10 (10), 881–905.

Lynch, A.P., Ahearne, M. (2017). Retinoic Acid Enhances the Differentiation of Adipose-Derived Stem Cells to Keratocytes In Vitro. *Transl. Vis. Sci. Technol.* 6 (1), 6.

Lynch, A.P., O'Sullivan, F., Ahearne, M. (2016). The effect of growth factor supplementation on corneal stromal cell phenotype in vitro using a serum-free media. *Exp. Eye Res.* 151, 26–37.

Määttä, M., Väisänen, T., Väisänen, M.R., Pihlajaniemi, T., Tervo, T. (2006). Altered expression of type XIII collagen in keratoconus and scarred human cornea: Increased expression in scarred cornea is associated with myofibroblast transformation. *Cornea*. 25 (4), 448–453.

Massoudi, D., Malecaze, F., Soler, V., Butterworth, J., Erraud, A., Fournié, P., Koch, M., Galiacy, S.D. (2012). NC1 long and NC3 short splice variants of type XII collagen are overexpressed during corneal scarring. *Investig. Ophthalmol. Vis. Sci.* 53 (11), 7246–7256.

Maurice, D.M. (1957). The Structure and Transparency of the Cornea. *J. Physiol.* 136, 263–286.

McDermott, B.T., Ellis, S., Bou-Gharios, G., Clegg, P.D., Tew, S.R. (2016). RNA binding proteins regulate anabolic and catabolic gene expression in chondrocytes. *Osteoarthr. Cartil.* 24 (7), 1263–1273.

McKee, H.D., Irion, L.C.D., Carley, F.M., Brahma, A.K., Jafarinasab, M.R., Rahmati-Kamel, M., Kanavi, M.R., Feizi, S. (2014). Re: Dua et al.: Human corneal anatomy redefined: a novel pre-Descemet layer (Dua's layer) (Ophthalmology 2013;120:1778–85). *Ophthalmology*. 121 (5), e24–e25.

Meek, K.M., Knupp, C. (2015). Corneal structure and transparency. *Prog. Retin. Eye Res.* 49, 1–16.

Meek, K.M., Leonard, D.W., Connon, C.J., Dennis, S., Khan, S. (2003). Transparency, swelling

and scarring in the corneal stroma. *Eye*. 17 (8), 927–936.

Menendez, L., Kulik, M.J., Page, A.T., Park, S.S., Lauderdale, J.D., Cunningham, M.L., Dalton, S. (2013). Directed differentiation of human pluripotent cells to neural crest stem cells. *Nat. Protoc.* 8 (1), 203–12.

Michelacci, Y.M. (2003). Collagens and proteoglycans of the corneal extracellular matrix. *Brazilian J. Med. Biol. Res.* 36 (8), 1037–1046.

Miki, H., Unno, K., Park, P., Ohnos, T., Nakajima, M. (1993). Morphogenesis and Origin of Fibrous Long-Spacing Collagen Fibers in Collagenase-Treated Mouse Skin Tissues. *Tissue Cell*. 25 (5), 669–680.

Minton, A.P. (2001). The Influence of Macromolecular Crowding and Macromolecular Confinement on Biochemical Reactions in Physiological Media. *J. Biol. Chem.* 276 (14), 10577–10580.

Miwa, H., Era, T. (2018). Tracing the destiny of mesenchymal stem cells from embryo to adult bone marrow and white adipose tissue via pdgfrα expression. *Dev.* 145 (2).

Mohan, Rahul R., Hutcheon, A.E.K., Choi, R., Hong, J.W., Lee, J.S., Mohan, Rajiv R., Ambrósio, R., Zieske, J.D., Wilson, S.E. (2003). Apoptosis, necrosis, proliferation, and myofibroblast generation in the stroma following LASIK and PRK. *Exp. Eye Res.* 76 (1), 71–87.

Møller-Pedersen, T. (2004). Keratocyte reflectivity and corneal haze. *Exp. Eye Res.* 78 (3), 553–560.

Mott, J.D., Thomas, C.L., Rosenbach, M.T., Takahara, K., Greenspan, D.S., Banda, M.J. (2000). Post-translational proteolytic processing of procollagen C-terminal proteinase enhancer releases a metalloproteinase inhibitor. *J. Biol. Chem.* 275 (2), 1384–1390.

Mukhey, D., Phillips, J.B., Daniels, J.T., Kureshi, A.K. (2017). Controlling human corneal stromal stem cell contraction to mediate rapid cell and matrix organization of real architecture for 3-dimensional tissue equivalents. *Acta Biomater.*

Mulholland, B., Tuft, S.J., Khaw, P.T. (2005). Matrix metalloproteinase distribution during early corneal wound healing. *Eye*. 19 (5), 584–588.

Murad, S., Grove, D., Lindberg, K.A., Reynolds, G., Sivarajah, A., Pinnellt, S.R. (1981). Regulation of collagen synthesis by ascorbic acid (prolyl hydroxylation/lysyl hydroxylation/human skin fibroblasts), Biochemistry.

Murad, S., Tajima, S., Johnson, G.R., Sivarajah, S., Pinnell, S.R. (1983). Collagen synthesis in cultured human skin fibroblasts: effect of ascorbic acid and its analogs. *J. Invest. Dermatol.* 81 (2), 158–162.

Muraglia, A., Cancedda, R., Quarto, R. (2000). Clonal mesenchymal progenitors from human

bone marrow differentiate in vitro according to a hierarchical model. *J. Cell Sci.* 113 (7), 1161–1166.

Musselmann, K., Alexandrou, B., Kane, B., Hassell, J.R. (2005). Maintenance of the keratocyte phenotype during cell proliferation stimulated by insulin. *J. Biol. Chem.* 280 (38), 32634–32639.

Myrna, K.E., Mendonsa, R., Russell, P., Pot, S.A., Liliensiek, S.J., Jester, J. V., Nealey, P.F., Brown, D., Murphy, C.J. (2012). Substratum Topography Modulates Corneal Fibroblast to Myofibroblast Transformation. *Investig. Opthalmology Vis. Sci.* 53 (2), 811.

Myrna, K.E., Pot, S.A., Murphy, C.J. (2009). Meet the corneal myofibroblast: The role of myofibroblast transformation in corneal wound healing and pathology. *Vet. Ophthalmol.* 12 (SUPPL. 1), 25–27.

Myshkin, N.K., Petrokovets, M.I., Kovalev, A. V. (2005). Tribology of polymers: Adhesion, friction, wear, and mass-transfer. *Tribol. Int.* 38 (11-12 SPEC. ISS.), 910–921.

Nakamura, K., Yoshimura, A., Kaneko, T., Sato, K., Hara, Y. (2014). ROCK inhibitor Y-27632 maintains the proliferation of confluent human mesenchymal stem cells. *J. Periodontal Res.* 49 (3), 363–370.

Naylor, R.W., McGhee, C.N.J., Cowan, C.A., Davidson, A.J., Holm, T.M., Sherwin, T. (2016). Derivation of Corneal Keratocyte-Like Cells from Human Induced Pluripotent Stem Cells. *PLoS One*. 11 (10), e0165464.

Newsome, D.A., Gross, J., Hassell, J.R. (1982). Human corneal stroma contains three distinct collagens. *Investig. Ophthalmol. Vis. Sci.* 22 (3), 376–381.

Nguyen, A.T., Sathe, S.R., Yim, E.K.F. (2016). From nano to micro: Topographical scale and its impact on cell adhesion, morphology and contact guidance. *J. Phys. Condens. Matter*. 28 (18).

Nikkhah, M., Edalat, F., Manoucheri, S., Khademhosseini, A. (2012). Engineering microscale topographies to control the cell-substrate interface. *Biomaterials*.

Ohara, P.T., Buck, R.C. (1979). Contact guidance in vitro. A light, transmission, and scanning electron microscopic study. *Exp. Cell Res.* 121 (2), 235–249.

Okamoto, T., Aoyama, T., Nakayama, T., Nakamata, T., Hosaka, T., Nishijo, K., Nakamura, T., Kiyono, T., Toguchida, J. (2002). Clonal heterogeneity in differentiation potential of immortalized human mesenchymal stem cells. *Biochem. Biophys. Res. Commun.* 295 (2), 354–361.

Padayatty, S.J., Levine, M. (2016). Vitamin C: the known and the unknown and Goldilocks. *Oral Dis.* 22 (6), 463–493.

Paige, M.F., Goh, M.C. (2001). A study of fibrous long spacing collagen ultrastructure and assembly by atomic force microscopy. *Micron*. 32 (3), 355–361.

Paige, M.F., Rainey, J.K., Goh, M.C. (1998). Fibrous long spacing collagen ultrastructure elucidated-by atomic force microscopy. *Biophys. J.* 74 (6), 3211–3216.

Paik, D.C., Trokel, S.L., Suh, L.H. (2018). Just What Do We Know About Corneal Collagen Turnover? *Cornea*. 37 (11), e49–e50.

Park, S.H., Kim, K.W., Chun, Y.S., Kim, J.C. (2012). Human mesenchymal stem cells differentiate into keratocyte-like cells in keratocyte-conditioned medium. *Exp. Eye Res.* 101, 16–26.

Parkinson, J., Kadler, K.E., Brass, A. (1995). Simple Physical Model of Collagen Fibrillogenesis. *Mol. Biol.* (1994), 823–831.

Pei, Y., Reins, R.Y., McDermott, A.M. (2006). Aldehyde dehydrogenase (ALDH) 3A1 expression by the human keratocyte and its repair phenotypes. *Exp. Eye Res.* 83 (5), 1063–1073.

Pei, Y., Sherry, D.M., McDermott, A.M. (2004). Thy-1 distinguishes human corneal fibroblasts and myofibroblasts from keratocytes. *Exp. Eye Res.* 79 (5), 705–712.

Pellegata, N.S., Dieguez-Lucena, J.L., Joensuu, T., Lau, S., Montgomery, K.T., Krahe, R., Kivelä, T., Kucherlapati, R., Forsius, H., De La Chapelle, A. (2000). Mutations in KERA, encoding keratocan, cause cornea plana. *Nat. Genet.* 25 (1), 91–95.

Pels, L. (1997). Organ culture: The method of choice for preservation of human donor corneas. *Br. J. Ophthalmol.* 81 (7), 523–525.

Peng, Y., Raghunath, M. (2010). Learning From Nature: Emulating Macromolecular Crowding To Drive Extracellular Matrix Enhancement For The Creation Of Connective Tissue in vitro, in: Eberli, D. (Ed.), Tissue Engineering. InTech, pp. 103–118.

Perdivara, I., Yamauchi, M., Tomer, K.B. (2013). Molecular characterization of collagen hydroxylysine O-glycosylation by mass spectrometry: Current status. *Aust. J. Chem.* 66 (7), 760–769.

Perrella, G., Brusini, P., Spelat, R., Hossain, P., Hopkinson, A., Dua, H.S. (2007). Expression of haematopoietic stem cell markers, CD133 and CD34 on human corneal keratocytes. *Br. J. Ophthalmol.* 91 (1), 94–99.

Pflugfelder, S.C., Stern, M.E. (2020). Biological functions of tear film. *Exp. Eye Res.*

Phinney, D.G., Kopen, G., Righter, W., Webster, S., Tremain, N., Prockop, D.J. (1999). Donor variation in the growth properties and osteogenic potential of human marrow stromal cells. *J. Cell. Biochem.* 75 (3), 424–436.

Phu, D., Wray, L.S., Warren, R. V., Haskell, R.C., Orwin, E.J. (2011). Effect of Substrate Composition and Alignment on Corneal Cell Phenotype. *Tissue Eng. Part A*. 17 (5–6), 799–807.

Pickard, A., Adamson, A., Lu, Y., Chang, J., Garva, R., Hodson, N., Kadler, K.E. (2018). Collagen assembly and turnover imaged with a CRISPR-Cas9 engineered Dendra2 tag. Manchester.

Pinnamaneni, N., Funderburgh, J.L. (2012). Concise review: Stem cells in the corneal stroma. *Stem Cells*. 30 (6), 1059–63.

Pinnell, S.R. (1985). Regulation of collagen biosynthesis by ascorbic acid: A review. *Yale J. Biol. Med.* 58 (6), 553–559.

Polisetty, N., Fatima, A., Madhira, S.L., Sangwan, V.S., Vemuganti, G.K. (2008). Mesenchymal cells from limbal stroma of human eye. *Mol. Vis.* 14, 431–42.

Powell, D.W., Mifflin, R.C., Valentich, J.D., Crowe, S.E., Saada, J.I., West, A.B. (1999). Myofibroblasts. I. Paracrine cells important in health and disease. *Am. J. Physiol. - Cell Physiol.*

Predović, J., Balog, T., Marotti, T., Gabrić, N., Bohać, M., Romac, I., Dekaris, I. (2008). The expression of human corneal MMP-2, MMP-9, proMMP-13 and TIMP-1 in bullous keratopathy and keratoconus. *Coll. Antropol.* 32 (SUPPL. 2), 15–19.

Prewitz, M.C., Stißel, A., Friedrichs, J., Träber, N., Vogler, S., Bornhäuser, M., Werner, C. (2015). Extracellular matrix deposition of bone marrow stroma enhanced by macromolecular crowding. *Biomaterials*. 73, 60–69.

Priyadarsini, S., McKay, T.B., Sarker-Nag, A., Allegood, J., Chalfant, C., Ma, J.X., Karamichos, D. (2016a). Complete metabolome and lipidome analysis reveals novel biomarkers in the human diabetic corneal stroma. *Exp. Eye Res.* 153, 90–100.

Priyadarsini, S., Nicholas, S.E., Karamichos, D. (2017a). 3D Stacked Construct: A Novel Substitute for Corneal Tissue Engineering, in: Pébay, A., Turksen, K. (Eds.), Sphingosine-1-Phosphate. Methods in Molecular Biology. Humana Press, New York, NY, pp. 173–180.

Priyadarsini, S., Rowsey, T.G., Ma, J.X., Karamichos, D. (2017b). Unravelling the stromal-nerve interactions in the human diabetic cornea. *Exp. Eye Res.* 164, 22–30.

Priyadarsini, S., Sarker-Nag, A., Rowsey, T.G., Ma, J.X., Karamichos, D. (2016b). Establishment of a 3D In vitro model to accelerate the development of human therapies against corneal diabetes. *PLoS One*. 11 (12), 1–17.

Proulx, S., d'Arc Uwamaliya, J., Carrier, P., Deschambeault, A., Audet, C., Giasson, C.J., Guerin,

S.L., Auger, F.A., Germain, L. (2010). Reconstruction of a human cornea by the self-assembly approach of tissue engineering using the three native cell types. *Mol Vis*. 16 (October 2009), 2192–2201.

Quantock, A.J., Winkler, M., Parfitt, G.J., Young, R.D., Brown, D.J., Boote, C., Jester, J. V. (2015). From nano to macro: Studying the hierarchical structure of the corneal extracellular matrix. *Exp. Eye Res.* 133, 81–99.

Rabinowitz, Y.S. (1998). Keratoconus. *Surv. Ophthalmol.*

Rada, J.A., Cornuet, P.K., Hassell, J.R. (1993). Regulation of corneal collagen fibrillogenesis in vitro by corneal proteoglycan (lumican and decorin) core proteins. *Exp. Eye Res.*

Radner, W., Zehetmayer, M., Aufreiter, R., Mallinger, R. (1998). Interlacing and Cross-Angle Distribution of Collagen Lamellae in the Human Cornea. *Cornea*. 17 (5), 537–543.

Ranamukhaarachchi, S.K., Modi, R.N., Han, A., Velez, D.O., Kumar, A., Engler, A.J., Fraley, S.I. (2019). Macromolecular crowding tunes 3D collagen architecture and cell morphogenesis. *Biomater. Sci.* 7 (2), 618–633.

Rashid, R., Lim, N.S.J., Chee, S.M.L., Png, S.N., Wohland, T., Raghunath, M. (2014). Novel Use for Polyvinylpyrrolidone as a Macromolecular Crowder for Enhanced Extracellular Matrix Deposition and Cell Proliferation. *Tissue Eng. Part C Methods*. 20 (12), 994–1002.

Refaaq, F.M., Chen, X., Pang, S.W. (2020). Effects of topographical guidance cues on osteoblast cell migration. *Sci. Rep.* 10 (1), 1–11.

Rehany, U., Ishii, Y., Lahav, M., Rumelt, S. (2000). Ultrastructural changes in corneas of diabetic patients: An electron-microscopy study. *Cornea*. 19 (4), 534–538.

Reinstein, D.Z., Archer, T.J., Gobbe, M., Silverman, R.H., Coleman, D.J. (2009). Stromal thickness in the normal cornea: three-dimensional display with artemis very high-frequency digital ultrasound. *J. Refract. Surg.* 25 (9), 776–86.

Ren, R., Hutcheon, A.E.K., Guo, X.Q., Saeidi, N., Melotti, S.A., Ruberti, J.W., Zieske, J.D., Trinkaus-Randall, V. (2008). Human primary corneal fibroblasts synthesize and deposit proteoglycans in long-term 3-D cultures. *Dev. Dyn.* 237 (10), 2705–2715.

Rezakhaniha, R., Agianniotis, A., Schrauwen, J.T.C., Griffa, A., Sage, D., Bouten, C.V.C., Van De Vosse, F.N., Unser, M., Stergiopulos, N. (2012). Experimental investigation of collagen waviness and orientation in the arterial adventitia using confocal laser scanning microscopy. *Biomech. Model. Mechanobiol.* 11 (3–4), 461–473.

Ricard-Blum, S. (2011). The Collagen Family. *Cold Spring Harb. Perspect. Biol.* 3 (1), 1–19.

Rider, P., Kačarević, Ž.P., Alkildani, S., Retnasingh, S., Barbeck, M. (2018). Bioprinting of tissue engineering scaffolds. *J. Tissue Eng.*

Riekstina, U., Parfejevs, V., Hoogduijn, M., Mc, E. (n.d.). Embryonic Stem Cell Marker Expression Pattern in Human Mesenchymal Stem Cells Derived from Bone Marrow, Adipose Tissue, Heart and Dermis.

Ringvold, A., Anderssen, E., Kjønniksen, I. (2000). Distribution of ascorbate in the anterior bovine eye. *Investig. Ophthalmol. Vis. Sci.* 41 (1), 20–23.

Romano, V., Tey, A., Hill, N.M.E., Ahmad, S., Britten, C., Batterbury, M., Willoughby, C., Kaye, S.B. (2015). Influence of graft size on graft survival following Descemet stripping automated endothelial keratoplasty. *Br. J. Ophthalmol.* 99 (6), 784–788.

Rønnow, S.R., Dabbagh, R.Q., Genovese, F., Nanthakumar, C.B., Barrett, V.J., Good, R.B., Brockbank, S., Cruwys, S., Jessen, H., Sorensen, G.L., Karsdal, M.A., Leeming, D.J., Sand, J.M.B. (2020). Prolonged Scar-in-a-Jar: An in vitro screening tool for anti-fibrotic therapies using biomarkers of extracellular matrix synthesis. *Respir. Res.* 21 (1), 1–14.

Rotherham, M., Henstock, J.R., Qutachi, O., El Haj, A.J. (2018). Remote regulation of magnetic particle targeted Wnt signaling for bone tissue engineering. *Nanomedicine Nanotechnology, Biol. Med.* 14 (1), 173–184.

Ruberti, J.W., Zieske, J.D. (2008). Prelude to corneal tissue engineering - Gaining control of collagen organization. *Prog. Retin. Eye Res.* 27 (5), 549–577.

Ruiz-Ederra, J., Verkman, A.S. (2009). Aquaporin-1-facilitated keratocyte migration in cell culture and in vivo corneal wound healing models. *Exp. Eye Res.* 89 (2), 159–165.

Ruoslahti, E., Pekkala, A., Engvall, E. (1979). Effect of dextran sulfate on fibronectin-collagen interaction. *FEBS Lett.* 107 (1), 51–54.

Saeidi, N., Guo, X., Hutcheon, A.E.K., Sander, E.A., Bale, S.S., Melotti, S.A., Zieske, J.D., Trinkaus-Randall, V., Ruberti, J.W. (2012a). Disorganized collagen scaffold interferes with fibroblast mediated deposition of organized extracellular matrix in vitro. *Biotechnol. Bioeng.* 109 (10), 2683–2698.

Saeidi, N., Karmelek, K.P., Paten, J.A., Zareian, R., DiMasi, E., Ruberti, J.W. (2012b). Molecular crowding of collagen: A pathway to produce highly-organized collagenous structures. *Biomaterials*. 33 (30), 7366–7374.

Sajjad, A. (2012). Ocular Prosthesis-A Simulation of Human Anatomy: A Literature Review.

Sandberg-Lall, M., Hägg, P.O., Wahlström, I., Pihlajaniemi, T. (2000). Type XIII collagen is widely expressed in the adult and developing human eye and accentuated in the ciliary muscle, the optic nerve and the neural retina. *Exp. Eye Res.* 70 (4), 401–410.

Satyam, A., Kumar, P., Cigognini, D., Pandit, A., Zeugolis, D.I. (2016). Low, but not too low, oxygen tension and macromolecular crowding accelerate extracellular matrix

deposition in human dermal fibroblast culture. *Acta Biomater.* 44, 221–231.

Satyam, A., Kumar, P., Fan, X., Gorelov, A., Rochev, Y., Joshi, L., Peinado, H., Lyden, D., Thomas, B., Rodriguez, B., Raghunath, M., Pandit, A., Zeugolis, D.I. (2014). Macromolecular crowding meets tissue engineering by self-assembly: A paradigm shift in regenerative medicine. *Adv. Mater.* 26 (19), 3024–3034.

Satyam, A., Tsokos, M.G., Tresback, J.S., Zeugolis, D.I., Tsokos, G.C. (2020). Cell-Derived Extracellular Matrix-Rich Biomimetic Substrate Supports Podocyte Proliferation, Differentiation, and Maintenance of Native Phenotype. *Adv. Funct. Mater.* 1908752, 1–11.

Schindelin, J., Arganda-Carreras, I., Frise, E., Kaynig, V., Longair, M., Pietzsch, T., Preibisch, S., Rueden, C., Saalfeld, S., Schmid, B., Tinevez, J.Y., White, D.J., Hartenstein, V., Eliceiri, K., Tomancak, P., Cardona, A. (2012). Fiji: An open-source platform for biological-image analysis. *Nat. Methods*.

Schlötzer-Schrehardt, U., Bachmann, B.O., Tourtas, T., Torricelli, A.A.M., Singh, A., González, S., Mei, H., Deng, S.X., Wilson, S.E., Kruse, F.E. (2015). Ultrastructure of the posterior corneal stroma. *Ophthalmology*. 122 (4), 693–699.

Schofield, A.L., Smith, C.I., Kearns, V.R., Martin, D.S., Farrell, T., Weightman, P., Williams, R.L. (2011). The use of reflection anisotropy spectroscopy to assess the alignment of collagen. *J. Phys. D. Appl. Phys.* 44 (33), 335302.

Scott, P.G., McEwan, P.A., Dodd, C.M., Bergmann, E.M., Bishop, P.N., Bella, J. (2004). Crystal structure of the dimeric protein core of decorin, the archetypal small leucine-rich repeat proteoglycan. *Proc. Natl. Acad. Sci. U. S. A.* 101 (44), 15633–15638.

Scott, S.G., Jun, A.S., Chakravarti, S. (2011). Sphere formation from corneal keratocytes and phenotype specific markers. *Exp. Eye Res.* 93 (6), 898–905.

Sejpal, K., Bakhtiari, P., Deng, S.X. (2013). Presentation, diagnosis and management of limbal stem cell deficiency, in: Middle East African Journal of Ophthalmology. Wolters Kluwer -- Medknow Publications, pp. 5–10.

Shaharuddin, B., Osei-Bempong, C., Ahmad, S., Rooney, P., Ali, S., Oldershaw, R., Meeson, A. (2016). Human limbal mesenchymal stem cells express ABCB5 and can grow on amniotic membrane. *Regen. Med.* 11 (3), 273–86.

Shamsah, A.H., Cartmell, S.H., Richardson, S.M., Bosworth, L.A. (2019). Mimicking the annulus fibrosus using electrospun polyester blended scaffolds. *Nanomaterials*. 9 (4), 537.

Shendi, D., Marzi, J., Linthicum, W., Rickards, A.J., Dolivo, D.M., Keller, S., Kauss, M.A., Wen,

Q., McDevitt, T.C., Dominko, T., Schenke-Layland, K., Rolle, M.W. (2019). Hyaluronic acid as a macromolecular crowding agent for production of cell-derived matrices. *Acta Biomater.* 100, 292–305.

Sidney, L.E., Branch, M.J., Dua, H.S., Hopkinson, A. (2015). Effect of culture medium on propagation and phenotype of corneal stroma–derived stem cells. *Cytotherapy*. 17, 1706–1722.

Sidney, L.E., Branch, M.J., Dunphy, S., Dua, H.S., Hopkinson, A. (2014). Concise Review: Evidence for CD34 as a common marker for diverse progenitors. *Stem Cells*. 32, 1380–1389.

Sidney, L.E., Hopkinson, A. (2018). Corneal keratocyte transition to mesenchymal stem cell phenotype and reversal using serum-free medium supplemented with fibroblast growth factor-2, transforming growth factor-β3 and retinoic acid. *J. Tissue Eng. Regen. Med.* 12 (1), e203–e215.

Siegel, G., Kluba, T., Hermanutz-Klein, U., Bieback, K., Northoff, H., Schäfer, R. (2013). Phenotype, donor age and gender affect function of human bone marrow-derived mesenchymal stromal cells. *BMC Med.* 11 (1).

Smelser, G.K., Polack, F.M., Ozanics, V. (1965). Persistence of donor collagen in corneal transplants. *Exp. Eye Res.* 4 (4), 349-IN8.

Smith, P.K., Krohn, R.I., Hermanson, G.T., Mallia, A.K., Gartner, F.H., Provenzano, M.D., Fujimoto, E.K., Goeke, N.M., Olson, B.J., Klenk, D.C. (1985). Measurement of protein using bicinchoninic acid. *Anal. Biochem.* 150 (1), 76–85.

Sorkio, A., Koch, L., Koivusalo, L., Deiwick, A., Miettinen, S., Chichkov, B., Skottman, H. (2018). Human stem cell based corneal tissue mimicking structures using laser-assisted 3D bioprinting and functional bioinks. *Biomaterials*. 171, 57–71.

Steiglitz, B.M., Kreider, J.M., Frankenburg, E.P., Pappano, W.N., Hoffman, G.G., Meganck, J.A., Liang, X., Höök, M., Birk, D.E., Goldstein, S.A., Greenspan, D.S. (2006). Procollagen C Proteinase Enhancer 1 Genes Are Important Determinants of the Mechanical Properties and Geometry of Bone and the Ultrastructure of Connective Tissues. *Mol. Cell. Biol.* 26 (1), 238–249.

Sugrue, S.P., Zieske, J.D. (1997). ZO1 in corneal epithelium: Association to the zonula occludens and adherens junctions. *Exp. Eye Res.* 64 (1), 11–20.

Sun, M., Chen, S., Adams, S.M., Florer, J.B., Liu, H., Kao, W.W.-Y., Wenstrup, R.J., Birk, D.E. (2011). Collagen V is a dominant regulator of collagen fibrillogenesis: dysfunctional regulation of structure and function in a corneal-stroma-specific Col5a1-null mouse

model. *J. Cell Sci.* 124 (23), 4096–4105.

Sun, M., Zafrullah, N., Devaux, F., Hemmavanh, C., Adams, S., Ziebarth, N.M., Koch, M., Birk, D.E., Espana, E.M. (2020). Collagen XII is a regulator of corneal stroma structure and function. *Investig. Ophthalmol. Vis. Sci.* 61 (5).

Sun, Y., Dos Santos, A., Balayan, A., Deng, S.X. (2020). Evaluation of Cryopreservation Media for the Preservation of Human Corneal Stromal Stem Cells. *Tissue Eng. - Part C Methods*. 26 (1), 37–43.

Svec, D., Tichopad, A., Novosadova, V., Pfaffl, M.W., Kubista, M. (2015). How good is a PCR efficiency estimate: Recommendations for precise and robust qPCR efficiency assessments. *Biomol. Detect. Quantif.* 3, 9–16.

Syed-Picard, F.N., Du, Y., Hertsenberg, A.J., Palchesko, R., Funderburgh, M.L., Feinberg, A.W., Funderburgh, J.L. (2016). Scaffold-free tissue engineering of functional corneal stromal tissue. *J. Tissue Eng. Regen. Med.*

Syed-Picard, F.N., Du, Y., Lathrop, K.L., Mann, M.M., Funderburgh, M.L., Funderburgh, J.L. (2015). Dental pulp stem cells: a new cellular resource for corneal stromal regeneration. *Stem Cells Transl. Med.* 4, 276–285.

Takahara, K., Kessler, E., Biniaminov, L., Brusel, M., Eddy, R.L., Jani-Sait, S., Shows, T.B., Greenspan, D.S. (1994). Type I procollagen COOH-terminal proteinase enhancer protein: identification, primary structure, and chromosomal localization of the cognate human gene (PCOLCE). *J. Biol. Chem.* 269 (42), 26280–26285.

Tamiello, C., Buskermolen, A.B.C., Baaijens, F.P.T., Broers, J.L.V., Bouten, C.V.C. (2016). Heading in the Right Direction: Understanding Cellular Orientation Responses to Complex Biophysical Environments. *Cell. Mol. Bioeng.* 9 (1), 12–37.

Tasheva, E.S., Koester, A., Paulsen, A.Q., Garrett, A.S., Boyle, D.L., Davidson, H.J., Song, M., Fox, N., Conrad, G.W. (2002). Mimecan/osteoglycin-deficient mice have collagen fibril abnormalities. *Mol. Vis.* 8 (September), 407–415.

Then, K.Y., Yang, Y., Ahearne, M., El Haj, A.J. (2011). Effect of microtopographical cues on human keratocyte orientation and gene expression. *Curr. Eye Res.* 36 (2), 88–93.

Thurston, A.J. (2007). Paré and prosthetics: The early history of artificial limbs, in: ANZ Journal of Surgery. COWLISHAW SYMPOSIUM, pp. 1114–1119.

Torbet, J., Malbouyres, M., Builles, N., Justin, V., Roulet, M., Damour, O., Oldberg, Å., Ruggiero, F., Hulmes, D.J.S. (2007). Tissue engineering of the cornea: Orthogonal scaffold of magnetically aligned collagen lamellae for corneal stroma reconstruction. *Annu. Int. Conf. IEEE Eng. Med. Biol. - Proc.* 28, 6399.

Torricelli, A.A.M., Santhanam, A., Wu, J., Singh, V., Wilson, S.E. (2016). The corneal fibrosis response to epithelial–stromal injury. *Exp. Eye Res.* 142, 110–118.

Torricelli, A.A.M., Singh, V., Agrawal, V., Santhiago, M.R., Wilson, S.E. (2013). Transmission electron microscopy analysis of epithelial basement membrane repair in rabbit corneas with haze. *Investig. Ophthalmol. Vis. Sci.* 54 (6), 4026–4033.

Torricelli, A.A.M., Wilson, S.E. (2014). Cellular and extracellular matrix modulation of corneal stromal opacity. *Exp. Eye Res.* 129, 151–160.

Tsiapalis, D., De Pieri, A., Spanoudes, K., Sallent, I., Kearns, S., Kelly, J.L., Raghunath, M., Zeugolis, D.I. (2020). The synergistic effect of low oxygen tension and macromolecular crowding in the development of extracellular matrix-rich tendon equivalents. *Biofabrication*. 12 (2).

Turk, V., Stoka, V., Vasiljeva, O., Renko, M., Sun, T., Turk, B., Turk, D. (2012). Cysteine cathepsins: From structure, function and regulation to new frontiers. *Biochim. Biophys. Acta - Proteins Proteomics*.

Uchida, S., Yokoo, S., Yanagi, Y., Usui, T., Yokota, C., Mimura, T., Araie, M., Yamagami, S., Amano, S. (2005). Sphere Formation and Expression of Neural Proteins by Human Corneal Stromal Cells In Vitro. *Investig. Opthalmology Vis. Sci.* 46 (5), 1620.

Uno, Y., Omoto, T., Goto, Y., Asai, I., Nakamura, M., Maitani, T. (2001). Molecular weight distribution of carrageenans studied by a combined gel permeation/inductively coupled plasma (GPC/ICP) method. *Food Addit. Contam.* 18 (9), 763–772.

Vandesompele, J., De Preter, K., Pattyn, F., Poppe, B., Van Roy, N., De Paepe, A., Speleman, F. (2002). Accurate normalization of real-time quantitative RT-PCR data by geometric averaging of multiple internal control genes. *Genome Biol.* 3 (7), research0034.1.

Vrana, N.E., Builles, N., Hindie, M., Damour, O., Aydinli, A., Hasirci, V. (2008). Contact guidance enhances the quality of a tissue engineered corneal stroma. *J. Biomed. Mater. Res. Part A*. 84A (2), 454–463.

Wagner, W., Bork, S., Horn, P., Krunic, D., Walenda, T., Diehlmann, A., Benes, V., Blake, J., Huber, F.X., Eckstein, V., Boukamp, P., Ho, A.D. (2009). Aging and replicative senescence have related effects on human stem and progenitor cells. *PLoS One*. 4 (6).

Wagner, W., Horn, P., Castoldi, M., Diehlmann, A., Bork, S., Saffrich, R., Benes, V., Blake, J., Pfister, S., Eckstein, V., Ho, A.D. (2008). Replicative senescence of mesenchymal stem cells: A continuous and organized process. *PLoS One*. 3 (5).

Walther, B., Lorén, N., Nydén, M., Hermansson, A.M. (2006). Influence of κ-carrageenan gel structures on the diffusion of probe molecules determined by transmission electron

microscopy and NMR diffusometry. *Langmuir*. 22 (19), 8221–8228.

Wang, S., Ghezzi, C.E., Gomes, R., Pollard, R.E., Funderburgh, J.L., Kaplan, D.L. (2017). In vitro 3D corneal tissue model with epithelium, stroma, and innervation. *Biomaterials*. 112, 1–9.

Wee, B., Pietras, A., Ozawa, T., Bazzoli, E., Uhrbom, L., Forsberg-nilsson, K., Djaballah, H., Michor, F. (2016). ABCG2 regulates self-renewal and stem cell marker expression but not tumorigenicity or radiation resistance of glioma cells. *Nat. Publ. Gr.* (April), 1–9.

Wells, R.G. (2008). The role of matrix stiffness in regulating cell behavior. *Hepatology*. 47 (4), 1394–1400.

Wen, C.K., Goh, M.C. (2006). Fibrous long spacing type collagen fibrils have a hierarchical internal structure. *Proteins Struct. Funct. Genet.* 64 (1), 227–233.

Wentz-Hunter, K., Cheng, E.L., Ueda, J., Sugar, J., Yue, B.Y.J.T. (2001). Keratocan Expression Is Increased in the Stroma of Keratoconus Corneas. *Mol. Med.* 7 (7), 470–477.

West-Mays, J.A., Dwivedi, D.J. (2006). The keratocyte: Corneal stromal cell with variable repair phenotypes. *Int. J. Biochem. Cell Biol.* 38 (10), 1625–1631.

White, J., Werkmeister, J.A., Ramshaw, J.A.M., Birk, D.E. (1997). Organization of fibrillar collagen in the human and bovine cornea: collagen types V and III. *Connect. Res.* 36 (0300–8207), 165–174.

Wiberg, C., Heinegård, D., Wenglén, C., Timpl, R., Mörgelin, M. (2002). Biglycan organizes collagen VI into hexagonal-like networks resembling tissue structures. *J. Biol. Chem.* 277 (51), 49120–49126.

Wijnholds, J. (2019). "Basal Cell Migration" in Regeneration of the Corneal Wound-Bed. *Stem Cell Reports*.

Williamson, K., Cooper, G., Lee, K., Beamish, E., Simpson, D., Carter, A., Gumbs, J., Cheung, G., Brown, D., Pettitt, R., Comerford, E., Clegg, P., Canty-Laird, E. (2020). Active synthesis of collagen (I) homotrimer and matrisomal proteins in Dupuytren's fibrosis. *bioRxiv*. 2020.07.13.195107.

Wilson, S.E. (2020). Corneal wound healing. *Exp. Eye Res.* 197 (May), 108089.

Wilson, S.E., He, Y.G., Weng, J., Li, Q., McDowall, A.W., Vital, M., Chwang, E.L. (1996). Epithelial injury induces keratocyte apoptosis: Hypothesized role for the interleukin-1 system in the modulation of corneal tissue organization and wound healing. *Exp. Eye Res.* 62 (4), 325–338.

Wilson, S.E., Mohan, Rahul R., Mohan, Rajiv R., Ambrósio, R., Hong, J.W., Lee, J.S. (2001). The corneal wound healing response: Cytokine-mediated interaction of the epithelium,

stroma, and inflammatory cells. *Prog. Retin. Eye Res.*

Wilson, S.E., Netto, M., Ambrósio, R. (2003). Corneal cells: chatty in development, homeostasis,wound healing, and disease. *Am. J. Ophthalmol.*

Wilson, S.L., Wimpenny, I., Ahearne, M., Rauz, S., El Haj, A.J., Yang, Y. (2012). Chemical and topographical effects on cell differentiation and matrix elasticity in a corneal stromal layer model. *Adv. Funct. Mater.* 22 (17), 3641–3649.

Wray, L.S., Orwin, E.J. (2009). Recreating the microenvironment of the native cornea for tissue engineering applications. *Tissue Eng Part A*. 15 (7), 1463–1472.

Wu, J., Du, Y., Mann, M.M., Funderburgh, J.L., Wagner, W.R. (2014a). Corneal stromal stem cells versus corneal fibroblasts in generating structurally appropriate corneal stromal tissue. *Exp. Eye Res.* 120, 71–81.

Wu, J., Du, Y., Mann, M.M., Yang, E., Funderburgh, J.L., Wagner, W.R. (2013). Bioengineering organized, multilamellar human corneal stromal tissue by growth factor supplementation on highly aligned synthetic substrates. *Tissue Eng. Part A*. 19 (17–18), 2063–75.

Wu, J., Du, Y., Watkins, S.C., Funderburgh, J.L., Wagner, W.R. (2012). The engineering of organized human corneal tissue through the spatial guidance of corneal stromal stem cells. *Biomaterials*. 33 (5), 1343–1352.

Wu, J., Rnjak-Kovacina, J., Du, Y., Funderburgh, M.L., Kaplan, D.L., Funderburgh, J.L. (2014b). Corneal stromal bioequivalents secreted on patterned silk substrates. *Biomaterials*. 35 (12), 3744–3755.

Xu, Y., Rivas, J.M., Brown, E.L., Liang, X., Höök, M. (2004). Virulence potential of the staphylococcal adhesin CNA in experimental arthritis is determined by its affinity for collagen. *J. Infect. Dis.* 189 (12), 2323–2333.

Yam, G.H.-F., Yusoff, N.Z.B.M., Kadaba, A., Tian, D., Myint, H.H., Beuerman, R.W., Zhou, L., Mehta, J.S. (2015). Ex Vivo Propagation of Human Corneal Stromal "Activated Keratocytes" for Tissue Engineering. *Cell Transplant.* 24 (9), 1845–1861.

Yam, G.H.F., Riau, A.K., Funderburgh, M.L., Mehta, J.S., Jhanji, V. (2020). Keratocyte biology. *Exp. Eye Res.*

Yam, G.H.F., Teo, E.P.W., Setiawan, M., Lovatt, M.J., Yusoff, N.Z.B.M., Fuest, M., Goh, B.T., Mehta, J.S. (2018). Postnatal periodontal ligament as a novel adult stem cell source for regenerative corneal cell therapy. *J. Cell. Mol. Med.* 22 (6), 3119–3132.

Yamauchi, M., Sricholpech, M. (2012). Lysine post-translational modifications of collagen. *Essays Biochem.* 52 (1), 113–133.

Yan, J., Qiang, L., Gao, Y., Cui, X., Zhou, H., Zhong, S., Wang, Q., Wang, H. (2012). Effect of fiber alignment in electrospun scaffolds on keratocytes and corneal epithelial cells behavior. *J. Biomed. Mater. Res. - Part A*. 100 A (2), 527–535.

Yang, Y.H.K., Ogando, C.R., Wang See, C., Chang, T.Y., Barabino, G.A. (2018). Changes in phenotype and differentiation potential of human mesenchymal stem cells aging in vitro. *Stem Cell Res. Ther.* 9 (1), 131.

Ye, J., Yao, K., Kim, J.C. (2006). Mesenchymal stem cell transplantation in a rabbit corneal alkali burn model: Engraftment and involvement in wound healing. *Eye*. 20 (4), 482–490.

Young, B.B., Zhang, G., Koch, M., Birk, D.E. (2002). The roles of types XII and XIV collagen in fibrillogenesis and matrix assembly in the developing cornea. *J. Cell. Biochem.* 87 (2), 208–220.

Young, R.D., Knupp, C., Koudouna, E., Ralphs, J.R., Ma, Y., Lwigale, P.Y., Jester, J. V., Quantock, A.J. (2019). Cell-independent matrix configuration in early corneal development. *Exp. Eye Res.* 107772.

Young, R.D., Knupp, C., Pinali, C., Png, K.M.Y., Ralphs, J.R., Bushby, A.J., Starborg, T., Kadler, K.E., Quantock, A.J. (2014). Three-dimensional aspects of matrix assembly by cells in the developing cornea. *Proc. Natl. Acad. Sci.* 111 (2), 687–692.

Zaki, A.A., Elalfy, M.S., Said, D.G., Dua, H.S. (2015). Deep anterior lamellar keratoplasty - Triple procedure: A useful clinical application of the pre-Descemet's layer (Dua's layer). *Eye*. 29 (3), 323–326.

Zeiger, A.S., Loe, F.C., Li, R., Raghunath, M., van Vliet, K.J. (2012). Macromolecular crowding directs extracellular matrix organization and mesenchymal stem cell behavior. *PLoS One*. 7 (5).

Zellin, G., Linde, A. (2000). Effects of recombinant human fibroblast growth factor-2 on osteogenic cell populations during orthopic osteogenesis in vivo. *Bone*. 26 (2), 161–168.

Zhang, B., Xue, Q., Li, J., Ma, L., Yao, Y., Ye, H., Cui, Z., Yang, H. (2019). 3D bioprinting for artificial cornea: Challenges and perspectives. *Med. Eng. Phys.* 71, 68–78.

Zhang, G., Chen, S., Goldoni, S., Calder, B.W., Simpson, H.C., Owens, R.T., McQuillan, D.J., Young, M.F., Iozzo, R. V., Birk, D.E. (2009). Genetic evidence for the coordinated regulation of collagen fibrillogenesis in the cornea by decorin and biglycan. *J. Biol. Chem.* 284 (13), 8888–8897.

Zhang, S., Espandar, L., Imhof, K., Bunnell, B. (2013). Differentiation of human adipose-derived stem cells along the keratocyte lineage in vitro. *J. Clin. Exp. Ophthalmol.* 4 (270).

Zhang, W., Chen, J., Backman, L.J., Malm, A.D., Danielson, P. (2016). Surface Topography and Mechanical Strain Promote Keratocyte Phenotype and Extracellular Matrix Formation in a Biomimetic 3D Corneal Model. *Adv. Healthc. Mater.* 1601238.

Zhou, L., Huang, L.Q., Beuerman, R.W., Grigg, M.E., Li, S.F.Y., Chew, F.T., Ang, L., Stern, M.E., Tan, D. (2004). Proteomic analysis of human tears: Defensin expression after ocular surface surgery. *J. Proteome Res.* 3 (3), 410–416.

Zhou, S., Greenberger, J.S., Epperly, M.W., Goff, J.P., Adler, C., Leboff, M.S., Glowacki, J. (2008). Age-related intrinsic changes in human bone-marrow-derived mesenchymal stem cells and their differentiation to osteoblasts. *Aging Cell*. 7 (3), 335–343.

Zhou, S., Schuetz, J.D., Bunting, K.D., Colapietro, A.-M., Sampath, J., Morris, J.J., Lagutina, I., Grosveld, G.C., Osawa, M., Nakauchi, H., Sorrentino, B.P. (2001). The ABC transporter Bcrp1/ABCG2 is expressed in a wide variety of stem cells and is a molecular determinant of the side-population phenotype. *Nat. Med.* 7 (9), 1028–1034.

Zimmermann, D.R., Trüeb, B., Winterhalter, K.H., Witmer, R., Fischer, R.W. (1986). Type VI collagen is a major component of the human cornea. *FEBS Lett.* 197 (1–2), 55–58.